U(IV)-Silicate Colloids and their Interactions with Sr in Natural and Engineered Alkaline Environments

A thesis submitted to the University of Manchester for the degree of Doctor of Philosophy in the Faculty of Science and Engineering

2018

Thomas S Neill

School of Earth and Environmental Sciences

Contents

List of Figures

Chapter 2: Literature review

Chapter 3: Experimental Methodology

Chapter 4: Stability, composition and core-shell particle structure of uranium(IV)-silicate colloids

Chapter 5: Interactions of Sr with UO_2 and U(IV)-silicate phases

Supporting Information

Chapter 6: Impact of carbonation on U(IV)-silicate particle stability and capacity for Sr sorption relevant to effluent treatment

Appendix 1: UV-vis spectra

List of Tables

Chapter 2: Literature review

Chapter 3: Experimental Methodology

Chapter 4: Stability, composition and core-shell particle structure of uranium(IV)-silicate colloids

Supporting Information

Chapter 5: Interactions of Sr with UO_2 and U(IV)-silicate phases

Supporting Information

Chapter 6: Impact of carbonation on U(IV)-silicate particle stability and capacity for Sr sorption relevant to effluent treatment

List of Abbreviations

AGR	Advanced gas-cooled reactor
BST	Bulk storage tank
CMS	Corroded Magnox sludge
DF	Decontamination factor
DIW	Deionised water
DLS	Dynamic light scattering
DLVO theory	Derjaguin, Landau, Verwey and Overbeek's theory of colloid stability
EDX	Energy dispersive X-ray
EELS	Electron energy loss spectroscopy
EXAFS	Extended X-ray absorption fine structure
FENAC	Facility for environmental nanoscience analysis and characterisation
FGMSP	First generation Magnox storage pond
FT-IR	Fourier Transform Infra-Red
GDF	Geological disposal facility
HAADF	High angle annular dark field
HEXS	High energy X-ray scattering
HLW	High level waste
ICP-AES	Inductively coupled plasma atomic emission spectroscopy
ICP-MS	Inductively coupled plasma mass spectrometry
ILW	Intermediate level waste
kDa	Kilodalton (a measure of atomic weight)
LLW	Low level waste
MOX	Mixed oxide fuel
PDF	Pair distribution function
PES	Polyethersulfone
pH_{pzc}	pH of the point of zero charge
ppb	Parts per billion
ppm	Parts per million
PWR	Pressurised water reactor
SAED	Selected area electron diffraction
SAXS	Small angle X-ray scattering

SIT	Specific ion theory
SIXEP	Site ion exchange effluent plant
SNF	Spent nuclear fuel
STEM	Scanning transmission electron microscopy
TEM	Transmission electron microscopy
UV-vis	Ultraviolet-visible spectroscopy
VLLW	Very low level waste
XANES	X-ray absorption near edge structure
XAS	X-ray absorption spectroscopy
XPS	X-ray photoelectron spectroscopy
XRD	X-ray diffraction

Abstract

Colloids have the potential to enhance the mobility of radionuclides in a range of scenarios, including legacy spent nuclear fuel storage facilities at sites such as Sellafield, UK. Some of the spent nuclear fuel stored in these facilities has corroded, resulting in the formation of corroded sludge. A greater understanding of the radionuclide speciation in these legacy facilities is required to predict radionuclide behaviour during sludge retrieval operations and decommissioning activities. Of particular interest is the highly abundant U and ^{90}Sr, a high yield fission product with high specific activity. Colloid formation may increase radionuclide migration within effluent plants, including the site ion exchange effluent plant (SIXEP).

In this study the formation, stability and structure of U(IV) silicate colloids, and the interactions of Sr with UO_2 and U(IV)-silicate phases was investigated. Particle size and colloidal stability were examined using ultrafiltration, SAXS and DLS. Colloids were stable at pH 6-10.5 when silicate concentrations exceeded those of U, and formed particles <10 nm. The colloids were more stable and less prone to aggregation under higher silicate concentrations. A combination EXAFS and PDF suggested a core-shell structure for these colloidal particles with a crystalline, 1.5 nm UO_2 core coated by a poorly ordered, silicate rich, U(IV)-silicate shell. Additionally, UO_2 and U(IV)-silicate were both shown to interact strongly with Sr, with UO_2 showing higher Sr sorption than U(IV)-silicate. EXAFS, TEM and desorption studies indicated Sr incorporated into the surface of UO_2 at pH >10 and formed Sr-silicates at pH >10 in the presence of U(IV)-silicate. The effect of CO_2 gassing on U(IV)-silicate with sorbed Sr was also investigated as CO_2 gassing is an important step in SIXEP that reduces the pH of effluents from ~11.5 to 7. CO_2 gassing resulted in immediate desorption of the majority of Sr from the U(IV)-silicate but also mobilisation of U(IV)-silicate colloid and increased dissolved U(IV) over 8 days, indicating that carbonation is successful in desorbing Sr but may mobilise U(IV). These results indicate that it is important to consider U(IV)-silicate colloids and UO_2 when assessing radionuclide mobility, particularly for ^{90}Sr. The improved understanding of U(IV)-silicate colloid particle structure and formation, and previously unknown Sr-U(IV) interactions are crucial to predicting radionuclide speciation and behaviour during nuclear decommissioning.

Declaration

The author of this thesis declares that no portion of the work referred to in the thesis has been submitted in support of an application for another degree or qualification of this or any other university or other institute of learning.

Copyright statement

i. The author of this thesis (including any appendices and/or schedules to this thesis) owns certain copyright or related rights in it (the “Copyright”) and s/he has given The University of Manchester certain rights to use such Copyright, including for administrative purposes.

ii. Copies of this thesis, either in full or in extracts and whether in hard or electronic copy, may be made only in accordance with the Copyright, Designs and Patents Act 1988 (as amended) and regulations issued under it or, where appropriate, in accordance with licensing agreements which the University has from time to time. This page must form part of any such copies made.

iii. The ownership of certain Copyright, patents, designs, trademarks and other intellectual property (the “Intellectual Property”) and any reproductions of copyright works in the thesis, for example graphs and tables (“Reproductions”), which may be described in this thesis, may not be owned by the author and may be owned by third parties. Such Intellectual Property and Reproductions cannot and must not be made available for use without the prior written permission of the owner(s) of the relevant Intellectual Property and/or Reproductions.

iv. Further information on the conditions under which disclosure, publication and commercialisation of this thesis, the Copyright and any Intellectual Property and/or Reproductions described in it may take place is available in the University IP Policy (see http://documents.manchester.ac.uk/DocuInfo.aspx?DocID=24420), in any relevant Thesis restriction declarations deposited in the University Library, The University Library’s regulations (see http://www.library.manchester.ac.uk/about/regulations/) and in The University’s policy on Presentation of Theses

Acknowledgements

First of all, I would like to thank my supervisors Sam Shaw, Kath Morris and Carolyn Pearce for their continued help throughout the project. Their advice and perseverance through dozens of iterations of papers and proposals were crucial to the progress of the project. Furthermore their input and guidance has provided me with numerous opportunities and has been key to my personal and professional development. I also thank Sellafield Ltd. and the University of Manchester for providing the funding that made this project possible.

I am also indebted to many other people for their assistance. I thank Nick Sherriff, Nick Bryan and Simon Kellet for sharing their extensive knowledge of Sellafield, Heath Bagshaw and Arne Janssen for their TEM expertise, Paul Lythgoe for analysing countless ICP-MS and AES samples and Phil Chater for his insights into PDF.

This project involved a significant amount of time spent at synchrotrons. My thanks go to all of those people who I have spent this time with and who made it not only bearable, but enjoyable. Special mentions go to Luke, with whom I spent many a night shift, Hannah for guiding me through my first few beamtimes with patience and enthusiasm, and Josh for being my SAXS and PDF buddy.

Finally, I thank my friends and family. A massive thank you goes to all of Manchester GeoMicro who are the friendliest research group I can imagine. Thanks also to those who have played weekly SEES football and the Friday Beers group for many good times in Deaf Institute and Footage.

My parents have provided me with constant encouragement throughout, despite my inconsistent communications. Thanks to Gareth and Lee for sticking around in Manchester and being the best friends I could hope for. Lastly, I thank Charlie for her endless support and patience.

Chapter 1: Introduction

1.1. Project context

The UK has had a civil nuclear power programme since the opening of the Calder Hall power station in 1956. Since then, a range of different reactor types have been used in the UK including Magnox reactors, advanced gas-cooled reactors (AGRs) and pressurized water reactors (PWRs) which has led to a various different types of nuclear wastes. Sellafield, located on the west coast of Cumbria, UK, has been the hub of UK nuclear activity since the 1950s and has stored and/or reprocessed a significant amount of the UK's spent nuclear fuel (SNF). SNF has been stored in multiple facilities in the subsequent decades and waste retrieval and decommissioning for a number of older legacy storage facilities is a high priority. These facilities include SNF storage ponds such as the First Generation Magnox Storage Pond (FGMSP), and legacy silos. Due to the extended periods of time that SNF has remained in these facilities, it has undergone corrosion. Currently, the focus at Sellafield is moving from waste reprocessing towards decommissioning of the site and waste retrieval operations. Therefore, understanding the composition of these wastes and the potential mobility of radionuclides within effluent treatment systems is essential to understanding the potential environmental impact.

Waste streams from these legacy storage facilities are passed through one of several effluent treatment plants including the site ion exchange effluent plant (SIXEP). These effluent treatment plants remove radionuclides from waste streams to allow the safe discharge of the solutions to the Irish Sea (Gray, Jones and Smith, 1995). Effluent treatment plants also manage effluent streams from spent fuel reprocessing activities. For example, sludge and effluents from FGMSP are transferred to settling tanks. Here, large particulates precipitate and the supernatant is transferred to SIXEP, where it is processed to remove dissolved radionuclides. The processed effluent can then be discharged to the sea while the solid sludge is contained for eventual encapsulation (currently the encapsulation approach for these wastes is grouting) and long term disposal.

One major area of interest in effluent treatment is colloids, which are suspended nanoparticulate solids, typically 1-1000 nm in size. Colloidal particulates are mobile in aqueous streams and are neither a true solution species nor large, easily filterable or settling solids. This makes them difficult to remove from solution using many conventional means such as particulate settling or ion exchange, resulting in them being considered a potential vector for radionuclides not just in effluent treatment but also at nuclear contaminated sites worldwide (Kersting *et al.*, 1999; Kersting, 2013; Zänker and Hennig, 2014). There are two different types of colloid that can form; intrinsic colloids form when the element of interest (in this case the radionuclide) is integral to the particle structure, and pseudo-colloids, where the radionuclide is absorbed to a pre-existing colloidal particle. These two different colloidal forms can show very different behaviours. It is therefore essential to understand the formation of colloids under conditions relevant to SNF storage, and their behaviour within effluent treatment systems, in order to effectively predict the potential hazard they may pose in future decommissioning activities. This project focuses on the characteristics of colloidal and nanoparticulate phases likely to form in legacy SNF storage ponds containing spent Magnox fuel, and the impacts these phases may have on mobility of U(IV) and Sr.

Uranium (U) is the major component of SNF by mass, making up approximately 95% of most spent nuclear fuel inventories (excluding non-radioactive components e.g. cladding) (Bruno and Ewing, 2006; NDA, 2017a). This means that U chemistry will not just dictate the behaviour of U in SNF storage, but it may also affect the mobility of other radionuclides. Under reducing conditions U(IV) will dominate U speciation. At high pH U(IV) has very low solubility, leading to solid formation and reduced mobility of U under alkaline, reducing conditions. However, if U(IV) could form a colloid under these conditions, this would greatly increase U mobility in SNF.

This project is focused on the conditions of SNF storage ponds containing spent Magnox fuel and corroded metallic U. However, a large amount of the work can also be applied to a variety of different systems. Radionuclide mobility is of concern in a range of scenarios, including those resulting from U mining activities at sites such as a wetland in France where colloidal U was found in excess of 10,000 ppm (Wang *et al.*, 2013), U contamination of groundwaters surrounding nuclear sites such as Sellafield, UK (Sellafield Ltd, 2014) and Cs at Hanford, USA (Flury, Mathison and Harsh, 2002), and

nuclear weapons test sites, as colloids have been shown to mobilise Pu at the Nevada Test Site (Kersting *et al.*, 1999). Therefore, the fundamental, underlying scientific progress that has been achieved, particularly in Chapter 4 and Chapter 5 focusing on the structure of U(IV)-silicate particles and Sr interactions with U(IV) phases, have applications for a wide range of scenarios and are not limited to SNF storage facilities.

1.2. Aims and objectives

The aim of this project was to gain an understanding of these colloidal U(IV) particles to understand how they form and behave under a range of conditions relevant to SNF storage and the other scenarios discussed above. To do this, molecular scale investigations into particle characteristics were performed to comprehensively understand particle formation, structure and colloidal stability. Additionally, the interactions of Sr, to represent the high-yield fission product ^{90}Sr, with two relevant U(IV) phases; U(IV)-silicate and UO_2 were investigated.

The following areas of research were therefore explored:

- Identifying U(IV)-silicate colloid formation and U(IV)-silicate particle structure under the conditions found in SNF storage facilities. U(IV) colloids are known to be stabilised by silicate (Dreissig *et al.*, 2011), but their structure and stability at high pH is not yet well understood. Colloid stability at high pH and under varying silicate concentrations was explored as this is key to predicting the conditions in which these particles may be colloidal, and therefore mobile, in nuclear facilities. Furthermore, the particle structure was investigated with the aim of identifying the role of silicate in colloid stabilisation, which would lead to a better comprehension of the factors that affect colloid formation. U(IV)-silicate particles were formed at alkaline pH (9-12) under a range of silicate concentrations (0-4) and their colloidal stability was monitored over time. The molecular-scale structure of these particles was also investigated across this range of conditions to highlight the structural characteristics that lead to high colloidal stability.
- The interactions of Sr with U(IV)-silicate and UO_2. U(IV) phases have the potential to affect the mobility of ^{90}Sr, a high-yield fission product and major contributor

to radioactivity in spent nuclear fuel. If ^{90}Sr is associated with U phases within SNF, this would alter Sr behaviour and impact on predicted Sr releases during waste retrieval operations. Additionally, if Sr is associated with colloidal U phases then this could have implications for effluent treatment plants, specifically the ion exchange beds found in SIXEP. The potential capacity for Sr sorption to these colloids will be high due to their high surface area. Therefore the capacity and mechanisms of Sr sorption to U(IV)-silicate and UO_2 are key factors in the mobility of ^{90}Sr in SNF. Sr sorption to these phases was measured across a wide range of pH (4-14) and the mechanism of these interactions was investigated in order to assess the capacity and reversibility of Sr-U(IV) interactions. This included spectroscopic investigations into Sr binding on both of the phases and sorption reversibility experiments.

- The impact of carbonation on U(IV)-silicate colloids, a step in the SIXEP effluent treatment plant. Effluents will be exposed to a carbonation tower during SIXEP which reduces effluent pH to 7 and increases the carbonate content for the solution. These colloids may not be affected by a SIXEP-like carbonation reaction as previous investigations showed these colloids were stable at pH 7 (Dreissig *et al.*, 2011). If this is the case, the colloids may well persist during SIXEP treatment. Although the risk posed by a small amount of U passing through the effluent treatment plant is low, if these colloids can act as vectors for other radionuclides, such as ^{90}Sr, ^{241}Pu and ^{241}Am, then this would increase the radioactivity of these particles and also their hazard. We investigated the changes in U(IV)-silicate particle size distribution, structure and Sr sorption capacity was analysed over 8 days after carbonation to assess the stability of these particles in effluent streams.

1.3. Thesis structure

This thesis has a research chapter dedicated to each of the hypotheses discussed above. These are preceded by a review of the relevant literature and previous work within these research areas and a detailed account of the methodologies used. The chapters are broken down as follows:

Chapter 2: Literature review. The nuclear fuel cycle and nuclear waste in the UK, focussing on the legacy storage ponds and effluent treatment processes. U(IV) chemistry, mineral formation and colloid formation. Interactions of U(IV) with silicate, and silicate colloidal behaviour. Sr solution chemistry and interactions with surfaces.

Chapter 3: Methodology. Contains descriptions of all the experimental methodologies used in this project, including both theoretical and practical details.

Chapter 4: Stability, composition and core-shell particle structure of uranium(IV)-silicate colloids. Research chapter. This chapter presents the results of extensive characterisation of U(IV)-silicate colloidal nanoparticles formed under alkaline, anaerobic conditions. A multi-technique approach, including extended X-ray absorption fine structure (EXAFS) spectroscopy, pair distribution function (PDF) analysis, small angle X-ray scattering (SAXS), ultrafiltration, transmission electron microscopy (TEM), dynamic light scattering (DLS) and zeta potential, was used to identify a core-shell structure to the particles, and define and rationalise their stability range.

Chapter 5: Interactions of Sr with UO_2 and U(IV)-silicate phases. Research chapter. This chapter presents the results of investigations into the sorption behaviour of Sr when in contact with two different U(IV) phases. Ultrafiltration, TEM and EXAFS analysis were used to probe the sorption capacities for the two U(IV) phases and also the mechanisms of Sr sorption.

Chapter 6: Impact of carbonation on U(IV)-silicate particle stability and capacity for Sr sorption relevant to effluent treatment. Research chapter. This chapter combines the understanding developed in the previous two chapters to the impact of effluent treatment processes, specifically the CO_2-gassing step in SIXEP, on U(IV)-silicate colloids and their potential as vectors for ^{90}Sr. Ultrafiltration and EXAFS were used to study the changes in U(IV) particle size and structure, as well as Sr sorption behaviour.

Chapter 7: Conclusions and further work. This chapter provides a summary of the results achieved and the wider implications the work has to nuclear decommissioning and other areas. Considerations for future directions for work in this area are also outlined.

A full list of references is provided after Chapter 7. A Separate reference list is retained for research chapter 4 to maintain the journal style.

Appendices include details of UV-vis investigations into U oxidation state and a list of conference presentations.

1.4. Paper status and author contributions

Chapter 4: *Stability, composition and core-shell particle structure of uranium(IV)-silicate colloids* accepted for publication to Environmental Science and Technology in July 2018.

Author	Contributions
T. S. Neill	Principal author. All laboratory work including collection of SAXS, XRD, TEM, DLS, XAS and PDF data, experiment design and sample preparation and all data analysis.
K. Morris	Input to experimental concept, aided with XAS data collection, extensive manuscript review pre- and post-submission.
C.I. Pearce	Input to experimental concept, manuscript review pre-submission.
N. K. Sherriff	Provided information about Sellafield SNF ponds and effluent treatment systems, manuscript review pre-submission.
M. G. Burke	Aided with TEM data collection.
P. A. Chater	Aided with PDF data collection and analysis and manuscript review pre-submission.
A. Janssen	Aided with TEM data collection.
L. Natrajan	Provision of UCl_4 powder starting material.
S. Shaw	Input to experimental concept, aided with SAXS, XAS and PDF data collection, extensive manuscript review pre- and post-submission.

Chapter 5: *Interactions of Sr with UO_2 and U(IV)-silicate phases,* to be submitted to Journal of Hazardous Materials, estimated September 2018.

Author	Contributions
T. S. Neill	Principal author. All laboratory work including collection of TEM and XAS data, experiment design and sample preparation and all data analysis.
K. Morris	Input to experimental concept, aided with XAS data collection, manuscript review.

C.I. Pearce	Input to experimental concept.
N. K. Sherriff	Provided information about Sellafield SNF ponds and effluent treatment systems.
S. Shaw	Input to experimental concept, aided with XAS data collection, manuscript review.

Chapter 6: *Impact of carbonation on U(IV)-silicate particle stability and capacity for Sr sorption relevant to effluent treatment*

Author	Contributions
T. S. Neill	Principal author. All laboratory work including collection of TEM and XAS data, experiment design and sample preparation and all data analysis.
K. Morris	Input to experimental concept, aided with XAS data collection, manuscript review.
C.I. Pearce	Input to experimental concept.
N. K. Sherriff	Provided information about Sellafield SNF ponds and effluent treatment systems.
S. Shaw	Input to experimental concept, aided with XAS data collection, manuscript review.

Chapter 2: Literature review

2.1. The UK's nuclear legacy

2.1.1. The nuclear fuel cycle

Nuclear power is generated from the energy released by fission of heavy atoms e.g. U, which is typically used as the fuel for nuclear power plants and is often enriched in the fissile ^{235}U isotope. In Magnox reactors commonly used in the UK, metallic, unenriched uranium is used. Magnox, a Mg rich alloy cladding, has a composition that allows a neutron chain reaction to be sustained using non-enriched uranium. Nuclear fuel typically resides in a nuclear reactor for between 1 and 2 years, after which the fuel is generally stored in either dry or wet storage to allow for the decay of the most short-lived, radioactive isotopes (Wilson, 1996). For Magnox spent nuclear fuel (SNF), this is normally achieved through storage in ponds maintained at a high pH (11.5-13) (Crossland, 2012). While a range of approaches to managing SNF have been employed in the past, modern approaches often involve reprocessing of SNF for separation of fission products, minor actinides, and U and Pu. U and Pu are often combined into mixed oxide (MOX) fuel. MOX is either reused as nuclear fuel (in a partially closed fuel cycle) or stored prior to future disposal as part of an open fuel cycle.

The complete fuel cycle, comprises of (Wilson, 1996):

- Mining and milling uranium ore
- Isolating the uranium in the ore and enriching the ^{235}U content (if required)
- Using the fuel in a nuclear reactor
- Interim storage of SNF to allow decay of most radioactive isotopes
- Reprocessing SNF to separate uranium and plutonium from other minor actinides and fission products (for reprocessing/closed fuel cycles)
- Reusing uranium and plutonium as MOX fuel (closed fuel cycle)
- Disposal of wastes

Although the composition of SNF varies greatly depending on the initial composition and the burn up (the duration it has spent in a nuclear reactor) , it generally consists of U

(>90 %) with fission products, plutonium and minor transuranics (Crossland, 2012). Therefore, along with the cladding material that contains the fuel, U will be the most abundant component of SNF. For this reason it is important to understand uranium speciation and behaviour in SNF during both short term storage and long term disposal. Furthermore, due to its abundance, U behaviour may impact on the mobility of other radionuclides in these scenarios.

As Figure 2.1 below indicates, despite the amount of U in nuclear wastes, it is not a major contributor to the radioactivity of intermediate level waste (ILW) in the first 100,000 years after generation. The most significant contributors to the radioactivity in the first 100 years for ILW and high level waste (HLW) are activation products and fission products such as ^{90}Sr and ^{137}Cs, after which transuranics are responsible for the much of the radioactivity (Figure 2.1). These high specific activity fission products will therefore account for a large amount of the hazard posed by nuclear waste during interim storage, but are less significant over longer timescales of geological disposal.

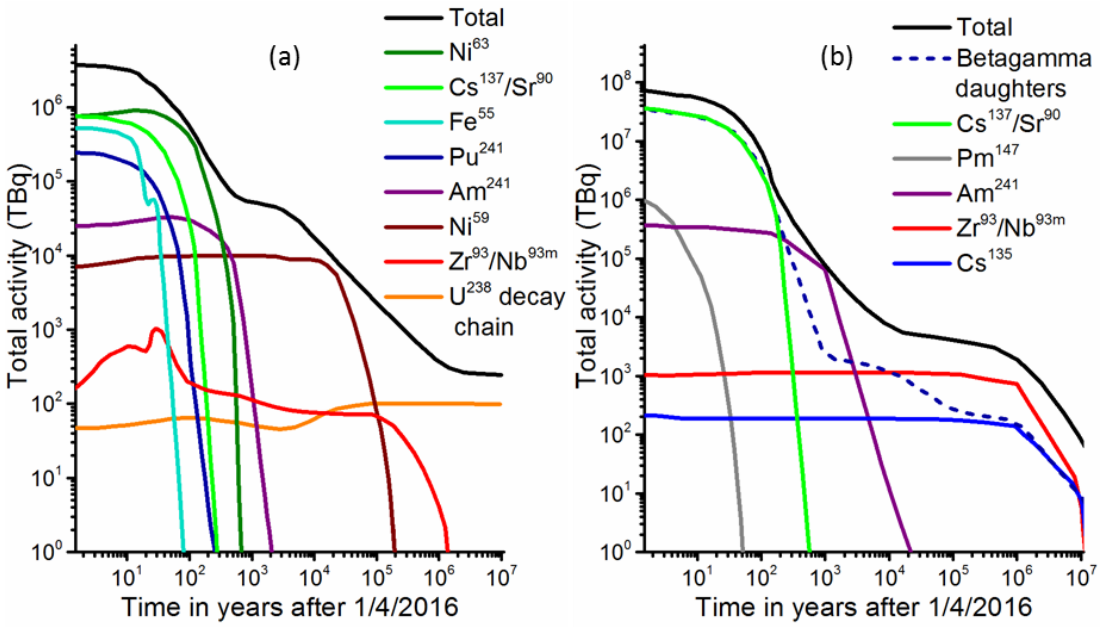

Figure 2.1: The decay activity for components of intermediate level waste (ILW) (a) and high level waste (HLW) (b) generated in the UK. Adapted from (NDA, 2017b).

2.1.2. Spent nuclear fuel storage and effluent treatment at Sellafield

The Sellafield site contains a range of facilities from across the UK's nuclear history including nuclear reactors, spent fuel storage ponds and silos, and fuel reprocessing plants. Decommissioning of the UK's nuclear legacy is a major and costly undertaking.

The majority of the cost is focussed on the decommissioning of Sellafield, which is expected to make up 74 % of the predicted total cost (NDA, 2016). One of the main targets of this decommissioning process is the retrieval of high hazard materials from Sellafield legacy ponds and silos (NDA, 2016). Legacy ponds and silos are some of the most hazardous nuclear facilities in the country (Sellafield Ltd, 2017). They are large concrete structures containing a complex mixture of fuel elements, debris, sludges and pond furniture requiring retrieval (Gregson, Hastings, *et al.*, 2011). One of these ponds, the first generation Magnox storage pond (FGMSP), is constantly purged with sodium hydroxide solution to maintain an elevated pond pH (approximately 11) and reduce radioactivity of pond effluent (Maher *et al.*, 2016). To facilitate the decommissioning of legacy facilities, waste retrieval operations will be undertaken which involve the removal of the waste from the ponds for processing, containment and disposal; the waste from these legacy facilities is not reprocessed. Due to historic issues with pond maintenance, the contents have resided in the pond for prolonged periods of time thus leading to the formation of corroded Magnox sludge (CMS), named after the Mg-rich Magnox cladding that was used for the fuel stored in the facilities. Retrievals will disturb the settled, corroded nuclear fuel which could lead to the mobilisation of certain phases from within the sludge, either as a dissolved or suspended solid species. This will result in novel waste streams for the treatment plants that handle these effluents, such as the site ion exchange effluent plant (SIXEP, Figure 2.2). An understanding of the potentially mobile phases that can form under the conditions found in these legacy storage facilities is essential to be able to predict the effectiveness of pre-existing effluent treatment processes.

There are several effluent treatment plants on the Sellafield site which are specifically designed to process the wide range of effluents generated. FGMSP effluents are processed by SIXEP which has been treating effluent from pond purges since 1985 (Gray, Jones and Smith, 1995). However, as waste retrieval operations begin to take place it is anticipated that these operations will generate effluents of different composition that will need to be processed. The main objective of SIXEP is to remove both solid and soluble radionuclides from the effluent streams, making them safe to discharge to the Irish Sea (Gray, Jones and Smith, 1995). For SIXEP to remain effective during waste retrieval and decommissioning phases it is essential to understand the composition of

the corroded SNF and radionuclide speciation in effluents. The presence of any colloidal matter in these feeds could complicate the process as colloidal particles may be mobile in effluents and would therefore be transported to SIXEP, where their interactions with the radionuclide removal processes are not well understood.

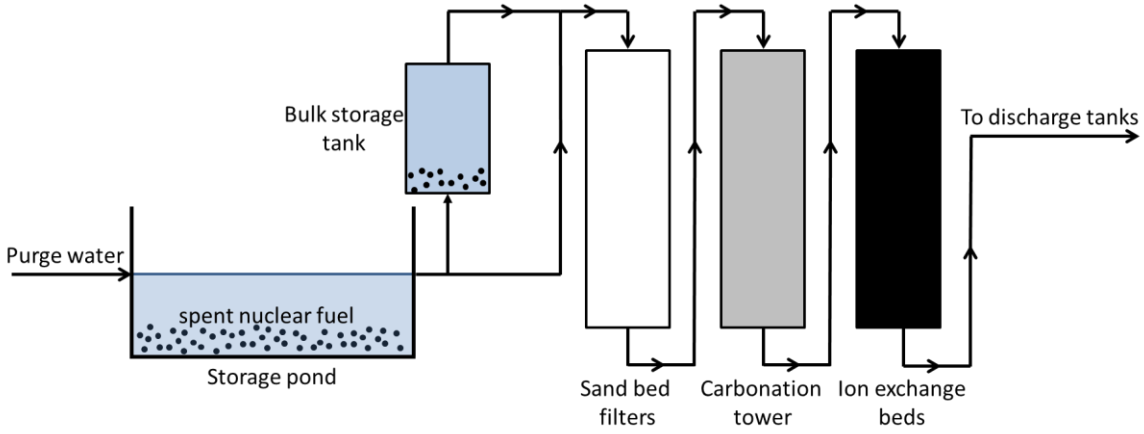

Figure 2.2: A simplified schematic of the site ion exchange effluent plant (SIXEP). Any feeds containing solids are first stored in bulk storage tanks to allow sedimentation and separation of solids and liquor. The effluent from the pond purge water passes through a sand bed filter to remove solids, before passing through a carbonation tower to lower the pH to approximately neutral. The effluent then passes through clinoptilolite ion exchange beds to remove strontium and caesium from the effluent before moving to the discharge tanks (Adapted from Parry et al. (2011)).

Interim spent fuel storage facilities such as FGMSP at the Sellafield site are maintained at a high pH to prevent corrosion of the SNF (Wilson, 1996). However, due to extended storage times, some of the SNF in legacy facilities has undergone extensive corrosion (van Veelen *et al.*, 2012). As the Magnox fuel was clad with a Mg alloy and the fuel consisted of metallic uranium, this has led to the formation of CMS. The major component of CMS is brucite ($Mg(OH)_2$), from the corrosion of the Mg rich Magnox fuel cladding, however other Mg-containing phases including hydrotalcite ($Mg_6Al_2(CO_3)(OH)_{16}.4H_2O$) like phases and possibly Mg-carbonate phases (e.g. Hydromagnesite, $Mg_5(CO_3)_4(OH)_2{\cdot}4H_2O$) and U, Pu and fission product containing phases have also been observed (Gregson, Goddard, *et al.*, 2011). These Mg phases are often present as interlocked platelets between 100 and 1000 nm in size, with brucite also known to form small colloids 1-6.5 nm in size (Pitois *et al.*, 2008; Gregson, Goddard, *et al.*, 2011; Maher *et al.*, 2016). While efforts are being made to characterise the sludge (Gregson, Goddard, *et al.*, 2011; Gregson, Hastings, *et al.*, 2011; van Veelen *et al.*, 2012), predicting the physical and chemical behaviour of CMS during waste retrieval operations

is not straightforward due to the range of components, including corroded cladding and uranium, transuranics and fission products. Additionally, it has been shown that sludges from different areas within legacy fuel storage ponds can exhibit diverse characteristics; a range particle morphologies were observed in samples from different regions (Gregson, Goddard, *et al.*, 2011). Caused by different flow levels and waste forms, these local variations illustrate the complicated nature of the characterisation of CMS and decommissioning of these facilities. Furthermore, due to the radioactivity of CMS, there are limitations in the amount of investigations that be carried out on samples. This makes it hard to predict the behaviour of CMS under the wide ranging conditions found in effluent treatment plants.

Gregson, Goddard *et al.* (2011) found the sludge had morphology consistent with brucite with elevated Al concentrations in some particulates and possibly some Mg-hydroxycarbonate phases. U, Ca, Ti Cr and Fe were found in discrete phases. The uranium encountered in this study was found to be UO_2 or similar based on Raman analysis, consistent with the corrosion of metallic uranium under anaerobic conditions (Kaminski *et al.*, 2005; Gubel *et al.*, 2013). The UO_2 particles analysed by Gregson et al were surrounded by an amorphous solid which was not identified. Fourier Transform Infra-Red (FT-IR) spectroscopy of the sludge samples indicated the presence of sorbed carbonate and a strong Si-O absorption peak at 1000 cm^{-1}. The detection of these species suggests they are collocated with uranium in CMS. Maher *et al.* (2016) recently investigated the distribution of Am and Pu in feed waters to the SIXEP plant. It was found that the majority of the Am and Pu was associated with Mg containing colloidal material 1 – 200 nm size, with Am being associated with larger particles under lower carbonate concentrations. Under high carbonate concentrations, Am was predominantly in the <1 nm (solution) and small colloidal fractions (1-6.5 nm). This is supported by a separate investigation (Gregson, Hastings, *et al.*, 2011) which also found Pu associated with the suspended solids in legacy storage pond and holding tank samples from the Sellafield site. It has been shown previously that brucite, the major component of CMS, can form colloidal species when in contact with a solution (Pitois *et al.*, 2008). As actinides, particularly An(IV) species, have a low solubility under alkaline, reducing conditions, colloids could present a transport vector for these otherwise immobile solid species present in the legacy ponds.

An investigation into the role of brucite colloids in the uptake of ^{152}Eu, an analogue of trivalent transuranics such as Am^{3+}, found that sorption to colloidal brucite was significant at low carbonate levels (< 10^{-3} M) (Pitois *et al.*, 2008). However, when Eu was exposed to bulk and colloidal brucite, preferential sorption to bulk was observed. Parry *et al.* (2011) showed Pu was removed from solution by a colloidal CMS simulant synthesised by corrosion of Magnox alloy turnings. At high pH and in the absence of carbonate the CMS simulant was most effective in removing Pu, showing a high capacity for Pu sorption. With addition of electrolyte the brucite colloid flocculated and Pu and CMS simulant were co-filtered from solution resulting in a high decontamination factor (DF, the ratio of activity prior to and after filtration). It was noted, however, that high carbonate concentrations led to a much lower DF of Pu in these systems due to the formation of Pu-CO_3 solution complexes.

To separate solid and liquid wastes in waste streams at Sellafield, particulate containing effluents from storage facilities are transferred to Bulk Storage Tanks (BSTs) for times from 10 hours to a week in order to separate solids from supernatant before the solution is processed in SIXEP (Maher *et al.*, 2016). The SIXEP process (Figure 2.2) involves several steps to facilitate removal of radionuclides from effluents, prior to disposal of the cleaned effluent to the Irish Sea (Maher *et al.*, 2016). First, sand bed filters remove particulates from the effluent. Secondly, the effluent is passed through the carbonation tower where CO_2 is bubbled through the effluent to reduce the pH from ~11 to 7 (Maher *et al.*, 2016). This is done to increase the efficiency of the ion exchange beds, which are made up of clinoptilolite ($(Na,K,Ca)_{2-3}Al_3(Al,Si)_2Si_{13}O_{36}\cdot 12H_2O$), a naturally occurring zeolite. The clinoptilolite is used as it is able to remove two major fission products, $^{137}Cs^+$ and $^{90}Sr^{2+}$, from solution selectively (Kaplun *et al.*, 1992; Minglu, Shijun and Chunkou, 1994; Borai *et al.*, 2009; Elizondo-Villarreal *et al.*, 2016). High selectivity is required due to the abundance of Ca^{2+} and Na^+ in solution from NaOH doping of the ponds and the high radioactivity of ^{90}Sr and ^{137}Cs (Wilson, 1996). It is important to note that while clinoptilolite shows high selectivity for dissolved Sr^{2+} and Cs^+ the effectiveness of clinoptilolite in removing colloidal radionuclides is unknown, meaning colloids have the potential to impact the mobility of ^{90}Sr and ^{137}Cs within SIXEP and therefore the efficiency of the plant. Furthermore, colloids will not settle out with other solids during

the settling stage in BSTs and may not be filtered out by sand bed filters, making them potentially an important factor in effluent treatment efficiency.

While the research discussed above has highlighted the potential importance of colloids for the transport of a range of radionuclides in alkaline SNF storage, there has been limited characterisation of the colloids. Understanding the structure and stability of the colloids that could form is needed in order to predict their behaviour under the wide ranging conditions found across sites such as Sellafield. This knowledge will also be applicable to the similar conditions found in geological disposal facilities, which are discussed below.

2.1.3. Geological disposal of nuclear waste

Alongside decommissioning of existing nuclear sites, the long-term disposal of nuclear waste is another major challenge for the nuclear industry. Nuclear waste is classified as one of the following, based on the level of radioactivity; very low level waste (VLLW), low level waste (LLW) intermediate level waste (ILW) or High level waste (HLW). Once the spent fuel has been removed from the legacy storage ponds, it will be separated from pond liquor and contained in preparation for long term geodisposal with ILW and HLW. In the UK VLLW and LLW is disposed of at the low level waste repository (Defra, 2007). The planned method for long term disposal of SNF, ILW and HLW internationally is a Geological Disposal Facility (GDF), an underground facility at a depth of between 200 and 1000 m below the surface, depending on the host geology (Department of Energy & Climate change, 2014). The GDF will use a multi-barrier approach to waste containment over the planned 100,000 – 1,000,000 years required for the waste to decay to background radioactivity (Department of Energy & Climate change, 2014). These barriers include the wasteform itself (e.g. the glass wasteform for vitrified waste), the waste container, which would be made up of steel or copper, a bentonite or cementitious backfill and the host geology (RWM, 2008; Hicks, White and Hooker, 2009; Department of Energy & Climate change, 2014)(Figure 2.3).

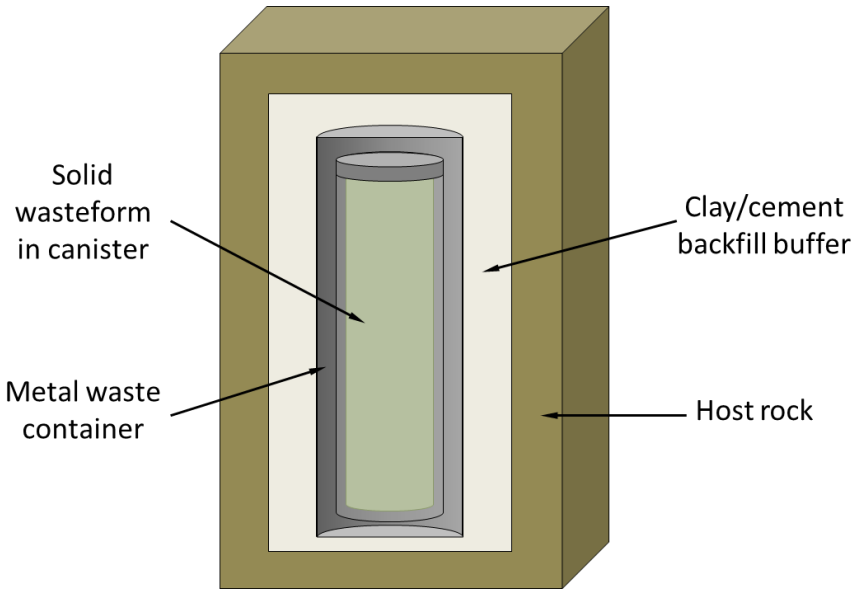

Figure 2.3: Schematic of the multi-barrier concept for the geological disposal of high level waste. The waste will be contained within a canister, which in turn is in a metal waste container. This container is then surrounded by a backfill of either cement or clay. Finally, the host geology of the site will also act as a barrier to incoming groundwater and any mobilised radionuclides.

Research around GDF capability and the safety case focusses on the mobility of radionuclides within the groundwater that will eventually permeate the multi-barrier system (RWM, 2008). As the aim of a GDF is to contain the radioactivity of the nuclear waste for sufficient time that it decays to background levels (>100,000 years), the mobilisation of radionuclides is the biggest concern for the safety case of a GDF. Radionuclides within the GDF could be mobilised via a number of routes; dissolution of the solid matrix into a stable dissolved species, formation of colloids, suspended nanoparticulate matter that is mobile within an aqueous system, or pseudocolloids, where the radionuclide is bound to a pre-existing colloid (Hicks, White and Hooker, 2009). To be able to understand whether radionuclide migration will occur, each of these scenarios must be comprehensively investigated.

Under geological disposal conditions, it is anticipated that eventual groundwater intrusion into the system will result in the formation of a cementitious plume (in cement backfilled repositories) (Beattie and Williams, 2012). This plume would initially have a high pH of ~12.5 which would eventually dilute leading to a reduction in alkalinity (Small and Thompson, 2009). In the wasteforms, there will be an abundance of metallic components, such as steel or copper waste canisters and possibly fuel cladding and building material. It is likely that subsequent to the intrusion of groundwater, the GDF

will initially be anaerobic due to the corrosion of these materials and the low O_2 levels in deep groundwaters (Beattie and Williams, 2012). A range of backfill materials and host geologies have been investigated for GDFs worldwide and the preferences vary between the countries (RWM, 2008; Department of Energy & Climate change, 2014). Compacted bentonite clay is considered by many to be the best backfill material due to its low porosity and high availability (Hicks, White and Hooker, 2009; RWM, 2011). Understanding the behaviour of radionuclides in this environment is crucial in order to predict their mobility, which is essential for the safety case for a GDF.

The speciation of uranium in a GDF scenario is a major part of the safety case due to its abundance in SNF. At the basic pH anticipated in a ground water intruded GDF, many species, in particular actinides, would be expected to be insoluble. Therefore, one of the most prominent areas of interest concerning radionuclide mobility is the formation of colloids (Möri *et al.*, 2003). Bots *et al.* (2014) recently highlighted the potential for U(VI) to form colloids under high pH, cement leachate conditions. If U(IV) can also form colloids under similar conditions then this would mean uranium could be potentially mobilised under both reducing an oxic conditions. It is therefore essential to understand the behaviour and mobility of U and other radionuclides in nuclear wastes in order to safely contain and decommission nuclear sites in the short term, and safely dispose of the waste in long term geological disposal facilities. Due to the low solubilities of many radionuclides, colloids may play an important role in this.

2.2. Uranium and actinide chemistry

2.2.1. Uranium redox, solubility and solution chemistry

Many actinides have multiple stable oxidation states (Table 2.1) which exhibit a range of characteristics. The different charges of actinide ions in different oxidation states result in diverse behaviours for these elements, depending on the redox conditions. For example, the tendency of actinides to form complexes follows the trend: An^{4+}> An^{3+}≈AnO_2^{2+}>AnO_2^{+}, reflecting the effective charge on the actinide ion (Clark, Hobart and Neu, 1995). At higher oxidation states (≥ +5), actinides have a tendency to form actinyl AnO_2^{n+} complexes where n = 1, 2 or 3. Due to the covalent nature of the An=O bonds in actinyl complexes, the formation of these complexes leads to a reduction in

the effective charge of the An ion in comparison to lower valence species. For example, the effective charge on U(IV) (U^{4+}) has been calculated using a hard sphere model to be 4.37, compared to an effective charge of 3.23 for U(VI) (UO_2^{2+})(Moriyama *et al.*, 1999) resulting in a higher charge density of the lower oxidation state U^{4+} ion.

Due to the formation of actinide-water complexes in solution and the high charge density of most actinide ions, they readily undergo hydrolysis. The degree of hydrolysis is dependent on the charge to radius ratio of the actinide ion and the solution pH. Hydrolysed actinides can oligomerise to form larger particles and solids (Knope and Soderholm, 2013), often leading to very low solubilities for actinides in anything but very acidic solutions. For example, U^{4+} will readily hydrolyse in solutions with even acidic pH ($[H^+]$ < 0.1 M) resulting in formation of U(IV)-oxyhydroxide solids. U(VI), present in solution as the uranyl UO_2^{2+} species, does not undergo hydrolysis until above pH 3 because of the lower effective charge on the uranyl U(VI) than U(IV) (Clark, Hobart and Neu, 1995). This leads to the low solubility of U(IV), relative to U(VI) and hence U(IV) is often considered immobile in aqueous systems due to this low solubility and propensity to form solids.

Table 2.1: The oxidation states of the most common actinide elements. Oxidation states in bold are the most environmentally relevant. Adapted from (Clark, Hobart and Neu, 1995).

Th	Pa	U	Np	Pu	Am	Cm
			+3	**+3**	**+3**	**+3**
+4	+4	**+4**	**+4**	**+4**		
	+5	+5	**+5**	**+5**		
		+6	**+6**	**+6**		
				+7		

The most common oxidation states for the major actinides are shown in Table 2.1. For uranium, the +4 and +6 oxidation states are the most common, with U(IV) forming under reducing and anaerobic conditions and U(VI) being common in oxic environments. U(V) does exist in certain scenarios, usually in non-aqueous solvents and solid phases (Roberts *et al.*, 2017) but is not stable in solution due to the tendency to disproportionate to U(IV) and U(VI) although a recent study has suggested the rate of

this disproportionation may be slower than previously thought (Collins and Rosso, 2017).

Inorganic ligands such as carbonate (CO_3^{2-}) can dramatically increase the solubility of actinides. Carbonate is of particular relevance in SNF storage ponds, as the high pH solutions are exposed to air and therefore likely to contain carbonate from dissolution of atmospheric CO_2. It has been shown previously that the presence of carbonate can increase the solubility of the uranyl species by formation of bidentate uranyl carbonate complexes $UO_2(CO_3)_n^{2-n}$ where n = 1, 2, 3 (Grenthe *et al.*, 1984; Elless and Lee, 1998; Gorman-Lewis *et al.*, 2008). This effect has also been observed for U^{4+}, where $U(CO_3)_5^{6-}$ dominates U speciation at high carbonate concentrations (Ciavatta *et al.*, 1983; Hennig, Ikeda-Ohno, *et al.*, 2010) and $U(OH)_2(CO_3)_2^{2-}$ can be significant at lower carbonate concentrations (Rai *et al.*, 1998). In SNF storage facilities where basic, anaerobic conditions are anticipated so U(IV) will be present and likely very insoluble but carbonate complexes may increase this solubility. Solutions of 0.05 M U(IV) were possible at pH 8.3 and 1 M CO_3^{2-} due to the formation of the $[U(CO_3)_5]^{6-}$ complex. This is significantly higher than U(IV) solubility in carbonate free solutions (Figure 2.4) which rarely exceeds 10^{-7} M (Hennig, Ikeda-Ohno, *et al.*, 2010; Dreissig *et al.*, 2011). These actinide-carbonate complexes have also been observed for Np, Pu and Th (Neck and Kim, 2000; Guillaumont *et al.*, 2003; Parry *et al.*, 2011) . Due to the abundance of carbonate likely in high pH solutions relevant to SNF storage, it is important to take into account the role these complexes may have on actinide solubility and mobility.

Another ligand of interest in SNF storage and geodisposal scenarios is orthosilicate (SiO_4^{4-}), frequently simplified to silicate. Silicate is expected to be present in legacy spent fuel storage ponds due to dissolution of cement from pond walls and legacy use of non-deionized water for pond purges. In a GDF scenario, silicate will be present in the ground water ingressions, and dissolution of vitrified waste and the cement backfill. It has been shown previously that silicate can complex uranium at low concentrations in solution at the underground laboratory site, Horonobe, Japan (Kozai, Ohnuki and Iwatsuki, 2013). Although U(VI) silicates display a low solubility, resulting in the abundance of U(VI)-silicate minerals in nature e.g. weeksite ($K_2(UO_2)_2Si_6O_{15}{\cdot}4(H_2O)$) and botlwoodite ($HK(UO_2)(SiO_4){\cdot}1.5(H_2O)$), it is possible that silicate can increase the solubility of U(IV). This has been observed previously for Th(IV) with the formation of the aqueous

$Th(OH)_3(H_3SiO_4)_3^{2-}$ complex at pH 6-12 (Rai *et al.*, 2008), and has been suggested for U(IV) (Mesbah *et al.*, 2015). Interestingly, the pH range for formation of this Th-silicate complex coincides with the pH of legacy storage ponds such as FGMSP and potentially geodisposal scenarios. Figure 2.4 below shows the relative solubilities of U(IV) and U(VI) in the presence of carbonate and silicate. It can be seen that U(IV) has much lower solubilities generally than U(VI). U(VI) has higher solubilities at low (< 4) and high (> 11) pH, with a solubility minimum in all systems except carbonate at pH ~ 8. Carbonate is seen to increase U(VI) solubility, while silicate reduces solubility due to the formation of U(VI)-silicate minerals as solubility limiting phases. In the U(IV) systems, 5 mM carbonate has very little effect on U(IV) solubility despite the fact that high carbonate concentrations (1 M) can significantly increase U(IV) solubility (Hennig, Ikeda-Ohno, *et al.*, 2010). 5 mM silicate, however, increases solubility of U(IV) by up to 10^4 between pH 7 and 13.

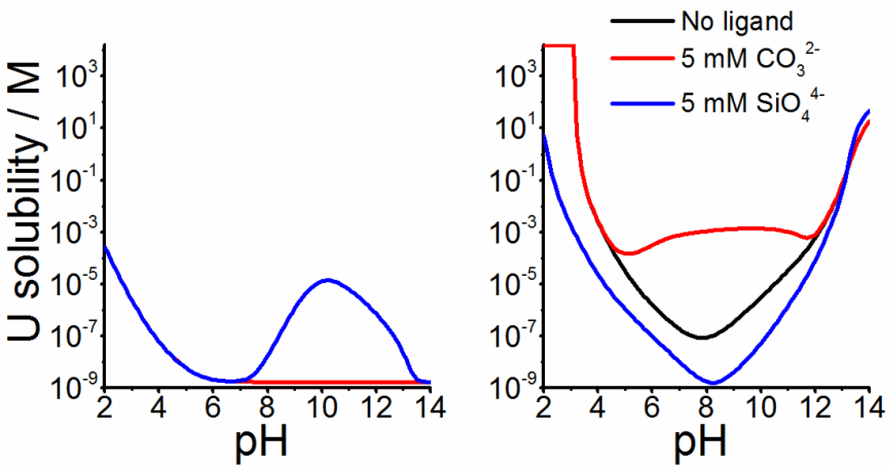

Figure 2.4: Comparisons of U(IV) (left) and U(VI) (right) solubility in the absence of complexing ligands, in the presence of 5 mM carbonate, or in the presence of 5 mM silicate. For U(IV), no ligand is overlapped by UCO_3. Solubility limiting phases used were $UO_2.2H_2O$ for all U(IV) phases, $UO_2(OH)_2$ for U(VI)-CO_3 and no ligand, and Soddyite ($(UO_2)_2SiO_4{\cdot}2H_2O$) for U(VI)-silicate system. Data is modelled using phreeqc using the SIT thermodynamic database and Mesbah *et al.* (2015).

2.2.2. Uranium mineralogy

Uranium mineralogy is a well-studied area due to the necessity for uranium as nuclear fuel. The Earth's crust contains approximately 2.7 ppm uranium (Taylor, 1964), with over 200 uranium-containing mineral species discovered (Fleischer, 1995). As mentioned previously, uranium is normally found in either the +4 or +6 oxidation states with few examples of U(V). U(VI) is found in a wide range of minerals with a complex range of

structures, whereas U(IV) minerals tend to have higher symmetry and are isostructural with other tetravalent cation containing minerals e.g. Zr^{4+} and Th^{4+} (Burns and Finch, 1999). U(IV) is generally coordinated to 6-8 ligands, with the two most common U(IV) minerals being uraninite (UO_2) and coffinite ($USiO_4$) (Figure 2.5). Uraninite, nominally UO_2 but normally found as the partially oxidised UO_{2+x}, is the most common U(IV) mineral species (Janeczek and Ewing, 1992b) with geologically aged uraninite also containing other cations e.g. Pb^{4+}, from radioactive decay of U, and Ca^{2+} via cationic substitution. Coffinite, $USiO_4 \cdot nH_2O$ where n = 0-2, is the second most abundant U(IV) mineral species (Burns and Finch, 1999). Coffinite is isostructural with zircon ($ZrSiO_4$) and cationic substitution at both the U and Si sites has been observed for a wide range of cations (Deditius *et al.*, 2010).

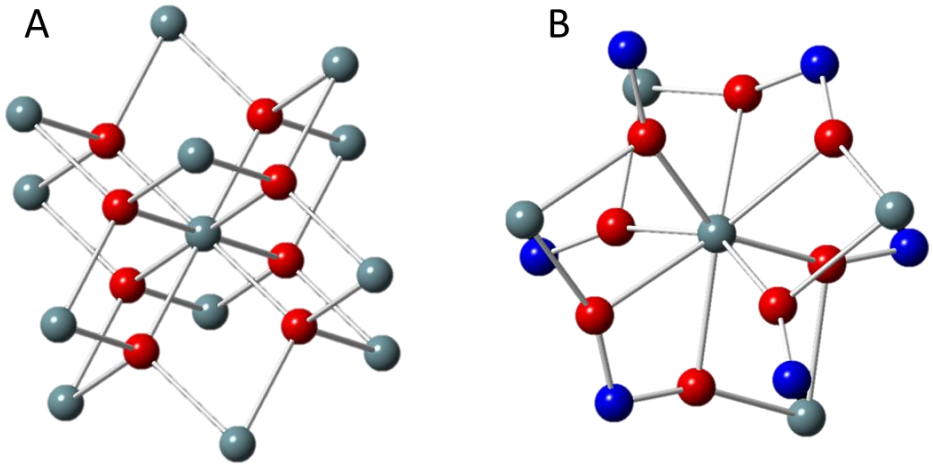

Figure 2.5: The coordination environment of U in uraninite (UO2) (A) and coffinite (USiO4) (B). Grey spheres are U, red spheres are O and blue spheres are Si.

Both uraninite and coffinite are important in the storage and geological disposal of SNF. Nuclear fuel is commonly in the form of UO_2, uraninite, or occasionally U metal which corrodes to UO_2 in the presence of water (Kaminski *et al.*, 2005; Gubel *et al.*, 2013), and this is likely to mix with silicate-rich ground waters (Amme *et al.*, 2005). This process has previously been shown to form coffinite, although the mechanism for this is poorly understood (Guo *et al.*, 2015). Whether it is a direct alteration phase of uraninite, or forms via oxidised, dissolved uranyl intermediates is not clear (Deditius, Utsunomiya and Ewing, 2008). While coffinite is abundant in nature, there have been numerous studies that highlight the difficulties in synthesising pure coffinite in the laboratory (Pointeau *et al.*, 2009; Mesbah *et al.*, 2015; Szenknect *et al.*, 2016). Studies have previously identified

mixed-phase products dominated by the thermodynamically favoured UO_2 and SiO_2 (Labs *et al.*, 2013), and recent work has identified possible colloidal and/or nanocrystalline phases responsible for the formation of coffinite in the laboratory (Mesbah *et al.*, 2015; Szenknect *et al.*, 2016). These studies into coffinite formation used synthesis conditions that coincided with those of U(IV)-silicate colloid formation (Dreissig *et al.*, 2011). Evidence of the potential contribution of colloidal particulates to coffinite formation in nature were also recently described, where U(IV)-silicate nanoparticles were present in a deep granitic aquifer containing coffinite. (Suzuki *et al.*, 2016) The evidence of nanoparticulate uranium phases in natural samples further reinforces the relevance of these particles in environmental transport of radionuclides and the range of processes they may influence.

It has been suggested that the formation of coffinite is linked to U(IV) solution complexes as well as U(IV)-silicate colloid formation (Mesbah *et al.*, 2015). The structure and thermodynamic stability of U(IV) solution complexes are not well understood, yet Mesbah *et al.* (2015) have approximated the solubility product constant for $U(OH)_3(H_3SiO_4)_3^{2-}$ based on available data for the thorium complex $Th(OH)_3(H_3SiO_4)_3^{2-}$ (Rai *et al.*, 2008). By doing this, they were able to show a pH range under which this complex is likely to form, pH 8-11, which coincides with the ideal conditions for coffinite synthesis in the laboratory. Additional work has shown that coffinite can form when UO_2 is exposed to a silicate containing solution, with [Si] > 1 mM, providing further evidence of the presence of U(IV)-silicate solution complexes (Janeczek and Ewing, 1992a). Silicate has also been shown to stabilise colloidal U(IV), Th(IV) and Np(IV), which will be discussed in more detail later (Dreissig *et al.*, 2011; Hennig *et al.*, 2013; Husar *et al.*, 2015; Zänker *et al.*, 2016).

U(VI) minerals exhibit a wider range of structures, leading to the much larger number of U(VI) minerals found in nature. U(VI) minerals generally retain the linear uranyl UO_2^{2+} cation (Evans, 1963), with a range of coordination polyhedra around the U cation from octahedral to hexagonal bipyramidal. The range of possible U(VI) coordination environments and the possibility of them coexisting within the same mineral leads to the high number of different U(VI) minerals.

2.2.3. Actinide clusters and mineral precursors

Actinides are known to form clusters between 6 and 60 actinide atoms in size. These clusters are potentially important intermediates to particle formation according to non-classical nucleation theory (Gebauer *et al.*, 2014) and consequently relevant to the formation of many solid phases. These clusters are formed by controlled hydrolysis of actinides in solutions containing capping ligands that prevent extensive hydrolysis into actinide oxyhydroxide nanoparticles. For U(IV) and Th(IV) these clusters are very small, with most consisting of less than 12 actinide atoms per cluster, and structures have been confirmed for 2 (Albrecht-Schmitt, Almond and Sykora, 2003; Natrajan *et al.*, 2005; Pohl *et al.*, 2009; Knope *et al.*, 2011), 3 (Kadish *et al.*, 1988), 4 (Calderazzo *et al.*, 1978; Rogers, Bond and Witt, 1991), 6 (Takao *et al.*, 2009), 8 (Knope *et al.*, 2012) and 12 (Nocton *et al.*, 2010) actinide atom clusters using a variety of techniques. Many of these clusters contained capping ligands such as dibenzoylmethanate (Nocton *et al.*, 2010), fomate ($HCOO^-$) (Takao *et al.*, 2009) and selenate (SeO_4^{2-}) (Knope *et al.*, 2012) which have similar properties to ligands present in the environmental or engineered scenarios such as carbonate, silicate and organics (e.g. humics), suggesting similar structures have the potential to form under more environmentally relevant conditions. Similar reactions with Pu(IV) resulted in larger, rod like structures which were found to be between 1 and 8 nm in diameter and up to 200 nm in length (Thiyagarajan *et al.*, 1990). Interestingly, a mixed oxidation state U(IV), U(V) pentamer with U-O bridges has also been identified with the authors suggesting the potential for these mixed oxidation species to be relevant to the speciation of uranium in the environment (Mougel, Pécaut and Mazzanti, 2012).

As well as small clusters, U(VI) peroxide nanoclusters made up of $([UO_2(O_2)OH]_{60})^{60-}$ core have been shown to self-assemble in U(VI)/H_2O_2 solutions (Soltis *et al.*, 2016). Recently $Fe(III)_{13}$-Keggin clusters have been identified as an important precursor in ferrihydrite formation (Weatherill *et al.*, 2016), which falls in to a wider area of research on prenucleation clusters and their relevance to particle formation (see (Gebauer *et al.*, 2014) and references therein). This work illustrates the potential importance of these small clusters to the eventual formation of larger nanoparticles, colloids and even

mineral formation as these clusters or similar structures will likely be some of the initial products of actinide hydrolysis.

2.2.4. Corrosion of metallic uranium in spent nuclear fuel

Metallic U was the fuel of choice for Magnox reactors employed in the UK and, as discussed previously in section 2.1.2., some spent Magnox fuel located in legacy wet storage facilities have undergone corrosion. In contact with water U metal is known to corrode to UO_2, generating a thin film of corrosion product (Kaminski *et al.*, 2005; Sinkov, Delegard and Schmidt, 2008). UO_2 is much less dense than U metal, meaning this corrosion results in an expansion of the surface and cracking and breaking up of the UO_2 film. Due to the formation of this UO_2 film, which coats the more reactive U metal and is rapidly replenished on the metal when cracking occurs, the kinetics of oxidation are controlled and this oxidation does not occur rapidly (Sinkov, Delegard and Schmidt, 2008). Under oxic conditions, the oxidation of UO_2 continues, forming first U_4O_9 and then U_3O_7 (Gubel *et al.*, 2013). The U oxide produced from anoxic corrosion experiments is often a very fine particulate (Sinkov, Delegard and Schmidt, 2008). Under anoxic conditions, the product of the reaction of U metal with water was believed to be slightly hyperstochiometric UO_{2+x}, where x is typically 0.08 (Hilton, 2000; Kaminski *et al.*, 2005), however more recent studies have suggested the hyperstochiometric UO_{2+x} product may be a result of the propensity for oxidation of small $UO_{2+0.00}$ particles, which are the true product of anoxic corrosion. The reaction of U metal with water releases H_2, which also leads to the formation of UH_3 from the corrosion of U metal, which in turn reacts with water to form UO_2 (Delegard and Schmidt, 2008; Sinkov, Delegard and Schmidt, 2008). From characterisation of corroded U metal sludges at Hanford, USA, a wide range of U-oxides, including UO_2, U_4O_9, U(VI) schoepites and U(VI) peroxides have been found, illustrating the complex nature of U corrosion and oxidation behaviour (Delegard and Schmidt, 2008).

Interestingly, Kaminski *et al.* (2005) showed that the corrosion of metallic U in the presence of silicate can lead to the formation of a UO_{2+x} colloid, where x = 0.08. Although it is known that U metal oxidised to UO_2 forms a nanoparticulate phase, it was expected to not be colloidal because of the tendency for aggregation in UO_2 particles, which is due to their low surface charge at near neutral pH. However, in this study the UO_{2+x}

particles only showed limited aggregation and remained in suspension over the duration of the experiment (125 days). The colloid formed in this study also showed similarities to U(IV)-silicate colloids, which are discussed more comprehensively in section 2.3.3..

2.3. Colloids

2.3.1. DLVO theory and colloid stability

Colloids are defined as particles suspended in solution with any dimension between 1 and 1000 nm in length (Hiemenz and Rajagopalan, 1997). However this definition is not absolute and particles both above and below this size range can form colloids in certain cases. Environmental colloids come from a variety of sources spanning both inorganic and organic materials. Natural and synthetic colloids have diverse applications, including physical chemistry (ion exchange) (Roy and Dzombak, 1996), environmental science (e.g. water purification) (Wolthoorn, Temminghoff and van Riemsdijk, 2004), petroleum science (oil recovery) (Thomas and Farouq Ali, 1990) and imaging technology (printing inks) (Tang, Yang and Wang, 2010). Colloids experience competition between destabilising gravitational force and random Brownian motion. In the case of a stable colloidal dispersion, these forces are in equilibrium. The small size of colloidal particles results in both small gravitational forces and significant Brownian motion, meaning the particles do not precipitate out of suspension.

There are many factors that dictate the stability of colloids. Colloids have two main routes to destabilization; they can dissolve to form a true solution, or the colloidal particles can aggregate into larger particles which may then sink out of suspension. Many colloids, in particular inorganic colloids, are thermodynamically unstable and are prone to irreversible aggregation and settling out. Their stability is generated by the kinetic stability of the system, which is caused by the electrostatic repulsion between charged surfaces (Hiemenz and Rajagopalan, 1997). As surface species will carry an overall charge at most pH, the electrostatic repulsion between these surfaces with the same charge and the double layer that is generated from this charge will be large. As a result of this there is a large kinetic barrier towards aggregation. Changing the conditions of the solution can reduce or increase this barrier. Increasing ionic strength, for example, can decrease this kinetic barrier by reduction of the electric double layer size (Figure 2.6)

and potentially cause aggregation in a previously stable colloidal system. On the other hand, addition of a surfactant, a species that stabilises the often unfavourable water-colloid surface interactions, can reduce aggregation rates in colloidal systems by reducing the thermodynamic drive for aggregation, or by sterically inhibiting aggregation (Tadros, 2011). Changing the pH of the system can either increase or decrease the stability of a colloidal system, depending on whether the change in pH increases or decreases the surface charge of the colloidal particles.

The colloid stability mentioned above is described by DLVO theory, which outlines the attractive and repulsive forces in effect in colloidal systems (Verwey, 1947; Derjaguin and Landau, 1993). The theory takes into account the attractive van der Waals forces and the repulsive electrostatic force between two charged lyophobic particles (particles that form unfavourable interactions with the solvent) which exhibit irreversible coagulation. The principles of DLVO theory can be summarised as:

1. The greater the charge potential of the double layer, the larger the interparticle repulsion will be.
2. The lower the electrolyte concentration (ionic strength of the solvent), the greater the distance from the particle surface to a major repulsion decrease.
3. A large Hamaker constant (determined by the polarisability of the interacting particles and the medium) results in a large attraction between particles.

DLVO provides an explanation for the interaction between two particles in terms of their potential energy (ϕ_T), as a product of the attractive van der Waals force (ϕ_A) and the repulsive electrostatic force (ϕ_R).

$$\phi \mathrm{T} = \phi \mathrm{A} + \phi \mathrm{R} \tag{2.1}$$

The van der Waals attraction can be described as the sum of all molecular interactions between the two particles and the molecules of a particle and the solvent, where r is the spherical particle radius, S is the distance between the particles and A is the Hamaker constant (Hiemenz and Rajagopalan, 1997).

$$\phi A = -\frac{A}{6}\left\{\frac{2r^2}{(S^2+4rS)} + \frac{2r^2}{(S^2+4rS+4r^2)} + ln\left[\frac{(S^2+4rS)}{(S^2+4rS+4r^2)}\right]\right\} \tag{2.2}$$

The electric repulsive potential can be written as:

$$\phi R = 2\pi\varepsilon\varepsilon_0 r\zeta^2 e^{-\kappa x} \quad (2.3)$$

Where ε is the solvent's dielectric constant, ε_0 is vacuum permittivity, ζ represents the zeta potential and κ is a function of the ionic concentration known as the Debeye parameter (Park and Seo, 2011), which is defined as:

$$\kappa = \left(\frac{2F^2 I \times 10^3}{\varepsilon\varepsilon_0 RT}\right)^{1/2} \quad (2.4)$$

Where *I* is the ionic strength in moles and *F* is the Faraday constant.

As the van der Waals attraction is not affected by the ionic strength (*I*), yet the repulsive electrostatic force is strongly dependent on the ionic strength of the solution, the overall potential energy is significantly affected by *I* as these two contributions will not cancel out. This means that *I* can have a significant effect on colloidal stability. *I* is a factor in electrostatic repulsion of colloids due to the formation of an electric double layer in solution, shown in Figure 2.6. The thickness of this double layer is equal to κ^{-1} in meters and therefore, according to Equation 2.4, inversely proportional to $I^{1/2}$ meaning that the double layer size and electrostatic repulsion both decrease with increasing ionic strength (Stumm and Morgan, 1995). This means that, at high *I*, the charge of the particle surface is rapidly diffused by a small, densely charged double layer which results in less interparticle repulsion. This reduces the barrier to particle coalescence and therefore results in a less stable colloidal suspension.

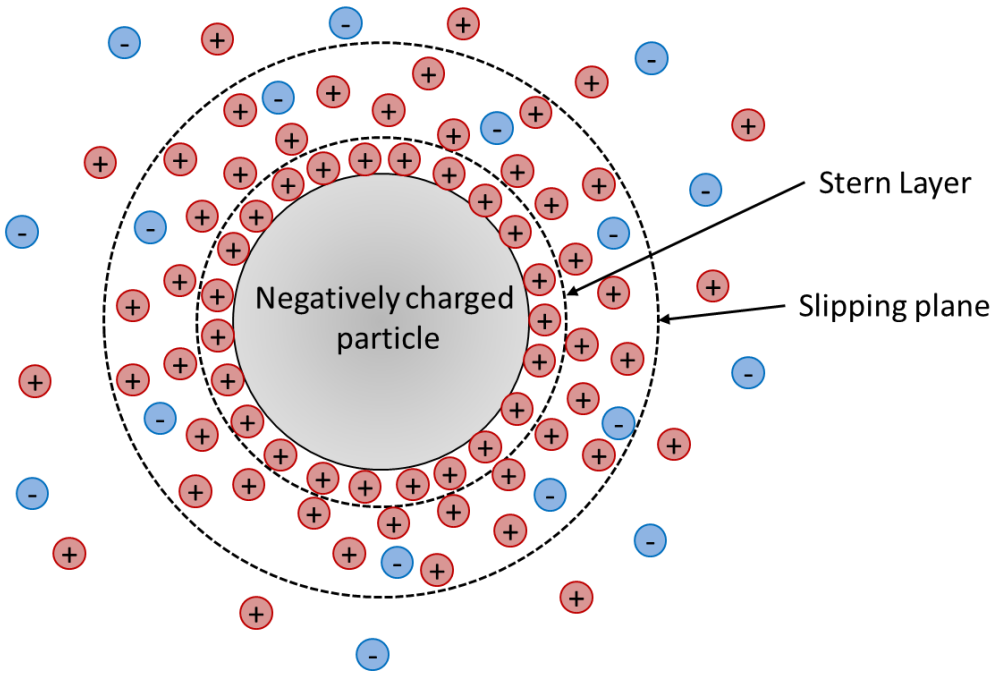

Figure 2.6: Illustration of the electric double layer for a negatively charged particle. The Stern ('fixed') layer consists of counterions at the particle surface and the slipping plane contains ions that are mobile with the particle. There is a higher concentration of positively charged counter ions near the negatively charged surface.

Due to the complex nature of colloidal particles and colloidal stability, there are several assumptions made by DLVO theory:

- The surface of the particle is an infinitely flat solid surface with uniform charge density
- There is a constant concentration profile of counter ions and surface ions
- Surface electric potentials remain constant
- There are no chemical reactions between surfaces and solvents

These assumptions can lead to shortcomings when looking at colloids that interact with the dispersion medium, for example with hydrogen bonding between water and biotic and abiotic colloids (Grasso *et al.*, 2002) and pH dependencies of stability on edge sites of clay nanoparticles (Missana and Adell, 2000). In addition, small colloids will have a highly curved surface, making the simplification to a flat surface less accurate.

Further to the points above, it is worth outlining the main limitations of DLVO theory (Park and Seo, 2011). Firstly the dispersion must be sufficiently dilute so the particles of interest are not affected by other particles in terms of charge density, distribution and

electric potential. No interfering forces such as a magnetic field or a contribution from gravity are considered. The geometry of the particles is assumed to be near spherical so the surface properties of the particle are uniform. Finally, the double layer is determined by only electric force, Brownian motion and entropic dispersion. These shortcomings mean that DLVO theory is not capable of accurately predicting colloidal behaviour for many systems that fall outside of its limitations. It does, however, outline the basic contributions toward the stability of a lyophobic colloidal dispersion. There have been many advances to DLVO theory since its creation, including the incorporation of non-uniform, roughened surfaces (Swanton and Vines, 2003), at high ionic strength where surface groups will interact more strongly with ions (Ehrl *et al.*, 2009), and with the addition of Lewis acid-base interactions (van Oss, 2008). Unfortunately, although these improvements have been shown to be effective in the specific areas of interest, they are often retrospective and there have been no complete solutions to the shortcomings of DLVO theory that can encompass predictions of all colloid systems.

Colloidal particles will be usually be suspended when they have a gravitational settling velocity (υ_s) of below 10^{-2} cm s^{-1} (Stumm and Morgan, 1995). The value of υ_s can be calculated using Stoke's law as described in Equation 2.5. Here, g is the gravity acceleration, ρ and ρ_s are the mass densities of water and the particle respectively, η is the absolute viscosity of water which is equal to 0.001005 kg m^{-1} s^{-1} at 20°C and d is the particle diameter (Stumm and Morgan, 1995).

$$\upsilon_s = \frac{g}{18}\frac{\rho_s - \rho}{\eta}d^2 \qquad (2.5)$$

Therefore, according to Equation 2.5, the settling velocity is proportional to d^2 and increases significantly with increasing particle size. As aggregation increases particle size, this will in turn increase the gravitational settling velocity of the particles by the square of the particle size. Additionally, the gravitational settling velocity is proportional to $\rho_s - \rho$, meaning an increase in the particle density will result in an increased gravitational settling velocity. For actinides this is significant as oxides such as UO_2 have a high density (10.97 g/cm^3, (Greaux *et al.*, 2008)). Due to this, particle aggregation is particularly relevant for actinide colloid stability, with larger aggregated particles of dense actinide oxides leading to high gravitational settling velocity and low colloid stability.

Silica (SiO_2) colloids, of high relevance in this thesis, show many non-classical DLVO characteristics. Many of these are down to the more favourable surface-solution interactions of silica surfaces (Iler, 1979). This is discussed in more detail in section 2.3.4..

2.3.2. Colloids and radionuclides

Colloids are of particular interest when looking at radionuclide mobility due to the low solubility of many radionuclides. Many inorganic and organic colloids found in both natural ground waters and in nuclear fuel storage facilities have been shown to sorb actinides and fission products strongly due to their high surface area and reactivity (Kersting *et al.*, 1999; Farr, Schulze and Honeyman, 2000; Pitois *et al.*, 2008; Gregson, Goddard, *et al.*, 2011; Gregson, Hastings, *et al.*, 2011; Kersting, 2013; Maher *et al.*, 2016). Some of these studies have shown how colloidal transport can greatly enhance the distance travelled by radionuclides, particularly those which possess low solubility (e.g. An(IV)) and therefore do not exist at significant concentrations as dissolved species. In these cases mobility would be expected to be very low, meaning colloid formation greatly enhances transport. However, the extent of radionuclide transport often depends on the form of colloids, as binding to pre-existing colloids, also known as pseudo-colloids, is often reversible. If the sorbed species is reversibly bound to the colloid surface in an outer/inner sphere sorption complex, it will dissociate from the colloid if the local concentration of the sorbed species drops or a change in pH leads to increase solubility, potentially resulting in limited transport (Zänker and Hennig, 2014). This is often the case for radionuclides such as ^{90}Sr at neutral pH (Vilks and Laboratories, 1991; Bekhit *et al.*, 2006; Albarran *et al.*, 2011), where it is known to bind in an outer sphere complex (O'Day *et al.*, 2000; Carroll *et al.*, 2008; Wallace *et al.*, 2012; Fuller *et al.*, 2016). Therefore, colloidal transport of Sr at neutral pH has been shown to be limited because of this reversibility of sorption. However, if the radionuclides are integral to the structure of the colloidal particles, forming an intrinsic colloid (or Eigen colloid), this can lead to greater transport (Farr et al. 2007).

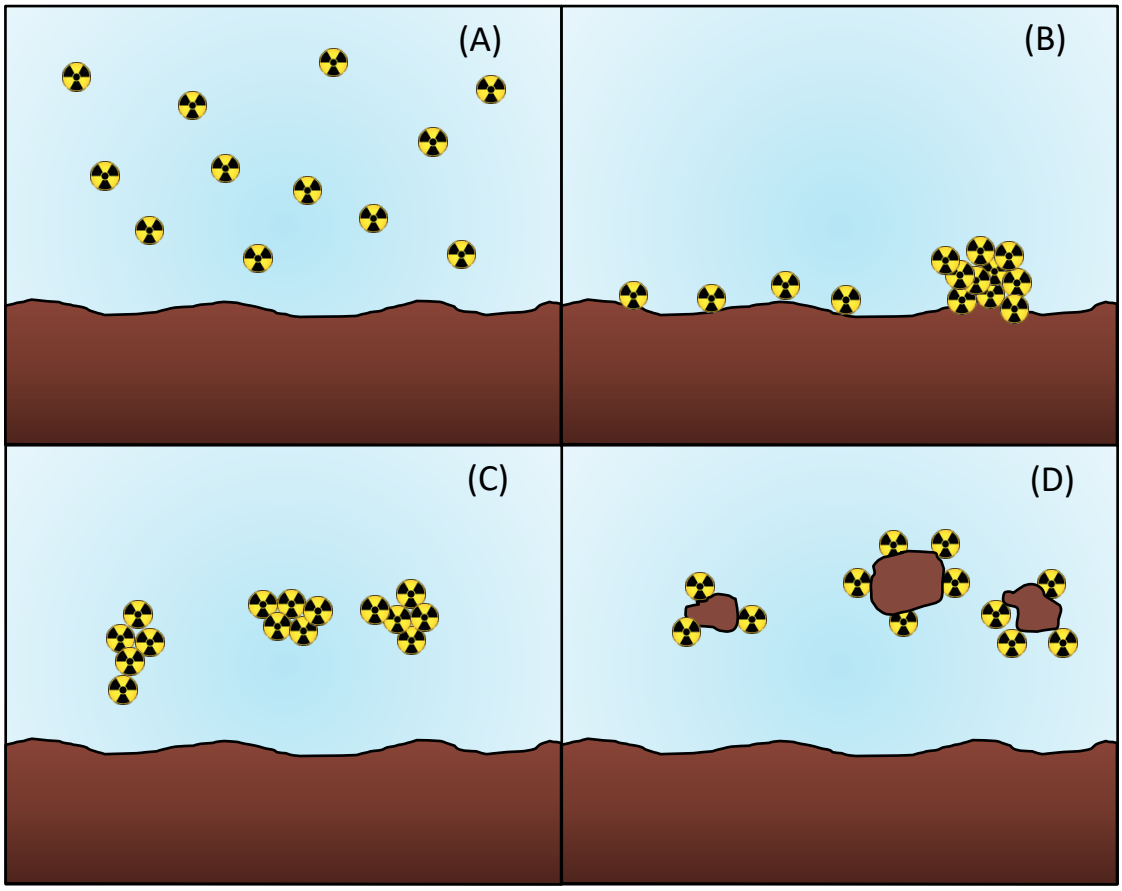

Figure 2.7: The possible fates of radionuclides, including (A) radionuclides as a solution species, (B) radionuclides immobilised by sorbing to sediment/rock (left) and forming intrinsic precipitate (right) (C) radionuclides form intrinsic colloid and (D) radionuclides sorb to organic or inorganic colloid to form a pseudo-colloid. Radionuclides are mobile in scenarios A, C and D.

Intrinsic colloids can also form from supersaturated solutions that would normally result in precipitation of immobile solid sediments (Kim et al. 2008). Formation of actinide colloids, which have low aquatic solubility (Fanghänel and Neck, 2002) can proceed via hydrolysis as actinides form intrinsic colloids (Neck and Kim, 2001). These intrinsic colloids have been shown to form for Pu (Neck *et al.*, 2007; Walther *et al.*, 2009) and U(VI) at both high and low pH (Priyadarshini *et al.*, 2013; Bots *et al.*, 2014) . For tetravalent actinides, which would be expected to be present in the anaerobic conditions found in SNF storage, An(IV)O_2 colloids have been observed at low pH. These colloids have been seen for UO_2, ThO_2, PuO_2 and in some cases have been responsible for overestimates in An(IV) solubility due to their very small size being mistaken for true solution species (Neck and Kim, 2001; Neck *et al.*, 2002; Dreissig *et al.*, 2011). However, of these, only PuO_2 is commonly believed to form stable oxide colloids at pH > 3 (Möri *et al.*, 2003; Huber *et al.*, 2011; Zänker and Hennig, 2014). This is due to the

hydrophobicity of the AnO_2 particle surfaces and the low surface charge of the particles at near neutral pH, which results in aggregation and precipitation. There is some evidence of colloidal and nanoparticulate U(IV) forming in nature from investigations into formation of uranium ore deposits. Both U(IV) silicate and UO_2 nanoparticles have been observed in coffinite and uraninite deposits respectively (Suzuki *et al.*, 2016; Schindler *et al.*, 2017), indicating that U(IV) nanoparticles have the potential to form in natural systems.

U(IV) colloids have been formed from the corrosion of metallic U found in SNF (Kaminski *et al.*, 2005). Non-irradiated and irradiated nuclear fuel were corroded in well water at pH 8.4, 1.5 mM silicate and 90 °C under oxic and anaerobic conditions (Kaminski and Goldberg, 2002; Kaminski *et al.*, 2005). Under anaerobic conditions a U(IV) colloidal phase formed that was stable for at least 125 days either as an intrinsic colloidal dispersion in the absence of clay, or mixed with clay colloids when they were present. When the anaerobic systems were exposed to air, the colloid remained present for a long period of time (>70 days) before eventually forming a U(VI)-silicate precipitate. The colloidal U(IV) phase formed was identified as UO_2 from selected area electron diffraction (SAED) but it is possible that silicate played a role in the colloidal stabilisation by coating the particles, previously observed in iron oxide and calcium carbonate systems (Mayer and Jarrell, 1996; Doelsch *et al.*, 2003; Kellermeier *et al.*, 2012). Silicate was present in high concentrations in the well water solution used and the colloidal particles formed possessed similar characteristics to U(IV) silicate colloids in terms of particle size and surface charge (Dreissig *et al.*, 2011). Additionally, when these colloidal particles were exposed to air they formed weeksite ($K_2(UO_2)_2Si_6O_{15}{\cdot}4H_2O$), a U(VI)-silicate precipitate, suggesting a U(IV)-silicate phase may be present prior to oxidation. This is supported by recent investigations highlighting a group of An(IV)-silicate colloids (where An = U, Th, Np), which have been shown to form at pH 7-9.5 (Dreissig *et al.*, 2011; Hennig *et al.*, 2013; Husar *et al.*, 2015; Zänker *et al.*, 2016).

2.3.3. Silicate stabilisation of colloidal nanoparticles

Intrinsic U(IV)-silicate colloids have been formed by the dilution of a U(IV) carbonate solution in a silicate solution at pH 7-9.5, achieving a colloidal U(IV) concentration of up to 1 mM (Dreissig *et al.*, 2011). When the concentration of silicate exceeded that of

U(IV), this resulted in the formation of U(IV)-silicate colloids. The colloidal nanoparticles were very small, below 10 nm in size under certain conditions, and stable for at least 3 years. The structure of these particles was confirmed by EXAFS as a U(IV) silicate phase, which appeared to be similar to coffinite, however the exact structure was not resolved. Colloidal stability was observed to increase with increasing silicate in solution (up to 2.7 mM) and increasing pH (up to pH 9.5), suggesting these colloids have a stability range beyond the pH explored in the study. When no silicate was present in the reactions, no stable colloid was formed by the U(IV)-oxyhydroxide product. The results show that silicate is required to form the U(IV) colloid, and that with increasing silicate concentrations, smaller particles and more stable colloids are formed. Additionally, zeta potential measurements showed that the pH_{pzc} of these particles decreased with increasing silicate concentrations, from pH 6 to pH 4.5, with values becoming closer to those of silica particles (~ pH 2 (Iler, 1979)). This suggests that it is the silicate in the structure of the colloidal nanoparticles that is stabilising them as a colloid and at high silicate concentrations the particles have more silica-like properties. However, the mechanism for the colloid formation and the structure of nanoparticles is not yet fully understood.

Studies on the pH_{pzc} of a series of colloidal An(IV)-silicates showed they were significantly lower than their corresponding oxides (Dreissig *et al.*, 2011; Hennig *et al.*, 2013; Husar *et al.*, 2015). Additionally, silicate enrichment at the particle surface was observed for Th(IV)-silicate systems by X-ray photoelectron spectroscopy (XPS) analysis, where a higher Si:Th ratio was seen on the particle surface than in the bulk (Hennig *et al.*, 2013). A silicate rich surface may lead to the high colloidal stability in these systems, relative to An(IV)-oxide nanoparticles. However, the composition and structure of these An(IV)-silicate particles has not been fully explored, especially for the redox sensitive U(IV) and Np(IV). Furthermore, their formation has not been characterised. It has previously been hypothesised that An(IV)-silicate particles form via a two-step process with hydrolysis of aqueous An(IV) followed by reactions with the silicate present in solution (Zänker *et al.*, 2016). As An(IV) hydrolysis is fast compared to silicate polymerisation, this results in the silicate enrichment at the particle surface observed for Th(IV)-silicate particles. While this formation process appears likely, there is a paucity of mechanistic evidence and the intermediates of this process are not well understood.

Therefore, more information is needed to be able to accurately predict the conditions of formation of such species and fully understand their formation process.

A silica-like coating has been seen previously on amorphous calcium carbonate nanoparticles (Kellermeier *et al.*, 2012). The particles were between 0.5 and 3 nm in size and the silica coating resulted in a stable amorphous calcium carbonate structure. In systems without silicate present the particles crystallized, suggesting the silicate was responsible for the preserved amorphous structure. The presence of silicate in solution led to silica-like coating of these pre-nucleation clusters which stabilised them in suspension as a colloid, preventing extensive aggregation and crystallization. While at pH 11 the silica coating prevented crystallization and stabilised the particles as a colloid, under lower pH conditions of pH 9.3-10.3, extensive aggregation of these particles occurred. At pH 10.3, the aggregation was sufficient enough to induce sedimentation and gel formation, but did not result in crystallisation of calcium carbonate, with the amorphous structure preserved. However, at pH 9.3 pre-nucleation clusters merged over time into larger calcium carbonate crystals. Interestingly, in the stable colloidal systems, the kinetic barriers to coalescence were estimated to be ~1.1 kT, which is significantly below the value of ~10 kT normally required to prevent aggregation in colloidal systems when using a purely DLVO based model of colloidal stability (Buscall and Ottewil, 1985). This indicates that the colloidal behaviour here is not typical of a simple DLVO based model, which is characteristic of silica colloids.

Silicate has also been shown to stabilise Fe(III) colloids across a pH range (3-10), in which Fe(III)-oxyhydroxide particles would not normally form a colloid (Mayer and Jarrell, 1996). At environmentally relevant levels (0.45 mM), silicate was found to promote ferrihydrite ($Fe_2O_3.0.5H_2O$) formation over more thermodynamically stable phases such as lepidocrocite (γ-FeO(OH)), upon oxidation of Fe(II) to Fe(III). This is a similar phenomenon to the calcium carbonate-silicate system discussed previously, where silicate prevents extensive crystallization to a more thermodynamically favoured phase by acting as a capping ligand while also stabilizing the nanoparticles as a colloidal phase. The ferrihydrite product of spherical particles approximately 0.1 μm in size were very similar to those observed in natural systems, suggesting a similar mechanism may stabilize natural Fe(III) colloids. Although these studies are laboratory based with limited field studies carried out on silicate stabilized colloids, much of the evidence from either

nanoparticles present in U(IV)-silicate ore deposits, or Fe(III)-oxides, suggests that many metal oxide colloids could be stabilised by silicate under environmental conditions.

2.3.4. Colloidal behaviour and chemistry of silica and silicate

Many of the systems discussed above show enrichment of silicate at the surface of the colloidal particles and similarities to the colloidal behaviour of silica. Therefore comparisons to silica colloids and the known properties of these particles are useful. Silica colloids exhibit very unusual colloidal behaviour; most inorganic colloids display behaviour very similar to that described by DLVO theory, but silica colloids do not due to their hydrophilic surface (Yotsumoto and Yoon, 1993; Chapel, 1994; Koopal, 1996; Grasso *et al.*, 2002; Valle-Delgado *et al.*, 2005; Johnson *et al.*, 2008). This means that silica or silicate-coated particles will have more favourable surface-solution interactions than most inorganic phases and therefore less of a thermodynamic driving force for particle aggregation and colloidal destabilisation. Consequently, there is a reduced dependence on kinetic stabilization, e.g. particle surface charge, for stability. The high colloidal stability and non-DLVO behaviour of silica is illustrated by the presence of silica colloids at the pH_{pzc} of silica and it's resistance to high ionic strengths, both of which would be expected to destabilize a colloid according to DLVO theory (Allen and Matijević, 1969). Silica colloid stability shows a general trend of aggregation and flocculation with increasing pH (Tschapek and Sanchez, 1976), which is also contradictory to DLVO theory given their increasing surface charge with higher pH. Silica shells can stabilise colloids made from a range of different phases, including TiO_2 (Duan and Liu, 2014), AgI (Kobayashi *et al.*, 2016), zero valent iron (Honetschlägerová *et al.*, 2015), $CaCO_3$ (Kellermeier *et al.*, 2012) and iron oxides (Mayer and Jarrell, 1996; Doelsch *et al.*, 2003).

In solution, monomeric silicic acid $(SiO_4H_x)^{x-4}$ exists in varying degrees of deprotonation depending on pH. At high concentrations and alkaline pH, silicate can also oligomerise in to dimers, trimers and higher degrees of polymerisation in a range of different structures. The degree of polymerisation depends on a range of variables including concentration of silicate, pH, temperature and the ionic strength of the solution. Furthermore, each of these oligomers may have a range of charges depending on pH and the degree of deprotonation (Tobler, Shaw and Benning, 2009; Gebauer *et al.*,

2014). Silica nanoparticles and colloids form from the aggregation of silicate polymers in saturated solutions. Polymers form initially, with continued oligomerisation leading to larger 1-2 nm particles, which continue to grow; first through surface reactions and then via aggregation and Ostwald ripening (Tobler, Shaw and Benning, 2009). These polymeric silicates were identified by Dreissig *et al.* (2011) as a significant factor in U(IV)-silicate colloid stabilisation, as U(IV)-silicates formed in the presence of polymeric silicates were more likely to form a colloid. The speciation of silicate in solution is significant as polymeric silicates have been shown to bind ionic metal species stronger than monomeric silicate (Taylor, Jugdaohsingh and Powell, 1997). This means that the possibility of a cation being complexed by silicate increases as the degree of polymerisation of silicate increases. As discussed previously, in the case of U(IV) and Th(IV) silicates, the Th(IV)-silicate solution complex $Th(OH)_3(H_3SiO_4)_3^{2-}$ (Rai *et al.*, 2008), which has also been estimated for U(IV), will form in the pH range 7-12 (Mesbah *et al.*, 2015) when sufficient silicate is present, meaning silicate may also influence U(IV) and Th(IV) solution speciation and solubility. Due to the links between silicate chemistry and U(IV)-silicate particle formation, and the inherent connection between silica and U(IV)-silicate colloidal properties, an understanding of silicate chemistry and the characteristics of colloidal silica are important when considering U speciation in the presence of silicate.

2.3.5. Radionuclide pseudo-colloids

While intrinsic colloids may be important to radionuclide mobility, there has been more significant evidence of pseudo-colloid transportation of radionuclides under environmental conditions. Previous studies have observed pseudo-colloid mediated transport of a range of radionuclides, including U (Wang *et al.*, 2013), Np (Suzuki *et al.*, 2002), Pu (Kersting *et al.*, 1999), Am (Degueldre and Wernli, 1993; Artinger *et al.*, 2002) and Sr (Chawla *et al.*, 2010). Pseudo-colloid formation is more likely under environmental conditions due to the abundance of colloids present in natural aqueous systems and the low concentration of the radionuclides in most environmental scenarios. In the above studies on pseudo-colloid transport, the formation of radionuclide pseudo-colloids has dramatically increased their mobility. In the case of Kersting *et al.* (1999), Pu containing colloids were detected 1.3 km away from the site of

contamination, significantly further than would be predicted for a dissolved species in groundwater. This could, in part, be due to the size-exclusion effect whereby a colloidal particle will be more likely to travel down larger, wider channels in the subsurface and therefore travel faster than the bulk groundwater.

Pseudo-colloids can form from either organic or inorganic colloidal phases with both proving to be significant in radionuclide transport (Ball, 1992; Degueldre and Wernli, 1993; Artinger *et al.*, 2002; Chawla *et al.*, 2010). The focus within the following section of the literature review will be on the sorption of radionuclides to inorganic colloids and sediments and the implications this has. In particular, the sorption behaviour of Sr under high pH conditions relevant to SNF storage. Although there is a paucity of knowledge on Sr sorption to colloidal phases, or Sr pseudo-colloids, there is a significant amount of research on Sr sorption behaviour to a range of minerals and sediments.

2.4. Strontium sorption and its relevance to spent nuclear fuel storage

Due to it short half-life and high fission yield, ^{90}Sr is a major contributor to the radioactivity of SNF. ^{90}Sr has a half-life of 28.8 years meaning it is relevant on the time scale of interim SNF storage and decommissioning at sites such as Sellafield. In aqueous systems Sr predominantly exists as the hydrated, divalent Sr^{2+} ion at pH <12 and is relatively highly soluble in the absence of carbonate. At neutral pH Sr mobility is dictated by sorption to solid phases, predominantly in weakly bound, outer sphere complexes. At higher pH the solubility of Sr^{2+} is reduced, particularly in the presence of carbonate or silicate and precipitation of Sr-carbonate (Busenberg, Plummer and Parker, 1984) and Sr-silicate (Nishi, 1997; Chorover *et al.*, 2003; Felmy *et al.*, 2003; Chang *et al.*, 2011) phases can dictate the mobility of Sr.

Sr has been shown to sorb to many sediments and minerals across a wide pH range, with outer sphere sorption occurring at pH <12.5. Generally, Sr sorption increases at higher pH as the surface charge of the substrate becomes increasingly negative and therefore has a higher affinity for the positively charged Sr^{2+} ion. Studies investigating the reversibility of Sr sorption onto sediments, clays, uranyl peroxides and iron oxides have found that under near neutral conditions Sr sorption is often reversible, suggesting the formation of an outer sphere complex with weakly bound Sr (Sureda *et al.*, 2010;

Wallace *et al.*, 2012; Fuller *et al.*, 2016). At pH >12, inner sphere sorption occurs on Fe(III) oxides, clays (Fuller *et al.*, 2016) and neo-formed zeolites (Wallace *et al.*, 2013), indicating a different binding mechanism that has been attributed to the formation of the hydrolysis product $Sr(OH)^+$ in solution in this high pH region. This inner sphere sorption could be more resistant to changing conditions such as ionic strength, with inner sphere sorption at high pH potentially being less reversible than the outer sphere sorption observed at lower pH, however this has not been systematically investigated in these systems.

At high pH, Sr is more likely to form solid phases that would retard Sr mobility. Of particular interest are strontium carbonate and strontium silicate phases, due to the presence of carbonate and silicate in SNF storage from dissolution of atmospheric CO_2 and cement pond linings respectively. Strontianite ($SrCO_3$) (Busenberg, Plummer and Parker, 1984), a tobermorite-like Sr silicate phase ($Sr_5Si_6O_{16}(OH)_2 \cdot 5H_2O$) (Felmy *et al.*, 2003) and strontium metasilicate ($SrSiO_3$) (Nishi, 1997) are increasingly insoluble with increasing pH up to ~ 13, meaning these phases are likely to occur in any areas of elevated Sr concentrations. There is likely to be a significant amount of inactive Sr also present in alkaline solutions in contact with cementitious materials, e.g. legacy nuclear fuel storage ponds, as cement will contain a certain amount of Sr substitution in Ca sites. Sr content has been recorded as between 0.02 and 0.39 wt% by for Portland cement (Diamond, 1955).

Under alkaline conditions related to SNF storage, Sr has been shown to sorb strongly to monosodium titanate ($NaTi_2O_5H$) (Hunt *et al.*, 2005) and iron oxides (Arafat *et al.*, 2010). Monosodium titanate has been investigated as a potential sink for aqueous ^{90}Sr at the Hanford and Savannah River sites (Hunt *et al.*, 2005; Kirillov, Lisnycha and Pendelyuk, 2006). It has also been found that Sr sorbs more to amorphous manganese oxide/titanium oxides than their crystalline counterparts (Kirillov, Lisnycha and Pendelyuk, 2006). This is relevant to the mobility and partitioning of ^{90}Sr in legacy storage facilities, where particulates will have a range of crystalline and amorphous states. Sr interactions with two U(VI) phases; studtite (UO_4) and uranophane ($Ca(UO_2)_2(SiO_3OH)_2.5H_2O$) have also been investigated. For studtite, Sr sorption increased with increasing pH, with almost complete removal of Sr from solution at pH >10 (Sureda *et al.*, 2010). Sr sorption was also high on uranophane (>90 % Sr was

removed from solution at pH 7), however this sorption was also reversible, with much lower sorption occurring at higher ionic strengths (Espriu-Gascon *et al.*, 2018).

Although sorption is often associated with the immobilisation of Sr, sorption to a colloidal species would not reduce the mobility of solution species and could in fact increase mobility in certain scenarios due to the size exclusion effect. Colloids are also significant in SNF storage and effluent treatment facilities, where existing treatment methods involve filtrations of large particulates or removal of solution species. It is possible, given the nanoparticulate nature of colloidal material, that they could evade both of these measures.

The sorption of Sr to silica colloids has been investigated at pH 4-7 in a column transport study (Bekhit *et al.*, 2006). At pH 4 - 5.4, it was found that the silica colloids retarded the mobility of Sr in the columns, caused by destabilisation of the silica colloid. This led to the silica precipitating, meaning the Sr was sorbed to a non-colloidal solid phase, although the authors also note the high sorption capacity of silica colloids for Sr under the conditions investigated. As mentioned previously, one of the limiting factors for the effectiveness of pseudo-colloids in contaminant transport is desorption. This has been observed for Sr in a range of scenarios including an investigation into Sr sorbed onto bentonite colloids (Albarran *et al.*, 2011). Here the Sr was sorbed on to bentonite colloids prior to entry into a granite column, and upon entry to the column Sr desorbed from the bentonite and sorbed to the granite of the column instead. A similar result was seen using natural colloids in a granitic fracture. In this case the Sr was found to sorb moderately to the granite, compared to the strongly sorbing Am(III), in the absence of any colloid (Vilks and Baik, 2001). Only a slight increase in Sr mobility was seen when Sr was sorbed to the colloidal phase prior to introduction into the facture suggesting the Sr is not irreversibly bound to the colloids and in fact had a higher affinity for the granite itself. ^{90}Sr has previously been found associated to a colloidal phase in natural samples of Alpine soil solutions (from atmospheric deposition), but the degree of this binding was relatively low compared to Pu (Chawla *et al.*, 2010). In this study, the majority of the colloidal matter was thought to be organic and Pu showed >80 % association with the colloidal fraction while Sr was more evenly distributed between colloidal, bulk and solution fractions. These studies illustrate the importance of understanding the mechanism of colloid formation, and the interactions of the radionuclides with the

colloids. If a radionuclide containing colloid has formed, this does not necessarily mean that this will result in increased transport of the radionuclide, especially if the colloid formed is a pseudo-colloid and the radionuclide is not incorporated into the colloidal particle's structure. In the case of Sr, pseudo-colloid mediated transport at circumneutral pH does not appear to be significant due to competing sorption from bulk solid phases, reversibility of Sr sorption and the inherent instability in many colloidal systems.

The studies discussed in the previous paragraph which show reversible binding of Sr to colloids are consistent with EXAFS investigations into Sr sorption at circumneutral pH. At neutral pH Sr was shown to bind as an outer sphere, and therefore exchangeable complex on a range of substrates (Sahai *et al.*, 2000; Carroll *et al.*, 2008; Wallace *et al.*, 2012; Fuller *et al.*, 2016; Espriu-Gascon *et al.*, 2018). There is a shortage of studies on colloidal stability of Sr at higher pH where it is known to sorb as a potentially less reversible, inner sphere complex. No studies were found that combined investigations into Sr sorption onto colloids with EXAFS, or a similar technique to interpret the mechanism of Sr sorption on colloidal materials. Furthermore, there is very little research to date on the interactions of Sr with U phases in the area of SNF storage and nuclear waste (Sureda *et al.*, 2010; Espriu-Gascon *et al.*, 2018). This is surprising given the colocation of Sr and U in SNF and the hazard posed by the high specific activity of ^{90}Sr. Sr has been shown to incorporate into the structure of UO_2 at high temperatures (Fujino, Yamashita and Tagawa, 1988; Perriot *et al.*, 2015) in studies relevant to nuclear reactor conditions and formation of ^{90}Sr from nuclear fission within a UO_2 matrix. Under more ambient temperature, aqueous conditions found in SNF storage ponds, it is not clear how Sr will interact with the U(IV) phases present.

Based on previous studies, it would be expected that Sr would bind as an outer sphere complex to U(IV) substrates at low pH and form inner sphere complexes at higher pH, however there is some evidence that Sr may incorporate into UO_2 from research into the behaviour of fission products in UO_2 fuel. These studies carried out at high temperature (T >1000 K) showed that Sr can substitute into sites within the UO_2 lattice during the production of fission products within a UO_2 matrix (Fujino, Yamashita and Tagawa, 1988; Perriot *et al.*, 2015). This could be due to the similarities in ionic radii of Sr^{2+} (1.26 Å for 8 coordinate Sr^{2+}) and U^{4+} (1.00 Å for 8 coordinate U^{4+}) making

substitution possible (Shannon, 1976). Further support is found in natural systems, where Ca^{2+} is commonly found substituting for U^{4+} in uraninite (UO_2) (Burns and Finch, 1999). A recent study (Bower *et al.*, 2016) provided evidence that Sr can incorporate into TiO_2 particles in a legacy SNF storage pond. The resulting structure was a perovskite-like $SrTiO_3$ structure common for di- and tetravalent cations e.g. $Ca_{1-x}Sr_xTiO_3$ (Yamanaka, Hirai and Komatsu, 2002) and $SrZrO_3$ (Ahtee *et al.*, 1976). The possibility of Sr forming a perovskite-like structure, or substitution for U^{4+} in UO_2 is therefore important and may affect the sorption capacity and, crucially, the reversibility of sorption for Sr on U(IV) phases.

2.5. Summary

Legacy storage facilities at sites such as Sellafield, UK, are coming to the end of their expected lifetimes. Waste retrieval is now a high priority at these facilities and with waste retrieval operations a greater range of effluent feeds is expected. Understanding the composition of these feeds in essential, in particular the potential for mobile particulates and colloids to form. Knowledge of the intrinsic properties of colloids that could form from alkaline SNF storage is required to predict their stability and assess viable treatment procedures.

While the importance of colloids to the transport of radionuclides is apparent, there have only been a few studies looking into the potential formation of colloids in alkaline SNF storage. U(IV) colloids have been shown to form from corroded metallic U spent fuel (Kaminski *et al.*, 2005), while U(IV)-silicate colloids have been shown to form under moderately alkaline conditions (Dreissig *et al.*, 2011). If these species can form under more alkaline conditions they could potentially mobilise U(IV) in effluent streams. There is, however, a paucity of knowledge on the underlying characteristics of these species, in both their formation pathways and molecular scale structure. Further understanding of the particle structure, stability range and formation pathway are required to understand their behaviour. While it is known the particles contain U(IV)-silicate bonding, their structure is not known and the exact role silicate has in stabilising the colloids has not been resolved. It is important to identify these characteristics to be able to assess the possible formation and persistence of U(IV)-silicate colloids in legacy storage ponds, and their behaviour during effluent treatment.

The hazard posed by mobile U(IV) particulates could be greatly increased by co-mobilisation of other radionuclides by a variety of mechanisms, including sorption, incorporation and coprecipitation. As discussed in Section 2.1.2., other radionuclides have been shown to associate with colloidal matter in SNF storage (Maher et al., 2016), and this could, in the case of Sr, result in incomplete removal from effluents. As colloids have a very large surface area, due to their small particle size, they have a large capacity for sorption, making them a likely candidate for Sr sorption. The potential for ^{90}Sr to interact with colloidal phases is high given the tendency of Sr to sorb to a range of surfaces at neutral and alkaline pH. At high pH, Sr is known to sorb as an inner sphere complex and even incorporate in some instances (Tits *et al.*, 2006; Wallace *et al.*, 2012, 2013; Fuller *et al.*, 2016). Despite the importance of understanding Sr mobility at nuclear sites, the interactions of Sr with colloidal phases at high pH are poorly understood. Sr is also known to incorporate into the structure of UO_2 at high temperature and TiO_2 in an alkaline spent fuel storage pond (Ball, 1992; Huang *et al.*, 1997; Bower *et al.*, 2016). Understanding the capacity for Sr sorption to U(IV) phases and the mechanism of this sorption is required to assess whether U(IV) phases will impact upon Sr removal from effluents as decommissioning and waste retrieval operations take place.

Finally, while the SIXEP plant at Sellafield has been successfully operating for over 30 years, effluent feeds from spent fuel retrieval and decommissioning of legacy facilities will present effluents of different compositions. Understanding the impact that the effluent treatment process has on potential mobile species in these novel feeds is necessary to assess the effectiveness of SIXEP and other effluent treatment plants going forward.

Chapter 3: Experimental Methodology

This chapter outlines the experimental methodology used in this project and describes the theory of the techniques used.

3.1. Experimental overview

To prevent oxidation of U(IV) to U(VI), all manipulations were carried out in a anaerobic N_2/H_2 atmosphere (Coy Chambers, USA). Routine analysis of samples at stages throughout the experiments using UV-vis spectroscopy was performed to confirm no oxidation of U(IV) to U(VI) had occurred (Appendix 1). All solutions were made up from degassed, deionised water (DIW) that had been degassed using Ar or N_2 for 15 minutes and equilibrated in an N_2/H_2 atmosphere for 24 hours. All analyses outside of a glove box (e.g. EXAFS analysis) were carried out in air-tight sample containers, and any U(IV) sample handling outside of the glove box was done under a flow of N_2 to prevent oxidation of U(IV).

Table 3.1: Summary of experimental conditions, description of investigation aims and analytical techniques used for each set of investigations carried out.

[Si]/ mM	pH	Sr present?	Investigation	Analytical techniques	Chapter
0	9, 10.5, 12.	No	Characterising particle	UF, EXAFS, TEM, PDF	4
2	9, 10.5, 12.	No	U(IV)-silicate colloid stability, particle size, composition and structure	UF, SAXS, DLS, Zeta potential, EXAFS, TEM, XRD, PDF	4
4	9, 10.5, 12.	No	U(IV)-silicate colloid stability, particle size, composition and structure	UF, SAXS, DLS, Zeta potential, EXAFS, TEM, STEM	4
0	3.7, 6, 8, 10, 12.	Yes*	Sr sorption onto UO2 – sorption capacity and mechanism	UF, TEM, EXAFS	5
4	4, 6, 8, 10, 12, 14.	Yes*	Sr sorption onto U(IV)-silicate – sorption capacity and mechanism	UF, TEM, EXAFS	5
4	11.5	Yes*	The effect of carbonation on U(IV)-silicates and their capacity for Sr sorption	UF, EXAFS	6

*Sr was present at 0.058 mM. UF = ultrafiltration, EXAFS = extended X-ray absorption fine structure spectroscopy, TEM = transmission electron microscopy, PDF = X-ray pair distribution function, SAXS = small angle X-ray scattering, DLS = dynamic light scattering, XRD = X-ray diffraction.

3.2. Synthesizing U(IV)-silicate and nanoparticulate UO_2

U(IV)-silicate colloids were synthesised from a method adapted from Dreissig *et al.* (2011). UCl_4 powder was prepared as described in Hermann *et al.* (1957) and dissolved in 0.25 M HCl, to give a U(IV)-HCl solution with [U] = 50 mM. The concentration of U was confirmed using inductively coupled plasma-mass spectrometry (ICP-MS) and the solution was also filtered with a 3 kDa filter to confirm it was a true solution (see section 3.7.1. below for more details on ultrafiltration). U(IV)-HCl solution was then diluted in a 1.66 M $NaHCO_3$ in a 1:1.5 U(IV)-HCl:$NaHCO_3$ solution ratio, forming a U(IV) carbonate solution with [U(IV)] = 20 mM and $[(CO_3)^{2-}]$ = 1 M. The high carbonate concentration allowed an elevated U(IV) concentration in true solution at a near neutral pH (pH ~ 8)(Hennig, Ikeda-Ohno, *et al.*, 2010; Dreissig *et al.*, 2011). This solution was once again filtered with a 3 kDa filter to confirm a true solution and not a colloidal suspension was formed.

Silicate solutions were prepared by dissolving known amounts of sodium metasilicate nonahydrate ($Na_2SiO_3 \cdot 9H_2O$) in degassed DIW. Solutions with 4.2 and 2.1 mM Si, as well as Si free solutions, were prepared to yield final experimental concentrations of 4, 2 and 0 mM Si. To adjust the pH of the final solutions, 1.5 M HCl or NaOH were added to the silicate solutions to yield the target concentration prior to addition of the U(IV) carbonate solution. The required amounts of acid or base were calculated using phreeqc thermodynamic modelling software (Parkhurst and Appelo, 2013) (more details in section 3.5). Dilution of the U(IV) carbonate solution in silicate solutions, at a 1:19 ratio, resulted in the formation of a U(IV) silicate phase (Dreissig *et al.*, 2011), with final concentrations of 1 mM U and 0, 2 or 4 mM Si. Samples were shaken immediately after spiking the U(IV) solution, pH was measured and adjusted if necessary using 1.5 M HCl or NaOH and the experiments were stored in sealed bottles for aging and analysis. Between pH 6 and 11, and silicate concentrations ≥2 mM, these U(IV)-silicate phases were stable as a colloid. The full range of experimental conditions and analyses are listed in Table 3.1. The samples were stored under a N_2/H_2 atmosphere to prevent any oxidation over time. Control samples were made in the absence of both U(IV) and Si to verify both were required to form a colloidal suspension. In the absence of U(IV), Si

remained in solution and in the absence of Si a solid precipitated U(IV)-oxyhydroxide phase formed.

3.3. Strontium sorption experiments

Strontium sorption experiments on both U(IV)-silicate (with a concentration of 4 mM Si) and U(IV)-oxide (UO_2) were prepared as described above, to form U(IV)-silicate and UO_2 at pH 9. To prevent formation of strontianite, $SrCO_3$, from the excess carbonate in the experiments the U(IV)-silicate and UO_2 phases formed at pH 9 were acidified to pH ~4 by addition of 1.5 M HCl. The samples were then stirred for 30 minutes to facilitate degassing of CO_2 from solution. According to phreeqc thermodynamic modelling, this would result in >99.9% removal of CO_3^{2-} from solution and therefore prevent formation of SrCO3 in the experiments. These systems were then readjusted to set pH values (3.7, 4, 6, 8, 10, 12 or 14) using NaOH (1.5 M for pH 3.7-12 systems and 8 M for pH 14). Ionic strength of experiments between pH 3.7 and 12 was balanced using NaCl to yield a total [Na^+] of 0.15 M. The samples were then equilibrated for 7 days before spiking with Sr. Strontium chloride solutions were prepared by dissolution of $SrCl_2.6H_2O$ in DIW. The concentration of a 20 mM Sr solution was verified by ICP-MS and this solution was spiked into the CO_2-free, pH adjusted U(IV) systems to give a final Sr concentration of 0.058 mM. The spiked Sr experiments were sealed and stored in an N_2/H_2 atmosphere and shaken daily for 7 days prior to filtration and EXAFS analysis on the solid phase.

For the Sr UO_2 systems at pH 3.7, 8, 10 and 12, desorption experiments were used to assess the lability of bound Sr. Here, samples of Sr sorbed to UO_2 were prepared as described above, then the pH of all the samples was reduced to 3.2. The samples were equilibrated for 24 hours and samples were filtered using 3 kDa filters (details in section 3.5.1.). The pH was subsequently adjusted to 2, and the samples were again filtered (3 kDa filters) after 24 hours. For both the original experiments and desorption experiments, filtrations were done in triplicate.

3.4. SIXEP carbonation tower simulation

To simulate the effect of the carbonation tower at the site ion exchange effluent plant (SIXEP) at Sellafield, a U(IV)-silicate sample was exposed to CO_2 gas acidification. In SIXEP, carbonation occurs by bubbling CO_2 gas up through a downward flow of effluent.

This occurs rapidly, with the total dwell time of effluent in SIXEP approximately 10 minutes. A 4 mM Si, 1 mM U, U(IV)-silicate system was prepared and CO_2 was removed from solution as described in Sections 3.2. and 3.3., and the pH was adjusted to 11.4 prior to spiking with Sr (0.058 mM). This sample was then equilibrated for 7 days. An Applikon MiniBio reactor was used for the CO_2 gassing experiment (Figure 3.1. (Weatherill *et al.*, 2016)). The reactor vessel was purged with N_2 gas for 1 hour prior to addition of U(IV)-silicate to generate an inert atmosphere and prevent sample oxidation. A positive pressure was maintained throughout the experiment to prevent O_2 ingress. Once the U(IV)-silicate sample was injected into the Applikon MiniBio reactor, stirring at 150 rpm under a positive N_2 pressure for 15 minutes was initiated. At this point, CO_2 was bubbled through the system and the N_2 inlet was switched off for 10 mins, resulting in a reduction in pH from 11.4 to 7. When the pH had dropped to 7, the CO_2 inlet was turned off to prevent further acidification and the N_2 inlet was turned on to maintain an O_2-free atmosphere during sample extraction.

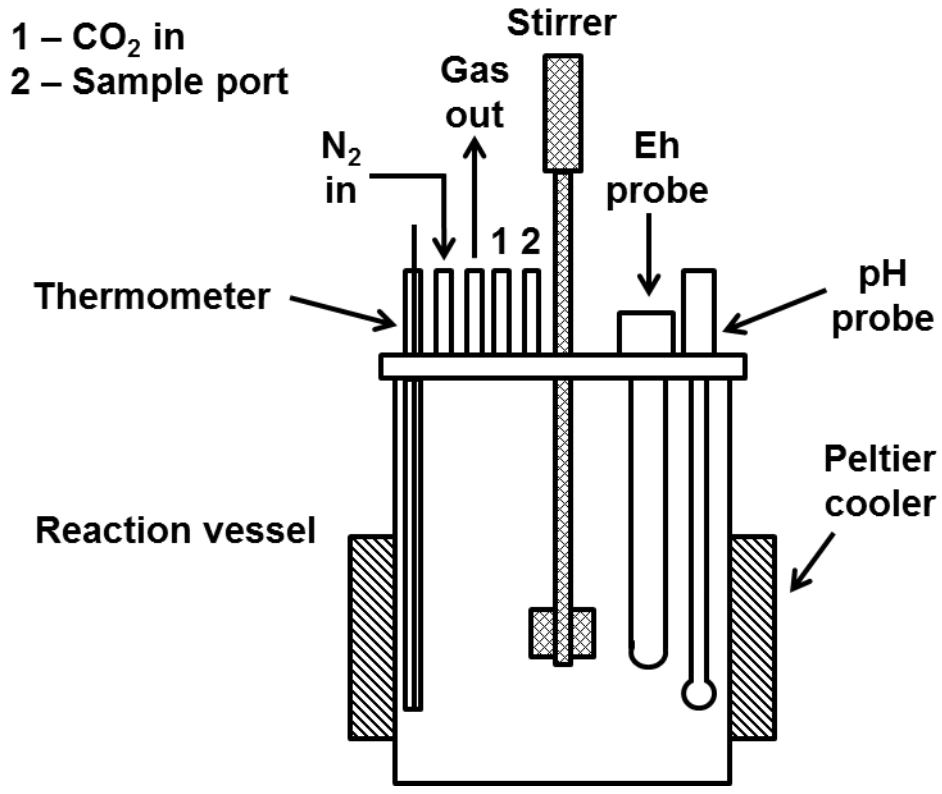

Figure 3.1: Schematic of the Applikon BioReactor configuration used for carbonation experiments.

Periodically, samples were removed from the reactor and stored in capped syringes during transport to the anaerobic chamber for analysis. Once inside the anaerobic

cabinet samples were transferred to closed, parafilm-sealed centrifuge tubes and rotated on an orbital shaker at 40 rpm. Samples were taken periodically for ultrafiltration (at -0.25 h, 0.25 h, 1 h, 4 h, 24h and 8 days after carbonation) and EXAFS (at -0.25 h, 0.25 h and 8 days) analysis. pH was recorded for each sample prior to analysis.

3.5. Phreeqc

PHREEQC thermodynamic modelling (Parkhurst and Appelo, 2013) was used to assess the solution speciation of uranium and strontium in the experiments, as well as U and Sr solubilities and thus the potential for formation of solid phases. Phreeqc calculations were performed using the SIT (specific ion interaction theory) database with additional equilibrium constants for $U(OH)_2(CO_3)_2^{2-}$ (Rai *et al.*, 1998) U-silicate $U(OH)_3(H_3SiO_4)_3^{2-}{}_{(aq)}$. The U-silicate species is adapted by Mesbah *et al.* (2015) from the equilibrium constant for Th-silciate derived by Rai *et al.* (2008). The equilibrium constant was therefore an approximation based on the relative solubilities of UO_2(am) and ThO_2(am). For uranium calculations, the solid phase used in the modelling to calculate solubility was $UO_2.2H_2O$ (am). Calculations were performed to examine the speciation of U and Sr across a range of pH and Si concentrations and investigate the effect of silicate on radionuclide speciation.

Table 3.2: Additional species used in Phreeqc calculations that are not present in the SIT database

Species	Reaction	$Log_{10}K^0$	Reference
$U(OH)_3(H_3SiO_4)_3^{2-}$	$U^{4+} + 3H_2O + 3H_4SiO_4 \leftrightarrow U(OH)_3(H_3SiO_4)_3^{2-} + 6H^+$	18.4 ± 1.7	Mesbah *et al.* (2015)
$U(OH)_2(CO_3)_2^{2-}$	$U^{4+} - 2H^+ + 2CO_3^{2+} + 2H_2O \leftrightarrow U(OH)_2(CO_3)_2^{2-}$	11.33	Rai *et al.* (1998)

3.6. Solid state sample preparation (for XAS and XRD/PDF analysis)

For analysis of solid samples, specifically for X-ray diffraction (XRD) and X-ray absorption spectroscopy (XAS), colloidal and sedimented samples required separation from solution. This was done using one of three methods depending on the colloidal stability of the sample. Firstly, if the sample was a sedimented solid without any colloid, the solid

was separated by centrifugation for 10 minutes at 7000g followed by decanting of the solution and harvesting the solid. Secondly, for colloids formed with a silicate concentration of 2 mM, a colloid destabilization approach was used; lowering the pH of the solution to 4 using 1.5 M HCl (Dreissig *et al*. 2011). At pH 4, separation by centrifugation as described above was possible. As centrifugation was done immediately, the colloid was in contact with the lower pH solution for a short amount of time and it was not anticipated that this method had any impact on the structure of the colloidal particles. Finally, for the 4 mM Si colloidal systems, colloidal destabilization could not be induced even after the pH was reduced to 4 for 1 hour. It was not possible to leave these systems at pH 4 for longer than 1 hour as this may have resulted in an altered particle structure. Therefore, the particulates were isolated by ultrafiltration using a 3 kDa centrifuge filter. Centrifugation-filtrations were repeated using several filters to collect sufficient amounts of sample for solid analysis. Using this methodology it was not possible to isolate sufficient solids for diffraction, therefore all diffraction and PDF investigations were only done on the 2 mM silicate, or silicate free (UO_2) systems. In all cases particles were left partially hydrated to allow a true representation of the structure in contact with the aqueous phase.

3.7. Solution and particle size analysis

3.7.1. Ultrafiltration

Ultrafiltration is a common technique for characterising the size distribution of small particles, typically below 1 µm. This makes it ideal for characterising colloidal dispersions. No pre-treatment of the filters was required as they were shown no to retain any solution species. This was tested by sequentially filtering a solution through 3 x 3 kDa filters, whereby no reduction in the concentrations of the solution species was observed in the latter 2 filtrations, indicating that the filters were not removing any of the elements of interest from the solution via sorption to the membrane. Pall Nanosep centrifuge filters, with polyethersulfone (PES) membranes were used due to their small pore sizes, small sample volumes required and the resistance of PES membranes to alkaline solutions (stability range pH 1-14).

Samples were analysed by ultrafiltration using Pall Nanosep ultracentrifugation filters (3, 10, 100 and 300 kDa, approximately corresponding to spherical particle size cut-offs of 1.5, 3, 7 and 12 nm) (Granath, 1958; Laurent and Granath, 1967; Dreissig *et al.*, 2011), and 0.22 µm syringe filter (Merck Millipore, PES membrane). Ultracentrifugation filters were spun for 12 minutes at 8,000 g. Concentrations of uranium and strontium in filtrates were analysed after acidification to 2 % HNO_3 using ICP-MS and ICP- atomic emission spectroscopy (ICP-AES) was used to measure silicon concentration.

3.7.1.1. U(IV)-silicate colloid stability investigations

For initial U(IV)-silicate colloid stability investigations (section 3.2), samples were prepared under a range of conditions (pH 9, 10.5 and 12, [Si] 0, 2 and 4 mM). Ultrafiltrations were performed at set time points (1 h, 2 d, 10 d, 30 d, 60 d) to investigate the size distribution of the colloidal particles over time. Initially, a full range of filters was used (3, 10, 100 and 300 kDa, and 0.22 µm), however if no colloid was formed further filtrations were done using only 0.22 µm filters to verify colloid formation did not occur over time. U and Si concentrations in filtrates were analysed.

3.7.1.2. Sr sorption onto U(IV)-silicate and UO_2

For Sr sorption investigations (section 3.3), samples were ultrafiltered 7 days after Sr spiking. For each pH (4, 6, 8, 10, 12 and 14 for U(IV)-silicate, 3.7, 6, 8, 10 and 12 for UO_2), experiments were done in triplicate. 3 kDa and 0.22 µm filters were used. U, Sr and Si (when present) were monitored in the filtrates. Results were averaged across triplicate experiments and errors were calculated as 1 standard deviation of the 3 data values.

3.7.1.3. Carbonation experiments

Ultrafiltrations of carbonated samples (section 3.4) were done at set time points before and after carbonation (-0.25 h, 0.25 h, 1 h, 4 h, 24h and 8 d). 3 and 300 kDa, and 0.22 µm filters were used for ultrafiltration and U, Sr and Si concentrations were analysed in the filtrates.

It has previously been reported that ultrafiltration analysis of samples can lead to artefacts such as induction of aggregation on the membrane which would increase the

apparent particle size (Maruyama *et al.*, 2001). Therefore further, non-invasive particle sizing techniques, SAXS and DLS, were also employed.

3.7.2. Inductively coupled plasma-mass spectrometry (ICP-MS) and Inductively coupled plasma-atomic emission spectroscopy (ICP-AES)

U, Si and Sr concentrations in solutions and filtrates were measured by ICP-MS (for Sr and U) and ICP-AES (for Si). Samples were diluted in 2 % HNO_3 and samples for ICP-MS had Sr and U concentrations < 100 ppb and for ICP-AES Si concentrations were < 10 ppm. After every 10 samples, standards were run with a concentration range above and below that of the samples (e.g. for samples ~50 ppb U, standards of 0, 1, 5, 10, 50 and 100 ppb U would be run).

3.7.3. UV-vis spectroscopy

UV-vis spectroscopy was routinely used in experiments to verify the +4 oxidation of uranium in solutions and colloidal suspensions. Samples were sealed in quartz cuvettes (10 mm path length) prior to analysis. Samples were analysed on a Jenway 6850 UV/vis spectrophotometer. Spectrum scans of samples at each stage of preparation (U(IV)-HCl solution, U(IV)-carbonate solutions and U(IV)-silicate colloidal suspensions) were recorded, and the absence of a multiplet of peaks at 400-475 nm confirmed no U(VI) was present (see Appendix 1).

3.7.4. Dynamic light scattering (DLS) and zeta potential

Dynamic light scattering (DLS) is a particle sizing technique that utilises the Stokes Einstein equation for determining particle size relating to Bownian motion:

$$D_h = \frac{k_B T}{3\pi\eta D_t} \quad (3.1)$$

Where D_h is the hydrodynamic diameter of the particles, D_t is the translational diffusion coefficient which is resolved by DLS, k_B is the Boltzmann constant, T is temperature and η is viscosity (Fischer and Schmidt, 2016). As the majority of components in the equation can either be controlled or are constants, only D_t is required to derive particle size, D_h. DLS resolves particle sizes by measuring the rate of changes in scattered light intensity

by a sample, which is caused by the speed at which the particles in the sample are moving. The faster the changes in light intensity, the faster the particles are moving hence a larger D_t. There is an inverse relationship between D_t and D_h, $D_h \alpha 1/D_t$, so the larger D_t, the smaller the particle size. These changes in light intensity at the detector are translated into an autocorrelation function. The intensity at a certain time point is compared to the same signal at a different time point. This can be plotted as a correlation curve, shown in Figure 3.2, which can be resolved by multi exponential fitting to result in a size distribution plot.

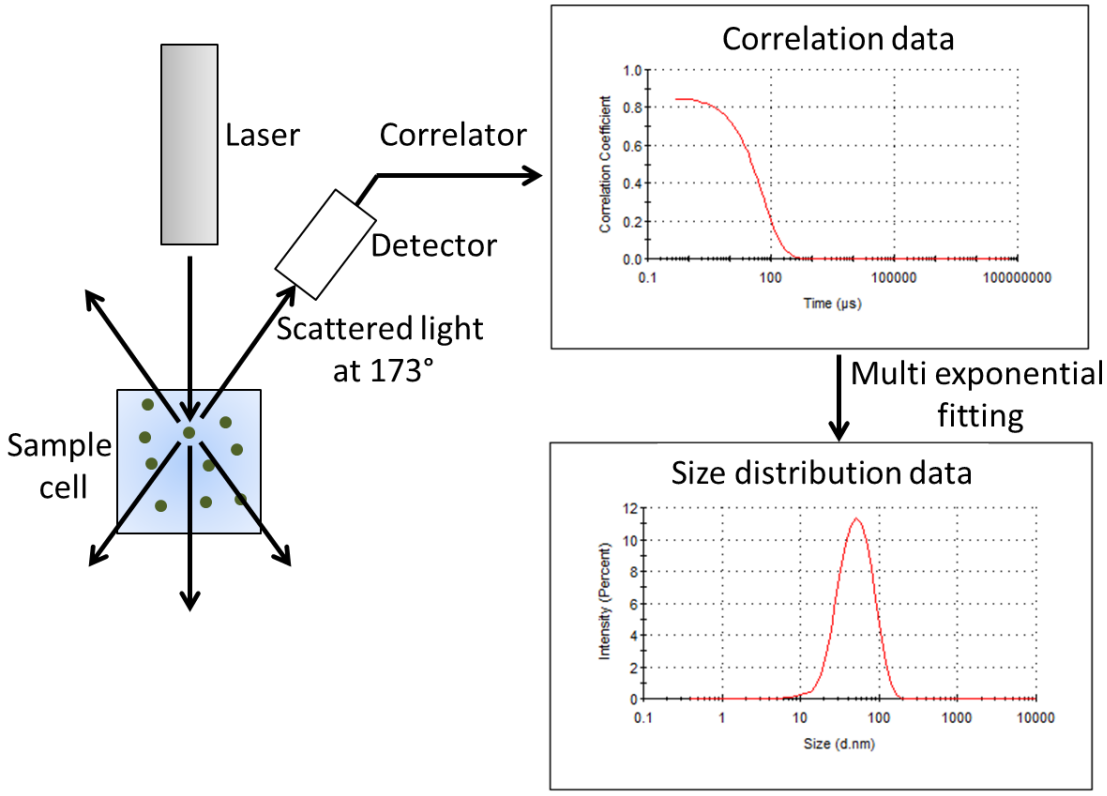

Figure 3.2: Schematic of how a size distribution is gained from dynamic light scattering. From the scattering data over time, a correlation plot is made. This is transformed into size distribution data using multi exponential fitting (Ramos, 2017).

While DLS is a technique that is widely used to determine particle sizes of monodisperse systems, the calculation of the autocorrelation function is more difficult for polydisperse samples. Due to the light scattering intensity measurements being heavily weighted towards larger particles (intensity $\alpha\ r^6$), scattering caused by smaller particles can be undetectable in the presence of larger particles (Dreissig *et al.*, 2011). In systems with a large degree of polydispersity, or multiple size populations, the accuracy of DLS measurements can be reduced. One way of overcoming these issues is weighting of the data, size distributions from DLS can be weighted by intensity, volume or number. These

3 weightings are proportional to the hydrodynamic radius (r_h) as $r_h^{\,6}$, $r_h^{\,3}$ and $r_h^{\,1}$ respectively. The effect of using these 3 different weightings on a bimodal particle population is illustrated in Figure 3.3 which shows the relative sensitivity of each weighting for smaller or larger particles. One advantage DLS has over several other particle sizing techniques, such as ultrafiltration and standard TEM, is that it is non-invasive. This means samples can be analysed in-situ without altering the conditions of the sample. This is important for colloidal materials as changing conditions can alter particle size, especially via particle aggregation.

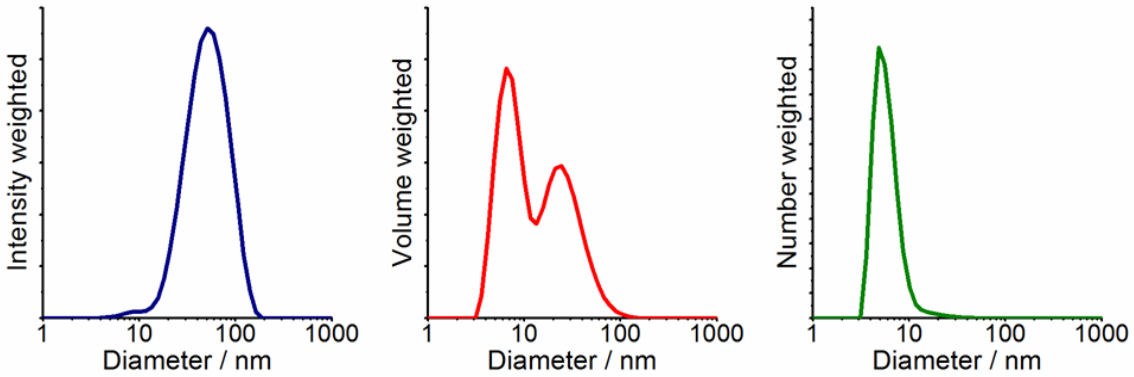

Figure 3.3: Particle size distributions acquired for a bimodal particle size distribution, showed as an intensity weighted size distribution (left), a volume weighted size distribution (centre) and a number weighted particle size distribution (right).

Zeta potential can be used as a measure of the charge at the slipping plane of a particle, and as an extension using DLVO theory (section 2.3.1.) to predict the stability of a colloidal system. The zeta potential is measured by applying a potential across the sample and measuring the velocity of the particles as they move towards the electrode. Generally, particles with larger zeta potentials (either positively or negatively charged) show higher colloidal stability, however there are exceptions to this rule, with colloids able to form from particles with low zeta potentials, and some colloids being unstable despite high zeta potential values (Smith *et al.*, 2017). While zeta potential is an effective estimate of surface charge, and therefore colloidal stability, it is not a measurement for the true surface charge of the particle or the Stern potential which is the net charge of the particle and directly sorbed ions. Instead the zeta potential is the measure of the charge at the slipping plane, which is the layer of ions that are mobile with the charged particle (Figure 3.4).

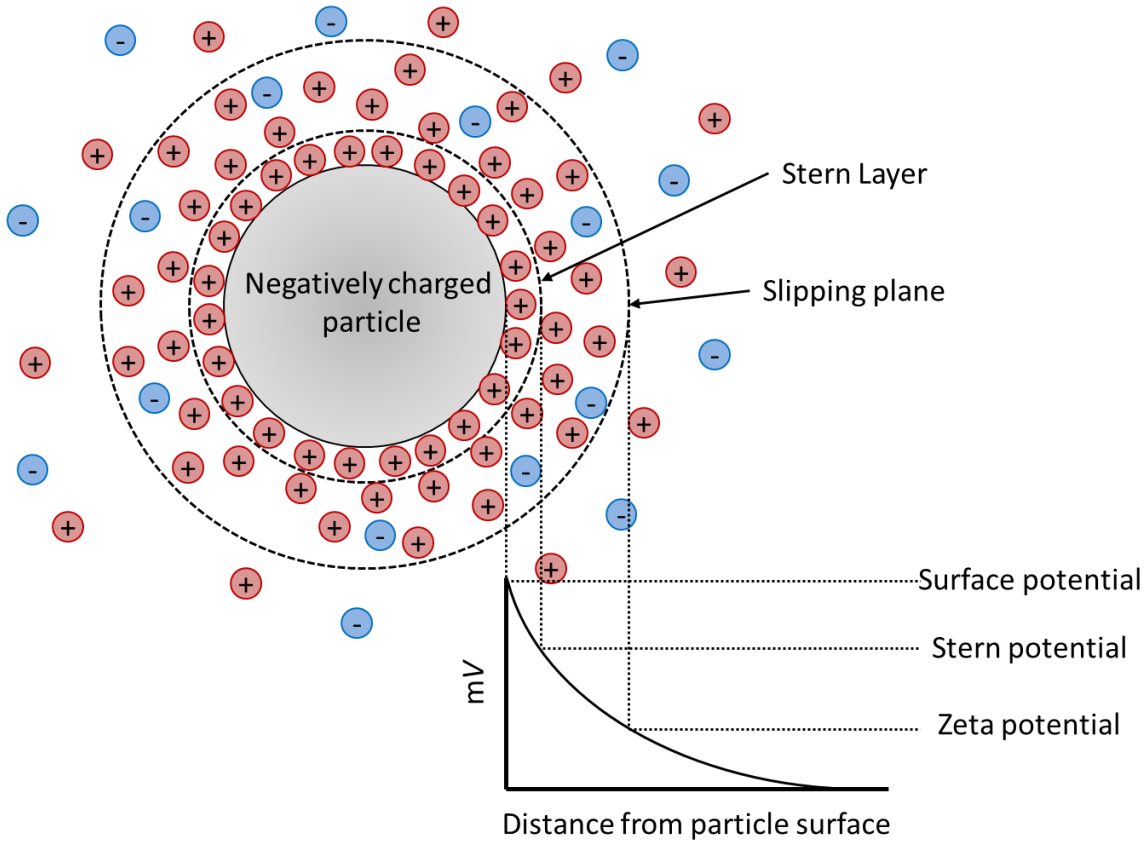

Figure 3.4: The electric double layer model for a negatively charged particle showing the stern layer of ions fixed at the particle surface and the slipping plane, where ions are mobile with the particle in solution. Graph below indicates how electric potential changes with distance from particle surface.

DLS and zeta potential measurements were recorded using disposable DTS1060 zeta potential and sizing U-bend cuvettes. Samples were prepared at the University of Manchester and measured at the FENAC laboratory at the University of Birmingham. Therefore, samples were loaded into capped syringes and stored in oxygen free jars for transport and analysis. To load the samples into the cuvettes, a flow of N_2 gas was first passed through the cuvette to remove any oxygen. The syringe was then uncapped under the flow of N_2 and the sample was injected into the U-bend cuvette and both ends were sealed with Teflon-coated stoppers. This method was successful in preventing oxidation of the samples before and during analysis. Samples were analysed on a ZetaSizer HPPS (Malvern Instruments) at 25 °C with a He-Ne laser (λ = 633 nm) measuring back-scattered light at 173°. At least 5 consecutive scans were collected per sample. Samples were analysed using Zetasizer Software (Malvern) and size distributions were reported as volume weighted size distributions. To translate from

intensity weighted volume distributions, the refractive index of coffinite (1.74) was used (Moench, 1962).

3.7.5. Transmission electron microscopy (TEM)

Transmission electron microscopy (TEM) is used to image features on the µm and nm scale using an electron beam. Electrons are used for imaging on this scale due to the higher achievable resolution compared to visible light. The limit of resolution in microscopy is represented as δ in Equation 3.2, where µsinβ, the numerical aperture, can be approximated to 1 and λ is the wavelength of radiation (Williams and Carter, 2009).

$$\delta = \frac{0.61\lambda}{\mu \sin\beta} \tag{3.2}$$

For visible light, for example λ = 550 nm (green light), δ is equal to 335.5 nm meaning this is the absolute limit of achievable resolution for a visual light microscope. Therefore, it is not possible to image very small particles using a visible light microscope. The wavelength of an electron of a given kinetic energy (e*V*) is described in Equation 3.3; h is Planck's constant, m_0 is the resting mass of an electron and c is the speed of light in a vacuum:

$$\lambda = \frac{\mathrm{h}}{[2m_0 eV\left(1 + \frac{eV}{2m_0 c^2}\right)]} \tag{3.3}$$

The above equation accounts for relativistic effects that will be relevant for most TEMs due to the high accelerating voltage. For an electron in a TEM with accelerating voltage of 200 kV, the relativistic wavelength of this electron will be 0.00251 nm. Using Equation 3.2 above this gives δ = 0.00153 nm. Due to machine-based constraints within electron microscopes, it is not possible to approach this theoretical wavelength-limited resolution but much higher resolution than optical light microscopes is achieved.

In TEM, images are acquired as an electron beam interacts with the sample. This leads to contrast in the resulting image that is predominantly caused by either mass-thickness or diffraction. Mass-thickness contrast is caused by incoherent elastic scattering of electrons by a sample. It is dependent on the atomic number of the elements contained

in the sample (or, alternatively, sample density) and the sample thickness. Diffraction can occur on crystalline samples when the electron beam angle satisfies Bragg's law (section 3.8.3.). Scanning TEM (STEM) mode can be used on some TEMs which allows scanning of samples and mapping of samples using several techniques. In this case, the electron beam is focused on to a small spot and the beam is rastered across the sample to build an image (Williams and Carter, 2009). STEM imaging allows the use of high angle annular dark field (HAADF) imaging with a high z-contrast, and elemental mapping of samples using either energy dispersive X-ray (EDX) spectroscopy or electron energy loss spectroscopy (EELS). In this project, as well as traditional TEM and HAADF imaging, EDX was used for both elemental mapping of samples and bulk sample composition analysis. EDX probes the emission of X-rays from a sample excited by an electron beam. The energies of the X-rays emitted are recorded on an energy-dispersive spectrometer and are characteristic of element specific emission lines.

Selected area electron diffraction (SAED) can also be applied using TEM (Williams and Carter, 2009). SAED uses the same theoretical basis as X-ray diffraction (XRD, section 3.8.3.). The wavelengths of electrons in TEM are shorter than interatomic distances, so TEM samples can act as a diffraction grating for the electron beam. One advantage SAED has over traditional XRD is that specific areas of a sample can be analysed.

One disadvantage of standard TEM imaging is that samples must be dry to be analysed. For colloidal samples this can induce aggregation and the loss of structural water can alter particle morphology (Bailey and Mecartney, 1992; Michen *et al.*, 2015). These changes can lead to larger, more aggregated particles being imaged than those that truly exist in suspension, or denser aggregates and particles forming upon drying and loss of hydration. Alternative sample preparations are possible, including in-situ TEM and cryo-TEM, however these techniques were not used in this project due to difficulties in sample preparation, machine access and reduction in resolution which would mean imaging of primary particles would not be possible.

Samples were prepared for TEM by dropping 2-3 µL of suspended solid onto a carbon coated copper grid. The sample was then left to dry until almost all of the water had dried off, resulting in deposition on sample onto the grid. This step was repeated 2-3 times for low concentration samples. Once the sample had been deposited onto the

grid, the grid was washed twice using DIW. A similar procedure was followed; a 2-3 µL DIW droplet was placed onto the grid, left for 30 seconds then wicked off the grid. This was done to remove any salt residues on the grid and the short contact time with DIW was deemed insufficient to significantly alter the phases of interest. For Sr-containing samples, it was found that washing of samples prior to imaging resulted in the dissolution and removal of Sr. Therefore, for Sr-containing samples the TEM grids were not washed with DIW after deposition of the sample. Prior to TEM analysis, all TEM grids were imaged on an optical microscope to ensure good sample coverage of the grid was achieved before being stored anaerobically prior to analysis. Either an FEI Talos F200X analytical transmission electron microscope operated at 200 kV, equipped with an integrated Super-X EDS system with 4 windowless silicon drift detectors (SDD)EDX/SAED, or an FEI TF30 analytical FEG TEM running at 300kV equipped with an Oxford Instruments Silicon Drift Detector EDS system using Oxford INCA software was used to image particles.

3.8. Synchrotron techniques

3.8.1. Synchrotron radiation

A synchrotron light source generates a high flux of radiation by the bending of the path of electrons travelling at relativistic speeds (approaching the speed of light). Bending the path of electrons results in a loss of energy in the form of radiation emitted in the direction of the electron motion. The radiation wavelengths range from hard X-ray to infra-red and, due to the difficulties in generating high-flux X-rays from other sources, it is the X-rays that are most commonly utilised at synchrotron sources. The extremely high flux at synchrotron sources allows collimation and monochromation of the beam without sacrificing signal strength. This means that low concentration analysis, rapid measurements for in-situ reactions or element specific techniques are all possible and a high signal to noise ratio can still be achieved.

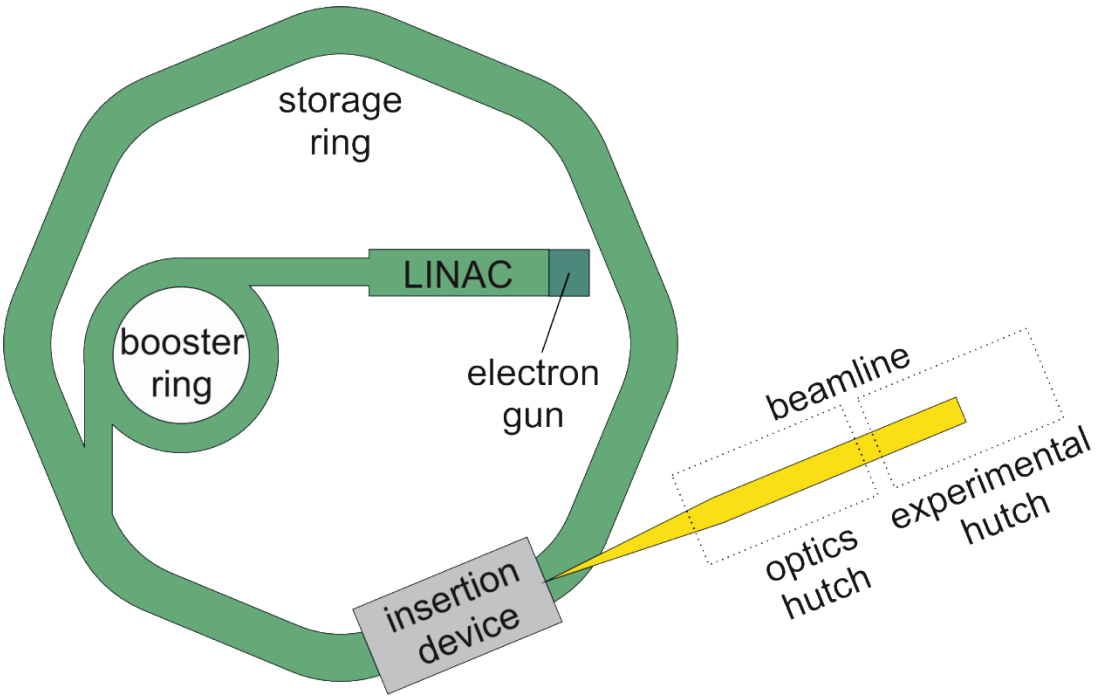

Figure 3.5: Schematic of a typical synchrotron facility.

Figure 3.5 outlines the basic components of a modern synchrotron. The electrons are first injected into a linear accelerator (LINAC) and then into a booster ring. Here, the electrons are further accelerated to speeds approaching the speed of light. From the booster ring, the electrons are injected into the storage ring, which is not a true circle and has a number of straight sides. Here, the electrons are circulated by use of bending magnets at the vertices and the electron velocity is maintained using radio frequency. The ring is maintained under ultra-high vacuum to prevent loss of electron momentum through collisions with air. It is the bending of the electron path in the storage ring that generates the radiation, and this can be amplified by implementation of insertion devices. Insertion devices such as wigglers induce repeated lateral movement of the electrons which results in the increased flux of radiation generated. The light beam generated from a bending magnet, and insertion device if present, is utilised in a beamline that is specialised to use a specific technique, or set of techniques. The beam first passes through an optics hutch where it is focused and filtered. Then the collimated beam enters the experimental hutch where it interacts with the sample and the data is recorded.

The synchrotron based experiments in this project were done at Diamond Light Source, which is a 3rd generation synchrotron based in Oxfordshire, UK. Diamond has over 20

beamlines, work for this project has been carried out on 3 of these: I22 non-crystalline diffraction (SAXS) beamline, I15 X-ray diffraction beamline and B18 EXAFS beamline.

3.8.2. Small angle X-ray scattering (SAXS)

While X-ray diffraction, discussed in section 3.8.3., uses large angles of diffraction, θ, to probe the very small distances between lattice planes, it is also possible to use much smaller angles of diffraction to investigate larger lattice spacings and even macromolecules (Guinier and Fourner, 1955). Small angle scattering is an in-situ technique for analysing the nanoscale size and structure of a material. Small angle scattering studies use either X-rays or neutrons for scattering. In this study, X-rays were used due to the high flux possible from a synchrotron X-ray source, combined with the high scattering contrast that would be provided by uranium containing samples (Guinier and Fourner, 1955; Glatter and Kratky, 1982; Willmott, 2011). SAXS was used to probe the particle size and structure under a range of conditions (2 and 4 mM Si and pH 9 and 10.5 experiments) at a range of different time points between 10 and 60 days aging.

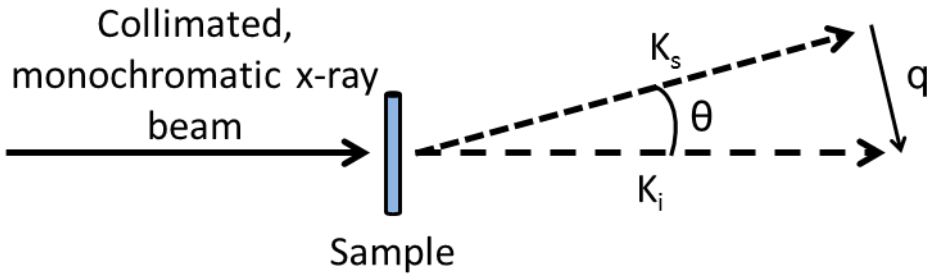

Figure 3.6: The basis of a small angle X-ray scattering experiment. The highly collimated beam is scattered by the sample, and the resulting scattering pattern is recorded in terms of q, the scattering vector. Adapted from Narayanan (2014).

Figure 3.6 outlines the basic setup of a SAXS experiment, whereby a highly collimated, monochromatic beam is scattered by a sample. The scattering is recorded by a 2D detector while the direct, unscattered beam is removed by a beamstop in front of the detector. The beam before and after interacting with the sample is in vacuum to prevent further scattering from air (Narayanan, 2014). The scattering vector, q, is equal to the difference between the wave vectors of the scattered and incident radiation (Figure 3.6) and can be described by the following:

$$q = \frac{4\pi \sin\theta}{\lambda} \quad (3.4)$$

The q range of a SAXS experiment is indicative of the length scales that can be probed. The units of q are reciprocal (nm^{-1} or $Å^{-1}$), meaning scattering from larger structures will occur in the lower q region of a SAXS pattern.

Due to the heterogeneous particle sizes generated in this study, and the scattering range that was used, McSAS, a Monte Carlo regression software package was used to assess particle size distributions from SAXS patterns. McSAS allows for selection of a scattering contribution model (shape) from a pre-set library and has the advantage of not requiring additional information on particle size distributions. When provided with data on an absolute scale, McSAS is capable of resolving asymmetric and multimodal distributions as well as providing uncertainty estimates on the results (Bressler, Pauw and Thünemann, 2015). A model is based upon a number of independent contributions, typically 1,000, based on both defined parameters (particle shape and scattering contrast between scatterer and medium) and a random allocation of values from the fitting parameter(s) (in this study, particle size). Each iteration changes the value of the particle size for one contribution. The quality of the fit, (χ_r^2) is calculated based on the difference between the model and measured data and is weighted by the uncertainty in the measured data. If an iteration results in an improved χ_r^2, the new iteration is used as the base for the next iteration. This is repeated for the programmed number of iterations, or until the convergence criterion (a set value of χ_r^2) is achieved. Uncertainty estimates are derived from the standard deviation of independent Monte Carlo solutions (Bressler, Pauw and Thünemann, 2015).

SAXS samples were analysed at the Diamond Light Source I22 beamline using a 12.6 keV monochromatic beam, a Pilatus 2D detector and a 1.918 m camera length, resulting in a recorded q range of 0.009 to 1 $Å^{-1}$. Samples were injected into 1.5 mm quartz capillaries from syringes on the beamline. N_2 gas was flushed through the capillary prior to sample loading, and flowed over the capillary and sample syringe during sample injection to prevent sample oxidation during loading. A background corresponding to the colloid-free, pH adjusted silicate solution was recorded after each sample. Capillaries were washed out 3 times with 2 % HNO_3 and 3 times with DIW between sample and

background measurements. For each sample 30 x 10 second scans were recorded however, due to the formation of bubbles within the samples, it was only possible to use between 15 and 20 of these scans for each sample. It was possible to identify the formation of these bubbles by an increase in the scattering intensity at low q values (q <0.015) and when this intensity increased by >5 % the scan was not used.

The resulting SAXS patterns were averaged, background subtracted and normalized using Microsoft Excel before being analysed using McSAS software (Pauw *et al.*, 2013; Bressler, Pauw and Thünemann, 2015). Samples were assumed to be spherical as no evidence of different morphologies was observed in TEM. Because SAXS investigations were focused on the smaller, primary particles, the full scattering features of the larger particles was not recorded and it was not possible to acquire a particle size from these partial scattering features. Therefore, for evaluation of SAXS data using McSAS, scattering from larger particles (q < 0.13) was removed from the data when present to allow size evaluation of primary particles only. A size range of radii between 0.8 and 20 nm was used initially, with a scattering length density difference, the contrast between the sample (U(IV)-silicate) and the background solution, was set to $2.48e^{-5}$. The convergence criterion, relating to the quality of the fit, was initially set at 5, and was iteratively reduced, along with the radii size range to optimise the fitting. This was done until the convergence criterion could not be reduced further, i.e. the quality of the fit could not be improved any more. 5 repetitions for the fitting were used in all iterations and the number of contributions to the model was 1,000. The resulting fits were exported, along with histograms of the particle size distributions and statistical values, including errors on the average particle size.

3.8.3. X-ray diffraction (XRD)

X-rays are diffracted by crystals according to Bragg's law where an X-ray of incident angle θ will be reflected at reflection angle θ when the Bragg condition is satisfied (Equation 3.5). Where λ is the wavelength of the X-ray, d is the distance between crystal lattice planes (also known as d-spacing), θ is the Bragg angle at which diffraction will occur, and n is the order of reflection, which is usually 1.

$$n\lambda = 2d \sin\theta \qquad (3.5)$$

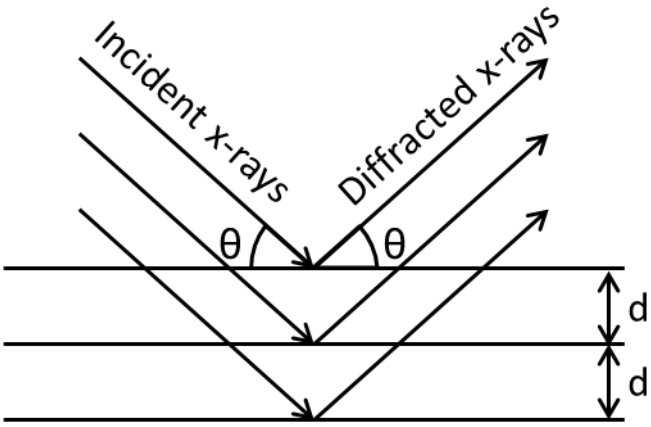

Figure 3.7: An illustration of Bragg diffraction from lattice planes of atoms with an interplane distance of d, adapted from (He, 2009).

X-ray diffraction patterns are characteristic of the sample analysed. The degree of crystallinity of a sample will affect the specific method of diffraction used, and also the resulting diffraction pattern. For powdered samples, a 2D diffraction pattern consisting of rings is collected due to the number of particles diffracting the X-rays in all orientations. These crystallites will have a range of different orientations leading to coaxial cones caused by the diffraction of these crystallites rings (Figure 3.8). This 2D diffraction pattern is translated into a 1D diffraction pattern with respect to 2θ. The peaks in the diffraction pattern correspond to specific values of 2θ according to Bragg's law; h, k and l (the Miller indices) are 3 integers that define each diffraction peak and $d_{h,k,l}$ is the spacing of the lattice planes (Equation 3.6). Due to the practicalities of compressing a 3D particle structure data into a 1D measurement, along with instrumental peak broadening and peak broadening due to crystallite size and disorder, it is often difficult to resolve a specific 3D structure from powder diffraction alone.

$$2\theta_{hkl} = 2\sin^{-1}\left(\frac{\lambda}{2d_{hkl}}\right) \tag{3.6}$$

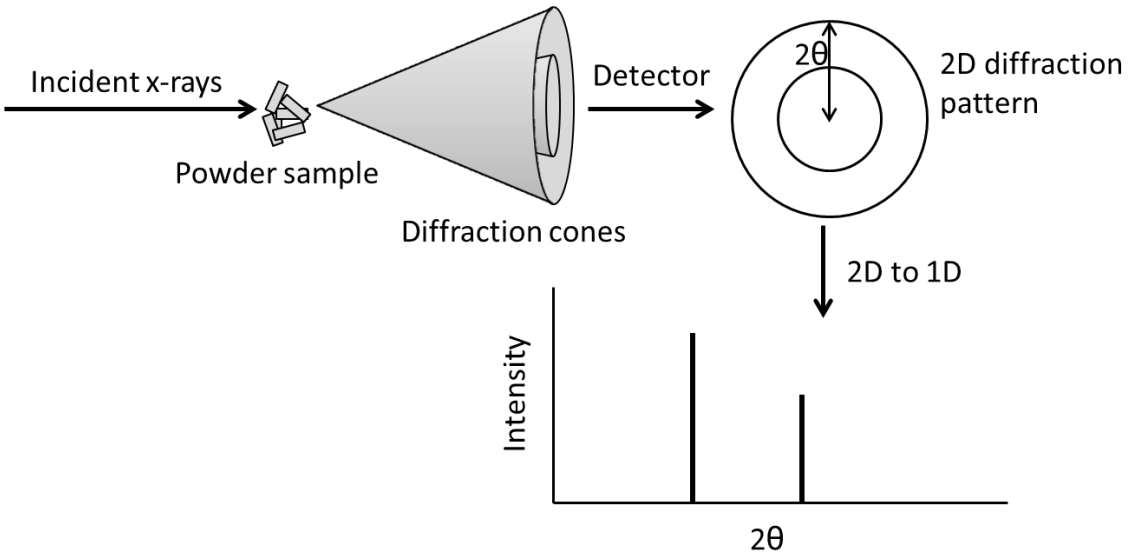

Figure 3.8: Flow diagram showing how a 2D diffraction pattern is generated from a powder sample with all crystal orientations present at once, and how this translates into a 1D diffraction pattern. Adapted from (Bruce, O'Hare and Walton, 2014)

For crystallites of a small size (<0.1 μm) it is possible to resolve the crystallite size from the peak broadening due to crystallite size (Bruce, O'Hare and Walton, 2014). It is important to note that this size represents the size of the crystalline domain of the particles and is not necessarily representative of the total particle size. For small particles, the diffraction peak width at full width half maximum ($\beta_{1/2}$) increases as crystallite size (D) decreases according to the Scherrer equation, where *K* is the shape factor that can be approximated to 0.9, assuming a spherical crystallite:

$$D = \frac{K\lambda}{\beta_{\frac{1}{2}} cos\theta} \tag{3.7}$$

X-ray diffraction patterns were recorded for U(IV)-silicates formed under a range of conditions. The XRD were measured on either laboratory-based Bruker D8Advance or on Diamond Light Source I15 beamline. For the laboratory-based sample, a 2 mM Si pH 10.5 sample (20 mg) was isolated from solution as described in section 3.6., resuspended in isopropanol and dropped onto a glass slide. This was repeated 3 times as the gel-like precipitate was found to dramatically reduce in size upon drying. The sample was scanned from 5-70° 2θ, with a step size of 0.02° and a count time of 0.2 s per step using a CuKα1 X-ray source with a wavelength of 1.5406 Å. For high energy X-ray scattering (HEXS) and pair distribution function (PDF) analysis samples were analysed on Diamond Light Source's I15 beamline using 0.1631 Å X-rays. Slurries of U(IV) silicate (2 mM Si pH

9, 10.5 and 12) and UO_2 (0 mM Si pH 10.5) were placed in capillaries (1 mm) and sealed with araldite for containment and to prevent sample oxidation. These samples were analysed as wet slurry and were not dried. Backgrounds of silicate solutions and H_2O were also recorded. 5 x 30 second scans, with a scanning range of 0-60 ° 2θ and a step size of 0.01° 2θ, were recorded for each sample and were averaged prior to data processing.

3.8.3.1. X-ray pair distribution function (PDF)

A PDF is calculated from the Fourier transform of the measured intensities of a diffraction pattern, normally collected using high energy X-rays to obtain a greater q range; hence this technique is occasionally called HEXS. The diffraction pattern contains both the simple Bragg reflections outlined above and used in analysis of XRD patterns, but also other, weaker intensities from diffuse scattering and structural defects (Proffen *et al.*, 2003, 2005). These defects are particularly evident in nanoparticles and more amorphous structures which do not have a regularly repeating unit cell (Bruce, O'Hare and Walton, 2014). A PDF is generated from the Fourier Transform of the total diffraction pattern and is a calculation of all the interatomic distances within the measured material. The more regularly occurring a correlation is, the more significant the peak intensity will be. While EXAFS investigates short range order, PDF focuses on short to medium range order. This makes it ideal for resolving the structure of nanoparticulate and amorphous materials, particularly in combination with other techniques (Proffen *et al.*, 2005).

The X-ray scattering data ($0.5 \leq q \leq 20$ Å^{-1}) were background subtracted, corrected and processed into PDF data using the program GudrunX (Soper and Barney, 2011). Although quantitative assessment and fitting of the X-ray PDFs was attempted, it was not possible to gain significant data from these fits. Instead, PDFs were compared on a qualitative scale and features were compared to candidate structures of UO_2 (which was also measured), and a simulated PDF for nanocrystalline coffinite ($USiO_4$) generated using the software PDFgui (Farrow *et al.*, 2007).

3.8.4. X-ray absorption spectroscopy (XAS)

X-ray absorption spectroscopy (XAS) is a powerful tool capable of probing oxidation state and coordination environment of an element of interest by excitation of a core electron. X-rays of a definite energy are fired at the sample and the amount of X-rays absorbed is measured. Normally, samples are scanned across a fixed range of X-ray energies to generate the X-ray absorption spectrum. This absorbance is normally measured in one of two ways:

- The difference between intensity of the incident beam (I_0, before the sample) and the transmitted beam (I_t) after the sample. This method is transmission XAS.
- The fluorescence emission (I_f) of the sample as an electron fills the now vacant core orbital (core-hole) generated by absorption of the incident X-ray. This is fluorescence-detected XAS.

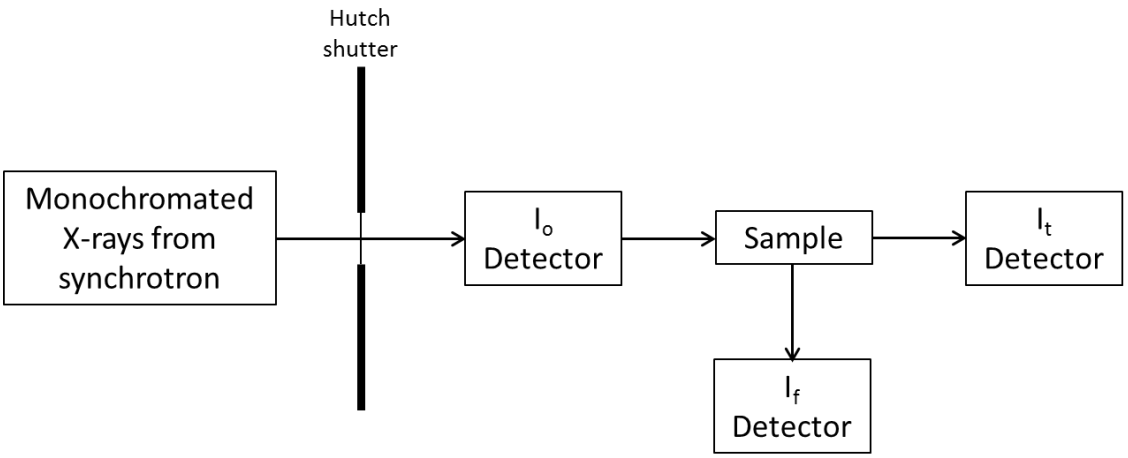

Figure 3.9: Simplified schematic of the experimental hutch of a typical XAS beamline. I_f detector shows the path of fluorescence detection, I_t is the transmission detector.

A typical absorption and emission schematic is shown in Figure 3.10 for the U L_3-edge absorbance (for U(IV)), the most commonly used edge for U XAS. It shows the absorption of an X-ray with energy above the edge position required to excite an electron from the 2p core orbital to 6d valence orbital. The emission shown is the $L\alpha_1$ emission which shows the relaxation from the excited state to a more stable state. This results in the generation of another X-ray which is detected in fluorescence mode XAS.

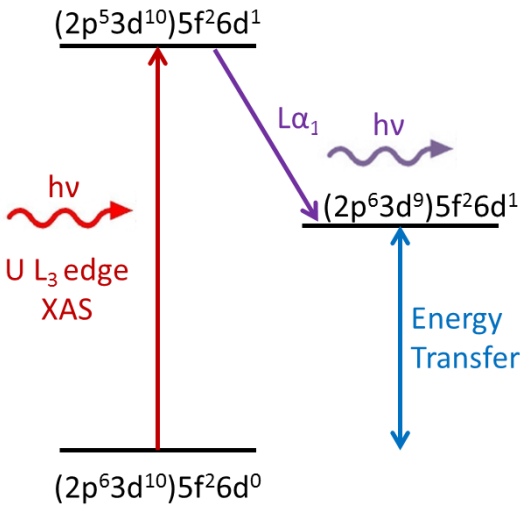

Figure 3.10: A schematic of the X-ray excitation and emission for the U L_{III} absorption edge and $L\alpha_1$ emmission line for U(IV) (adapted from (Bès *et al.*, 2016).

An example of an X-ray absorption spectrum is shown in Figure 3.11. The two main features of the X-ray absorption spectrum are highlighted. Firstly, the X-ray absorption near edge structure (XANES) region includes the edge, the energy at which the photons have sufficient energy to excite the targeted core electron. This feature is characteristic of the oxidation state of the element of interest and therefore used for determination of oxidation state. The edge is defined as the inflection point of the upward curve, or peak of the first derivative of this upward curve, and is used to characterise the oxidation state of the element of interest. The XANES region can also be characteristic of the coordination environment of the sample and can therefore be used to elucidate some information on this using linear combination fitting of model systems (Salbu *et al.*, 2003; Bernier-Latmani *et al.*, 2010; Alessi *et al.*, 2014).

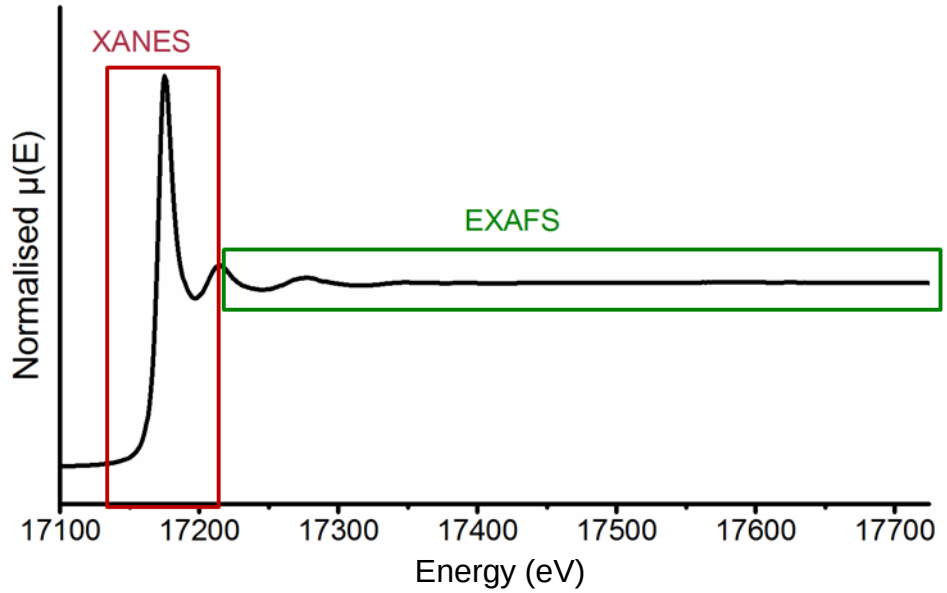

Figure 3.11: Schematic of an X-ray absorption spectrum, highlighting the X-ray absorption near edge structure (XANES) and extended X-ray absorption fine structure (EXAFS) regions.

At energies above the edge, the oscillations are known as the extended x-ray absorption fine structure (EXAFS) region. Here, a photoelectron is excited with sufficient energy to be ejected into the continuum. The oscillations in the EXAFS region are representative of the relative absorbance induced by constructive or destructive interference of a photoelectron with itself when scattering off neighbouring atoms in a sample. The EXAFS equation is shown in Equation 3.8, below. S_0 is the amplitude reduction factor, N is the degeneracy of a scattering path, f(k) is the proportionality constant based on the possibility of scattering off a certain atom, k is the wavenumber of the photoelectron, D is the half path length of the scattering, λ(k) is the mean free path of the photoelectron, σ is the variance in D caused by disorder, also known as Debye-Waller factor and δ is the phase shift.

$$\chi(k) = S_0^2 \sum_i N_i \frac{f_i(k)}{kD_i^2} e^{-\frac{2D_i}{\lambda(k)}} e^{-2k^2\sigma_i^2} \sin(2kD_i + \delta_i(k)) \qquad (3.8)$$

With the use of modelling software, it is possible to derive values for D, N, σ^2 for each scattering path as well as S_0 (Calvin 2013). This allows resolution of the number of scattering paths, the number of neighbouring atoms in each scattering path, the distance these atoms are away from the excited atom and the structural variance of the path length. Therefore, EXAFS is a very useful technique to probe the average

coordination environment of the element of interest in samples. Specifically, it is possible to resolve the neighbouring atoms, the number of neighbouring atoms and the interatomic distances involved. For samples with low crystallinity, it is normally only possible to resolve 1 or 2 shells of atoms at R <4 Å from the central atom due to low long range order (Fletcher *et al.*, 2010; Dreissig *et al.*, 2011; Morin *et al.*, 2016). Additionally, because XAS is an X-ray technique, and X-rays and photoelectrons interact strongly with heavy atoms, this technique is more effective at resolving heavy elements e.g. U. This means that XAS is not best suited to the study of lighter elements; however for this project XAS was used to probe the local coordination environments of Sr and U and therefore was an invaluable technique.

(XAS) analysis was carried out to probe both uranium oxidation state and particle structure. Uranium oxidation state investigations were done using U L_3 edge XANES spectroscopy and particle structure was probed using EXAFS spectroscopy. Sr K edge XAS was used to probe to coordination environment of Sr sorbed to UO_2 and U(IV)-silicate phases. XAS were recorded at Diamond Light Source's B18 beamline using a Si (1 1 1) monochromator at liquid nitrogen temperature with the exception of solution samples, which were recorded at room temperature. Solid U-L_3 edge samples were analysed in transmission mode, solution U-L_3 edge samples and Sr K-edge samples were analysed in fluorescence mode. The data was analysed using Demeter software package Athena and Artemis, FEFF6.

XAS analysis of colloidal suspensions of U(IV)-silicate was not possible because of beam damage effects. Due to the relatively low concentration of U(IV) in suspension, it was very challenging to acquire EXAFS data for these samples on the Diamond Light Source's B18 beamline. Therefore, it was necessary to use Diamond Light Source's I20 beamline – a high flux, low concentration XAS beamline. Any colloidal samples analysed on this beamline were oxidised to U(VI) immediately after exposure to the beam, even when the samples were analysed in a liquid nitrogen cooled cryostat. To verify that this was beam damage, a sample was analysed on B18 and then subsequently analysed on I20. Figure 3.12 shows the resulting XANES and the clear sample oxidation in the I20 data.

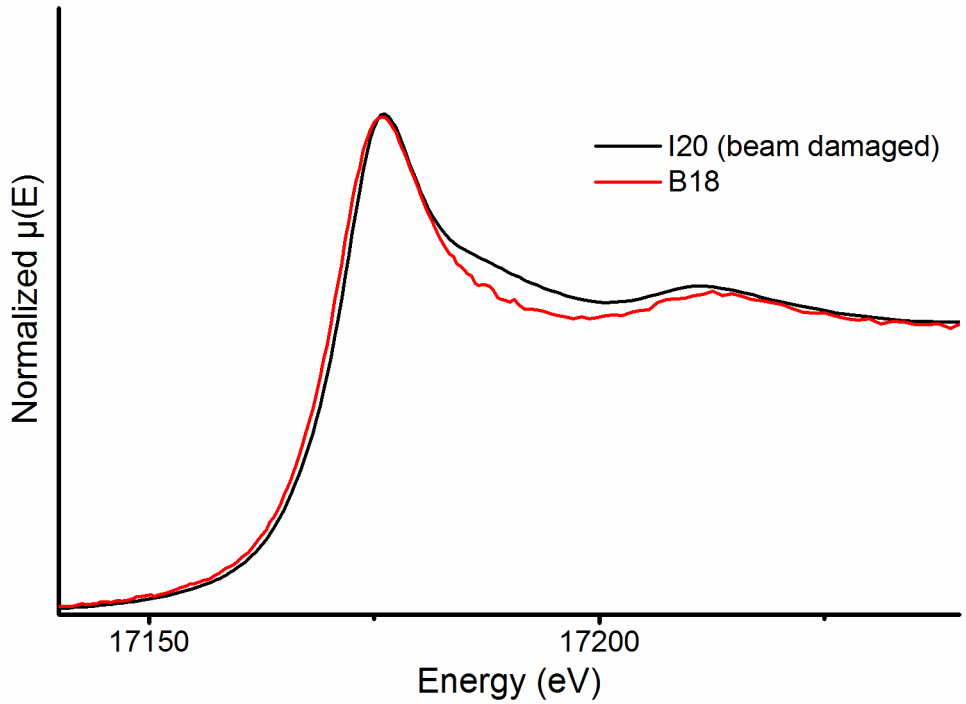

Figure 3.12: XANES of A 4mM Si/pH 9 colloidal suspension analysed on B18 and I20, showing oxidation of sample occuring on beamline I20 resulting in the formation of U(VI)

For U L_3 edge EXAFS, solid samples were required and were isolated as described in section 3.6.. These solid samples were diluted in cellulose, compressed into pellets (10 mm diameter) and stored in a cryovial (2 mL capacity). The final U concentration was 1 wt %, which was optimal for transmission EXAFS. For Sr K edge EXAFS, solid samples of Sr sorbed to UO_2 or U(IV)-silicate were placed in a small cryovial (200 µL capacity), within a larger cryovial (2 mL) because of restrictions on sample mass available. Sr loadings were between 1 and 0.1 wt % on U(IV) phases. Solution samples (of U(IV)-carbonate and U(IV)-HCl solutions) were also placed in a small cryovial within a larger cryovial.

EXAFS analysis was carried out using the Athena and Artemis XAS processing software (Ravel and Newville, 2005). Samples were aligned, merged and splined in Athena and EXAFS fitting was performed using Artemis. U(IV)-silicate samples were fitted using Feff scattering pathways generated from coffinite crystal structure (Fuchs and Gebert, 1958). k ranges for EXAFS fitting were selected independently for each data set depending on data quality and signal to noise ratio. The UO_2 sample was fitted using Feff scattering patterns generated from uraninite crystal structure (Barrett *et al.*, 1982). For Sr K edge EXAFS fitting, Feff scattering patterns were generated from $SrSiO_3$ and Sr in a U site of UO_2. Validity of new shells were tested using the F-test (Downward *et al.*, 2007); here,

shells with a statistical validity of >95 % were deemed true and implemented into the fitting.

Chapter 4: Stability, composition and core-shell particle structure of uranium(IV)-silicate colloids

This chapter is a manuscript published in the journal Environmental Science & Technology in July 2018.

The full citation for the published manuscript is as follows:

Neill T. S.; Morris K; Pearce C. I.; Sherriff N. K.; Burke G. M.; Chater P.; Janssen A.; Natrajan L. S.; Shaw S. 'Stability, composition and core-shell particle structure of uranium(IV)-silicate colloids' *Environmental Science & Technology* **Just Accepted Manuscript** DOI: 10.1021/acs.est.8b01756

Environmental Science & Technology

Article

Cite This: Environ. Sci. Technol. XXXX, XXX, XXX−XXX

pubs.acs.org/est

Stability, Composition, and Core−Shell Particle Structure of Uranium(IV)-Silicate Colloids

Thomas S. Neill,[‡] Katherine Morris,[‡] Carolyn I. Pearce,[§] Nicholas K. Sherriff,[⊥] M. Grace Burke,[†] Philip A. Chater,[∥] Arne Janssen,[†,∥] Louise Natrajan,[#] and Samuel Shaw*[,‡]

[‡]Research Centre for Radwaste and Disposal, Williamson Research Centre, The University of Manchester, Oxford Road, Manchester M13 9PL, U.K.

[§]Pacific Northwest National Laboratory, Richland, Washington 99354, United States

[⊥]National Nuclear Laboratory, Chadwick House, Warrington Road, Birchwood Park, Warrington WA3 6AE, U.K.

[†]Materials Performance Centre, The University of Manchester, Oxford Road, Manchester M13 9PL, U.K.

[#]School of Chemistry, The University of Manchester, Oxford Road, Manchester M13 9PL, U.K.

[∥]Diamond Light Source, Harwell Campus, Didcot, Oxfordshire OX11 0DE, U.K.

Supporting Information

ABSTRACT: Uranium is typically the most abundant radionuclide by mass in radioactive wastes and is a significant component of effluent streams at nuclear facilities. Actinide(IV) (An(IV)) colloids formed via various pathways, including corrosion of spent nuclear fuel, have the potential to greatly enhance the mobility of poorly soluble An(IV) forms, including uranium. This is particularly important in conditions relevant to decommissioning of nuclear facilities and the geological disposal of radioactive waste. Previous studies have suggested that silicate could stabilize U(IV) colloids. Here the formation, composition, and structure of U(IV)-silicate colloids under the alkaline conditions relevant to spent nuclear fuel storage and disposal were investigated using a range of state of the art techniques. The colloids are formed across a range of pH conditions (9−10.5) and silicate concentrations (2−4 mM) and have a primary particle size 1−10 nm, also forming suspended aggregates <220 nm. X-ray absorption spectroscopy, ultrafiltration, and scanning transmission electron microscopy confirm the particles are U(IV)-silicates. Additional evidence from X-ray diffraction and pair distribution function data suggests the primary particles are composed of a UO_2-rich core and a U-silicate shell. U(IV)-silicate colloids formation correlates with the formation of $U(OH)_3(H_3SiO_4)_3^{2-}$ complexes in solution indicating they are likely particle precursors. Finally, these colloids form under a range of conditions relevant to nuclear fuel storage and geological disposal of radioactive waste and represent a potential pathway for U mobility in these systems.

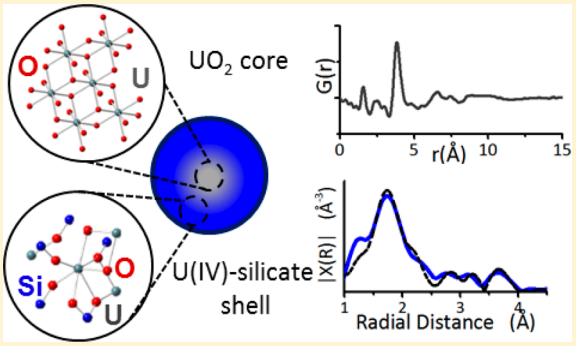

INTRODUCTION

Uranium (U) is the most abundant radionuclide by mass in both the nuclear fuel cycle and many higher activity radioactive waste inventories.[1] Its mobility in engineered and environmental systems is a major concern in a range of scenarios, including waste storage systems (e.g., nuclear fuel storage ponds), contaminated land, and geodisposal facilities. The speciation of U is key to controlling its mobility and therefore informing effluent treatment/remediation options. Of particular importance is the oxidation state of U. U(VI), typically present in aqueous systems as uranyl UO_2^{2+}, is relatively soluble, particularly in the presence of carbonate.[2] By contrast, U(IV) is poorly soluble under the anoxic and neutral-basic pH conditions expected in radioactive waste storage/disposal and contaminated land scenarios[3,4] and is often present as $UO_{2(s)}$[5,6] or noncrystalline U(IV)[7−9] in anoxic systems. This means U is considered to be immobile under reducing conditions. Therefore, reduction from soluble U(VI) to U(IV), either biotically[10,11] or abiotically,[12] is seen as a possible immobilization mechanism for U in environmental and waste treatment systems. However, studies have highlighted that colloids can mobilize actinides in a range of scenarios.[13−16] These include interim storage facilities at sites such as Sellafield, UK, where legacy spent fuel storage ponds are maintained at a high pH and where colloids are present.[17−20] Additionally, colloids have the potential to mobilize radionuclides in geodisposal facilities,[21] at nuclear weapons testing sites,[13] U mine drainage sites,[22] and during ore deposit formation.[23,24] It is therefore important to have a detailed understanding of the formation,

Received: April 3, 2018
Revised: July 11, 2018
Accepted: July 12, 2018
Published: July 12, 2018

DOI: 10.1021/acs.est.8b01756
Environ. Sci. Technol. XXXX, XXX, XXX−XXX

composition, structure, and surface properties of colloidal U(IV) species under relevant (geo)chemical conditions to assess their impact on U speciation and mobility in a range of natural and engineered environments. Despite significant research into colloidal transport of radionuclides, U colloid formation and stability mechanisms are poorly constrained. There is a particular scarcity of knowledge under alkaline, anoxic conditions relevant to spent nuclear fuel storage[25] and long-term geodisposal.[26]

The formation of U oxide colloids at acidic pH has been well established for both U(IV)[27] and U(VI).[28] Under environmentally relevant anoxic, circumneutral pH conditions, UO_2 colloids have been shown to form during anaerobic corrosion of spent nuclear fuel.[21] The resultant colloidal particles were <250 nm and showed resistance to oxidation, persisting for 70 days during exposure to air before oxidation to U(VI)-silicate (weeksite, $K_2(UO_2)_2Si_6O_{15}\cdot 4H_2O$). In addition, colloidal U(IV)-silicate nanoparticles have been shown to form under anoxic conditions at pH 6.9−9.5[29] similar to those within radioactive waste storage and disposal environments. The nanoparticles, <20 nm in size, formed stable colloids for up to 2 years at pH 6.9 and showed an increase in size over time. Additionally, EXAFS analysis identified the nanoparticles as a U(IV)-silicate phase, but their atomic structure was not fully determined. The pathway of crystalline U(IV)-silicate formation is unclear in many systems, with thermodynamic studies showing that coffinite ($USiO_4$) is metastable with respect to UO_2 and quartz but potentially able to form when UO_2 is in contact with aqueous Si at elevated concentrations (>1 mM).[30,31] Furthermore, recent studies suggest the presence of U(IV)-silicate solution complexes and colloids are essential precursors to coffinite formation.[32,33] Understanding the formation of U(IV)-silicate species is therefore essential to understanding U(IV)-silicate mineral formation as well as U(IV) mobility. U silicate solution complexes have also been observed within groundwaters at the underground research laboratory in Horonobe, Japan.[34] Here, U was associated with low molecular weight polysilicates in saline groundwaters from 500 m depth providing field based evidence that U(IV)-silicate solution species and/or nanoparticles have the potential to enhance U(IV) mobility in anoxic systems.

Studies of actinide(IV) (An(IV)) silicate colloids have found that Th(IV) and Np(IV) silicate colloids can form under similar conditions to those favoring U(IV)-silicate colloid formation.[35−37] X-ray photoelectron spectroscopy (XPS) of Th(IV)-silicate particles suggested that the structure of the individual nanoparticles may not be homogeneous, with evidence for silica enrichment at the particle surface under initially elevated Si concentrations. Enrichment of silicate on the surface of An(IV) particles (where An = U, Th, Np) is thought to stabilize the colloidal nanoparticles via increasing the charge and reducing the hydrophobicity of the particle surface.[37] This mechanism of stabilization has also been observed for other silicate containing colloidal systems including Fe(III) hydrolysis products[38] and amorphous calcium carbonate where silica was observed at the particle surface.[39] Overall, An(IV)-silicate nanoparticles have been reported across a range of systems and may have a significant impact on An(IV) mobility in reducing engineered and natural environments where actinides and elevated Si concentrations exist (e.g., groundwater). Information on the formation, composition, structure, and stability of U(IV)-silicate phases and colloids at conditions relevant to interim spent nuclear fuel storage and geodisposal of radioactive waste (i.e., pH > 10) is crucial to predicting the long-term mobility and fate of An(IV) in natural and engineered systems.

In this study we have characterized U(IV)-silicate colloids at a range of silicate concentrations and high pH conditions ([Si] 0−4 mM, pH 9−12) relevant to spent nuclear fuel storage and radioactive waste disposal. This was achieved using a multitechnique approach to determine the size, stability, and structure of the colloidal nanoparticles. Here, a combination of ultrafiltration, small-angle X-ray scattering (SAXS), dynamic light scattering (DLS), zeta potential analysis, scanning transmission electron microscopy (STEM), extended X-ray absorption fine structure (EXAFS) spectroscopy, powder X-ray diffraction (XRD), and X-ray Pair Distribution Function (PDF) provided unprecedented atomic to nanoscale insight into properties of U(IV)-silicate colloids. Results show the U(IV) colloids consisted of particles <10 nm with a "core-shell" structure comprised of a crystalline UO_2 core and a poorly ordered, U(IV)-silicate rich shell. Our data suggest that silicate stabilizes U(IV) colloids at high pH conditions, providing a potential pathway for U mobility under conditions relevant to storage and disposal of radioactive materials.

EXPERIMENTAL METHODS

Sample Preparation. Experiments were performed in a controlled atmosphere glovebox (N_2/H_2 atmosphere, <20 ppm of O_2) at room temperature, and all solutions were made from degassed, deionized water (18 MΩ). U(IV)-silicate colloids were made using a method adapted from Dreissig et al. (2011).[29] Briefly, U(IV) solutions were prepared by dissolution of UCl_4, prepared by published methods,[40] in 0.25 M HCl to form a stock solution of 0.05 M U(IV). This was added to 1.6 M $NaHCO_3$ to yield a 1 M $NaHCO_3$, 0.02 M U(IV)-carbonate solution, and the U oxidation state was verified by UV−vis and X-ray absorption near edge structure (XANES) spectroscopy (Figure S17). Silicate solutions (0−4.2 mM) were prepared by dissolution of $Na_2SiO_4\cdot 9H_2O$. U(IV)-silicate colloids were generated by dilution of the U(IV)-carbonate solution into the silicate solutions in a 1:19 U(IV):silicate ratio to yield a final concentration of 1 mM U(IV). Experiments were prepared under a range of silicate concentrations (0−4 mM) and pH (9−12) with the pH of the colloidal suspensions adjusted by addition of NaOH or HCl to the silicate solutions, prior to U(IV)-carbonate addition (Table S1).

Size and Colloidal Stability Characterization. The colloidal size distribution was analyzed over 60 days using poly(ether sulfone) ultrafiltration centrifugation filters (Pall Nanosep). Filtration occurred at 8000 g for 12 min with molecular weight cutoff sizes of 3, 10, 100, and 300 kDa, equivalent to 1.5, 3, 7, and 12 nm[29,41,42] and 0.22 μm syringe filters (Merck Millipore). Total U and Si concentrations were measured by ICP-MS (Agilent 7500cx) and ICP-AES (PerkinElmer Optima 5300 dual view) respectively. Colloidal stability and particle size were further investigated using SAXS and DLS. SAXS analysis of samples aged for 10, 30, 50, and 60 days was carried out at the Diamond Light Source I22 beamline[43] at λ = 12.4 keV and a 1.918 m camera length. The scattering patterns were collected using a 2D PILATUS 2 M detector.[44] Samples were loaded into quartz capillaries, and SAXS patterns were collected (30 scans, 10 s per scan). Backgrounds from silicate solutions were recorded before data collection. The SAXS data obtained were fit using the Monte

DOI: 10.1021/acs.est.8b01756
Environ. Sci. Technol. XXXX, XXX, XXX−XXX

Carlo based software package McSAS[45,46] to evaluate primary particle size distributions, assuming a spherical particle shape. Dynamic light scattering (DLS) and zeta potential were recorded using five consecutive scans per sample (ZetaSizer HPPS, Malvern Instruments) at 25 °C with a He−Ne laser (λ = 633 nm) measuring backscattered light at 173° and disposable DTS1060 zeta potential and sizing cuvettes. DLS analysis was carried out on samples from 2 mMSi/pH9, 2 mMSi/pH10.5, 4 mMSi/pH9, and 4 mMSi/pH10.5 systems aged for between 2 and 60 days. Zeta potential measurements were taken for 2 and 4 mM Si systems, and pH was between 7 and 11.

Structure Investigations. TEM samples were prepared under anaerobic conditions by depositing experimental dispersions onto carbon coated copper TEM grids (Agar Scientific) and washing with degassed deionized water. Colloids were imaged using an FEI TF30 analytical FEG TEM or FEI Talos F200X. Powder X-ray diffraction (XRD) (Bruker D8Advance with CuK_α X-rays with a wavelength of 1.5406 Å) and X-ray PDF data were obtained for U(IV) precipitates which had been aggregated by adjusting the pH to 4, followed by centrifugation.[29] High energy X-ray scattering patterns for PDF analysis were recorded at the Diamond Light Source I15 beamline using a monochromatic 76 keV beam and a PerkinElmer 1621 detector. The X-ray scattering data ($0.5 \leq Q \leq 20$ Å^{-1}) were background subtracted, corrected, and processed into PDF data using the program GudrunX.[47] For X-ray absorption spectroscopy (XAS) analysis, solid samples were sedimented by adjusting the pH to 4[29] or by collection of the solid on 3 kDa filters. XAS standards of $U(IV)_{(aq)}$ at pH 1 and U(IV) carbonate solution samples (20 mM U(IV)) were also analyzed (Figure S19, Table S3). Data collection was carried out at Diamond Light Source B18 beamline at the U L_{III}-edge at liquid nitrogen temperature in transmission mode (solid samples) and at room temperature in fluorescence mode (solution samples). The data were analyzed using the Demeter software package Athena and Artemis, FEFF6.[48] Samples for XRD, PDF, and XAS were aged for 30 days prior to analysis. A summary of the techniques used to analyze the samples is given in Table S1, and further information on sample preparation is available in the SI.

Thermodynamic Modeling. Details of thermodynamic modeling can be found in the Supporting Information.

RESULTS AND DISCUSSION

To investigate particle size distributions and colloidal stability samples were ultrafiltered. Results indicated colloids were formed where [Si] ≥ 2 mM at pH 9−10.5 (experiments 2 mMSi/pH9, 2 mMSi/pH10.5, 4 mMSi/pH9, and 4 mMSi/pH10.5). Results from the ultrafiltration of the 4 mMSi/pH9 and 2 mMSi/pH9 experiments are shown in Figure 1 and for the other systems in Figure S1. Where stable colloids formed, the majority (≥50%) of the U was within the 1.5−220 nm particle size fraction over the first 30 days. At pH 12 and 2−4 mM Si green precipitates were clearly visible, and <0.5% of the U(IV) passed through the 0.22 μm filter. There was a small amount (<10%) of unfilterable U in all experiments, which was assumed to be in solution.

After 30 days in the 4 mMSi/pH9 system, 80% of U was in the 7 to 1.5 nm size fraction (Figure 1 a,b). In the 2 mMSi/pH9 system 95% of the U was associated with particles >12, indicating larger overall colloidal particle size (Figure 1 d,e). Data were similar for the pH 10.5 systems, with the 4 mMSi/

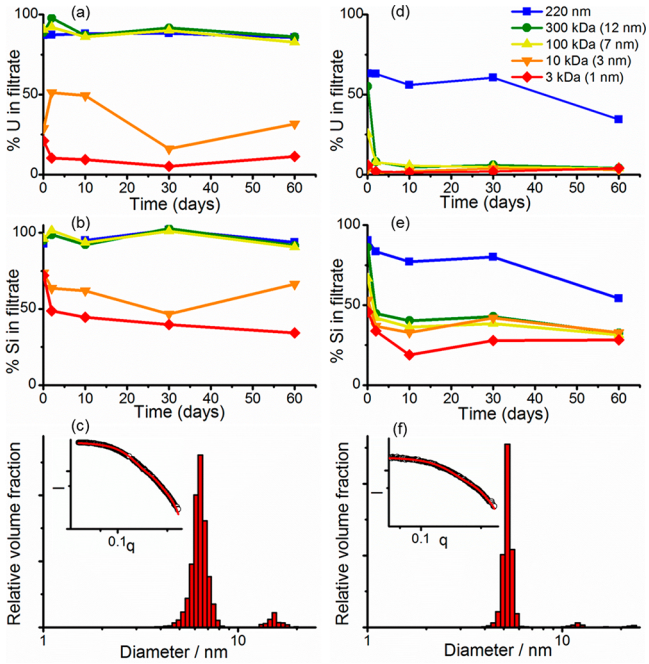

Figure 1. Results from ultrafiltration and SAXS experiments showing (a) U concentration changes with time in filtrates of various filter pore sizes, (b) corresponding Si concentrations for 4 mMSi/pH9, and (c) primary particle size distribution from SAXS modeling, with SAXS pattern and fit inset, of the 30 day aged sample of 4 mMSi/pH9. (d) U and (e) Si filtrate concentrations for 2 mMSi/pH9 and (f) primary particle size distribution, with fit and SAXS pattern inset, from SAXS modeling of a 30 day aged sample of 2 mMSi/pH9.

pH10.5 ultrafiltration data indicating 80% U associated with particles <12 nm in size and the 2 mMSi/pH10.5 system indicating 90% of U > 12 nm. The filtration data also provided molar Si/U ratios for the particles, calculated at the 30 day time point. Here, Si/U ranged from 1.5 for 2 mMSi/pH10.5 and 2 mMSi/pH9, to 2.2−2.5 for 4 mMSi/pH10.5 and 4 mMSi/pH9 in the colloidal experiments. Where no stable U-bearing colloids formed, the Si/U ratio of the solid was 0.9−1 (4 mMSi/pH12 and 2 mMSi/pH12), significantly lower than that observed in the systems with colloidal particles.

Ultrafiltration data showed that the colloids which formed in the 4 mM silicate experiments displayed elevated colloidal stability compared to the 2 mM silicate systems (Figures 1, S1). No significant change was observed in the particle size distribution in the 4 mMSi/pH9 system over 60 days (Figure 1). In the 4 mMSi/pH10.5 system, while the average particle size increased over time, the proportion of colloidal U (<220 nm) in the system did not change significantly (Figure S1). By contrast, in the 2 mMSi/pH9 and 2 mMSi/pH10.5 experiments between 30 and 60 days there was a clear decrease in the amount of suspended colloidal U (<220 nm) from 55% to 35% (2 mMSi/pH9) and 50% to 5% (2 mMSi/pH10.5), indicating a reduced stability with time at lower silicate concentrations.

Primary particle size and aggregate structure were probed by SAXS. Analysis of the SAXS data from the 2−4 mM Si and pH 9−10.5 experiments indicated the average primary particle diameter was 4.6−6.3 nm with no significant trends with changing pH, silicate concentration, or age (Figure 1, S8). Increased scattering was observed in the low-q region of the SAXS data in aged samples of the 2 mMSi/pH10.5 (≥30 days) and 4 mMSi/pH10.5 (≥50 days) experiments (Figures S4, S5)

DOI: 10.1021/acs.est.8b01756
Environ. Sci. Technol. XXXX, XXX, XXX−XXX

confirming formation of a population of aggregated particles over 1−2 months. The Porod slope, with a gradient of 2.00 for 2 mMSi/pH10.5 at 50 days and 2.13 for 4 mMSi/pH10.5 system at 50 days, indicated the larger particles were mass fractal aggregates of the primary particles. A size for these aggregates was undetermined due to the q-range in the SAXS data.

DLS and zeta potential data provided further information on particle size and colloid stability. Intensity weighted DLS results (Figure S9) show a radius of hydration, R_H, between 4 and 20 nm for the 4 mMSi/pH9 (30 days) dispersion, and a mean size of 8.54 nm. In the 2 mMSi/pH9 (30 days) system the majority of particles observed were 20−200 nm in size. Over time the higher silicate, lower pH conditions i.e. 4 mMSi/pH9, yielded more stable primary particle dispersions with the average particle size increasing significantly in 2 mMSi/pH9 and 2 mMSi/pH10.5 experiments (Figure S10). The larger particle size determined from DLS, compared to SAXS, is likely caused by the heavy weighting of DLS data toward larger particles when they are present in suspension. The zeta potential values recorded were between −27 and −35 mV (Figure S11) with no clear trend with pH or silicate concentration indicating the surface charge of the particles was the same in all systems.

TEM images of the colloidal particles (2 mMSi/pH10.5 and 4 mMSi/pH10.5, Figures 2, S16) showed they are ≈2−10 nm in size with no lattice fringes observed in any high resolution images. The primary particles were observed to form mass fractal aggregates between 20 nm and >5 μm in size (Figure 2a). High resolution EDX and HAADF-STEM mapping of the particles (4 mMSi/pH10.5), with a 0.16 nm resolution, showed no discrete U or Si rich areas consistent with the particles being intrinsic U(IV)-silicates (Figure 2c,d,e). XRD analysis on a precipitated dispersion from the 2 mMSi/pH9 experiment showed two very broad peaks at 2θ = 23 to 33° and 43 to 56°, which are consistent with nanocrystalline uraninite (UO_2) (Figure S14). Scherrer analysis[49] (Equation S1) indicated the crystallite size was <2 nm. Thus, the XRD and TEM data seem to be contradictory with the EDX mapping showing no discrete U or Si phases and XRD data showing evidence for subnm uraninite crystallites. By contrast in the silicate-free system (0 mMSi/pH10.5) TEM images of the particles show lattice fringes with spacing of 3.2 Å, consistent with uraninite[24] (Figure S12), indicating significant crystallinity in these particles.

To explore this apparent contradiction in the particle structure, PDF analyses were performed on selected U(IV)-silicate (2 mMSi/pH9, 2 mMSi/pH10.5, 2 mMSi/pH12) and UO_2 (0 mMSi/pH10.5) samples (Figure 3). The PDF data for the U(IV)-silicate samples showed interatomic correlations over a limited r(Å) range, with peaks diminishing at high r(Å) indicating crystallite sizes of approximately 14.3 Å for 2 mMSi/pH9 and 2 mMSi/pH10.5 samples and 15.2 Å for 2 mMSi/pH12. The peaks in the PDF data for all U(IV)-silicate samples (2 mMSi/pH12, 2 mMSi/pH10.5, and 2 mMSi/pH9) were compared to data from the silicate free, UO_2 system (0 mMSi/pH10.5) and a computed coffinite standard[50] (Figures 3, S15, S16, structures of coffinite and UO_2 are shown in Figure S23). All the U(IV)-silicate samples had peaks at 1.6, 2.4, 3.1, and 3.8 Å which correlated with the Si−O (1.58 Å), U−O (2.32 Å, 2.51 Å), U−Si (3.13 Å, 3.83 Å), and U−U (3.83 Å)

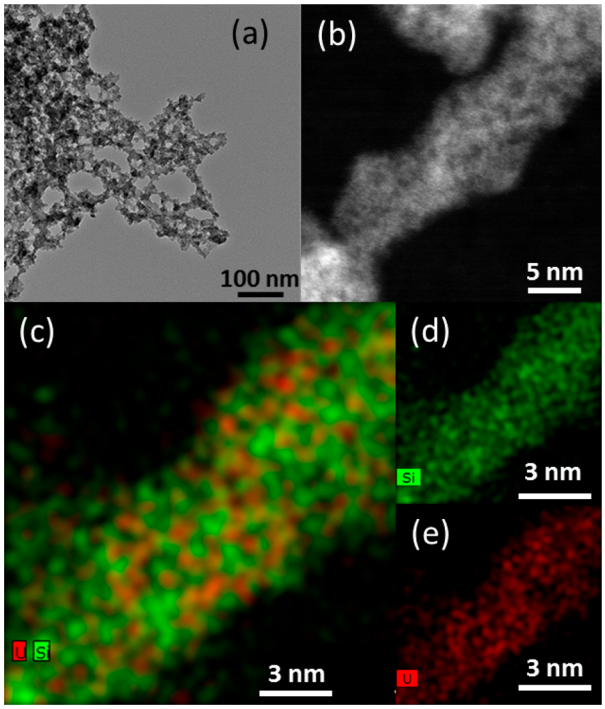

Figure 2. TEM images of U(IV)-silicate particles formed in 4 mMSi/pH10.5 experiment. (a) Sample from the colloidal dispersion showing mass fractal aggregation presumably as an artifact of sample preparation. (b) High resolution high-angle annular dark-field (HAADF) image. (c,d,e) EDX elemental map showing Si (green) and U (red) distribution throughout the nanoparticles.

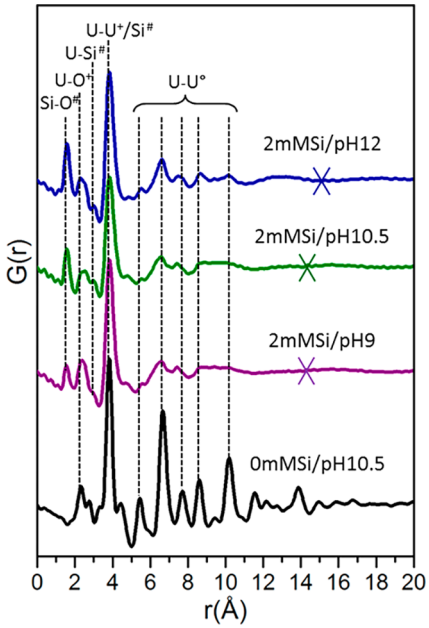

Figure 3. X-ray pair distribution function (PDF) $G(r)$ for U(IV)-silicate particles formed in the 2 mMSi/pH12, 2 mMSi/pH10.5, and 2 mMSi/pH9 systems and nanocrystalline UO_2 (0 mMSi/pH10.5). Dashed lines indicate interatomic pairs responsible for major peaks; crosses indicate where signals are at background for U(IV)-silicate particles, defining the locally ordered crystalline domains. # indicates interatomic distances from coffinite only, + indicates interatomic distances from coffinite and uraninite, and ° indicates interatomic distances from uraninite only.

DOI: 10.1021/acs.est.8b01756
Environ. Sci. Technol. XXXX, XXX, XXX−XXX

interatomic distances respectively in coffinite.[50] However, the U−O and U−U distances also correlated with those in uraninite (2.37 and 3.87 Å respectively); this suggested the presence of both uraninite and U(IV)-silicate within the samples. At higher r(Å) values in the PDF, there were features at 5.4, 6.6, 7.7, 8.6, and 10.1 Å in all the U(IV)-silicate samples which correlated only with U−U interatomic distances in the UO_2 standard and not in coffinite (Figure 3). The magnitude of these U−U peaks increased with increasing pH, suggesting a trend to an increasingly crystalline UO_2-like structure with increasing pH. The interatomic distances in coffinite showed no correlation with those in the PDF of U(IV)-silicate samples at r(Å) greater than 4 Å (Figure S15) indicating that the longer range structure (>4 Å) seen in the PDF of the samples was UO_2-like.

Particle structure and U oxidation state was assessed using XAS. XANES analysis of the U(IV)-silicate samples confirmed that U was in the +4 oxidation state as expected (Figure S17). Fitting of the U L_{III}-edge EXAFS data (Figure 4, Table 1) for

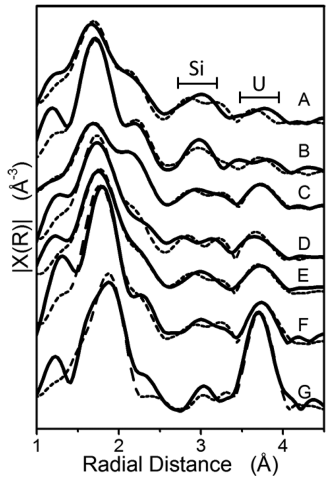

Figure 4. Fourier transformed EXAFS spectra for A 4 mMSi/pH9, B 4 mMSi/pH10.5, C 2 mMSi/pH9, D 2 mMSi/pH10.5, E 4 mMSi/pH12, F 2 mMSi/pH12, G 0 mMSi/pH10.5. Black lines are k^3 weighted data with fits overlaid (dashed lines). Fit parameters are provided in Table 1, and EXAFS are provided in Figure S20.

the U(IV)-silicate nanoparticle was informed by the structures of coffinite ($USiO_4$),[50] uraninite (UO_2),[51] and previous studies of An(IV)-silicates.[29,35,36] All systems were fit with an oxygen coordination containing two shells at 2.28 ± 0.03 Å and 2.46 ± 0.02 Å with coordination numbers between 3.7−4.7 and 3.0−3.9, respectively. The total first shell U−O coordination numbers ranged from 7.4 to 8.1. This split shell environment is similar to that in coffinite and markedly different from the single O shell, consisting of 8 O at 2.37 Å, found in uraninite. The EXAFS data therefore suggest that the U speciation was dominated by a U(IV)-silicate local coordination environment. Additional shells consistent with Si in edge- and corner-sharing configurations at 3.18 ± 0.01 Å and 3.73 ± 0.03 Å, respectively,[50] as well as U backscatterers at 3.82 ± 0.04 Å were also successfully fitted (Table 1). Overall, the coordination environment was consistent with a coffinite-like U(IV)-silicate structure. Interestingly, with the exception of the 2 mMSi/pH12 EXAFS where an elevated U−U coordination occurred, lower coordination numbers for the Si and U shells (0.9−1.6 and 0.8−2.5 for the 2 Si backscatterers and 1−2.8 for U) were observed relative to those in crystalline coffinite (2 and 4 for Si and 4 for U). This suggests the U(IV)-silicate was generally poorly ordered and/or nanoparticulate in nature.[52−54] Furthermore, the Si and U coordination numbers showed systematic variations under different experimental conditions. At higher silicate conditions (4 mMSi/pH10.5), the EXAFS fits showed a higher Si coordination number (total 3.6) and reduced U coordination (1.8) compared to the parallel, lower concentration silicate system (2 mMSi/pH10.5), with corresponding coordination numbers for Si and U of 2.4 and 2.6 respectively.

U(IV)-Silicate Nanoparticle Core−Shell Structure. Overall, we present clear evidence for stable, nanoparticulate U(IV) colloidal phases across a range of conditions. The structure of the nanoparticles varied systematically across the different experimental systems, and, interestingly, different analyses yielded apparently conflicting results. The EXAFS fits for the U(IV)-silicates were consistent with those presented previously for similar particles[29] and were fitted well with a U(IV)-silicate structure. In contrast, both XRD and PDF data indicated the presence of nanocrystalline uraninite (UO_2). Indeed, the PDF data presented clear evidence for short-range U(IV)-silicate environment but showed no evidence for an ordered U(IV)-silicate structure. The PDF data also suggested locally ordered crystalline domains of less than 1.4−1.5 nm, significantly smaller than the 5−6 nm particle size derived from SAXS and TEM analyses. Combining these multiple lines of evidence, we propose that the results are, in fact, not contradictory and are consistent with the particles having a core−shell structure. Here, a nanocrystalline UO_2 core of ∼1.5 nm (identified by PDF/XRD) is encased within a poorly ordered U(IV)-silicate shell (identified by EXAFS) with a particle size of approximately 5−6 nm (supported by SAXS, ultrafiltration, TEM, and DLS analyses). Assuming a 1.5 nm UO_2 "core" within a 5 nm particle, the uraninite core would constitute only ∼2.6% of the total volume with ∼97.4% occupying the "shell". Therefore, despite the higher density within the UO_2 core, the vast majority of the U would be present in the particle shell. As EXAFS resolves the average U coordination environment throughout the sample, the EXAFS fits would be dominated by the signal from the "shell" of the particles i.e. the poorly ordered U(IV)-silicate and would not resolve the contribution from the UO_2 core. The XRD data are only sensitive to the crystalline core of the material, while the X-ray PDF data can resolve both crystalline and noncrystalline components and is most sensitive to the more strongly scattering U−U interactions. At r > 4 Å, the U−U distances in the PDF correlate with those in UO_2 but not $USiO_4$. Therefore, it is possible to identify a crystalline UO_2 particle core and confirm there is no long-range (>4 Å) structure in the U(IV)-silicate shell. The U(IV)-silicate shell model is also supported by the zeta potential results, which suggest surface charge behavior similar to that of silica.[55] It was not possible to resolve the core−shell structure of the particles using STEM due to the small crystalline core size relative to the U(IV)-silicate shell, which in 3-dimensions would likely obscure the core from being imaged in 2-dimensions.

It was also possible to resolve details of the average U coordination environment by EXAFS fitting. The split oxygen coordination shell and presence of U−Si coordination across all silicate-containing experiments confirmed U(IV) was predominantly U(IV)-silicate. The elevated Si/U ratios seen in the ultrafiltration of colloidal particles (Si/U = 1.5 − 2.5,

DOI: 10.1021/acs.est.8b01756
Environ. Sci. Technol. XXXX, XXX, XXX−XXX

Table 1. EXAFS Fitting Parameters[a]

sample	path	N	R[c] (Å)	σ^2[c]	ΔE_0[c]	R
4 mMSi/pH9	U−O.1	4.3	2.26(1)	0.009(1)[b]	4.1(10)	0.0124
	U−O.2	3.8	2.44(1)	0.009(1)[b]		
	U−Si.1	1.1	3.17(2)	0.010(3)		
	U−Si.2	2.5	3.70(3)	0.013(4)		
	U−U	1	3.78(5)	0.013(7)		
4 mMSi/pH10.5	U−O.1	4.5	2.28(1)	0.006(1)[b]	5.5(9)	0.0076
	U−O.2	3.5	2.46(1)	0.006(1)[b]		
	U−Si.1	1.6	3.18(2)	0.011(3)		
	U−Si.2	2	3.73(4)	0.014(5)		
	U−U	1.8	3.79(4)	0.014(5)		
2 mMSi/pH9	U−O.1	3.7	2.28(1)	0.008(1)[b]	6.5(5)	0.0024
	U−O.2	3.9	2.47(1)	0.008(1)[b]		
	U−Si.1	1	3.19(1)	0.009(2)		
	U−Si.2	1	3.76(3)	0.013(2)		
	U−U	2.5	3.85(1)	0.013(4)		
2 mMSi/pH10.5	U−O.1	4.4	2.28(1)	0.007(1)[b]	4.5(8)	0.0124
	U−O.2	3.5	2.45(1)	0.007(1)[b]		
	U−Si.1	0.9	3.17(2)	0.007(3)		
	U−Si.2	1.5	3.74(4)	0.011(5)		
	U−U	2.6	3.80(3)	0.013(3)		
4 mMSi/pH12	U−O.1	4.4	2.29(1)	0.007(1)[b]	6.1(6)	0.0042
	U−O.2	3.0	2.46(1)	0.007(1)[b]		
	U−Si.1	1.6	3.19(2)	0.013(3)		
	U−Si.2	0.8	3.71(5)	0.012(7)		
	U−U	2.8	3.84(2)	0.013(2)		
2 mMSi/pH12	U−O.1	4.7	2.30(1)	0.005(1)[b]	6.2(8)	0.0121
	U−O.2	3.3	2.46(1)	0.005(1)[b]		
	U−Si.1	1	3.18(3)	0.009(5)		
	U−Si.2	1.8	3.75(5)	0.014(7)		
	U−U	5	3.86(2)	0.015(2)		
UO_2[d]	U−O	8	2.37			
	U−U	12	3.87			
$USiO_4$[d]	U−O.1	4	2.32			
	U−O.2	4	2.51			
	U−Si.1	2	3.13			
	U−Si.2	4	3.83			
	U−U	4	3.83			

[a]Coordination numbers (N), U bond distances (R (Å)), Debye−Waller factors (σ^2), shift in energy from calculated Fermi level (ΔE_0), and "goodness of fit" factor (R). Coordination numbers were fixed, and amplitude factors were fixed as 1. [b]Denotes tied σ^2 values. [c]Numbers in parentheses are the standard deviation on the last decimal place. [d]UO_2 and $USiO_4$ interatomic distances are taken from Barrett et al. (1982)[51] and Fuchs and Gerbert (1958).[50]

Table S1), compared to coffinite (Si/U = 1), suggest that the U(IV)-silicate shell is highly silicate enriched compared to coffinite. Additionally, the U−Si distance for the corner sharing silicate was consistently shorter across all fits (3.73 ± 0.03 Å) than that in coffinite (3.83 Å). The shortening of this U−Si distance is likely due to the relaxation of the structural constraints present in crystalline coffinite leading to a shorter average U−Si distance. The reduced coordination numbers in the EXAFS fits relative to crystalline coffinite are indicative of structural disorder and/or the nanoparticulate character which leads to a significant fraction of the U being associated with surface or near surface sites.[52−54] Overall, we consider the U(IV)-silicate shell to be most accurately described as poorly ordered U(IV)-silicate.

For the high pH, low silicate conditions in the 2 mMSi/pH12 experiment, the EXAFS and PDF results were consistent. Here, compared to the other systems, EXAFS fitting showed an elevated U−U coordination number in excess of that expected for coffinite suggesting a higher proportion of uraninite in these particles than those formed at lower pH. The PDF results for this sample also showed an increased UO_2 core size and crystallinity relative to the lower pH systems, again consistent with increased proportion of uraninite in the sample.

U(IV)-Silicate Nanoparticle Formation Mechanism. The core−shell model for the U(IV)-silicate nanoparticles is consistent with the formation mechanism suggested for An(IV)-silicate colloids, whereby An(IV) hydrolysis occurs at a higher rate than the An(IV) reaction with silicate.[37] We suggest that the rapid hydrolysis of aqueous U(IV) allows formation of the nanosized UO_2 particle core. As particle formation continues, the relative concentration of U(IV)-silicate solution complexes such as $U(OH)_3(H_3SiO_4)_3^{2-}$, important in coffinite formation,[32] increases. Indeed, in this scenario, the U(IV)-silicate solution complexes may inhibit extensive hydrolysis of U(IV) to $U(OH)_{4(aq)}$ and thus inhibit

DOI: 10.1021/acs.est.8b01756
Environ. Sci. Technol. XXXX, XXX, XXX−XXX

formation of larger UO_2 nanoparticles. Consequently, this would lead to a transition from U(IV)-oxide formation in the core to the formation of the poorly ordered U(IV)-silicate shell. With this formation mechanism, the particles will likely have a diffuse core−shell structure, with an elevated U concentration and reduced Si concentration near the core and reduced U and elevated Si toward the particle surface consistent with recent observations on Th(IV)-silicate particles.[36]

The proposed formation pathway suggests that $U(OH)_3(H_3SiO_4)_3^{2-}$ aqueous complexes are significant in the formation of the U(IV)-silicate colloids. An equilibrium constant for this species has recently been estimated,[32] based on experimental data for the $Th(IV)(OH)_3(H_3SiO_4)_3^{2-}$ complex.[56] Thermodynamic modeling of our experiments using these data shows $U(OH)_3(H_3SiO_4)_3^{2-}$ dominates the equilibrium solution speciation of U(IV) over the pH range examined (Figures S21, S22). Indeed, the model suggests that $U(OH)_3(H_3SiO_4)_3^{2-}$ causes an increase in the solubility of UO_2, which could promote the formation of U(IV)-silicate over U(IV)-oxide. This is consistent with past work showing coffinite forms in preference to uraninite in silicate rich solutions[31] and supports the proposed mechanism for core shell particle formation we propose. We suggest the polymerization of the $U(OH)_3(H_3SiO_4)_3^{2-}$ solution species is the key pathway to the formation of the U(IV)-silicate particle shell. Indeed, our work combined with Dreissig et al. (2011) shows the U(IV)-silicate colloids are stable over pH 6.9−10.5,[29] coinciding with the region that modeling suggests $U(OH)_3(H_3SiO_4)_3^{2-}$ will be present. Additionally, Mesbah et al. also highlighted that the interaction of U with silicate is likely underestimated using this method, given the higher stability constants for a range of ligands with U, compared to Th,[32] meaning the $U(OH)_3(H_3SiO_4)_3^{2-}$ may be even more prevalent than shown here. U-polysilicate complexes are also relevant in natural systems[34] and complex to metal ions at levels several orders of magnitude higher than monomeric silicate[57] further reinforcing the role that U(IV)-silicate solution complexes seem to play in U(IV)-silicate formation pathways. Although the thermodynamic modeling suggests formation of $U(OH)_3(H_3SiO_4)_3^{2-}$ complexes occurs at pH > 10.5, our work showed the stability of the U(IV)-silicate colloids decreased at pH 12. This could be due to uncertainty in the stability constant approximation for $U(OH)_3(H_3SiO_4)_3^{2-}$ and/or because of the lower solubility of U(IV) with respect to UO_2 at elevated pH. This would result in reduced silicate enrichment of the particle surface and therefore lower colloidal stability as observed. Clearly, an improved understanding of U(IV)-silicate aqueous complex formation and polymerization is needed to further develop accurate predictions of U(IV)-silicate colloid formation.

Trends in Particle Size and stability. Overall, our data confirm that silicate stabilizes U(IV) colloids across pH 9−10.5 for at least 30 days, expanding their envelope of stability to pH 7−10.5[29] with colloidal stability at pH < 7 not explored. Over this pH range, the zeta potential of the colloids shows a significant negative surface charge (−27 to −35 mV) consistent with the observed high colloidal stability (Figure S11). This behavior is similar to that of silica which has a constant zeta potential at pH > 7[55] and is significantly different than what would be expected for UO_2, which would have an increasingly negative zeta potential between pH 7 and 10.[58] A study on corrosion of metallic U fuel in the presence of silicate also showed colloids had a zeta potential characteristic of silica or U(IV)-silicate colloids.[21] The U was present in colloidal form and described as UO_2; however, the pH_{pzc} of the U particles was pH 2−3, significantly lower than 4.9−6 previously reported for UO_2.[29,58] It is possible silicate was associated with these particles as the experiments were carried out at a near neutral pH where UO_2 would not be expected to be colloidal, and the zeta potential trends are very similar to zeta potential studies on U(IV)-silicate colloids.[29]

The significance of a silica coating is clear: silica surfaces show more favorable interactions with aqueous solutions than most inorganic phases, and as a result, silica often exhibits high colloidal stability due to electrostatic and non-DLVO processes.[59−67] In our U(IV)-silicate systems, there is a direct correlation between silicate content in particles and colloid stability. At pH 12, where the colloid does not form, there was a clear decrease in the Si/U ratio within the particles. This is likely because of the high solubility of silicate at these elevated pH levels and, as a consequence, the lower stability of colloidal U(IV)-silicate phases relative to UO_2. Therefore, the U(IV) particles at pH 12 become depleted in silicate which results in a more UO_2-like surface and, consequently, colloid destabilization. Based on these observations, it appears the colloidal stability is dependent on the silicate content of the particles which in turn is related to the pH of the solution as this affects the silicate content.

Ultrafiltration results for the 4 mMSi/pH9 system showed no evidence of particle aggregation. The 4 mMSi/pH10.5 system showed modest aggregation over 60 days but no destabilization of the colloid. By contrast, in the 2 mMSi/pH9 and 2 mMSi/pH10.5 experiments ultrafiltration suggested significant aggregation occurred during the first 10 days of the reaction, while the SAXS and DLS data showed evidence for aggregation over 30−60 days. Here, membrane induced aggregation[68] may cause artifacts in the ultrafiltration data, but overall, there is clear evidence for enhanced aggregation compared to the 4 mM systems. The aggregation of the primary particles in the 2 mMSi/pH9 and 2 mMSipH10.5 systems appears to be gradual; primary particles initially form, which then aggregate into larger particles over time. These larger particles continue to aggregate and become too large to remain suspended over weeks to months leading to a destabilization of the colloid. This is consistent with the above hypothesis of silicate stabilization, as the 2 mM Si systems have intermediate Si/U ratios: lower than the stable 4 mMSi/pH9 and 4 mMSi/pH10.5 colloids and above the 2 mMSi/pH12 and 4 mMSi/pH12 systems. Therefore, it would be expected that these systems exhibit the observed intermediate stability − with initial colloid formation but aggregation leading to gradual colloid destabilization over time.

Implications for An(IV) Environmental Mobility. Using a range of state of the art techniques, in particular X-ray PDF and EXAFS spectroscopy, we evidence a core−shell structure for the U(IV)-silicate colloidal particles. Furthermore, we propose a mechanism for their formation and stability. By identifying the particle structure, it has been possible to explore their formation pathway and the likely controlling influence of U(IV)-silicate solution species on their formation. The silica-rich surface of these particles explains the high colloidal stability observed and emphasizes their potential significance in a wide range of scenarios where alkaline pH conditions dominate including nuclear decommissioning, where spent fuel has been corroded in alkaline conditions in the presence of

DOI: 10.1021/acs.est.8b01756
Environ. Sci. Technol. XXXX, XXX, XXX−XXX

silicate and in conditions relevant to a typical geological disposal facility (GDF) for radioactive wastes where cementitious materials are used.

The stability range of these colloids means that they could also form and persist under neutral pH conditions more relevant to accidental discharges and radioactively contaminated land scenarios. It is also clear that U(IV)-silicate colloids may also be used as an analogue for predicting the behavior of the transuranic, An(IV)-silicate colloids. Indeed, their small size and long-term persistence means they are potentially environmentally mobile.

■ ASSOCIATED CONTENT

Supporting Information

The Supporting Information is available free of charge on the ACS Publications website at DOI: 10.1021/acs.est.8b01756.

Additional information on colloid synthesis, ultrafiltration results, dynamic light scattering, DLS, XAS, XRD, SAXS, and TEM results, and thermodynamic modeling (PDF)

■ AUTHOR INFORMATION

Corresponding Author

*E-mail: sam.shaw@manchester.ac.uk.

ORCID

Katherine Morris: 0000-0002-0716-7589

Carolyn I. Pearce: 0000-0003-3098-1615

Louise Natrajan: 0000-0002-9451-3557

Samuel Shaw: 0000-0002-6353-5454

Author Contributions

The manuscript was written through contributions of all authors. All authors have given approval to the final version of the manuscript.

Notes

The authors declare no competing financial interest.

■ ACKNOWLEDGMENTS

Sellafield Ltd. and The University of Manchester cofunded this work via the Effluents and Decontamination Centre of Excellence. We acknowledge the NERC funded Facility for Environmental Nanoscience Analysis and Characterization (FENAC) and the STFC Environmental Radioactivity Network (ST/N002474/1) for their financial support. Diamond Light Source provided beamtime awards (EE15276-1, SM12704-1, SM15966-1 and SP13559-2), and we thank Andy Smith, Nick Terrill, Steven Parry, and Annette Kleppe for beamline assistance. We also thank J. Fred Mosselmans and Tomasz Stawski for assistance with data analysis, Christine Elgy, Paul Lythgoe, and Heath Bagshaw for data acquisition, and Kathryn George and Vanessa Timmermann for the synthesis of UCl_4.

■ REFERENCES

(1) 2016 UK Radioactive waste & materials inventory. *UK radioactive waste inventory report*; 2017.

(2) Clark, D. L.; Hobart, D. E.; Neu, M. P. Actinide Carbonte Complexes and Their Importance in Actinide Environmental Chemistry. *Chem. Rev.* **1995**, *95* (1), 25−48.

(3) Neck, V.; Kim, J. I. Solubility and hydrolysis of tetravalent actinides. *Radiochim. Acta* **2001**, *89* (1), 1−16.

(4) Opel, K.; Weiß, S.; Hübener, S.; Zänker, H.; Bernhard, G. Study of the solubility of amorphous and crystalline uranium dioxide by combined spectroscopic methods. *Radiochim. Acta* **2007**, *95* (3), 143−149.

(5) Casas, I.; de Pablo, J.; Giménez, J.; Torrero, M. E.; Bruno, J.; Cera, E.; Finch, R. J.; Ewing, R. C. The role of pe, pH, and carbonate on the solubility of UO2 and uraninite under nominally reducing conditions. *Geochim. Cosmochim. Acta* **1998**, *62* (13), 2223−2231.

(6) Newsome, L.; Morris, K.; Lloyd, J. R. Uranium Biominerals Precipitated by an Environmental Isolate of Serratia under Anaerobic Conditions. *PLoS One* **2015**, *10* (7), e0132392.

(7) Bernier-Latmani, R.; Veeramani, H.; Vecchia, E. D.; Junier, P.; Lezama-Pacheco, J. S.; Suvorova, E. I.; Sharp, J. O.; Wigginton, N. S.; Bargar, J. R. Non-uraninite Products of Microbial U(VI) Reduction. *Environ. Sci. Technol.* **2010**, *44* (24), 9456−9462.

(8) Fletcher, K. E.; Boyanov, M. I.; Thomas, S. H.; Wu, Q.; Kemner, K. M.; Löffler, F. E. U(VI) Reduction to Mononuclear U(IV) by Desulfitobacterium Species. *Environ. Sci. Technol.* **2010**, *44* (12), 4705−4709.

(9) Sharp, J. O.; Lezama-Pacheco, J. S.; Schofield, E. J.; Junier, P.; Ulrich, K.-U.; Chinni, S.; Veeramani, H.; Margot-Roquier, C.; Webb, S. M.; Tebo, B. M.; Giammar, D. E.; Bargar, J. R.; Bernier-Latmani, R. Uranium speciation and stability after reductive immobilization in aquifer sediments. *Geochim. Cosmochim. Acta* **2011**, *75* (21), 6497−6510.

(10) Newsome, L.; Morris, K.; Trivedi, D.; Bewsher, A.; Lloyd, J. R. Biostimulation by Glycerol Phosphate to Precipitate Recalcitrant Uranium(IV) Phosphate. *Environ. Sci. Technol.* **2015**, *49* (18), 11070−11078.

(11) Bargar, J. R. R.; Bernier-Latmani, R.; Giammar, D. E. E.; Tebo, B. M. M. Biogenic Uraninite Nanoparticles and Their Importance for Uranium Remediation. *Elements* **2008**, *4* (6), 407−412.

(12) Jing, C.; Li, Y. L.; Landsberger, S. Review of soluble uranium removal by nanoscale zero valent iron. *J. Environ. Radioact.* **2016**, *164*, 65−72.

(13) Kersting, A. B.; Efurd, D. W.; Finnegan, D. L.; Rokop, D. J.; Smith, D. K.; Thompson, J. L. Migration of plutonium in ground water at the Nevada Test Site. *Nature* **1999**, *397* (6714), 56−59.

(14) Novikov, A. P.; Kalmykov, S. N.; Utsunomiya, S.; Ewing, R. C.; Horreard, F.; Merkulov, A.; Clark, S. B.; Tkachev, V. V.; Myasoedov, B. F. Colloid Transport of Plutonium in the Far-Field of the Mayak Production Association, Russia. *Science (Washington, DC, U. S.)* **2006**, *314* (5799), 638−641.

(15) Kersting, A. B. Plutonium Transport in the Environment. *Inorg. Chem.* **2013**, *52* (7), 3533−3546.

(16) Matsunaga, T.; Nagao, S.; Ueno, T.; Takeda, S.; Amano, H.; Tkachenko, Y. Association of dissolved radionuclides released by the Chernobyl accident with colloidal materials in surface water. *Appl. Geochem.* **2004**, *19* (10), 1581−1599.

(17) Gregson, C. R.; Goddard, D. T.; Sarsfield, M. J.; Taylor, R. J. Combined electron microscopy and vibrational spectroscopy study of corroded Magnox sludge from a legacy spent nuclear fuel storage pond. *J. Nucl. Mater.* **2011**, *412* (1), 145−156.

(18) Gregson, C. R.; Hastings, J. J.; Sims, H. E.; Steele, H. M.; Taylor, R. J. Characterisation of plutonium species in alkaline liquors sampled from a UK legacy nuclear fuel storage pond. *Anal. Methods* **2011**, *3* (9), 1957.

(19) Parry, S. a.; O'Brien, L.; Fellerman, A. S.; Eaves, C. J.; Milestone, N. B.; Bryan, N. D.; Livens, F. R. Plutonium behaviour in nuclear fuel storage pond effluents. *Energy Environ. Sci.* **2011**, *4* (4), 1457.

(20) Maher, Z.; Ivanov, P.; O'Brien, L.; Sims, H.; Taylor, R. J.; Heath, S. L.; Livens, F. R.; Goddard, D.; Kellet, S.; Rand, P.; Bryan, N. D. Americium and plutonium association with magnesium hydroxide colloids in alkaline nuclear industry process environments. *J. Nucl. Mater.* **2016**, *468*, 84−96.

(21) Kaminski, M. D.; Dimitrijevic, N. M.; Mertz, C. J.; Goldberg, M. M. Colloids from the aqueous corrosion of uranium nuclear fuel. *J. Nucl. Mater.* **2005**, *347* (1−2), 77−87.

(22) Wang, Y.; Frutschi, M.; Suvorova, E.; Phrommavanh, V.; Descostes, M.; Osman, A. A. A.; Geipel, G.; Bernier-Latmani, R.

Mobile uranium(IV)-bearing colloids in a mining-impacted wetland. *Nat. Commun.* **2013**, *4* (May), 1−9.
(23) Suzuki, Y.; Mukai, H.; Ishimura, T.; Yokoyama, T. D.; Sakata, S.; Hirata, T.; Iwatsuki, T.; Mizuno, T. Formation and Geological Sequestration of Uranium Nanoparticles in Deep Granitic Aquifer. *Sci. Rep.* **2016**, *6* (1), 22701.
(24) Schindler, M.; Lussier, A. J.; Bellrose, J.; Rouvimov, S.; Burns, P. C.; Kyser, T. K. Mobilization and agglomeration of uraninite nanoparticles: A nano-mineralogical study of samples from the Matoush Uranium ore deposit. *Am. Mineral.* **2017**, *102* (9), 1776−1787.
(25) Pitois, A.; Ivanov, P. I.; Abrahamsen, L. G.; Bryan, N. D.; Taylor, R. J.; Sims, H. E. Magnesium hydroxide bulk and colloid-associated 152Eu in an alkaline environment: colloid characterisation and sorption properties in the presence and absence of carbonate. *J. Environ. Monit.* **2008**, *10* (3), 315.
(26) Bots, P.; Morris, K.; Hibberd, R.; Law, G. T. W.; Mosselmans, J. F. W.; Brown, A. P.; Doutch, J.; Smith, A. J.; Shaw, S. Formation of Stable Uranium(VI) Colloidal Nanoparticles in Conditions Relevant to Radioactive Waste Disposal. *Langmuir* **2014**, *30* (48), 14396−14405.
(27) Ikeda-Ohno, A.; Hennig, C.; Tsushima, S.; Scheinost, A. C.; Bernhard, G.; Yaita, T. Speciation and Structural Study of U(IV) and -(VI) in Perchloric and Nitric Acid Solutions. *Inorg. Chem.* **2009**, *48* (15), 7201−7210.
(28) Steppert, M.; Walther, C.; Fuss, M.; Büchner, S. On the polymerization of hexavalent uranium. An electrospray mass spectrometry study. *Rapid Commun. Mass Spectrom.* **2012**, *26* (6), 583−591.
(29) Dreissig, I.; Weiss, S.; Hennig, C.; Bernhard, G.; Zänker, H. Formation of uranium(IV)-silica colloids at near-neutral pH. *Geochim. Cosmochim. Acta* **2011**, *75* (2), 352−367.
(30) Guo, X.; Szenknect, S.; Mesbah, A.; Labs, S.; Clavier, N.; Poinssot, C.; Ushakov, S. V.; Curtius, H.; Bosbach, D.; Ewing, R. C.; Burns, P. C.; Dacheux, N.; Navrotsky, A. Thermodynamics of formation of coffinite, USiO $_4$. *Proc. Natl. Acad. Sci. U. S. A.* **2015**, *112* (21), 6551−6555.
(31) Janeczek, J.; Ewing, R. C. Dissolution and alteration of uraninite under reducing conditions. *J. Nucl. Mater.* **1992**, *190* (C), 157−173.
(32) Mesbah, A.; Szenknect, S.; Clavier, N.; Lozano-Rodriguez, J.; Poinssot, C.; Den Auwer, C.; Ewing, R. C.; Dacheux, N. Coffinite, USiO 4, Is Abundant in Nature: So Why Is It So Difficult To Synthesize? *Inorg. Chem.* **2015**, *54* (14), 6687−6696.
(33) Szenknect, S.; Mesbah, A.; Cordara, T.; Clavier, N.; Brau, H.-P.; Le Goff, X.; Poinssot, C.; Ewing, R. C.; Dacheux, N. First experimental determination of the solubility constant of coffinite. *Geochim. Cosmochim. Acta* **2016**, *181*, 36−53.
(34) Kozai, N.; Ohnuki, T.; Iwatsuki, T. Characterization of saline groundwater at Horonobe, Hokkaido, Japan by SEC-UV-ICP-MS: Speciation of uranium and iodine. *Water Res.* **2013**, *47* (4), 1570−1584.
(35) Husar, R.; Weiss, S.; Hennig, C.; Hübner, R.; Ikeda-Ohno, A.; Zänker, H. Formation of Neptunium(IV)−Silica Colloids at Near-Neutral and Slightly Alkaline pH. *Environ. Sci. Technol.* **2015**, *49* (1), 665−671.
(36) Hennig, C.; Weiss, S.; Banerjee, D.; Brendler, E.; Honkimäki, V.; Cuello, G.; Ikeda-Ohno, A.; Scheinost, A. C.; Zänker, H. Solid-state properties and colloidal stability of thorium(IV)−silica nanoparticles. *Geochim. Cosmochim. Acta* **2013**, *103*, 197−212.
(37) Zänker, H.; Weiss, S.; Hennig, C.; Brendler, V.; Ikeda-Ohno, A. Oxyhydroxy Silicate Colloids: A New Type of Waterborne Actinide(IV) Colloids. *ChemistryOpen* **2016**, *5* (3), 174−182.
(38) Doelsch, E.; Masion, A.; Rose, J.; Stone, W. E. E.; Bottero, J. Y.; Bertsch, P. M. Chemistry and structure of colloids obtained by hydrolysis of Fe(III) in the presence of SiO4 ligands. *Colloids Surf., A* **2003**, *217* (1−3), 121−128.
(39) Kellermeier, M.; Gebauer, D.; Melero-García, E.; Drechsler, M.; Talmon, Y.; Kienle, L.; Cölfen, H.; García-Ruiz, J. M.; Kunz, W. Colloidal stabilization of calcium carbonate prenucleation clusters with silica. *Adv. Funct. Mater.* **2012**, *22* (20), 4301−4311.
(40) Hermann, J. A.; Suttle, J. F.; Hoekstra, H. R. Uranium(IV) chloride. In *Inorganic Syntheses*; McGraw-Hill Book Co., Inc.: New York, NY, 1957; pp 143−145.
(41) Laurent, T. C.; Granath, K. a. Fractionation of dextran and Ficoll by chromatography on Sephadex G-200. *Biochim. Biophys. Acta, Gen. Subj.* **1967**, *136* (2), 191−198.
(42) Granath, K. A. Solution properties of branched dextrans. *J. Colloid Sci.* **1958**, *13* (4), 308−328.
(43) Burke, I. T.; Mosselmans, J. F. W.; Shaw, S.; Peacock, C. L.; Benning, L. G.; Coker, V. S. Impact of the Diamond Light Source on research in Earth and environmental sciences: current work and future perspectives. *Philos. Trans. R. Soc., A* **2015**, *373* (2036), 20130151−20130152.
(44) Kraft, P. PILATUS 2M A Detector for Small Angle X-ray Scattering, 2010; 28, DOI: 10.3929/ethz-a-006023165.
(45) Bressler, I.; Pauw, B. R.; Thünemann, A. F. McSAS: Software for the retrieval of model parameter distributions from scattering patterns. *J. Appl. Crystallogr.* **2015**, *48*, 962−969.
(46) Pauw, B. R.; Pedersen, J. S.; Tardif, S.; Takata, M.; Iversen, B. B. Improvements and considerations for size distribution retrieval from small-angle scattering data by Monte Carlo methods. *J. Appl. Crystallogr.* **2013**, *46* (2), 365−371.
(47) Soper, A. K.; Barney, E. R. Extracting the pair distribution function from white-beam X-ray total scattering data. *J. Appl. Crystallogr.* **2011**, *44* (4), 714−726.
(48) Ravel, B.; Newville, M. ATHENA, ARTEMIS, HEPHAESTUS: data analysis for X-ray absorption spectroscopy using IFEFFIT. *J. Synchrotron Radiat.* **2005**, *12* (4), 537−541.
(49) Patterson, A. L. The Scherrer Formula for X-Ray Particle Size Determination. *Phys. Rev.* **1939**, *56* (10), 978−982.
(50) Fuchs, L. H.; Gebert, E. X-ray studies of synthetic coffinite, thorite and uranothorites. *Am. Mineral.* **1958**, *43*, 243−248.
(51) Barrett, S. A.; Jacobson, A. J.; Tofield, B. C.; Fender, B. E. F. The preparation and structure of barium uranium oxide BaUO 3+ x. *Acta Crystallogr., Sect. B: Struct. Crystallogr. Cryst. Chem.* **1982**, *38* (11), 2775−2781.
(52) Marshall, T. A.; Morris, K.; Law, G. T. W. W.; Mosselmans, J. F. W.; Bots, P.; Parry, S. A.; Shaw, S. Incorporation and Retention of 99-Tc(IV) in Magnetite under High pH Conditions. *Environ. Sci. Technol.* **2014**, *48* (20), 11853−11862.
(53) Suzuki, Y.; Kelly, S. D.; Kemner, K. M.; Banfield, J. F. Radionuclide contamination: Nanometre-size products of uranium bioreduction. *Nature* **2002**, *419* (6903), 134−135.
(54) O'Loughlin, E. J.; Kelly, S. D.; Cook, R. E.; Csencsits, R.; Kemner, K. M. Reduction of Uranium(VI) by Mixed Iron(II)/Iron(III) Hydroxide (Green Rust): Formation of UO 2 Nanoparticles. *Environ. Sci. Technol.* **2003**, *37* (4), 721−727.
(55) Pham, K. N.; Fullston, D.; Sagoe-Crentsil, K. Surface Charge Modification of Nano-Sized Silica Colloid. *Aust. J. Chem.* **2007**, *60* (9), 662.
(56) Rai, D.; Yui, M.; Moore, D. A.; Lumetta, G. J.; Rosso, K. M.; Xia, Y.; Felmy, A. R.; Skomurski, F. N. Thermodynamic model for ThO2(am) solubility in alkaline silica solutions. *J. Solution Chem.* **2008**, *37* (12), 1725−1746.
(57) Taylor, P. D.; Jugdaohsingh, R.; Powell, J. J. Soluble Silica with High Affinity for Aluminum under Physiological and Natural Conditions. *J. Am. Chem. Soc.* **1997**, *119* (38), 8852−8856.
(58) Husain, A. Charge development at the uranium oxide-solution interface. *J. Colloid Interface Sci.* **1984**, *102* (2), 389−399.
(59) Iler, R. K. *The chemistry of silica*; 1979.
(60) Kobayashi, M.; Juillerat, F.; Galletto, P.; Bowen, P.; Borkovec, M. Aggregation and Charging of Colloidal Silica Particles: Effect of Particle Size. *Langmuir* **2005**, *21* (13), 5761−5769.
(61) Valle-Delgado, J. J.; Molina-Bolívar, J. A.; Galisteo-González, F.; Gálvez-Ruiz, M. J.; Feiler, A.; Rutland, M. W. Hydration forces between silica surfaces: Experimental data and predictions from different theories. *J. Chem. Phys.* **2005**, *123* (3), 034708.

DOI: 10.1021/acs.est.8b01756
Environ. Sci. Technol. XXXX, XXX, XXX−XXX

(62) Chapel, J.-P. Electrolyte Species Dependent Hydration Forces between Silica Surfaces. *Langmuir* **1994**, *10* (11), 4237−4243.
(63) Grabbe, A.; Horn, R. G. Double-Layer and Hydration Forces Measured between Silica Sheets Subjected to Various Surface Treatments. *J. Colloid Interface Sci.* **1993**, *157* (2), 375−383.
(64) Johnson, A.-C. J. H.; Greenwood, P.; Hagström, M.; Abbas, Z.; Wall, S. Aggregation of Nanosized Colloidal Silica in the Presence of Various Alkali Cations Investigated by the Electrospray Technique. *Langmuir* **2008**, *24* (22), 12798−12806.
(65) Koopal, L. K. Mineral hydroxides: From homogeneous to heterogeneous modelling. *Electrochim. Acta* **1996**, *41* (14 SPEC. ISS), 2293−2306.
(66) Vigil, G.; Xu, Z.; Steinberg, S.; Israelachvili, J. Interactions of Silica Surfaces. *J. Colloid Interface Sci.* **1994**, *165* (2), 367−385.
(67) Yotsumoto, H.; Yoon, R.-H. Application of Extended DLVO Theory: II. Stability of Silica Suspensions. *J. Colloid Interface Sci.* **1993**, *157*, 434−441.
(68) Maruyama, T.; Katoh, S.; Nakajima, M.; Nabetani, H. Mechanism of bovine serum albumin aggregation during ultrafiltration. *Biotechnol. Bioeng.* **2001**, *75* (2), 233−238.

DOI: 10.1021/acs.est.8b01756
Environ. Sci. Technol. XXXX, XXX, XXX−XXX

Supporting Information: Stability, composition and core-shell particle structure of uranium(IV)-silicate colloids

S4.1. U(IV)-silicate synthesis

U(IV) solutions were prepared by dissolution of UCl_4 in 0.25 M HCl to form a stock solution of 0.05 M U(IV). This solution was added to 1.6 M $NaHCO_3$ to yield a 1 M $NaHCO_3$, 0.02 M U(IV) solution with U(IV) present as the $U(CO_3)_5^{6-}$ aqueous species. The oxidation state of uranium in the solution was verified by UV-vis and XANES and the solution was filtered through a 3 kDa molecular weight cut-off (MWCO) filter membrane to confirm it was a true solution without colloids. Finally, EXAFS analysis was performed on the sample to define the local coordination environment (Figure S4.9) which showed the uranium was present as $[U(CO_3)_5]^{6-}$, identified by Hennig *et al.* 2010.

Silicate solutions were formed by dissolution of sodium metasilicate nonahydrate ($Na_2SiO_4.9H_2O$). All silicate solutions were filtered through a 3 kDa MWCO membrane to verify no colloids or polysilicate molecules were present above this size. The pH of the final solutions was controlled by addition of NaOH or HCl to silicate solutions prior to U(IV)-carbonate solution addition. U(IV)-silicate colloids were generated by dilution of U(IV)-carbonate solution in solutions of silicate in a 1:19 U(IV) solution:silicate solution ratio, yielding a range of silicate concentrations (0-4 mM) and pH (9-12) (see Table S4.1 for more details).The colloidal phase is believed to form due to the decrease in carbonate concentration, coupled with an increase in hydroxide concentration in solution upon dilution leading to U(IV) hydrolysis and polymerization and reaction with silicate. Control experiments with no silicate present at pH 9-12 were also carried out.

Table S4.1 Summary of experimental conditions and analytical techniques used for each set of experiments conditions. In all cases [U] = 1 mM. UF = Ultrafiltration. 4mMSi/pH9 and 4mMSi/pH10.5 experiments could not be isolated in sufficient quantities to investigate by XRD and PDF. Si/U ratio taken from ultrafiltration data after 30 days.

Experiment Code	Experimental pH	[Si]/ mM	Colloid formed?	Si:U ratio	Techniques used
0mMSi/pH9	9	0	No	N/A	UF
2mMSi/pH9		2	Yes	1.5	UF, SAXS, DLS, Zeta potential, EXAFS, TEM, XRD, PDF
4mMSi/pH9		4	Yes	2.5	UF, SAXS, DLS, Zeta potential, EXAFS, TEM
0mMSi/pH10.5	10.5	0	No	N/A	UF, EXAFS, TEM, PDF
2mMSi/pH10.5		2	Yes	1.5	UF, SAXS, DLS, Zeta potential, EXAFS, TEM, PDF
4mMSi/pH10.5		4	Yes	2.2	UF, SAXS, DLS, Zeta potential, EXAFS, TEM, STEM
0mMSi/pH12	12	0	No	N/A	UF
2mMSi/pH12		2	No	1.0	UF, EXAFS, TEM, PDF
4mMSi/pH12		4	No	0.9	UF, EXAFS, TEM

S4.2. Supplementary ultrafiltration results

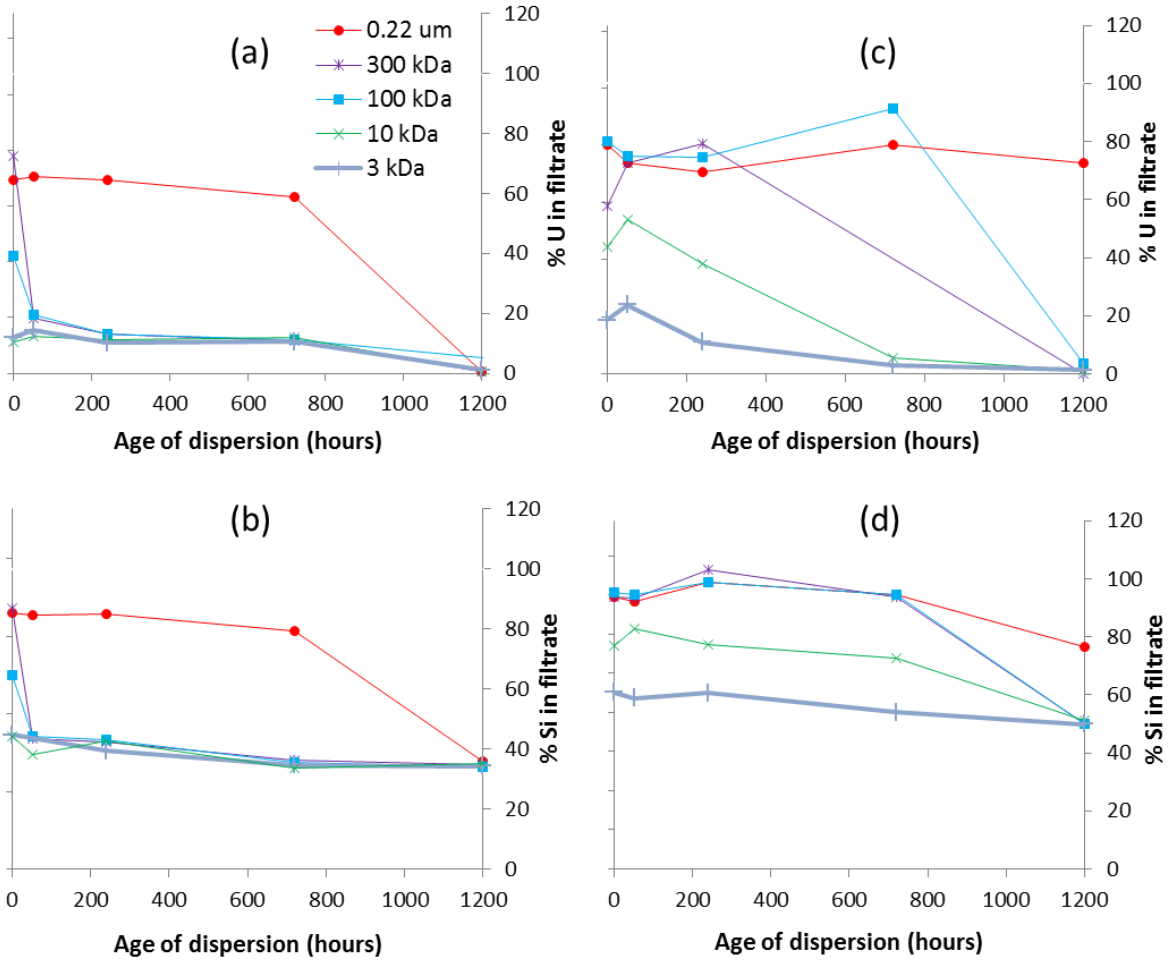

Figure S4.1: Ultrafiltration results for the 2mMSi/pH10.5 (left) for uranium (a) and silicon (b) passing through filters between 0.22 um and 3 kDa in size. 4mMSi/pH10.5 (c) for uranium (d) and silicon (bottom right) passing through filters between 0.22 um and 3 kDa in size.

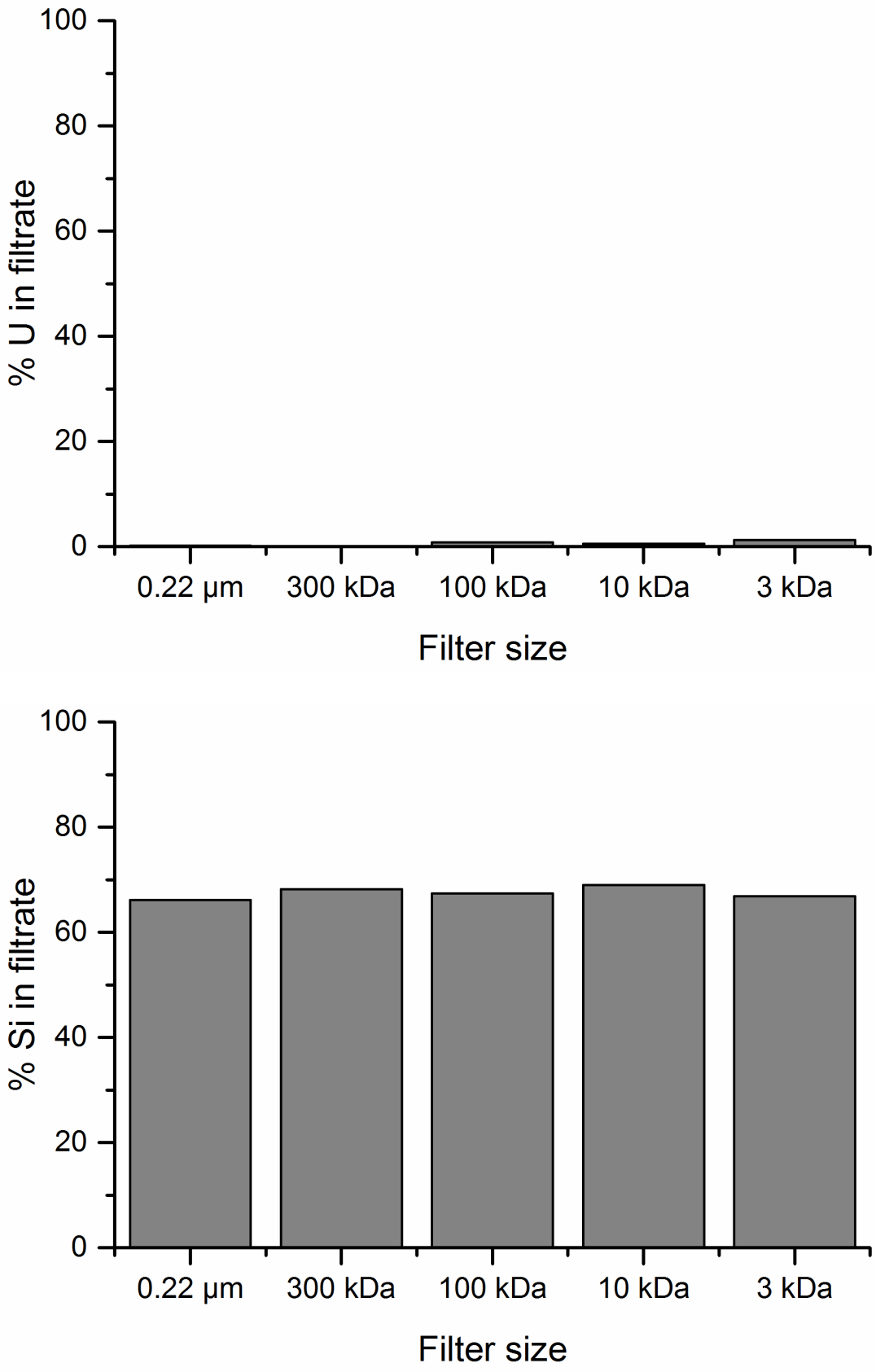

Figure S4.2: Ultrafiltration results from 4mMSi/pH12 system after 50 hours indicating no colloidal uranium is present

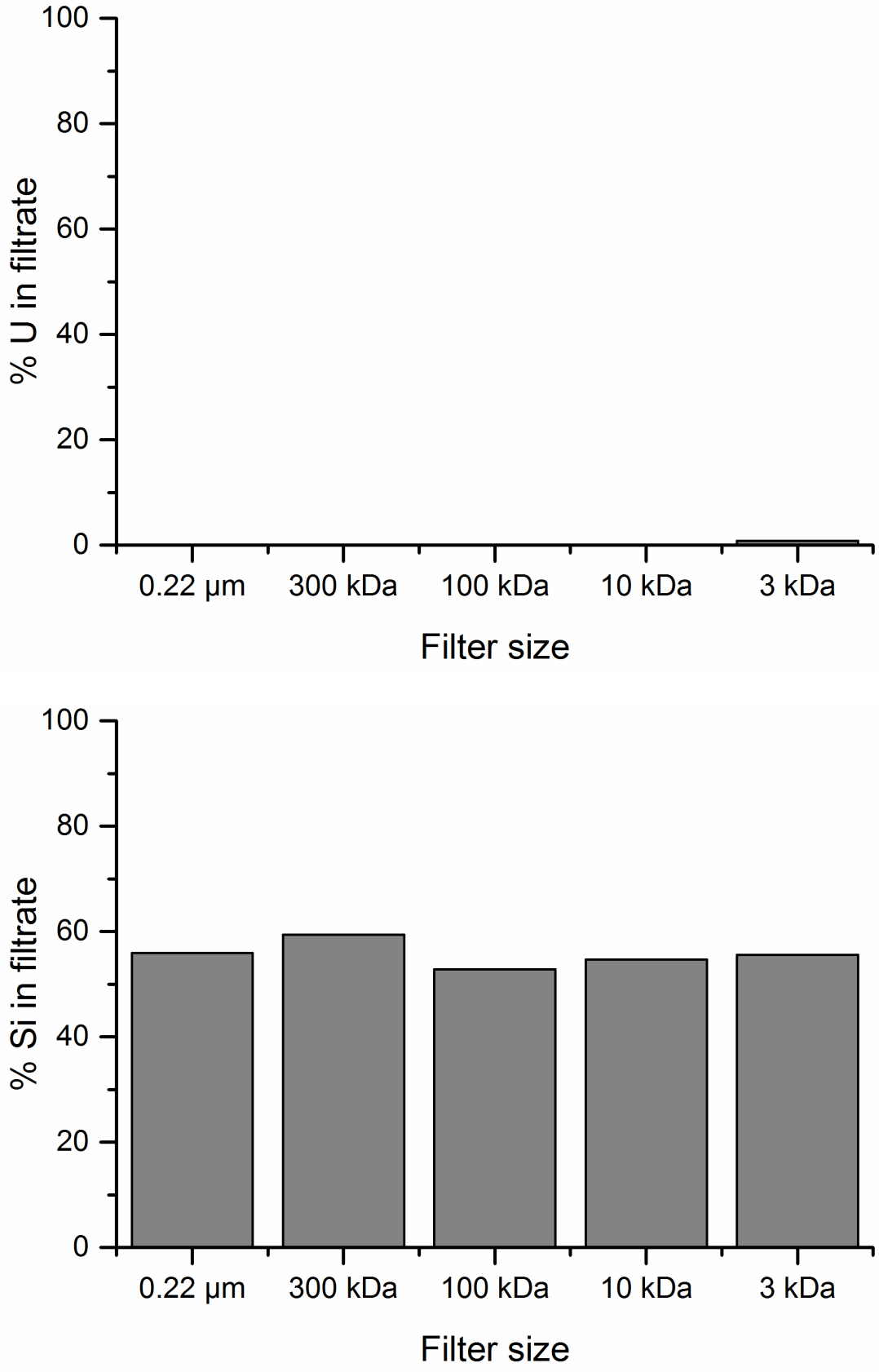

Figure S4.3: Ultrafiltration results from 2mMSi/pH12 system after 50 hours indicating no colloidal uranium is present

S4.3. Small angle x-ray scattering

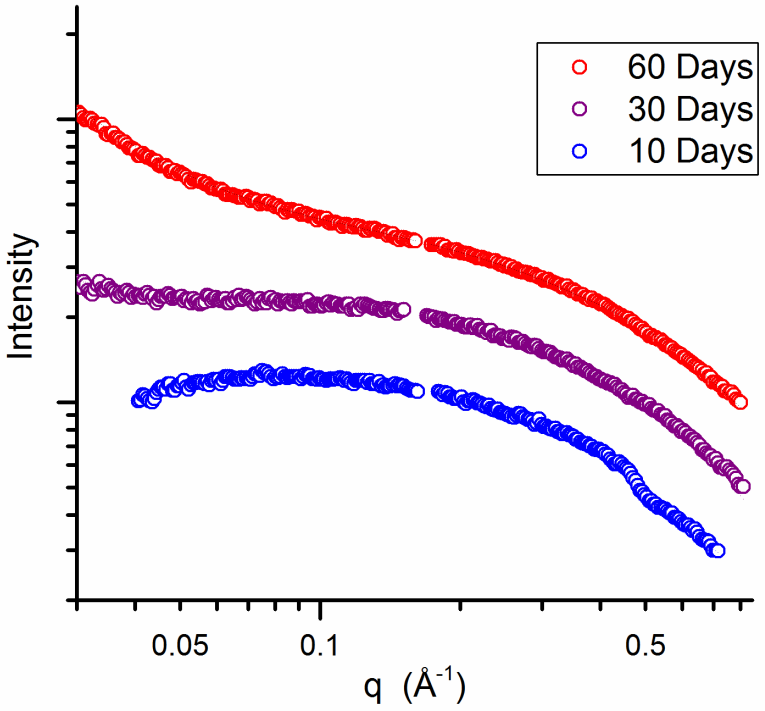

Figure S4.4: SAXS patterns from 2mMSi/pH10.5 system, aged for 10, 30 and 60 days

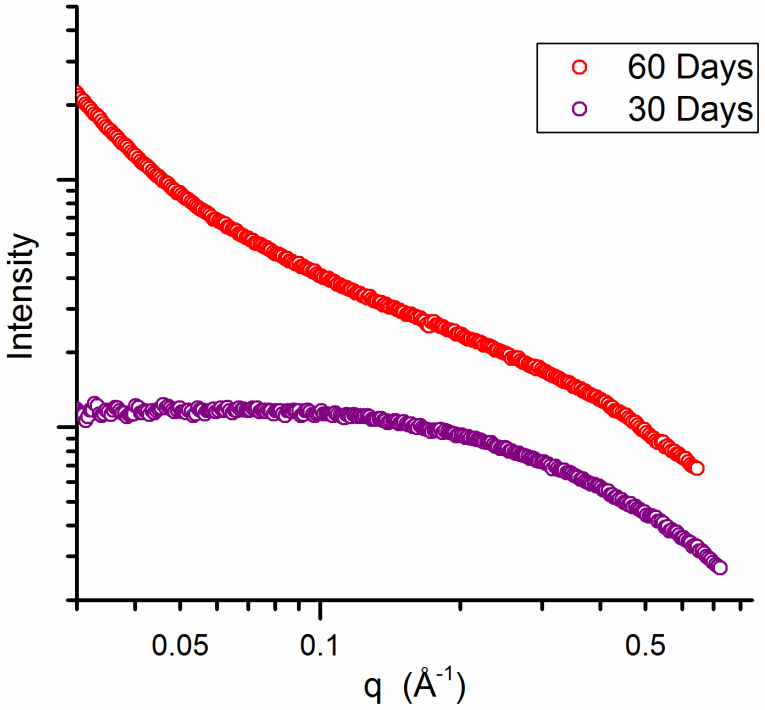

Figure S4.5: SAXS patterns from 4mMSi/pH10.5 system, aged for 30 and 60 days

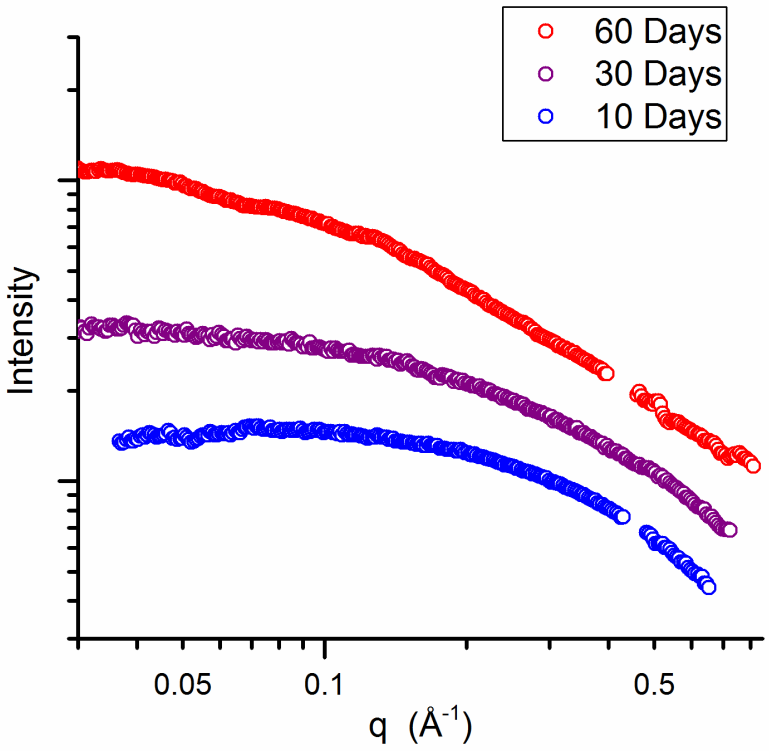

Figure S4.6: SAXS patterns from 2mMSi/pH9system, aged for 10, 30 and 60 days

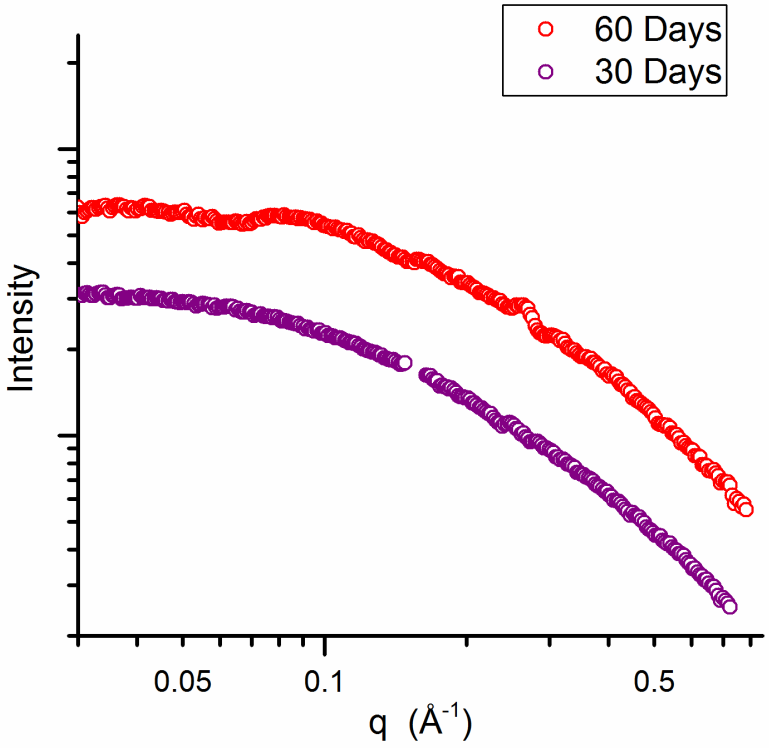

Figure S4.7: SAXS patterns from 4mMSi/pH9 system, aged for 30 and 60 days

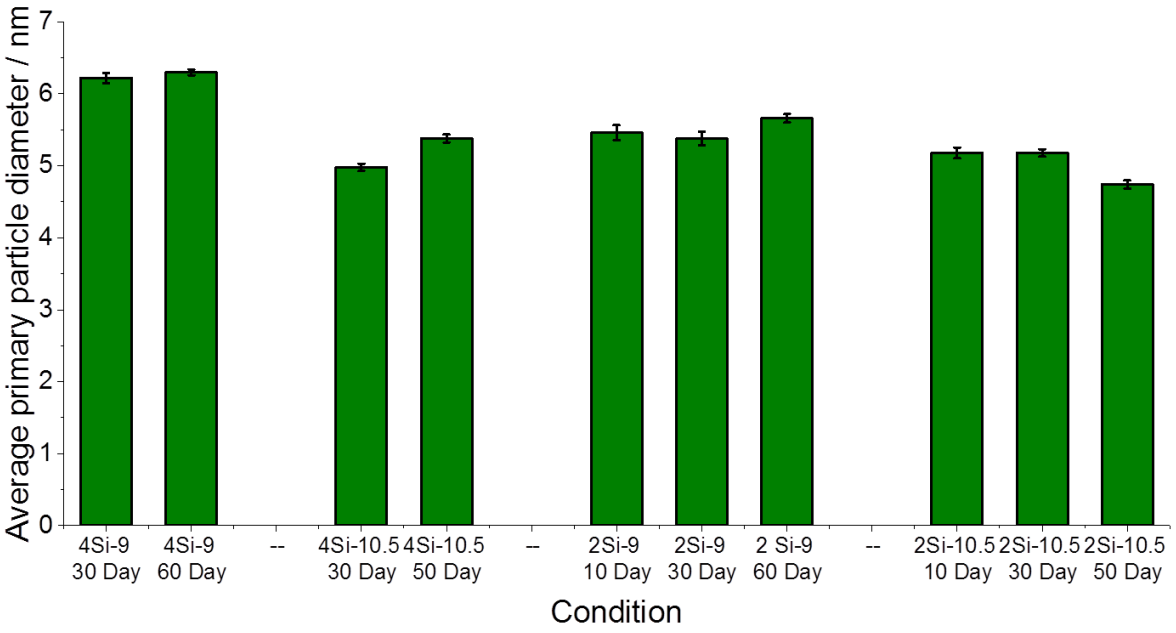

Figure S4.8: Average diameter of primary particles as derived from McSAS SAXS fitting. All conditions at 10, 30 and 60 day time points where available.

S4.4. Dynamic light scattering and zeta potential

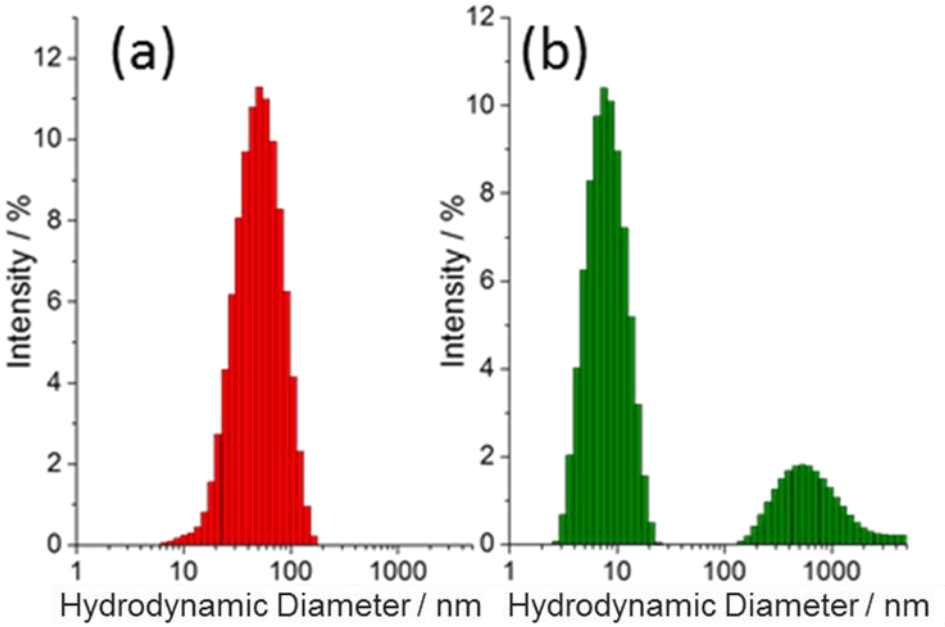

Figure S4.9: Intensity weighted DLS patterns for 30 day aged samples of (a) U(IV)-silicate colloidal dispersion 2mMSi/pH9 showing a mean particle size of 55 nm. (b) U(IV)-silicate colloidal dispersion 4mMSi/pH9 with a mean particle size of 8.54 nm (from first peak).

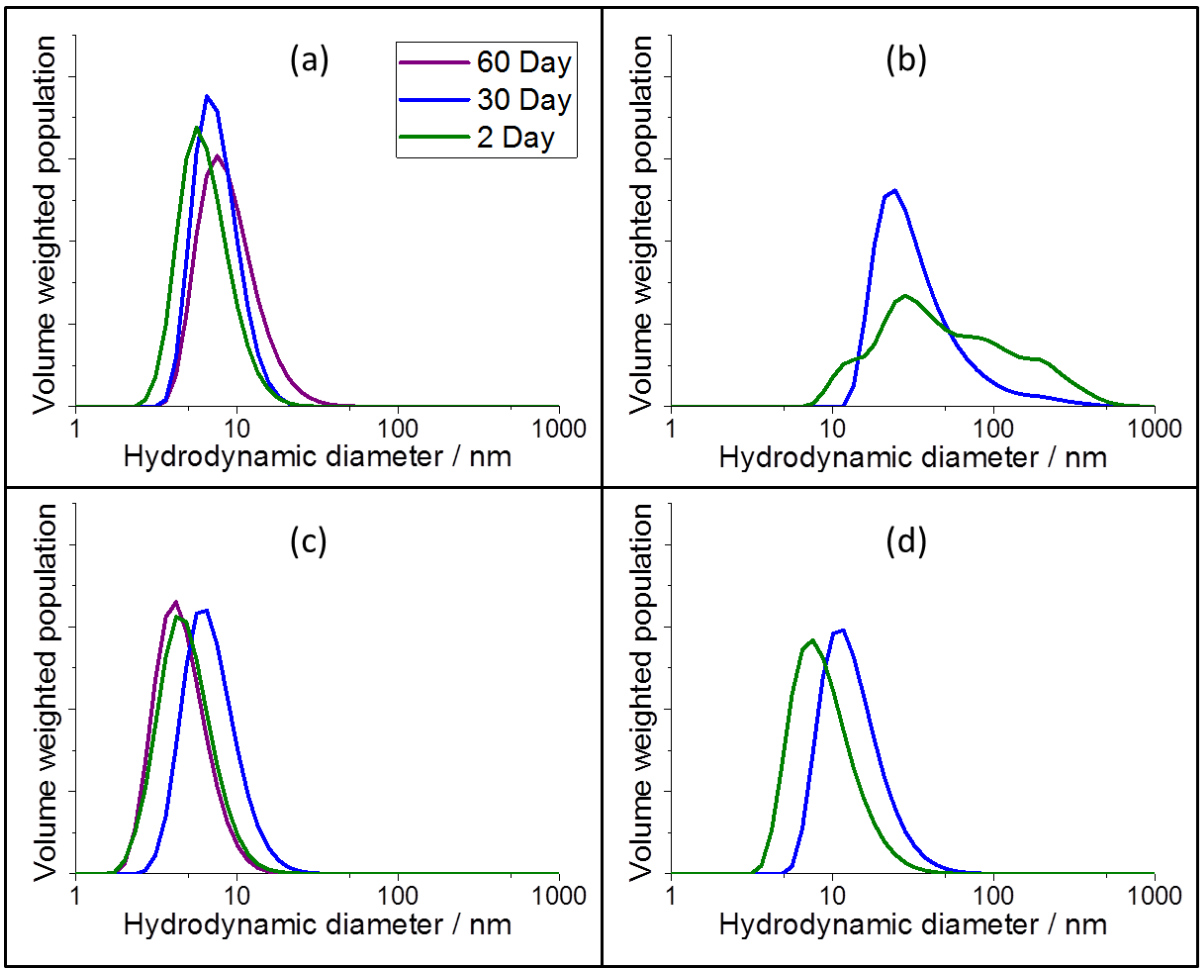

Figure S4.10: Particle size distributions gained from volume weighted Dynamic Light Scattering, using the refractive index of coffinite (1.74) (a) 4mMSi/pH9, (b) 2mMSi/pH10.5, (c) 4mMSi/pH10.5, (d) 2mM Si/pH9.

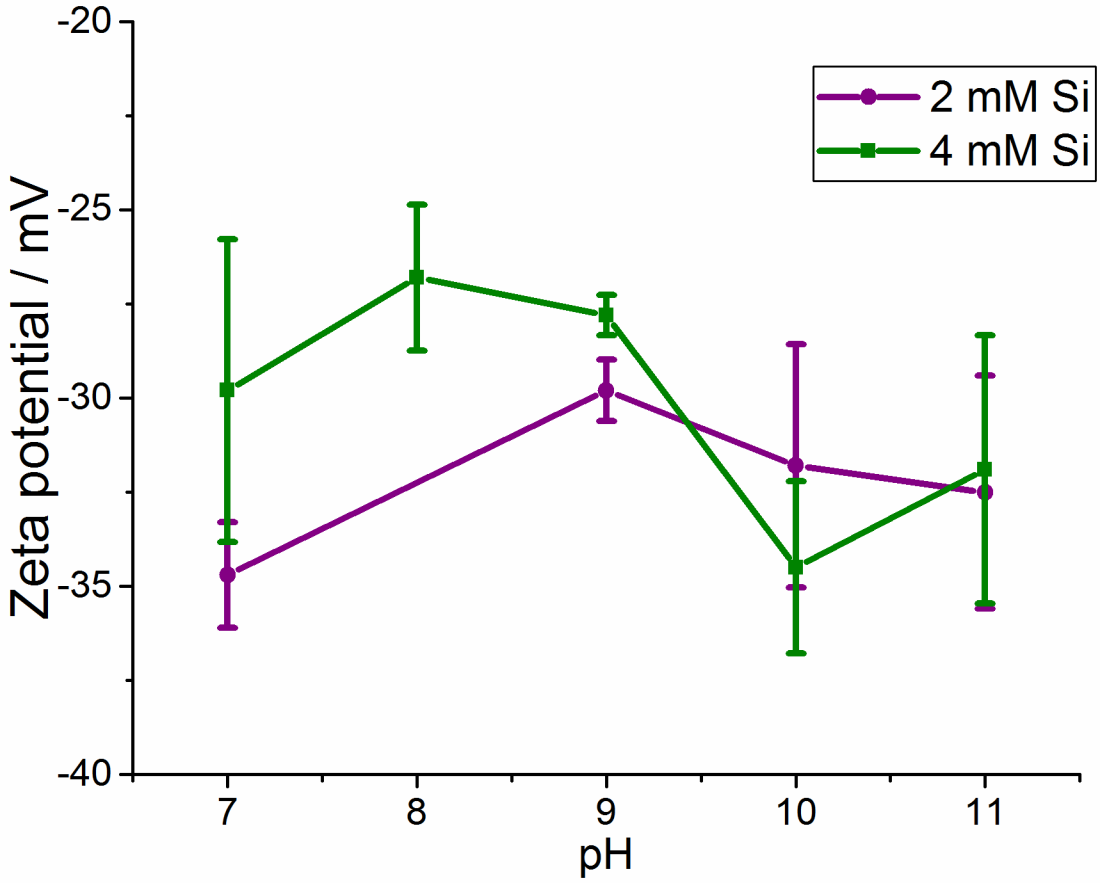

Figure S4.11: Zeta potential values of U(IV)-silicate colloids with 2 mM (purple) and 4 mM (green) silicate, recorded at pH 7-11.

S4.5. Transmission electron microscopy

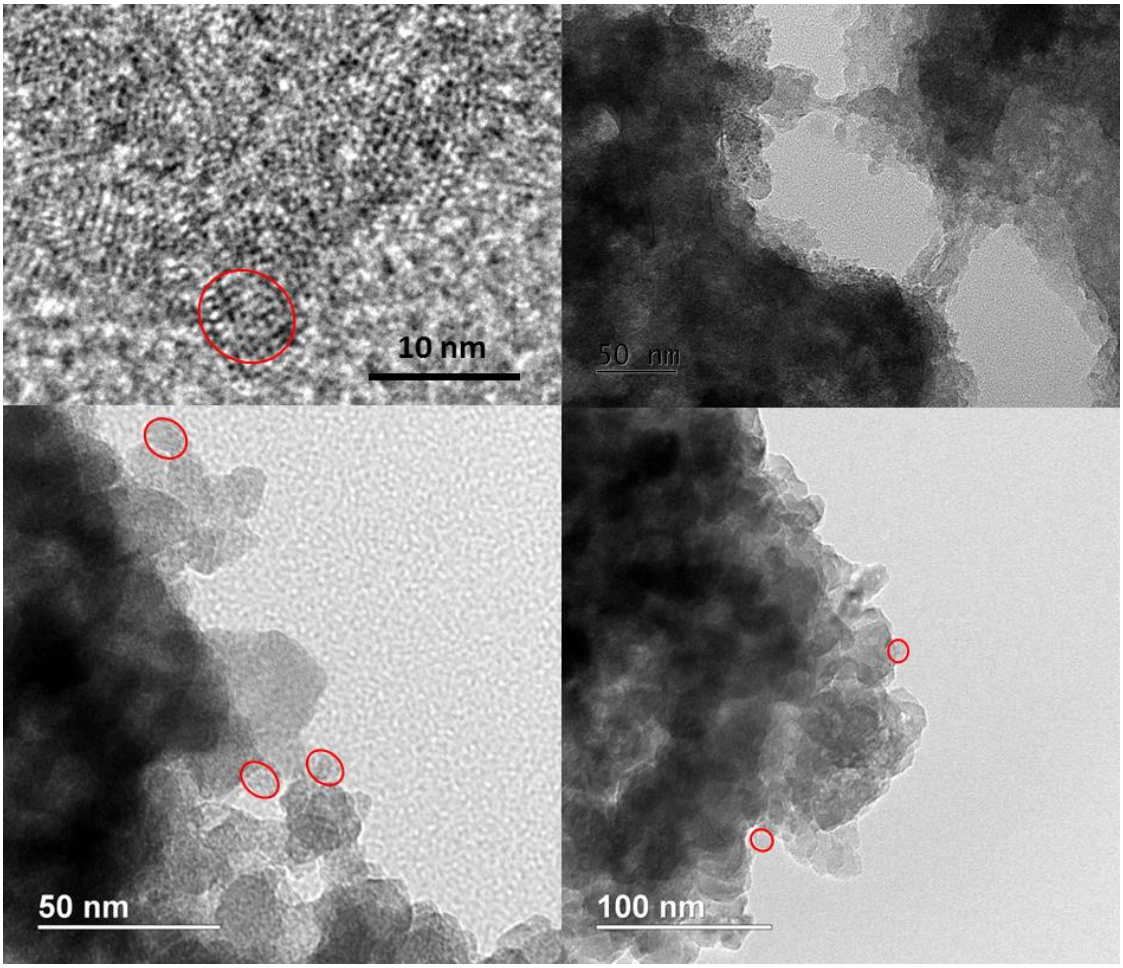

Figure S4.12: TEM images from 0mMSi/10.5 (a), 2mMSi/pH12 (b), 4mMSi/pH10.5 (c) and 2mMSi/pH10.5 (d) showing very little difference across conditions. Primary particles circled in red for clarity.

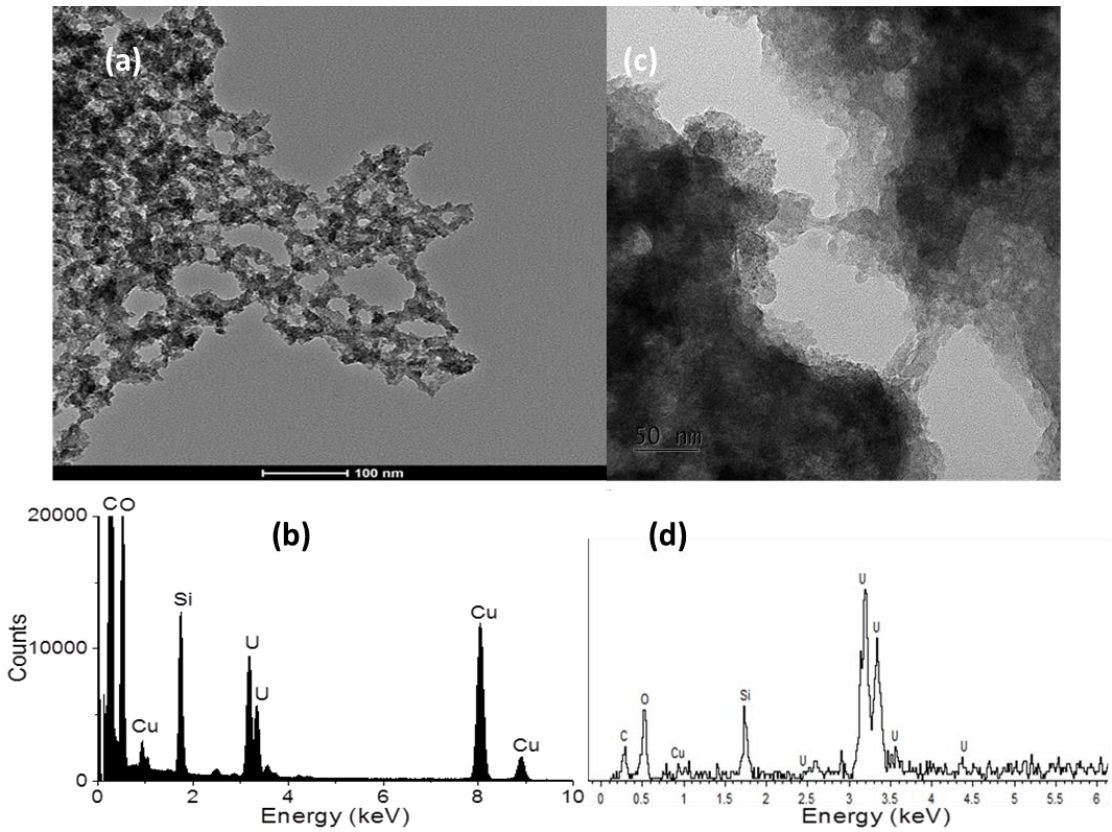

Figure S4.13: Comparative TEM and Energy Dispersive X-ray (EDX) spectra for U(IV)-silicate colloids/nanoparticles formed in the conditions: 4mMSi/pH10.5 (a,b) and 2mMSi/pH12 (c,d) showing higher Si:U ratio in the 4mMSi/pH10.5 system.

S4.6. Powder X-ray diffraction and X-ray pair distribution function

Samples for X-ray diffraction and X-ray pair distribution function analysis were prepared by sedimentation at pH 4 (Dreissig et al. 2011) and centrifugation (7000g for 10 minutes). For XRD analysis, the U(IV)-silicate was resuspended in isopropyl alcohol and dropped onto a silica glass slide. This sample was then dried and contained in an X-ray transparent, Poly(methyl methacrylate) (PMMA) anaerobic sample holder for XRD analysis (Bruker). The sample was scanned from 5-70° 2θ, with a step size of 0.02° and a count time of 0.2 s per step with Cu Kα X-rays with a wavelength of 1.5406 Å. A silica glass slide background was also recorded and used for background subtraction. For PDF analysis, wet slurries of U(IV)-silicate samples were injected into glass capillaries (1 mm) and sealed with araldite. 5 x 30 second scans were recorded between 0 and 50° 2θ with a step size of 0.01° and a 76 keV X-ray energy.

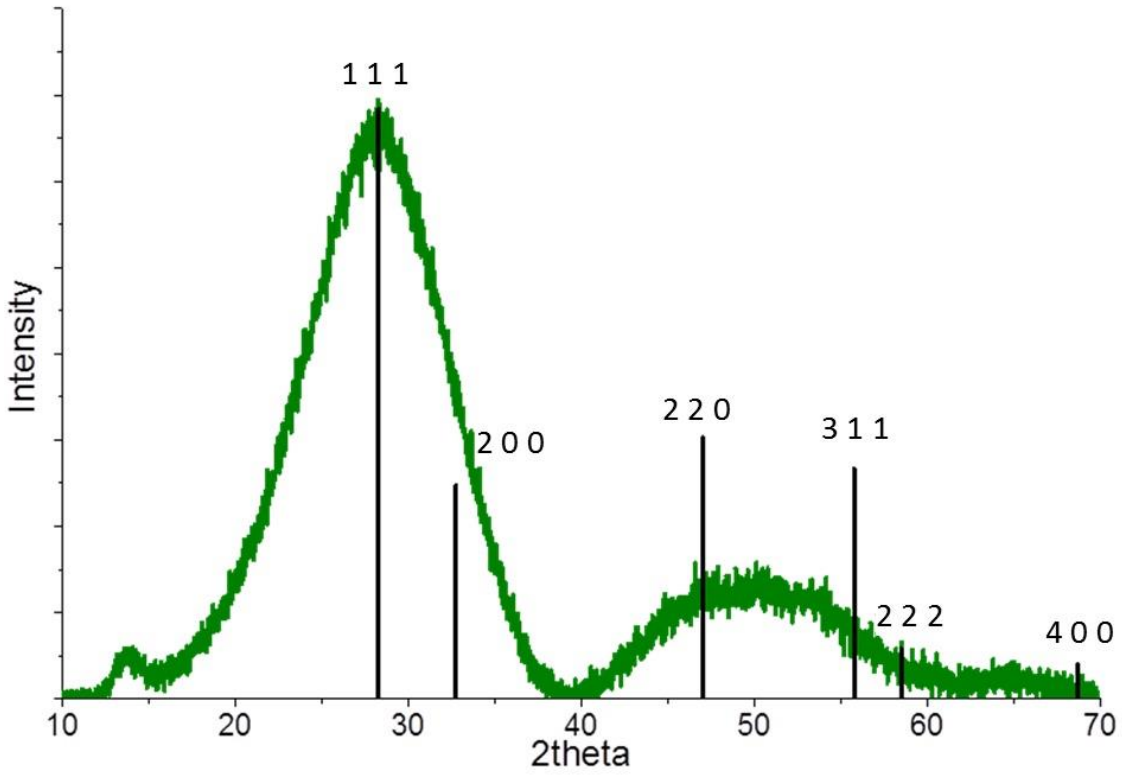

Figure S4.14: X-ray powder diffraction pattern for a precipitated colloidal dispersion 2mMSi/pH9 (green) and uraninite peak positions with miller indices (black).

$$D = \frac{k\lambda}{\beta_{\frac{1}{2}} cos\theta}$$

Equation S4.1: Scherrer equation, used for size estimation of crystallites using peak broadening where *D* is the crystallite size, *k* is a shape constant of 0.9, assuming the particles are spherical, λ is the x-ray wavelength, $\beta_{1/2}$ is the full width at half maximum of the broadened peak and ϑ is the Bragg angle of the selected peak.

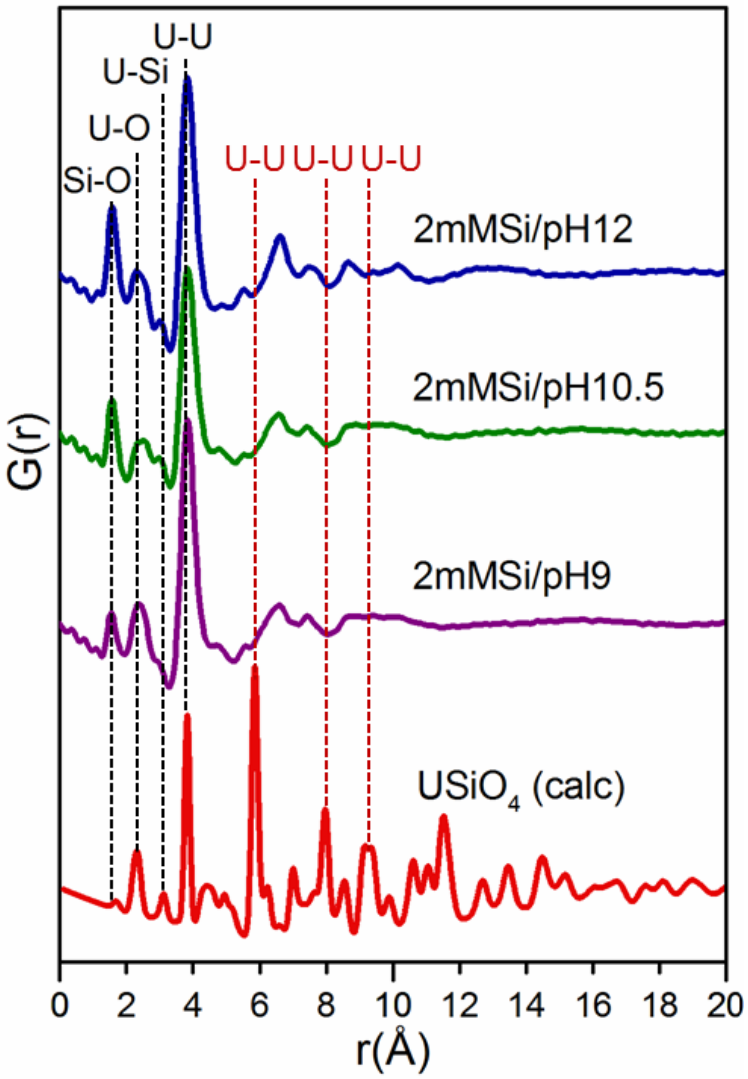

Figure S4.15: X-ray pair distribution functions (PDF) of 3 synthesised U(IV)-silicates (2mMSi/pH12, 2mMSi/pH10.5 and 2mMSi/pH9) compared with a calculated PDF of coffinite ($USiO_4$). Black dashed lines indicate shared peaks between synthesised U(IV)-silicates and coffinite, red dashed lines indicate peaks present in coffinite and not synthesised U(IV)-silicates.

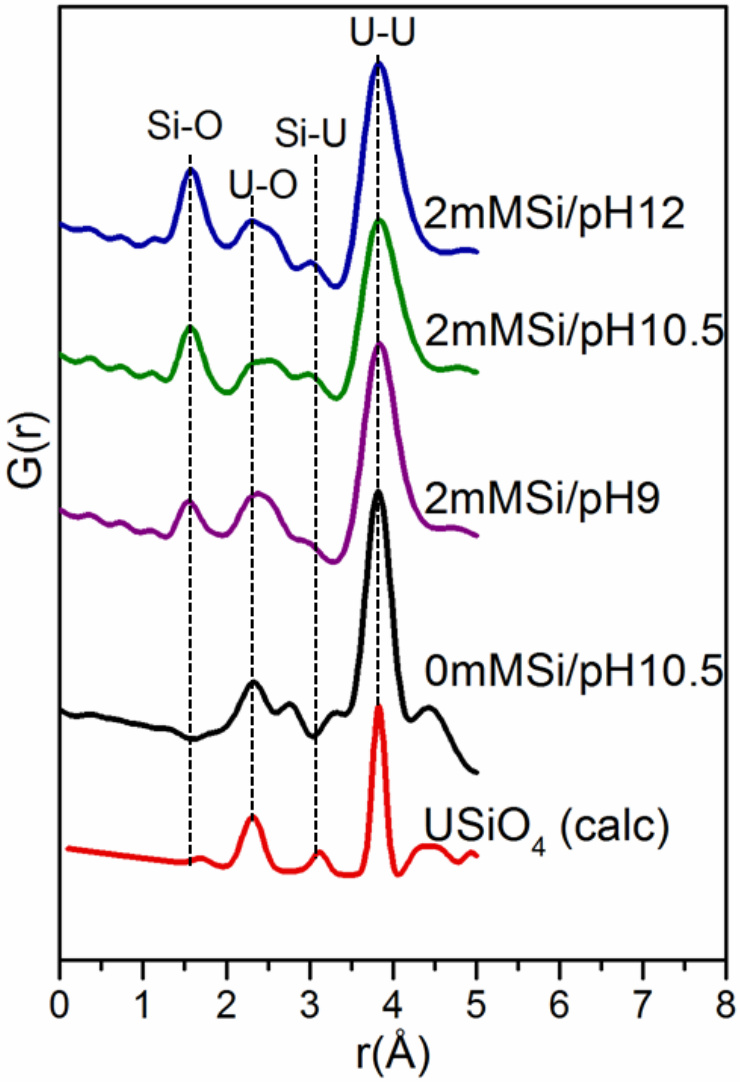

Figure S4.16: X-ray pair distribution functions (PDF) of 3 synthesised U(IV)-silicates (2mMSi/pH12, 2mMSi/pH10.5 and 2mMSi/pH9) compared with a nano-UO2 sample (0mMSi/pH10.5) and calculated PDF of coffinite ($USiO_4$).

Table S4.2: Interatomic distances in UO_2 (Barrett *et al.*, 1982) and $USiO_4$ (Fuchs and Gebert, 1958) which would be most prevalent in an X-ray PDF.

Structure	Interatomic pair	Distance (Å)
UO_2	U-O	2.36
	O-O	2.72
	U-U	3.85
	O-O	3.85
	U-O	4.51
	U-U	5.45
	U-U	6.67
	U-U	7.70
	U-U	8.61
	U-U	10.19
	U-U	11.55
	U-U	13.88
$USiO_4$	Si-O	1.58
	U-O	2.32
	U-O	2.51
	U-Si	3.13
	U-Si	3.83
	U-U	3.83
	U-O	4.26-4.80
	U-U	5.86
	U-U	7.98
	U-U	9.12
	U-U	10.62
	U-U	11.71

S4.7. X-ray absorption spectroscopy

Solid samples for XAS were prepared according to the following procedures. For samples of 2 and 4 mM Si, pH 12 and 0 mM Si pH 10.5, where samples were precipitated, these were separated from solution by centrifugation (7000g for 10 minutes). For samples of U(IV)-silicates at 2 mM Si pH 9 and 10.5, these samples were first acidified to pH 4 and then centrifuged (7000g for 10 minutes), according to the literature (Dreissig *et al.* 2011). It was not possible to separate samples of U(IV)-silicate colloidal particles at 4 mM Si pH 9 and 10.5 from solution using the above methods and therefore these samples were collected on 3 kDa filters. Samples were not dried, to maintain their hydrated structure, and diluted in cellulose to form pellets for XAS measurements.

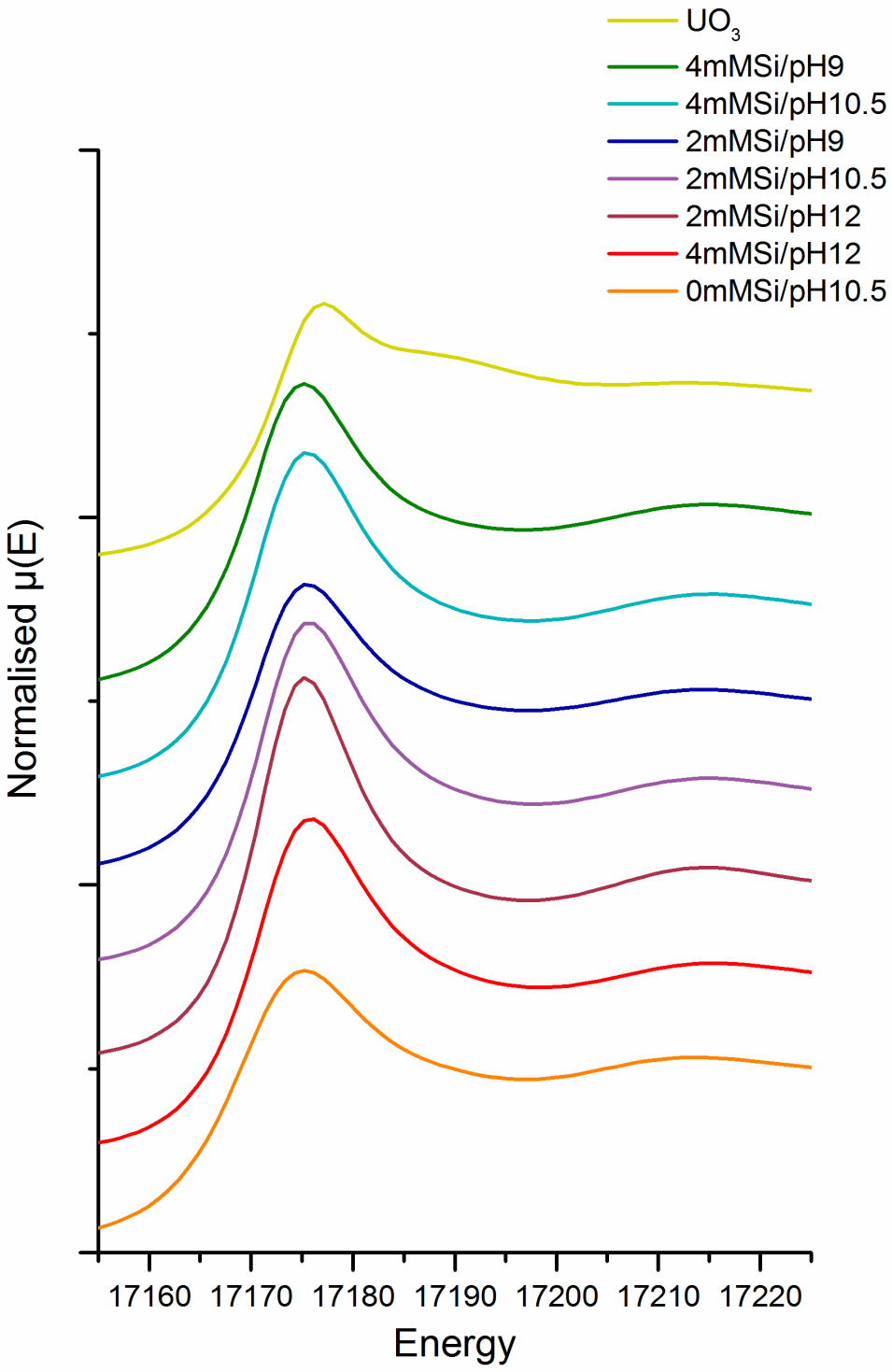

Figure S4.17: XANES spectra for all U(IV)-silicate samples along with U(IV)O_2 (0mMSi/pH10.5) and U(VI)O_3 (UO_3) standards.

Figures S4.18 and S4.19 show the EXAFS of U(IV)-HCl and U(IV)-CO_3^{2-} solutions respectively. The U(IV)-HCl EXAFS have been fit with a first shell coordination of water (8.9 x U-OH_2 bonds) and Cl^- (0.8 x U-Cl bond). The fixed U-O and U-Cl distance parameters used (Table S4.3) were those proposed by Hennig *et al*. (2005) for U(IV) chloride complexes in aqueous solutions. 9.6 coordinate hydrated uranium complex is consistent with that seen in Hennig et al (2005) as is the H_2O:Cl ligand ratio.

The U(IV)-carbonate system was fit using the model from Hennig *et a.l* (2010), based on the $U(CO_3)_5^{6-}$ solution complex.

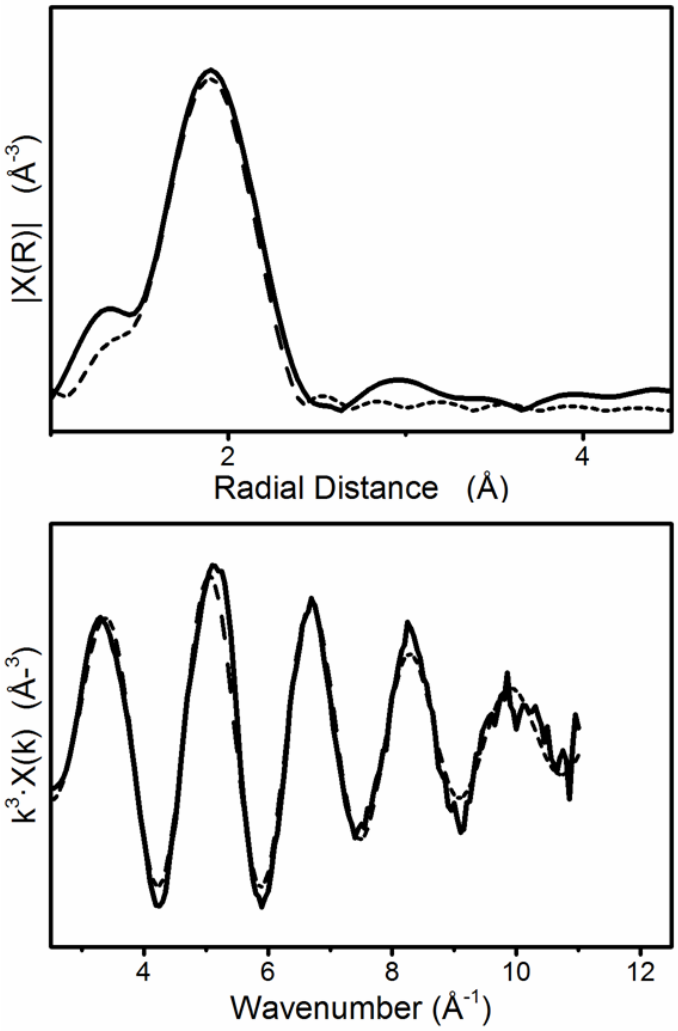

Figure S4.18: Data and fit for EXAFS (above) and EXAFS FT of U(IV)-HCl solution complex

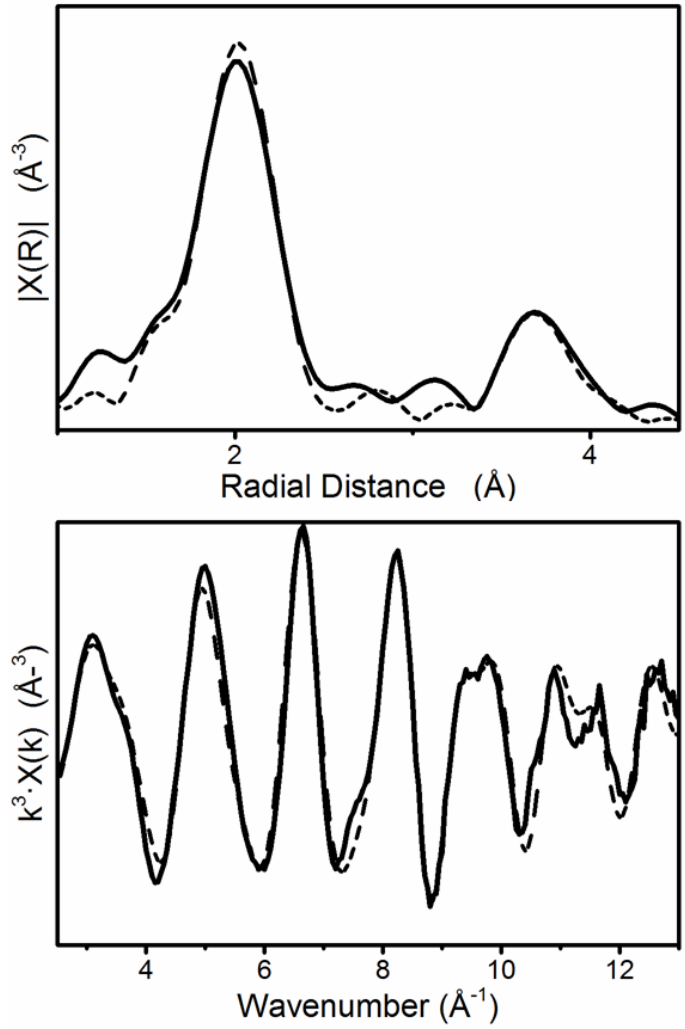

Figure S4.19: Data and fit for EXAFS (above) and EXAFS FT of U(IV)-CO3 solution complex

Table S4.3: EXAFS fit parameters for U(IV) solution species U(IV)-HCl (Figure S4.18) and U(IV)-CO3 (Figure S4.19), and UO2 (Figure 4.4G, S4.20G). Coordination numbers (N), U interatomic distances (R (Å)), Debye-Waller factors (σ2), shift in energy from calculated Fermi level (ΔE0) and 'goodness of fit' factor (R). Coordination numbers were fixed, amplitude factors were fixed as 1, a indicates fixed R values. b indicates fitted coordination numbers, c denotes fixed σ^2 values, d indicates tied σ^2 values. Numbers in parentheses are the standard deviation on the last decimal place.

	Shell	**R / Å**	**N**	**σ^2**	**ΔE_0 (eV)**	**R**
U-HCl	U-O	2.41[a]	8.9(5)[b]	0.007[c]	3.6	0.0069
	U-Cl	2.71[a]	0.7(3)[b]	0.004[c]		
U-CO_3	U-O	2.46(1)	10	0.005(1)	9.5(10)	0.024
	U-C	2.91(2)	5	0.003(2)		
	U-O(dist)	4.18(2)	5	0.004(1)[d]		
	U-C-O MS	4.18(2)	10	0.004(1) [d]		
	U-C-O-C MS	4.18(2)	5	0.004(1) [d]		
UO_2	U-O	2.34(1)	7	0.010(7)	3.5(7)	
	U-U	3.84(1)	5	0.007(1)		

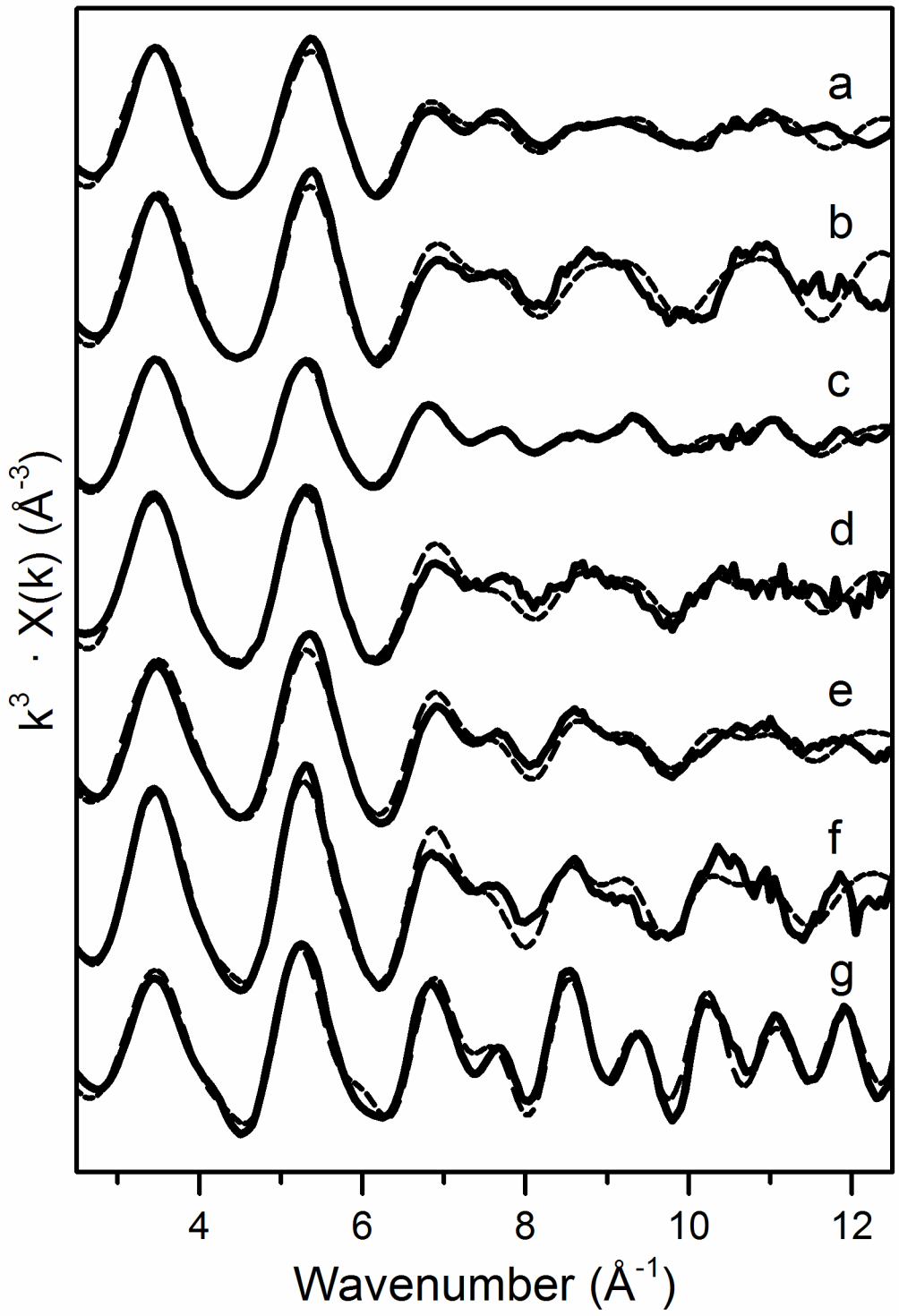

Figure S4.20: EXAFS spectra for a 4mMSi/pH9, b 4mMSi/pH10.5, c 2mMSi/pH9, d 2mMSi/pH10.5, e 4mMSi/pH12, f 2mMSi/pH12, g 0mMSi/pH10.5 (black lines) with fits overlaid (dashed lines).

S4.8. Thermodynamic modelling

Thermodynamic modelling was performed using the PHREEQC software package and the specific ion theory (SIT) database, augmented with the aqueous $U(OH)_3(H_3SiO_4)_3^{2-}$ species defined by Mesbah *et al.* (2015) ($U^{4+} + 3H_2O + 3H_4SiO_4 \leftrightarrow U(OH)_3(H_3SiO_4)_3^{2-} + 6H^+$, log $K°$ = 18.39 ± 1.7) and $U(OH)_2(CO_3)_2^{2-}$ species defined by Rai *et al.* (1998) ($U^{+4} - 2H^+ + 2CO_3^{-2} + 2H_2O = U(OH)_2(CO_3)_2^{2-}$, log $K°$ = 11.33). $UO_2.2H_2O$ was used over UO_2 as it is believed to be a more accurate representation of U(IV)-oxides formed in these systems.

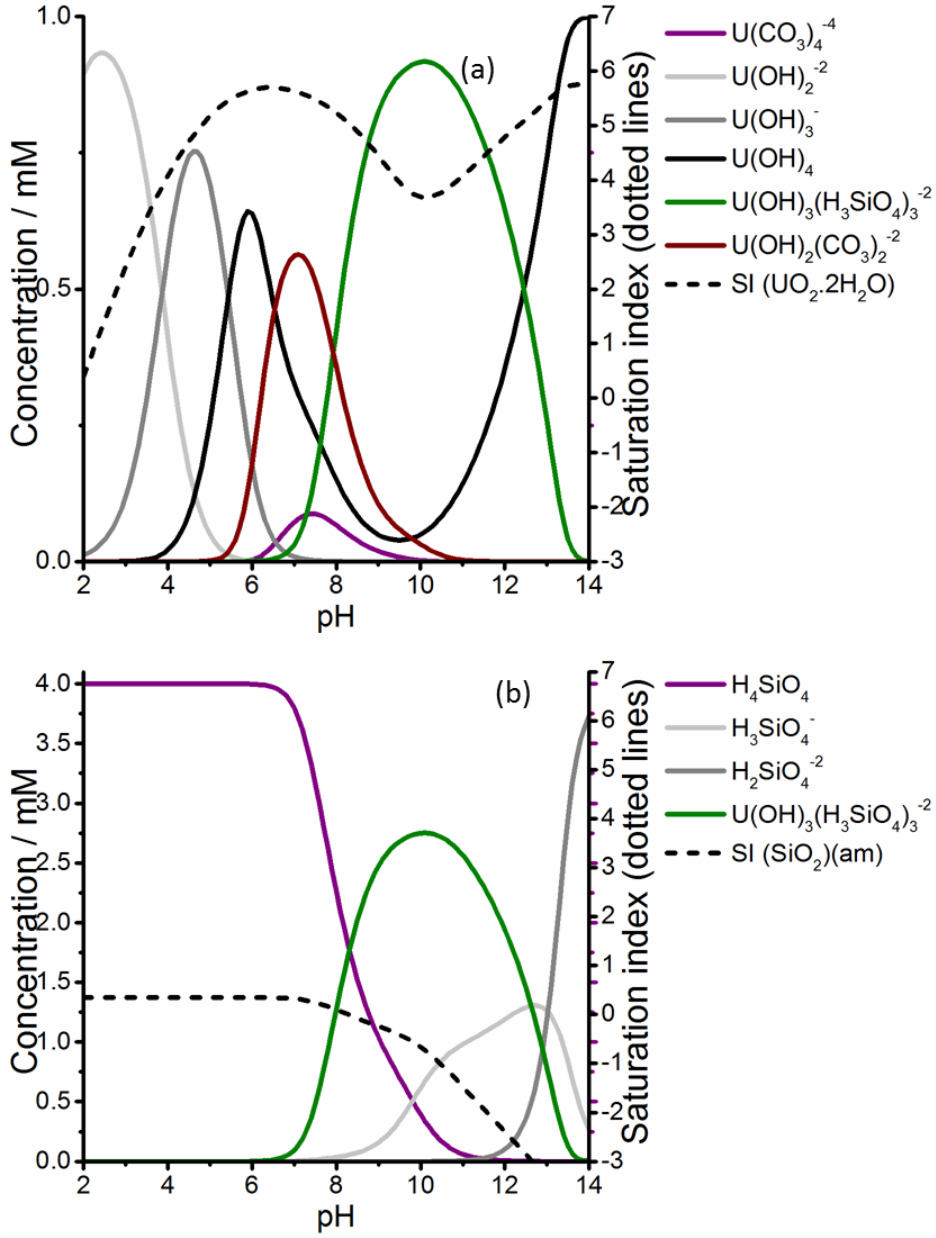

Figure S4.21: Speciation of uranium (a) and silicon (b) with pH for a 4 mM Si, 1 mM U system

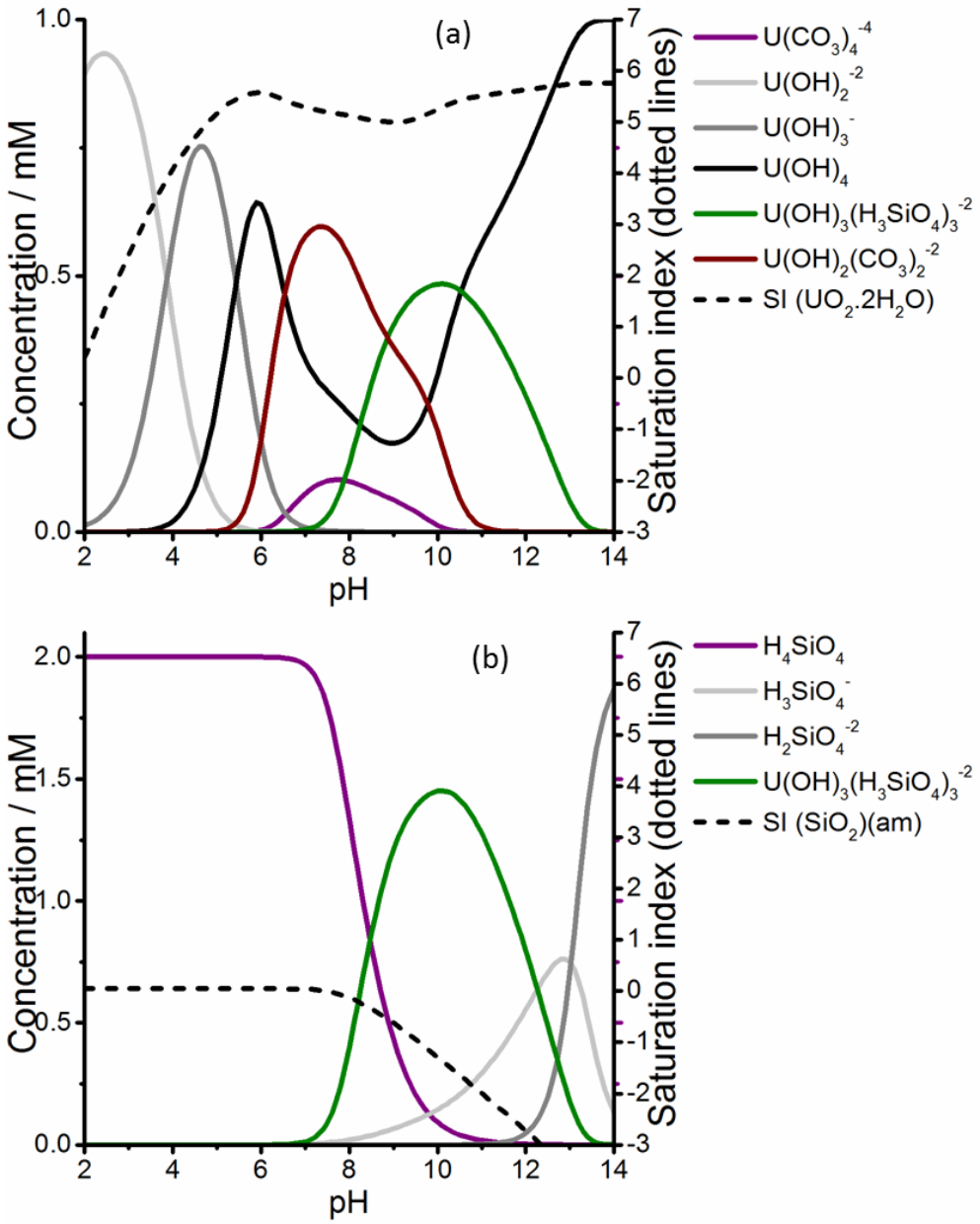

Figure S4.22: Speciation of uranium (a) and silicon (b) with pH for a 2 mM Si, 1 mM U system

S4.9. Atomic structures of uraninite (UO_2) and coffinite ($USiO_4$)

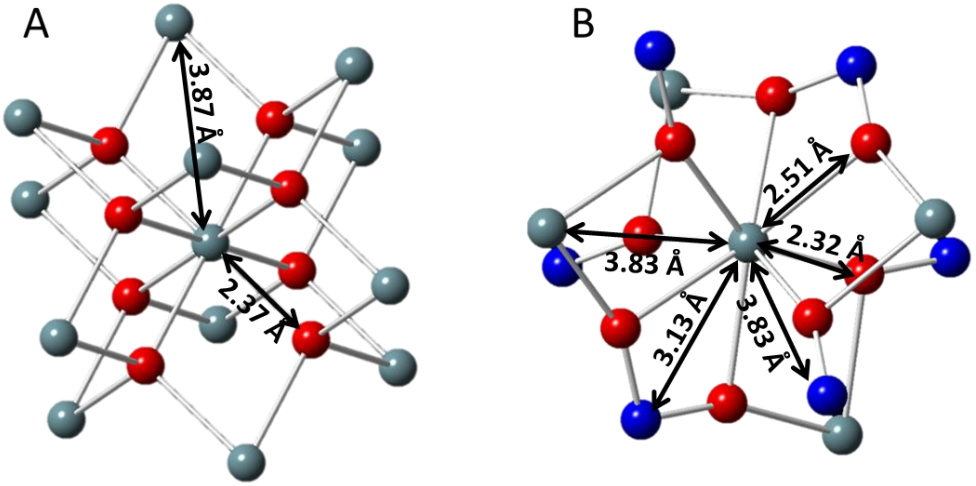

Figure S4.23: The local structure of uraninite (A) and coffinite (B) with interatomic distances from uranium annotated. Grey = U, Red = O, Blue = Si.

Chapter 5: Interactions of Sr with UO_2 and U(IV)-silicate phases

Thomas S. Neill[a], Katherine Morris[a], Carolyn I. Pearce[b], Nicholas K Sherriff[c], and Samuel Shaw[a]*

[a]Research Centre for Radwaste Disposal and Williamson Research Centre, School of Earth & Environmental Scineces, The University of Manchester, Oxford Road, Manchester M13 9PL, UK

[b]Pacific Northwest National Laboratory, Richland, WA 99354, USA

[c] National Nuclear Laboratory, Chadwick House, Warrington Road, Birchwood Park, Warrington WA3 6AE, UK

*Corresponding author: sam.shaw@manchester.ac.uk

5.1. Abstract

Spent nuclear fuel contains both uranium and high yield fission products including ^{90}Sr, which is highly relevant as a contaminant at nuclear facilities. Both U and ^{90}Sr will be present in facilities where spent nuclear fuel has been processed including in storage ponds and tanks, and the interactions between Sr and U phases are not well understood. We investigate the Sr sorption behaviour when contacted with two nuclear fuel cycle relevant U(IV) phases; UO_2 and U(IV)-silicate, over pH 4-14. UO_2 is a product of the anaerobic corrosion of metallic uranium and is also the form of U in many nuclear fuels, and U(IV)-silicates can form colloids under neutral to alkaline pH conditions representative of fuel storage ponds. Here, Sr was shown to have a higher affinity for UO_2 between pH 6 and 12, and a significant degree of Sr sorption also occurred to U(IV)-silicate phases at pH ≥6. EXAFS, TEM and desorption data for the UO_2 system suggested surface incorporation of Sr on UO_2 occurred at pH 10 and 12. EXAFS investigations on U(IV)-silicate samples indicated that outer sphere sorption of Sr dominated at low pH with intrinsic Sr-silicates forming at pH ≥12. The impact that these U(IV) phases have on Sr behaviour indicates a previously unrecognised control on Sr mobility in environments where spent nuclear fuel management and storage is undertaken.

5.2. Introduction

Over 60 years of nuclear research and power generation has resulted in a significant global nuclear legacy for decommissioning and disposal. Uranium (U) is typically the most abundant radionuclides by mass in spent nuclear fuel (Bruno and Ewing, 2006; NDA, 2017a). Additionally, high yield, high specific activity fission products (e.g. ^{90}Sr and ^{137}Cs) dominate the radioactivity inventory of many wastes (NDA, 2017b). For example, ^{90}Sr (half-life 29 years) is a high energy beta emitter and a significant contributor to external dose in many nuclear fuel cycle scenarios. Understanding ^{90}Sr speciation in conditions relevant to decommissioning and waste disposal is essential for the safe management of nuclear legacy facilities. Despite the co-location of ^{90}Sr and U in many SNF storage facilities, the interactions of Sr with U phases are poorly understood in these challenging environments. Understanding these interactions, specifically Sr sorption mechanisms and capacity, is essential for predicting the behaviour of ^{90}Sr in these environments.

^{90}Sr and U are co-located in intensely radioactive, legacy spent fuel storage ponds within globally significant nuclear facilities. Spent fuel ponds are often maintained at a high pH to minimise corrosion (Lumetta, Wagner and Carlson, 1996; Wilson, 1996; Parry *et al.*, 2011). Several of the UK legacy ponds at the Sellafield nuclear facility contain corroded Magnox spent fuel which consisted of Mg rich metallic cladding and metallic U spent fuel. In the ponds, the spent fuel was stored for extended periods which led to corrosion and formation of corroded Magnox sludge (CMS). CMS consists mainly of brucite ($Mg(OH)_2$), and other Mg-carbonate, hydroxide and Mg-Al hydroxides, components of SNF and corroded metallic U (Gregson, Goddard, *et al.*, 2011). The corrosion of metallic U under these conditions generates UO_2 (Kaminski *et al.*, 2005; Delegard and Schmidt, 2008; Sinkov, Delegard and Schmidt, 2008; Gregson *et al.*, 2011). Additionally, many other forms of nuclear fuel use UO_2 as a fuel matrices (Bruno and Ewing, 2006), making UO_2 abundant in most spent nuclear fuel storage scenarios. Furthermore, under groundwater conditions (pH 8.4, 41 ppm Si), corrosion of metallic U in SNF can lead to the formation of U(IV) colloids (Kaminski and Goldberg, 2002; Kaminski *et al.*, 2005). Whilst the nanoparticulate structure of these colloids was identified as UO_2, reappraisal suggests they showed some similarities to U(IV)-silicate colloids which are stable under

conditions related to SNF storage (Dreissig *et al.*, 2011; Neill, Morris, Pearce, Sherriff, Burke, *et al.*, 2018), making it likely that these UO_2 colloidal particles may have a silicate coating. Importantly, the mobility of these relatively newly identified colloidal phases is predicted to be high, in turn this could impact on the mobility of associated radionuclides, including ^{90}Sr, during effluent treatment. Thus, the interaction of ^{90}Sr with both UO_2 and U(IV) silicate colloids is of high relevance to fuel pond storage and radioactive effluent treatment systems.

The mobility and speciation of Sr is likely to impact on the effectiveness of its removal from effluents at nuclear facilities. Effluent from the legacy spent fuel storage ponds at Sellafield, UK is treated in the site ion exchange effluent plant (SIXEP)(Parry *et al.*, 2011; Maher *et al.*, 2016). Here, the clinoptilolite $(Na,K,Ca)_{2\text{-}3}Al_3(Al,Si)_2Si_{13}O_{36}{\cdot}12H_2O$, a naturally occurring zeolite ion exchanger, is highly effective in selectively removing ^{90}Sr and ^{137}Cs from circumneutral, high ionic strength effluents prior to discharge under authorisation to the Irish Sea (Gray, Jones and Smith, 1995; Maher *et al.*, 2016). However, as plant operations change in the future, understanding the role of different components of SNF, particularly U(IV) phases, on ^{90}Sr mobility is crucial in underpinning future effluent treatment systems.

The behaviour of Sr at circumneutral pH is dominated by adsorption of the soluble Sr^{2+} ion to a range of solid phases as a reversible, outer sphere complex (Livens and Baxter, 1988; Sahai *et al.*, 2000; Carroll *et al.*, 2008; Wallace *et al.*, 2012; Fuller *et al.*, 2016). In general, Sr sorption increases with increasing negative surface charge of the substrate. As the pH exceeds the pH_{pzc} of the surface, a net negative surface charge results which has increased affinity for positively charged Sr^{2+}. At pH >12.5, Sr has been shown to form an inner sphere complex with clays, iron oxides and sediments (Wallace *et al.*, 2012; Fuller *et al.*, 2016). This change in behaviour is linked to the formation of the $Sr(OH)^+$ species in solution at pH >12 (Fuller *et al.*, 2016). Sr mobility is also affected by solubility at high pH. In the presence of carbonate, strontianite ($Sr(CO)_3$) may form (Busenberg, Plummer and Parker, 1984) and in the presence of silicate, strontium silicates have also been observed (Chorover *et al.*, 2003; Felmy *et al.*, 2003; Chang *et al.*, 2011). Sr is also known to readily substitute for calcium in calcite ($CaCO_3$) (Parkman *et al.*, 1998; Fujita *et al.*, 2004) and calcium silicate hydrate (C-S-H) cement phases (Tits *et al.*, 2006; Wieland *et al.*, 2008). C-S-H, a significant component of cement, was shown to uptake Sr via

bonding to silanol (Si-O-H) groups (Wieland *et al.*, 2008), highlighting Sr-silicate interactions in controlling radionuclide behaviour. The effect of hyperalkaline pH on sediments and Sr mobility has also been investigated (Choi *et al.*, 2006; Chorover *et al.*, 2008; Wallace *et al.*, 2013). For example, past work where sediments were reacted with cement leachate for 1 year resulted in Sr inner sphere bound to an aluminosilicate gel alteration phase after reaction at room temperature, and zeolite phases forming after reaction at 70 °C with Sr incorporated into the newly formed zeolite (Wallace *et al.*, 2013).

There have been several investigations into Sr uptake by colloids, including clay (Albarran *et al.*, 2011), silica (Bekhit *et al.*, 2006) and natural groundwater (Vilks and Baik, 2001) colloids. Here, Sr was sorbed to the colloidal matter and, as expected at circumneutral pH, the sorption was reversible in most cases suggesting outer sphere sorption dominated. Furthermore, in most cases the colloids did not significantly enhance the transport of Sr and retardation of Sr mobility occurred due to aggregation of colloidal particles which lead to precipitation of both the suspended phase and the sorbed Sr. There is a paucity of information on Sr-colloid interactions under the high pH conditions expected in both SNF ponds and intermediate level radioactive waste disposal. Previous Sr sorption studies at high pH suggests more varied Sr-substrate interactions such as inner sphere complexation to colloidal particles may occur (Wallace *et al.*, 2012; Fuller *et al.*, 2016).

In terms of Sr interactions with U phases, data is sparse. Sorption of Sr on to uranyl peroxide, studtite (UO_4), has a strong pH dependence, with greater sorption at higher pH and Sr sorption dominating at pH >10 (Sureda *et al.*, 2010). Sr has been shown to sorb strongly to substrates such as monosodium titanate ($NaHTiO_5$) in alkaline spent nuclear fuel storage (Hunt *et al.*, 2005). Additionally, amorphous substrates have been shown to have an elevated affinity for Sr compared to their more crystalline counterparts (Kirillov, Lisnycha and Pendelyuk, 2006). Sr can also bind to TiO_2 particles in SNF ponds, with EXAFS data fits suggesting evidence for some incorporation in the rutile (Bower *et al.*, 2016). These studies highlight the importance of understanding Sr sorption processes when predicting Sr mobility and speciation in SNF storage. The interaction of UO_2 with Sr has been well studied in the field of nuclear fuel due to the formation of ^{90}Sr in UO_2 fuel matrices during nuclear fission. SrO is known to form a solid

solution with UO_2 at high temperatures and pressures (Fujino, Yamashita and Tagawa, 1988; Perriot *et al.*, 2015) relevant to nuclear reactors and uraninite (UO_2) ores are known to contain high amounts of Ca^{2+} and other divalent cations, including Sr^{2+} (Ram *et al.*, 2013; Alexandre *et al.*, 2015). However there is scant research into the interactions of Sr with UO_2 under low temperature, aqueous conditions of spent nuclear fuel pond storage and management.

In this study, sorption of Sr onto well characterised nano-UO_2 and U(IV)-silicate colloids and precipitates (Dreissig *et al.*, 2011; Neill, Morris, Pearce, Sherriff, Burke, *et al.*, 2018), was investigated across a range of pH (4-12 and 4-14 respectively). Ultrafiltration using 1.5 nm and 220 nm filters was used to assess the extent of absorption to both colloidal and precipitated phases. TEM and desorption experiments were also used to analyse Sr-UO_2 interactions, while EXAFS was employed on selected samples to further probe the sorption mechanisms of Sr to these two key phases.

5.3. Methods

Triplicate experiments were carried out under a N_2/H_2 atmosphere with <20 ppm O_2, with solutions prepared from deoxygenated, deionized water (18 MΩ). Nano-particulate UO_2 was prepared by dilution of a U(IV)-carbonate solution (20 mM) in deionized water at a 1:19 ratio (Dreissig *et al.*, 2011; Neill, Morris, Pearce, Sherriff, Burke, *et al.*, 2018). This phase has previously been characterised as nanoparticulate UO_2 (Neill, Morris, Pearce, Sherriff, Burke, *et al.*, 2018). U(IV)-silicate samples were prepared by a 1:19 dilution of a 20 mM U(IV)-carbonate solution into 4.2 mM Na_2SiO_3 (Dreissig *et al.*, 2011; Neill, Morris, Pearce, Sherriff, Burke, *et al.*, 2018). The pH of the UO_2 and U(IV)-silicate samples was lowered to pH 4 by acid titration (1.5 M HCl) with stirring for 30 minutes to degas CO_2. The pH was then adjusted to target values (pH 4, 6, 8, 10, 12 and 14 for U(IV)-silicate experiments, 3.7, 6, 8, 10 and 12 for UO_2 experiments) with NaOH. The ionic strength of the experiments (pH 3.7-12) was controlled to 0.15 M by addition of NaCl. Experiments were equilibrated for 7 days with stable pH recorded throughout. 0.05 M $SrCl_2$ was spiked to yield a Sr concentration in solution of 0.058 mM. Samples were reacted for a further 7 days before analysis to ensure equilibrium.

Sr sorption to UO_2 and U(IV)-silicate phases was assessed using centrifugation-ultrafiltration at 8000 g for 12 mins using polyethersulfone (PES) filters (3 kDa, ~1.5 nm (Granath, 1958; Laurent and Granath, 1967; Dreissig *et al.*, 2011)) and filtration (0.22 µM, PES filters). Total U and Sr in the filtrates was measured by ICP-MS (Agilent 7500cx) and in the U(IV) silicate systems total silicon was measured using ICP-AES (Perkin-Elmer Optima 5300 dual view).

In an attempt to assess the nature of the binding of Sr to UO_2, acid leaching desorption experiments were performed on Sr sorbed to UO_2 at pH 12, 10, 8 and 3.7. After 7 days equilibration with Sr, the solution pH was decreased to 3.2 (± 0.1 pH unit) in all samples. Samples were filtered after 24 hours using centrifugation-filtration (3 kDa, 1.5 nm PES filters), and total Sr and U analysed in filtrates. The pH was then reduced to 2 and filtrations were repeated after a further 24 hours. Experiments were carried out in triplicate.

Transmission electron microscopy (TEM) samples for selected Sr/UO_2 experiments (pH 8 and 12) were mounted on carbon coated copper TEM grids (Agar Scientific) and imaged using an FEI TF30 analytical FEG TEM. For Sr XAS analysis, samples were centrifuged (7500g, 10 minutes) to isolate solids from solution and mounted in anaerobic cells. In U(IV)-silicate experiments at pH 6, 8 and 10, solid samples were collected by centrifugation-filtration on 3 kDa PES filters (Neill, Morris, Pearce, Sherriff, Burke, *et al.*, 2018). XAS samples had between 1,000 and 10,000 ppm Sr present on solids. Samples were analysed at Diamond Light Source B18 beamline, at the Sr k-edge using a Si (1 1 1) monochromator at liquid nitrogen temperature in fluorescence mode. The data were analysed using Demeter software package Athena and Artemis, FEFF6. Finally, thermodynamic modelling of speciation was performed using PHREEQC with the SIT database (see SI).

5.4. Results and discussion

5.4.1. U(IV) phases.

In UO_2 systems there was no evidence for colloidal uranium, with precipitates forming across the pH range (Figure 5.1 a,b). In U(IV)-silicate experiments, U (Figure 5.1 c,d) and Si (Figure S5.1) filtration data showed a strong correlation confirming that an intrinsic

uranium silicate phase was formed in all systems (pH 4 – 14). The molar Si/U ratio of these U(IV)-silicate phases, in the colloidal and/or precipitate fraction (>1.5 nm) was 2.1 at pH 4 and increased to 2.4 at pH 6. The ratio then stabilised at 2.4 from pH 6 to 10 and dropped to 1.8 at pH 12 and 0.8 at pH 14 (Figure S5.2). Stable colloidal U(IV)-silicates were formed between pH 6 and 10, coinciding with the highest Si/U ratios. A small fraction of truly dissolved uranium (<3 kDa fraction) occurred between pH 6 and 10 for both the U(IV) silicate and UO_2 systems and similar to past observations (Dreissig *et al.*, 2011; Neill, Morris, Pearce, Sherriff, Burke, *et al.*, 2018) Overall, these observations are consistent with past work (Neill, Morris, Pearce, Sherriff and Shaw, 2018)confirming that pH adjustment to pH 4 to facilitate CO_2 degassing in experiments had no significant effect on the colloidal behaviour and composition of these phases.

5.4.2. Sr/UO_2 filtration and desorption investigations

Sr was sorbed to UO_2 across pH 4-12 with sorption increasing with increasing pH (Figure 5.1 a,b). At pH 3.7, only 7 % of Sr was removed from solution (to the >220 nm fraction), this increased to 24 % at pH 6. At pH 8, 93 % of Sr was sorbed, increasing to 99 % at pH 10 and >99 % at pH 12. There was no evidence for colloidal Sr (1.5-220 nm) in any of the UO_2 experiments, consistent with Sr being sorbed to the UO_2 precipitate.

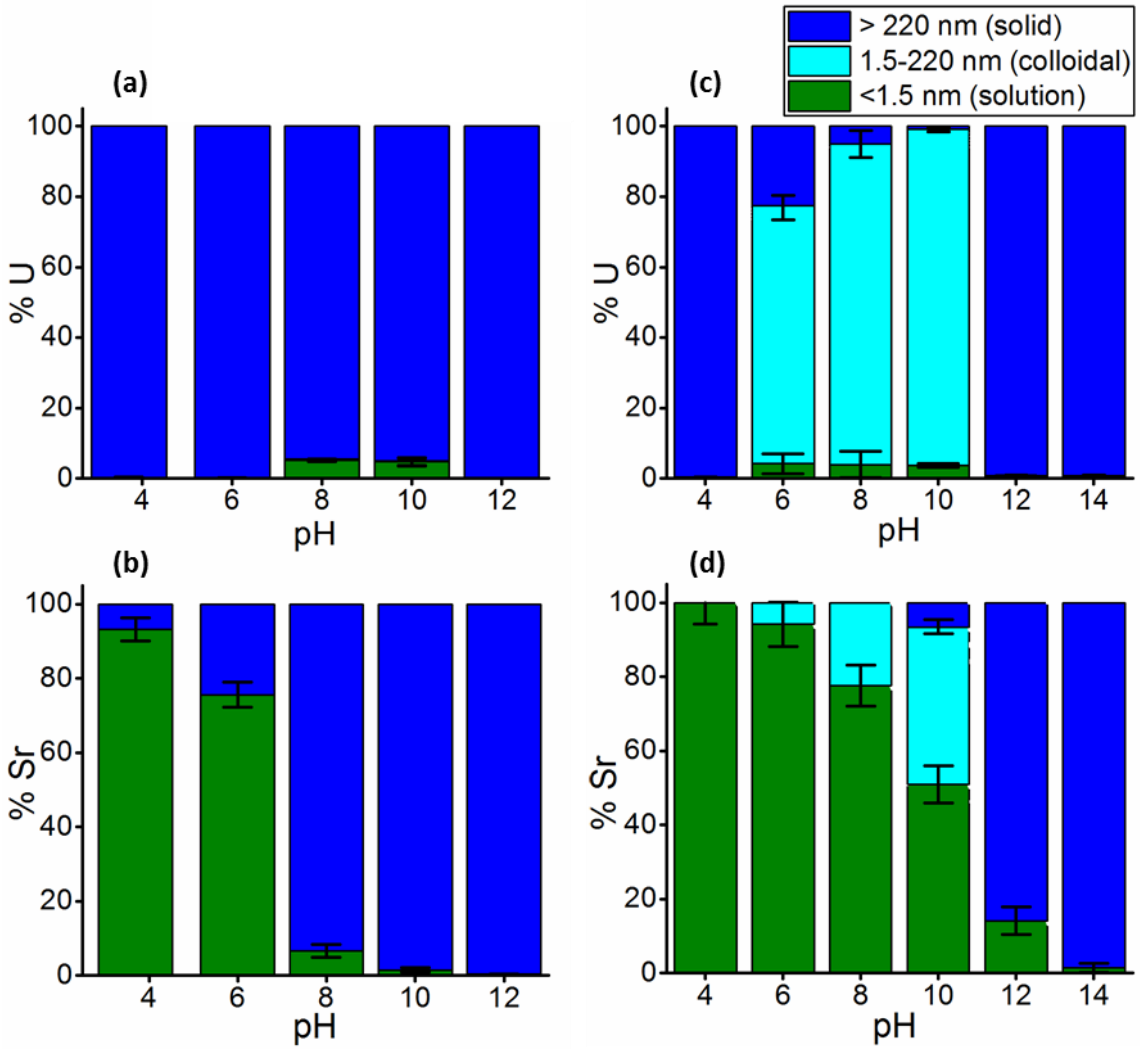

Figure 5.1: Filtration results for UO2 experiments showing size distribution of uranium species (a) and strontium (b) and U(IV)-silicate experiments showing size distribution of uranium species (c) and strontium (d) . Species below 1.5 nm in size are assumed to be in true solution, 1.5-220 nm colloidal and > 220 nm are sedimented (solid).

A significant fraction of the Sr was removed from solution in the presence of UO_2. A higher degree of Sr removal from solution was seen for UO_2 systems compared to U(IV)-silicate systems of the same pH, indicating that Sr has a strong affinity for UO_2 particles (Figure S3). The increasing Sr removal from solution with increasing pH can be explained in part by the surface charge of the UO_2. As Sr speciation is dominated by the hydrated Sr^{2+} ion at pH <12, then at pH below pH_{pzc} of UO_2, sorption will be low as electrostatic repulsion occurs. UO_2 has a pH_{pzc} of 5.8 (Husain, 1984) so would be positively charged at pH <6. With increasing pH, the UO_2 surface becomes more negative, increasing the affinity for the positively charged Sr^{2+} ion. While the trend for increasing sorption at higher pH is anticipated, the magnitude of Sr sorption onto UO_2 in this study is much higher at pH 8 and 10 than seen in previous studies on Sr sorption to U(VI)-peroxide

(Sureda *et al.*, 2010), CSH (Wieland *et al.*, 2008) and Fe(III)oxyhydroxides, clays, and sediments (Fuller *et al.*, 2016). Indeed, when the distribution coefficient (K_d) is compared to values for U(IV)-silicate, and other substrates (Wieland *et al.*, 2008; Sureda *et al.*, 2010; Fuller *et al.*, 2016), Sr shows a significantly higher solid partitioning in the presence of UO_2 than these other substrates (Figure S5.4).

Acid leaching, desorption experiments were carried out on pH 3.7, 8, 10 and 12 Sr-UO_2 systems (Figure S5.5). The pH of 3.2 was selected for initial desorption to target surface-bound Sr, however Sr incorporated into crystalline UO_2 would be expected remain in the solid phase at this pH as UO_2 solubility is very low. Data from pH 3.2 desorption step showed no evidence for an irreversibly bound Sr fraction; essentially all of the Sr was re-released under 24 h pH 3.2 leaching conditions for all starting pH and there were no variations in Sr release from experiments of different starting pH. At this pH, <0.5 % of U was in solution in all systems, confirming that there was minimal dissolution of the UO_2. This suggests that Sr was labile in all systems, likely concentrated at the near surface of the particles and not incorporated into the nano-crystalline UO_2 particles where it would be significantly occluded.

5.4.3. Sr/UO_2 interaction mechanisms

TEM imaging and energy dispersive X-ray (EDX) spectroscopy (Figure 5.2) confirmed that the Sr was co-located with UO_2 aggregates at pH 8 and 12 and the UO_2 morphology was consistent with past work (Newsome, Morris and Lloyd, 2015; Neill, Morris, Pearce, Sherriff, Burke, *et al.*, 2018). Selected area electron diffraction (SAED) analyses confirmed the presence of UO_2 (Figure S5.6). In both samples there was no evidence for discrete, Sr rich phases.

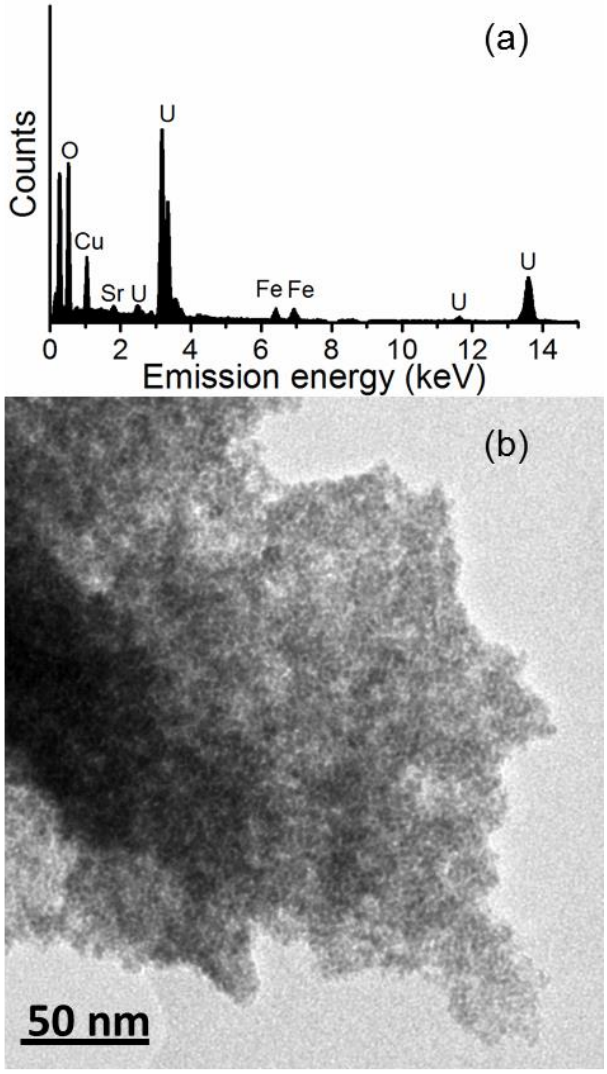

Figure 5.2: TEM image of UO2 particles formed at pH 12 with Sr associated (a), EDX spectrum showing colocation of Sr and U (b) (Fe peaks are background features from the instrument).

Sr K-edge EXAFS were analysed for the UO_2 systems at pH 8, 10 and 12. The EXAFS and Fourier transforms are shown in Figure 5.3, with fitting details presented in Table 5.1. For all three samples there was evidence for significant order in the samples with features in the Fourier transform at 3.5-4 Å. This is different to past work on Sr sorption behaviour with other substrates where, typically, outer sphere sorption dominates at pH ≤ 12 and no peaks in the Fourier transformed Sr K-edge EXAFS are observed at > 2.5 Å (Sahai *et al.*, 2000; Carroll *et al.*, 2008; Wallace *et al.*, 2012; Fuller *et al.*, 2016). At pH, 8, the EXAFS were best fit with 9 O backscatterers at 2.63 Å. In addition, the fit was improved by inclusion of a second shell of 1.5 U backscatterers at 3.67 Å. The presence of this second coordination shell, and the fact that this shell can be fit with U

backscatterers suggests Sr is sorbed as an inner sphere complex onto the UO_2 surface. At pH 10, the EXAFS could also be fitted with 9 O backscatterers in the first shell. However the fit was improved by splitting the O shell resulting in 2 Sr-O distances of 2.58 and 2.72 Å, with coordination numbers of 7.2 and 3.8 respectively. Fitting for the pH 12 system was also improved by splitting the O shell, with Sr-O distances of 2.58 and 2.74 Å and coordination numbers of 7 and 4 respectively. Furthermore, there was a clear increase in the coordination numbers for the U backscatterers at 3.66±0.01 with increasing pH from 1.5 to 1.8 and 3.5 backscatterers at pH 8, 10 and 12 respectively. This was indicative of a more structured local coordination environment for Sr occurring with increasing pH. While the pH 8 EXAFS suggested an inner sphere complex was forming, the split O shell in the pH 10 and 12 EXAFS fits, along with the high U coordination at 3.66±0.01 Å clearly indicated that an alternative structure, likely due to incorporation or surface precipitation of a Sr-U-oxide was occurring in these systems. The splitting of the O shell, and increase U coordination at pH 10 and 12 represent a structured Sr environment which is not representative of Sr incorporated into UO_2 via substitution into the U^{4+} sites. 8 coordinate Sr would be expected for incorporated Sr with Sr-O distances in the region of 2.38 Å which is not the case (Barrett *et al.*, 1982). Additionally, the Sr-U bond distance was consistently ~ 3.66 ± 0.01 Å for all samples, which is significantly shorter than the U-U distance in uraninite (3.87 Å, (Barrett *et al.*, 1982)). As Sr^{2+} has a larger atomic radius than U^{4+}, this would not be expected for Sr-substituted UO_2. This is supported by desorption results, which indicate reversible Sr sorption in these experiments that is not consistent with wholly incorporated Sr. Therefore, Sr is most likely to in a highly ordered inner sphere complex, surface incorporated or surface precipitated at pH 10-12.

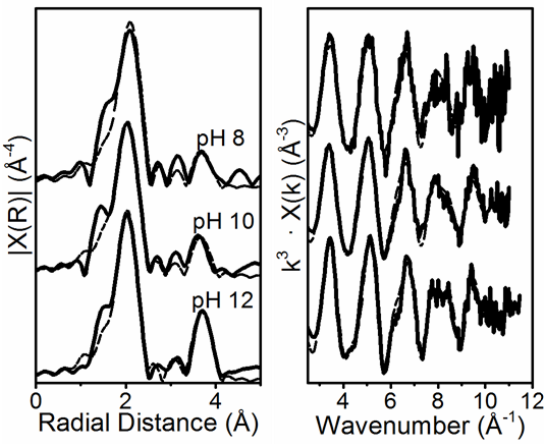

Figure 5.3: Sr k-edge EXAFS (right) and Fourier transforms (left) for Sr bound to UO2 at pH 8, 10 and 12. The feature at 3.8 Å in the Fourier transform clearly suggests Sr is not outer sphere bound and is instead in a more structured coordination environment.

Table 5.1: EXAFS fit data for Sr-UO_2 systems

Sample	Path	N	R (Å)	σ^2	ΔE_0	R
pH 8	**Sr-O**	9	2.63(1)	0.009(1)	4.2(11)	0.023
	Sr-U	1.5	3.67(3)	0.009(4)		
pH 10	**Sr-O.1**	7.2	2.58(1)	0.008(2)	-2.6(10)	0.0078
	Sr-O.2	3.8	2.72(1)	0.009(5)		
	Sr-U	1.75	3.65(3)	0.010(2)		
pH 12	**Sr-O.1**	7	2.58(1)	0.006(1)	4.2(8)	0.0092
	Sr-O.2	4	2.74(3)	0.008(4)		
	Sr-U	3.8	3.66(2)	0.011(2)		

Coordination numbers (N), U bond distances (R (Å)), Debye-Waller factors (σ^2), shift in energy from calculated Fermi level (ΔE_0) and 'goodness of fit' factor (R). Coordination numbers were fixed, amplitude factors were fixed as 1. Numbers in parentheses are the standard deviation on the last decimal place.

Sr-U-oxides have been formed previously at high temperatures; however there is little evidence of their formation under ambient temperatures. Mixed Sr-U-oxides have been observed at T >1,000 K as either a Sr substituted into U sites in UO_2 (Fujino, Yamashita and Tagawa, 1988; Perriot *et al.*, 2015), or formation of a Perovskite $SrUO_3$ structure (Ball, 1992; Cordfunke *et al.*, 1997). Further support for the formation of tertiary Sr,U oxide is found in a study which formed a mixture of $SrUO_3$ and UO_2 under high temperature conditions (Huang *et al.*, 1997). Several studies have shown negligible differences in the thermodynamics of formation of $SrUO_3$ compared to the binary oxides UO_2 and SrO, suggesting $SrUO_3$ formation is possible and perhaps favoured in the presence of an excess of UO_2 (Grenthe *et al.*, 1992; Fuger, Haire and Peterson, 1993;

Cordfunke and Ijdo, 1994; Guillaumont *et al.*, 2003). Additionally, in the current study, the high surface area of the UO_2 may promote Sr reactions on the UO_2 surface. The split shell and high coordination number of O in the EXAFS fitting indicate that the Sr coordination environment is perovskite-like (Ahtee *et al.*, 1976; Yamanaka, Hirai and Komatsu, 2002). The coordination environment and number is consistent with the Sr coordination environment within $Ca_{1-x}Sr_xTiO_3$, where 12 O atoms are in the first coordination shell (Yamanaka, Hirai and Komatsu, 2002). Furthermore, the Sr-U distance of 3.66±0.01 Å is also consistent with a perovskite-like structure and significantly different to the U backscatterer expected in UO_2. The Sr-Ti distance in analogous $SrTiO_3$ is 3.36 Å (Yamanaka, Hirai and Komatsu, 2002)and Sr-Zr distances in $SrZrO_3$ at room temperature average 3.5 Å (Ahtee *et al.*, 1976). Given the relative ionic radii follow the trend $U^{4+} > Zr^{4+} > Ti^{4+}$, the Sr-U distance of 3.67 Å observed here seems credible for a $SrUO_3$-like environment. However, EXAFS fitting shows reduced Sr-U coordination numbers compared to those expected if the Sr was in a crystalline Sr-U-oxide, suggesting that a separate, crystalline $SrUO_3$ phase is unlikely (Sr-Ti coordination in a comparable structure, $SrTiO_3$, is 8 (Yamanaka, Hirai and Komatsu, 2002)). Additionally, Sr-Sr coordination which would be expected in a Sr-U-oxide phase was not observed in the EXAFS fitting. TEM imaging and SAED analysis also showed no indication of an intrinsic Sr-U-oxide, with Sr apparently associated with nanoparticulate UO_2.

Considering the evidence discussed above, the low solubility of UO_2 under these conditions and the high surface area of the UO_2, the most likely explanation is surface incorporation of Sr on UO_2, resulting in a perovskite-like Sr coordination environment at the UO_2 surface. This is consistent with the EXAFS fitting, which showed Sr-U coordination across pH 8-12, TEM showing Sr was co-located with UO_2 and desorption experiments indicating Sr is labile even after exposure to UO_2 at high pH. Given the clear trend in the EXAFS with pH, this Sr surface reaction appears to be pH dependent, with Sr in a less structured inner sphere complex at pH 8, and in a more structured environment at pH 12. This explains why, despite the high Sr-U coordination in the EXAFS for the pH 12 system, Sr is still labile under acid leaching, as this Sr-UO_2 reaction is highly pH dependent and the significant decrease in pH during acid leaching would dissolve the surface phase. As only ~1 % Sr by weight was sorbed to the UO_2 particles, the Sr would be unlikely to significantly alter the bulk structure of UO_2 because Sr

complexation would occur in the poorly order near-surface region of the UO_2. This would allow for this alternative Sr coordination environment and the consequent disorder generated without inducing strain on a crystalline lattice. Furthermore as Sr loading is likely to be low, compared to the amount of near surface U available, this would also explain that the lack of a Sr-Sr backscatter.

5.4.4. Sr/U(IV)-silicate interactions

In the U(IV)-silicate systems, the removal of Sr from solution again increased with increasing pH (Figure 5.1 c,d). No Sr removal was observed at pH 4. At pH 6, 6% of Sr was in the colloidal size fraction, which increased to 22 % at pH 8. At pH 10, 43 % of Sr was in the colloidal size fraction, with 5 % in the >220 nm fraction. At pH 12, 86 % of Sr was associated in the > 220 nm fraction and, at pH 14, 99 % of Sr was in the >220 nm fraction. At pH 4, 12 and 14, where no colloidal U was present, no Sr was associated with colloidal size fraction. When U was colloidal between pH 6 and 10, the majority of non-solution (>1.5 nm) Sr was associated with the colloidal phase. No colloidal Sr was observed when there was no colloidal U, confirming Sr was associated with the U(IV)-silicate colloid.

Sr removal from solution increased with increasing pH, as observed in the UO_2 system. At pH ≤10, this can be attributed to an increasing negative surface charge of the U(IV)-silicate at pH 4-10; U(IV)-silicate particles, with a pH_{pzc} approximately pH 4-4.5 will have a positive charge at low pH which becomes negative at $pH>pH_{pzc}$ (Dreissig *et al.*, 2011). The presence of colloidal Sr and U(IV) at pH 6-10 suggests that U(IV)-silicate colloids could also be important vectors for Sr. Indeed, up to 43% Sr association with colloidal material occurred at pH 10 (equivalent to 0.025 mM suspended Sr). Although the extent of Sr removal from solution increases at pH >10, the Sr was not colloidal meaning the mobility of Sr at pH >10 is reduced by interactions with U(IV)-silicate. These results highlight U(IV)-silicate as both a colloidal vector for Sr at pH 6-10, and at pH > 10 a potential sink for Sr.

5.4.5. Sr/U(IV)-silicate interaction mechanisms

Sr EXAFS of the U(IV)-silicate systems (pH 6, 8, 10, 12 and 14) are shown with corresponding best fits in Figure 5.4, and Table 5.2. Throughout, the first shell was fitted

with 9 oxygen atoms at 2.61 Å. At pH 6, 8 and 10 no additional backscatterers improved the fit confirming outer sphere sorption dominated, similar to past work on a range of environmental matrices at circumneutral pH (Sahai *et al.*, 2000; Carroll *et al.*, 2008; Wallace *et al.*, 2012; Fuller *et al.*, 2016). It is also in agreement with studies into colloidal transport of Sr which showed Sr to be reversibly bound to colloidal particles at circumneutral pH (Vilks and Baik, 2001; Bekhit *et al.*, 2006; Albarran *et al.*, 2011). Overall, this suggests at pH <10 the Sr bound to colloidal U(IV)-silicates is likely to be labile.

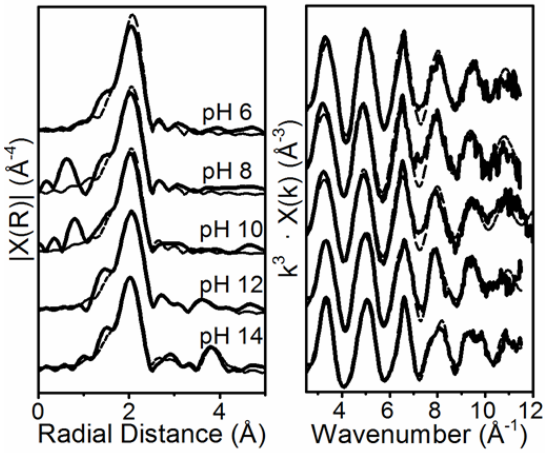

Figure 5.4: Sr k-edge EXAFS (right) with accompanying Fourier transforms (left) for Sr bound to U(IV)-silicate at pH 6-14. Features at R+ΔR > 2.3 Å in the Fourier transforms indicates inner sphere sorption and incorporation at pH >10.

Table 5.2: EXAFS fit data for Sr-U(IV)Silicate systems

Sample	Path	N	R (Å)	σ^2	ΔE_0	R
pH 6	**Sr-O**	9	2.61(1)	0.008(1)	0.7(10)	0.024
pH 8	**Sr-O**	9	2.61(1)	0.008(1)	-2.3(13)	0.011
pH 10	**Sr-O**	9	2.61(1)	0.009(1)	-2.3(11)	0.013
pH 12	**Sr-O**	9	2.61(0)	0.009(2)	-2.2(3)	0.0018
	Sr-Si	0.8	3.26(2)	0.009(2)		
	Sr-Sr	2	4.16(1)	0.012(2)		
pH 14	**Sr-O**	9	2.60(0)	0.010(1)	-2.8(11)	0.013
	Sr-Si.1	1.8	3.26(4)	0.014(6)[a]		
	Sr-Si.2	1.7	3.96(8)	0.014(6)[a]		
	Sr-Sr	4.5	4.28(3)	0.012(3)		
$SrSiO_3$	**Sr-O***	8	2.65			
	Sr-Si.1	4	3.34			
	Sr-Si.2	2	3.87			

Sr-Sr*	6	4.12

Coordination numbers (N), U bond distances (R (Å)), Debye-Waller factors (σ^2), shift in energy from calculated Fermi level (ΔE_0) and 'goodness of fit' factor (R). Coordination numbers were fixed, amplitude factors were fixed as 1. Numbers in parentheses are the standard deviation on the last decimal place. [a] indicates tied Debeye-Waller factors, *indicates weighted average of similar paths. $SrSiO_3$ structure from (Nishi, 1997).

At pH 12 and 14, features at >2.3 Å in the Fourier transforms were present suggesting Sr was in a more structured coordination environment. There was no evidence for $SrCO_3$ in the EXAFS confirming that CO_2 ingress was minimal as expected. Therefore the most likely scenarios were either strong inner sphere sorption to the U(IV)-silicate particles, or formation of an intrinsic Sr silicate phase e.g. $SrSiO_3$. While the pH 12 system could be fitted with Si and U shells (Table S5.2), suggesting the possibility of inner sphere sorption/incorporation of Sr into U(IV)-silicate particles similar to the surface precipitation observed for UO_2, a statistically improved fit (with lower R-factor) was achieved fitting to a Sr silicate structure. The structure here appeared to be disordered, with low coordination numbers of 0.8 bidentate bound (edge sharing) Si at 3.26 Å and 2 Sr backscatterers at 4.16 Å, distances characteristic of $SrSiO_3$. At pH 14, Sr silicate structure also provided the best fit. Here, a total of 3.5 Si backscatterers, 1.8 bidentate Si at 3.26 Å and 1.7 monodentate (corner sharing) Si at 3.96 Å, and 4.5 Sr backscatterers at 4.28 Å were fit. These are similar to distances recorded for edge-and corner-sharing SiO_4 polyhedra respectively in $SrSiO_3$ (Nishi, 1997). Although the Sr-Sr distance in the pH 14 fit was longer than the average Sr-Sr distance of 4.12 Å in $SrSiO_3$ (Table 2), it is similar to the most distant Sr backscatterer at 4.30 Å (Table S5.1). Coordination numbers for the Sr and Si backscatterers are much lower in the pH 12 fit, compared to the pH 14 fit. This could be due to Sr being partitioned between a Sr silicate phase and outer sphere complex observed in the lower pH systems. Alternatively, the Sr silicate phase formed at pH 12 may be poorly ordered compared to the phase formed at pH 14.

The possibility of a Sr-silicate phase forming is supported by previous investigations that have confirmed the formation of Sr-silicates at high pH (Felmy *et al.*, 2003) and how Sr mobility and solubility is greatly reduced in the presence of silicate (Chang *et al.*, 2011). These EXAFS results are also supported by thermodynamic modelling of the U(IV)-silicate/Sr system (Figure S5.7). At pH >11, modelling shows the solution becoming oversaturated with respect to $SrSiO_3$, which supports the presented EXAFS data indicating the formation of a Sr silicate phase at pH 12 and 14. These results indicate

that silicate is likely to be an important factor in Sr mobility in high pH systems. While outer sphere sorption to U(IV)-silicates is important at pH <10, and is particularly relevant at pH 6-10 where U(IV)-silicate colloids form, at high pH where U(IV)-silicate colloids do not form, Sr-silicate formation, potentially aided by the presence of U(IV)-silicate particles, resulted in reduced Sr mobility.

5.5. Conclusions

Here we show two key U(IV) phases demonstrate elevated Sr sorption under the pH conditions relevant to SNF storage, contaminated land scenarios and radioactive waste disposal where radioactive ^{90}Sr and U will coexist. A combination of ultrafiltration, TEM and EXAFS analysis has demonstrated the capacity for these U(IV) phases to sorb Sr and also provided insights into the mechanism of Sr removal from solution. The high capacity for sorption to UO_2 and the formation of Sr-silicates suggests these phases will be key factors in controlling Sr mobility.

As legacy spent fuel storage ponds at Sellafield are maintained at approximately pH 11 (Maher *et al.*, 2016), it would be expected that a large amount of the Sr in these systems would be bound to any U(IV) phases present. Significantly, at this pH, U(IV)-silicate is potentially colloidal suggesting any associated Sr may be subject to enhanced mobility. It is therefore essential to understand the binding mechanism and reversibility of Sr to these phases to be able to predict the behaviour of these systems during effluent treatment processes. While colloidal U(IV)-silicate sorbed Sr as an outer sphere complex at a relatively high capacity, Sr silicates formed at pH ≥12 and incorporation occurred for Sr with UO_2. Although UO_2 did not form a colloid under the conditions of this study, previous work has indicated that UO_2-based particles are capable of forming a colloid at moderately alkaline pH in the presence of silicate(Kaminski *et al.*, 2005). As silicate may play a role in this colloidal stabilisation, and U(IV)-silicate colloids can form at alkaline pH, it is important to understand the impact of both UO_2 and U(IV)-silicates on Sr behaviour to predict Sr mobility in spent nuclear fuel and other scenarios where Sr and U are both present. Desorption experiments suggested that the Sr is still labile after incorporation into UO_2, but it is not known whether Sr would be removed from UO_2 by effluent treatment processes that exist at sites such as Sellafield. Further work is

ongoing investigating the impact of effluent treatment processes on U(IV) phases and their ability to transport Sr.

Supporting Information:Interactions of Sr with UO_2 and U(IV)-silicate phases

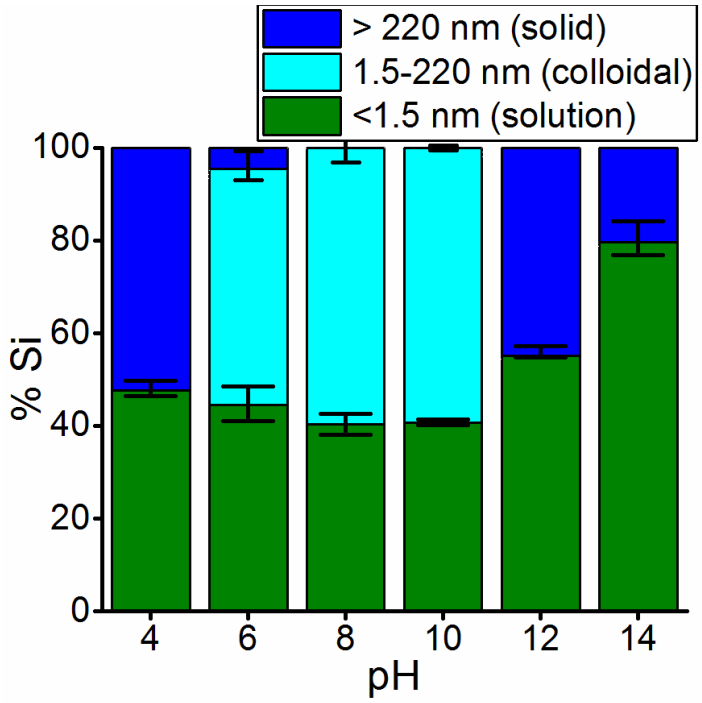

Figure S5.1: Filtration results for U(IV)-silicate experiments showing the size distribution of silicon. Species below 1.5 nm in size are assumed to be in solution, 1.5-220 nm colloidal and > 220 nm are sedimented.

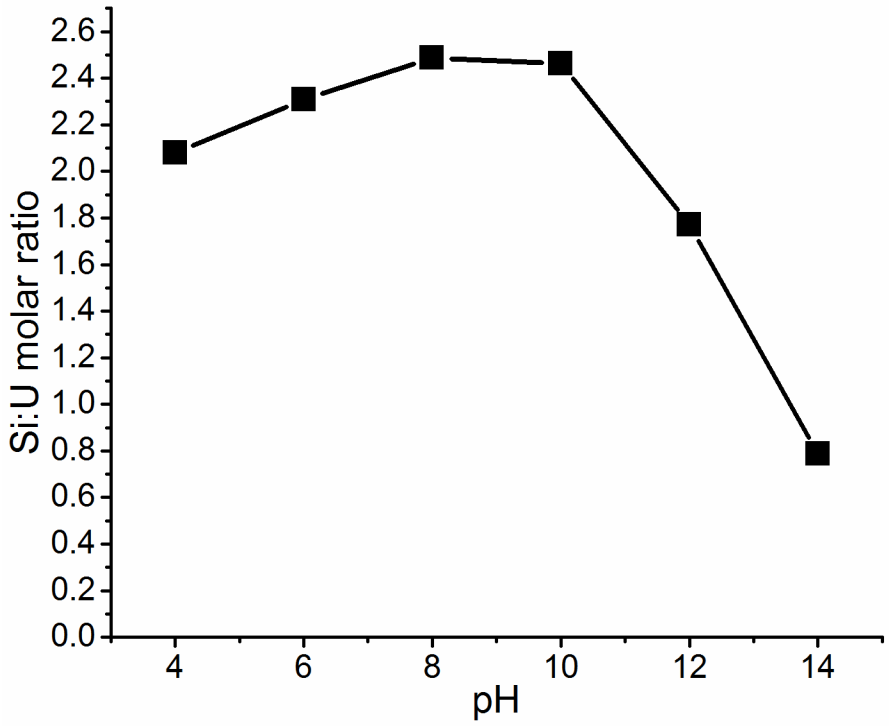

Figure S5.2: Si:U molar ratio taken from particulates >1.5 nm. Figure shows increasing Si:U ratio at low pH, followed by subsequent decline in Si:U ratio at pH >8.

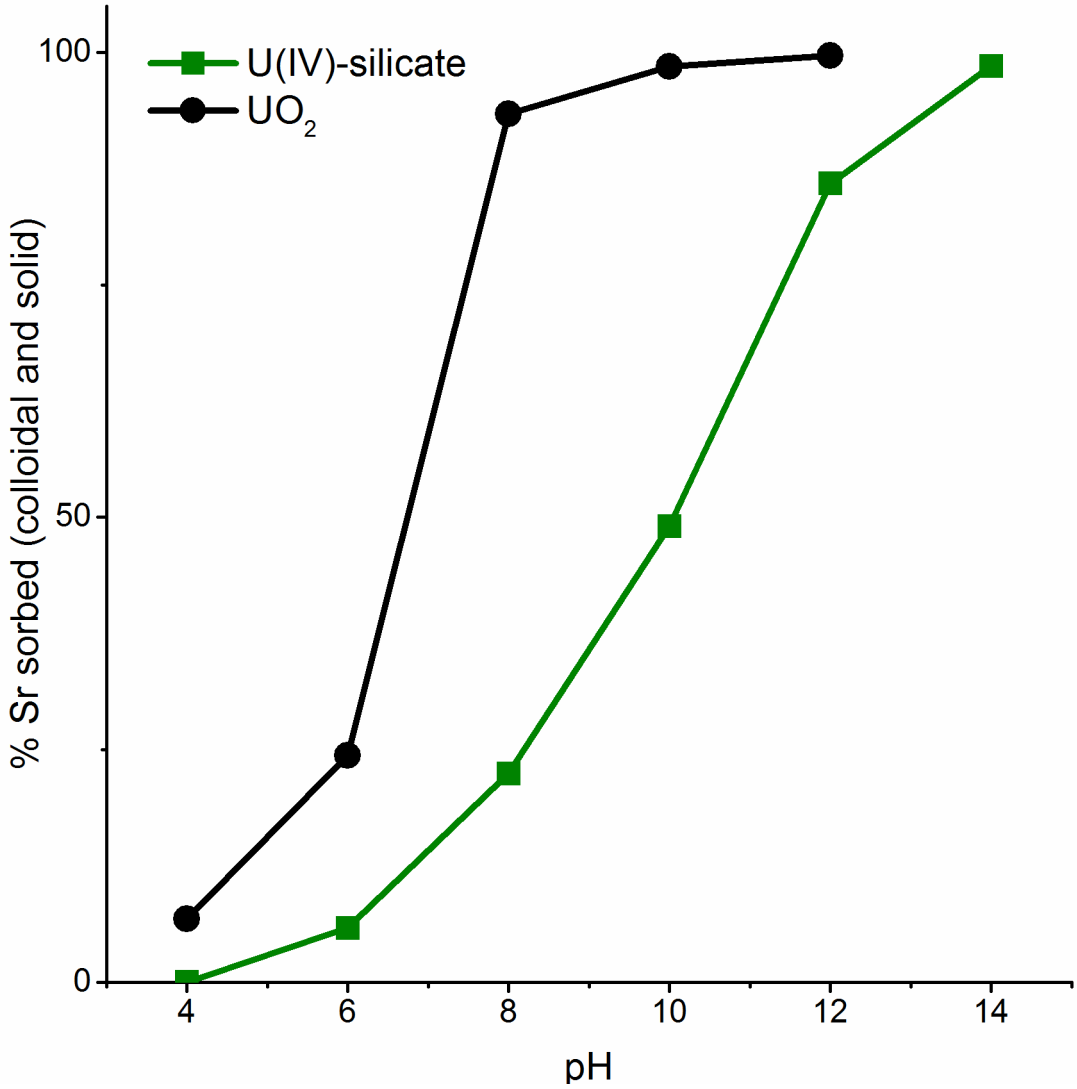

Figure S5.3: Comparison of the sorption of Sr in UO_2 and U(IV)-silicate systems showing higher sorption of Sr, at a lower pH, on UO_2.

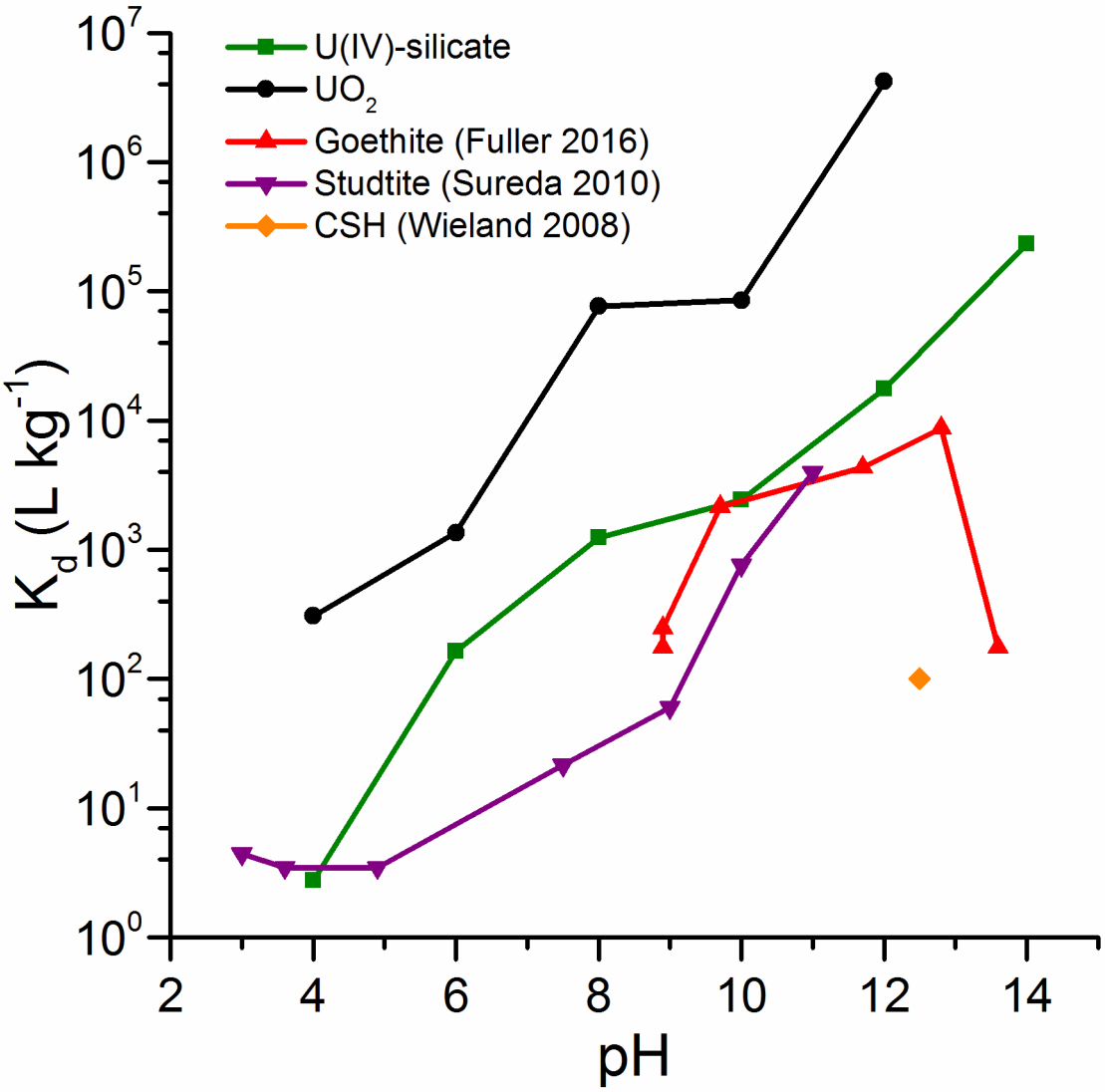

Figure S5.4: A comparison of dissociation constants (Kd) for Sr on U(IV)-silicate, UO_2 (both from this study), Goethite (Fuller *et al. (*2016)), Studtite (Sureda *et al.* (2010)) and CSH (Wieland *et al*. (2008)).

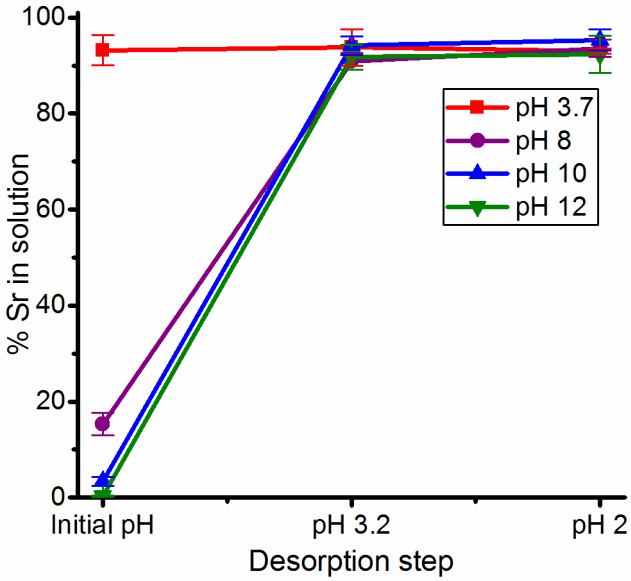

Figure S5.5: Results from Sr-UO_2 desorption experiments carried out at starting pH 3.7, 8, 10 and 12. In desorption experiments, the pH was reduced to 3.2 for 24 hours and the true solution (< 1.5 nm) sampled, and then pH 2 for a further 24 hours and the true solution re-sampled to investigate the lability of Sr sorbed to UO_2.

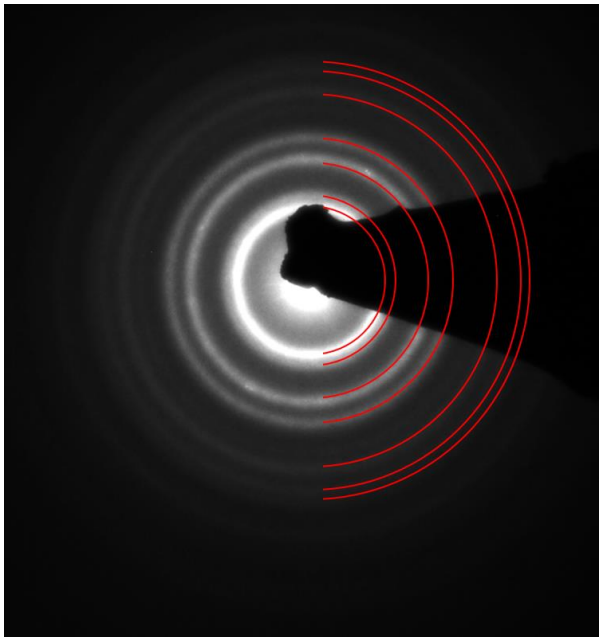

Figure S5.6: Selected area electron diffraction (SAED) of UO_2 particles formed at pH 12, with Sr incorporated. Red rings represent diffraction rings expected for UO_2.

S5.1. Thermodynamic modelling

Thermodynamic modelling was performed using the PHREEQC software package and the specific ion theory (SIT) database.

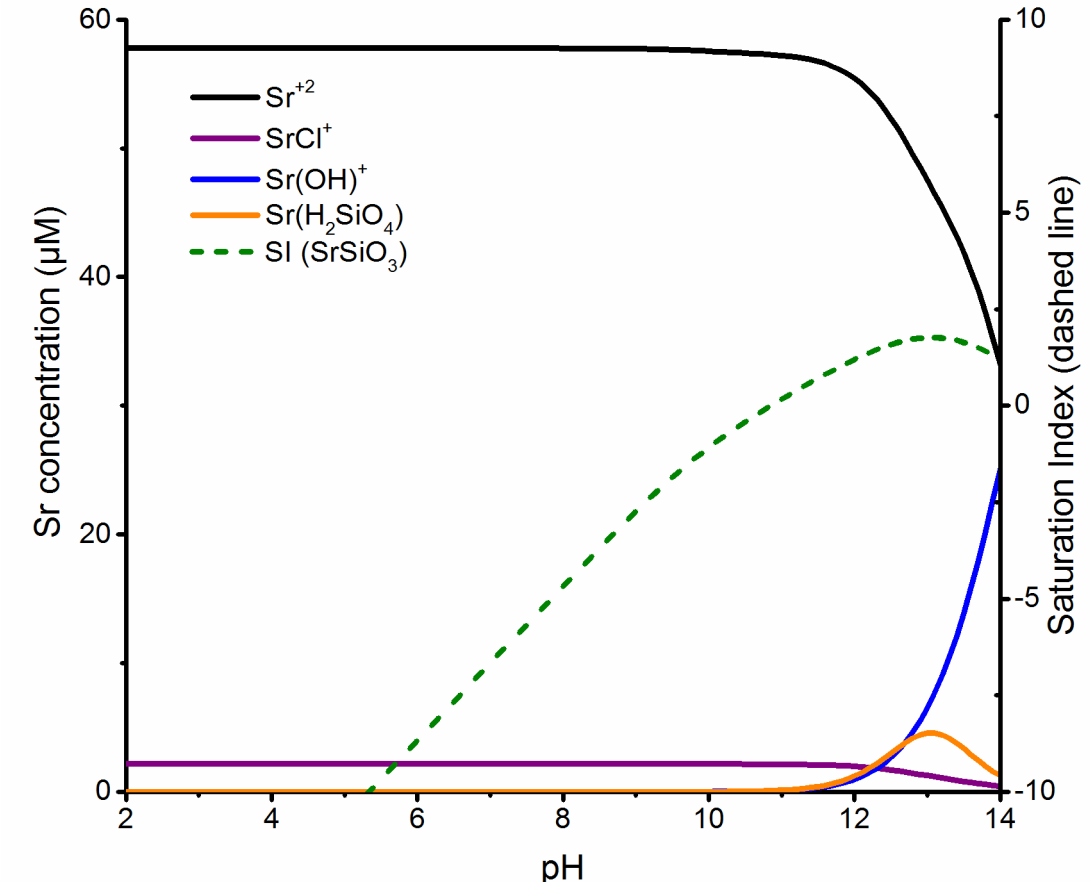

Figure S5.7: Thermodynamic modelling of Sr speciation and saturation index of strontium metasilicate, $SrSiO_3$, indicating that Sr is oversaturated at pH 12 and 14 wrt $SrSiO_3$.

S5.2. EXAFS fitting

Table S5.1: Full list of first shell Sr-O, Sr-Si and Sr-Sr interatomic distances for $SrSiO_3$ (Nishi, 1997)

Path	N	R(Å)
Sr-O.1	2	2.46
Sr-O.2	4	2.69
Sr-O.3	2	2.74
Sr-Si.1	4	3.34
Sr-Si.2	2	3.87
Sr-Sr.1	2	4.02
Sr-Sr.2	1	4.05
Sr-Sr.3	2	4.16
Sr-Sr.4	1	4.30

Table S5.2: EXAFS fits for Sr/U(IV)-silicate system at pH 12 and pH 14 showing fits to Sr-U-Si coordination environment. In both cases, R value (goodness of fit) is significantly higher that for Sr-silicate fitting (Table 2), indicating lower quality of fit.

Sample	Path	N	R (Å)	σ^2	ΔE_0	R
pH 12	**Sr-O**	9	2.61(1)	0.009(5)	0.5 (7)	0.0088
	Sr-Si	1.8	3.59(5)	0.013(7)		
	Sr-U	1.8	3.75(4)	0.012(5)		
pH 14	**Sr-O**	9	2.60(1)	0.010(1)	0.4(10)	0.027
	Sr-Si	1.8	3.46(3)	0.012(5)		
	Sr-U	1.7	3.64(4)	0.015(5)		

Coordination numbers (N), U bond distances (R (Å)), Debye-Waller factors (σ^2), shift in energy from calculated Fermi level (ΔE_0) and 'goodness of fit' factor (R). Coordination numbers were fixed, amplitude factors were fixed as 1. Numbers in parentheses are the standard deviation on the last decimal place.

Chapter 6: Impact of carbonation on U(IV)-silicate particle stability and capacity for Sr sorption relevant to effluent treatment.

Thomas S. Neill[a], Katherine Morris[a], Carolyn I. Pearce[b], Nicholas K Sherriff[c], and Samuel Shaw[a]*

[a]Research Centre for Radwaste Disposal and Williamson Research Centre, School of Earth & Environmental Scineces, The University of Manchester, Oxford Road, Manchester M13 9PL, UK

[b]Pacific Northwest National Laboratory, Richland, WA 99354, USA

[c]National Nuclear Laboratory, Chadwick House, Warrington Road, Birchwood Park, Warrington WA3 6AE, UK

*Corresponding author: sam.shaw@manchester.ac.uk

6.1. Abstract

Understanding the speciation and mobility of radionuclides derived from spent nuclear fuel during waste retrieval in legacy fuel pond facilities and effluent treatment at Sellafield, UK, is essential for safe and efficient decommissioning of the site. Furthermore, the effects of effluent treatment processes on colloids will define any potential for colloidal mobilisation of radionuclides in effluents. Here, we present investigations into the impact of CO_2 gassing, a step in effluent treatment at Sellafield, on the stability of U(IV)-silicate nanoparticles and their potential to transport strontium. U(IV)-silicate nanoparticles were prepared at pH 11.4 and exposed to CO_2 gas via bubbling to reduce the pH to 7, mimicking the site carbonation process. Ultrafiltration of the solution and X-ray absorption spectroscopy on the solids was carried out at selected time points throughout the carbonation treatment. Prior to carbonation, U(IV)-silicate was not colloidal but present as sedimented aggregates, with Sr largely sorbed to this phase. Results indicate little immediate impact of carbonation on the U(IV)-silicate particle size, but after 24 h, U was partitioned to both colloidal and dissolved fractions. After 8 days, a U(IV)-silicate structure was maintained but minor structural

differences compared to the initial U(IV)-silicate were evident. During carbonation, >70 % Sr immediately desorbed from the solid phase however 11 % Sr was still associated with U(IV)-silicate colloids after 8 days. Overall, carbonation increased the mobility of the U(IV)-silicate aggregate and caused significant desorption of Sr. Results indicate that the presence of U(IV)-silicate colloids may be critical controls on the mobility of U and Sr in effluent treatment.

6.2. Introduction

The UK has a significant amount of high and intermediate level radioactive waste from a combination of weapons production, energy production and research spanning over 70 years (NDA, 2017b). A large proportion of this waste has been stored and reprocessed at the Sellafield site in Cumbria, UK. In certain legacy facilities at Sellafield, spent nuclear fuel (SNF) elements have undergone corrosion due to extended residencies in interim SNF storage ponds. Within legacy ponds containing spent Magnox fuel, this had led to the formation of corroded Magnox sludge (CMS), comprising of corroded Magnox fuel cladding (an Mg-rich alloy), corroded metallic uranium (U), transuranics and fission products which are stored in alkaline conditions (pH >11) (Wilson, 1996; Parry *et al.*, 2011; Maher *et al.*, 2016). These facilities represent serious hazards and are subject to accelerated decommissioning in order to reduce the risk they pose at the site (Sellafield Ltd, 2017). While efforts have been made to characterise CMS (Gregson, Goddard, *et al.*, 2011; Gregson, Hastings, *et al.*, 2011; van Veelen *et al.*, 2012; Maher *et al.*, 2016), the complex matrix of materials stored in the ponds has resulted in a wide range of different corrosion and precipitation products. These include Mg-based minerals such as brucite ($Mg(OH)_2$), Mg-carbonate and Mg-Al-hydroxides, UO_2, and iron sulphides, consistent with reducing conditions (Gregson, Goddard, *et al.*, 2011). One area of interest is the formation of colloids from the pond sludges as these could enhance radionuclide mobility in legacy storage facilities and potentially in effluent treatment as these facilities are decommissioned (Maher *et al.*, 2016). Colloids are worthy of further characterisation as they may evade extant radionuclide removal treatments which are focused on filtering large particulates or removing solution species. Colloids can mobilise radionuclides in two ways; either incorporated into the colloidal particle structure as an intrinsic colloid (e.g. U(IV), Th(IV) and Np(IV)-silicate colloids (Dreissig *et al.*, 2011;

Hennig *et al.*, 2013; Husar *et al.*, 2015; Neill, Morris, Pearce, Sherriff, Burke, *et al.*, 2018)), or sorbed to the surface of colloidal particles as a pseudo-colloid (e.g. U(IV) sorbed to Al-P-Fe-Si aggregates (Wang *et al.*, 2013) or Pu sorbed to clay and zeolite colloids (Kersting *et al.*, 1999)). U is a major component of spent nuclear fuel (Bruno and Ewing, 2006; Marshall *et al.*, 2015) and if U can form intrinsic colloids under representative SNF pond corrosion conditions, then these colloids may be present in significant quantities. Intrinsic U colloids may challenge effluent treatment in themselves and they may also impact on the mobility of other radionuclides via incorporation and/or sorption processes. For example, ^{90}Sr may associate with U(IV) colloids thus potentially enhancing ^{90}Sr mobility during effluent treatment as these pseudo-colloidal species may be more difficult to remove from effluent than dissolved ^{90}Sr. U(IV) has been shown to form intrinsic colloids upon corrosion of SNF (Kaminski *et al.*, 2005) and U(IV)-silicate colloids have been shown to form under SNF fuel pond conditions (Neill, Morris, Pearce, Sherriff, Burke, *et al.*, 2018). Significantly, colloidal U(IV)-silicates have also been shown to sorb Sr, meaning U(IV)-silicates and their interactions with Sr are worthy of further study (Neill, Morris, Pearce, Sherriff and Shaw, 2018).

At Sellafield, a key effluent treatment facility is the site ion exchange effluent plant (SIXEP). SIXEP is a multi-stage effluent treatment plant that contains sand beds to filter out large particulates from effluents. After this effluents are passed through a carbonation tower that lowers the pH of incoming effluents from approximately pH 11 to pH 7. Finally, the pH 7 effluent is passed through ion exchange beds comprised of clinoptilolite ($(Na,K,Ca)_{2\text{-}3}Al_3(Al,Si)_2Si_{13}O_{36}\cdot 12H_2O$), a zeolite with high ion exchange selectivity for aqueous $^{90}Sr^{2+}$ and $^{137}Cs^{+}$, two of the major fission products in SNF (Minglu, Shijun and Chunkou, 1994; Borai *et al.*, 2009; Maher *et al.*, 2016). SIXEP has been operating at Sellafield since 1985 and routinely processes effluents from legacy SNF storage facilities, including storage ponds containing spent Magnox fuel (Gray, Jones and Smith, 1995; Parry *et al.*, 2011). With decommissioning and waste retrieval operations gathering momentum at Sellafield, it is anticipated a wider range of effluents will be produced and they may require treatment. Therefore, understanding how potentially mobile, nanoparticulate phases will be altered during the SIXEP process is essential to underpinning future effluent treatment processes.

An(IV)-silicate colloids have been identified as potentially vectors for U(IV), Th(IV) and Np(IV) (Dreissig *et al.*, 2011; Hennig *et al.*, 2013; Husar *et al.*, 2015) and the formation, stability and characteristics of U(IV)-silicates under conditions representative of SNF storage ponds have been investigated (Neill, Morris, Pearce, Sherriff, Burke, *et al.*, 2018). U(IV)-silicate nanoparticles form colloids between pH 6 and 10.5, with changing compositions and particle structures under different pH and silicate conditions. These particles have been shown to be silicate rich at near neutral pH, and have an increasing U(IV) content at more alkaline pH above pH 10.5. Further characterisation of the nanoparticles confirmed that they have a core-shell structure with a UO_2-like core and a silicate-enriched surface, leading to silica-like colloidal behaviour (Dreissig *et al.*, 2011; Neill, Morris, Pearce, Sherriff and Shaw, 2018; Neill, Morris, Pearce, Sherriff, Burke, *et al.*, 2018). Understanding the fate of these particles during carbonation (as part of effluent treatment) is essential in defining their potential impact on abatement efficiency as post operational clean out and decommissioning effluents are produced.

As well as the intrinsic hazard posed by U containing colloids, both U(IV)-silicates and UO_2 nanoparticles have been shown to strongly sorb Sr (Neill, Morris, Pearce, Sherriff and Shaw, 2018). As the ion exchange processes used at nuclear sites treat aqueous ^{90}Sr, it is uncertain as to whether the presence of pseudo-colloidal Sr would impact negatively on effluent treatment. Indeed, the behaviour U(IV) colloids and any Sr associated with U(IV) colloids is unclear during carbonation. The effect of carbonation on alkaline effluents is twofold; there is an increase in aqueous carbonate concentration and also the pH of effluents is reduced from ~11 to 7. Understanding the impact of these two changes on the colloidal stability of U(IV) and sorption of Sr will provide mechanistic insight into the changes that occur in these systems during carbonation. U(IV)-silicate colloids have been shown to be stable at pH 7 under moderate carbonate concentrations (Dreissig *et al.*, 2011; Neill, Morris, Pearce, Sherriff, Burke, *et al.*, 2018). However, under the elevated carbonate concentrations in the post carbonation effluents, U may have enhanced solubility. For example, high concentrations of dissolved carbonate may increase the solubility of U(IV) dramatically via formation of $U(CO_3)_5^{6-}$ and $U(OH)_2(CO_3)_2^{2-}$ (Rai *et al.*, 1998). While decreasing pH has been shown to reduce the sorption of Sr to U(IV)-silicate (Neill, Morris, Pearce, Sherriff and Shaw, 2018),

Sr may exhibit reduced solubility under high carbonate concentrations due to the formation of strontianite ($SrCO_3$) (Busenberg, Plummer and Parker, 1984).

This study investigates the impact of the SIXEP carbonation tower on the stability and structure of U(IV)-silicate colloids and their potential to transport Sr. U(IV)-silicate prepared at pH 11.4, with Sr sorbed to the U(IV) phase, was exposed to CO_2 by bubbling to reduce the pH to 7. Samples were taken periodically before and after the carbonation treatment and analysed by ultrafiltration and X-ray absorption spectroscopy (XAS) to identify any changes to particle size distribution and particle structure, as well as the fate of Sr, during carbonation.

6.3. Methods

U(IV) silicate was prepared at pH 11.4, to mimic the average pH of a Sellafield legacy storage pond (Maher *et al.*, 2016), with an initial silicate concentration of 4 mM and a U(IV) concentration of 1 mM (Dreissig *et al.*, 2011; Neill, Morris, Pearce, Sherriff and Shaw, 2018; Neill, Morris, Pearce, Sherriff, Burke, *et al.*, 2018). The resulting precipitate was aged for 7 days before Sr was spiked into solution at a Sr concentration of 0.058 mM. The experiment was left to equilibrate for 7 days before carbonation.

Carbonation of the U(IV)-silicate/Sr sample (total volume 180 mL) was carried out using an automated computer-controlled chemostat reactor (Applikon MiniBio) with temperature control (Peltier heater/cooler, 25 °C). The chemostat was purged with N_2 gas for 45 minutes prior to addition of the U(IV)-silicate/Sr sample, also under N_2, to prevent oxidation of U(IV) to U(VI). The sample was then stirred in the chemostat under a positive pressure of N_2 gas at 125 rpm for 10 minutes. CO_2 was bubbled through the sample at a low, constant rate for 10 minutes, with stirring maintained at 125 rpm, until the pH reduced to pH 7. At this point, the CO_2 flow was stopped and a positive pressure of N_2 gas was once again introduced to prevent any exposure of the sample to oxygen while samples were extracted. Under N_2, samples were extracted and then stored in an anaerobic cabinet (N_2/H_2 mix, <10 ppm O_2) on an orbital shaker (40 rpm) until further analysis.

Samples were taken before carbonation (-0.25 h), immediately after carbonation (0.25 h) and at subsequent intervals (1 h, 4 h, 24 h, 8 d). The pH of samples was monitored,

and the samples were filtered using 3 and 300 kDa ultracentrifuge filters (Pall Nanosep) and and 0.22 µm syringe filters (PES, Merck Millipore). The ultracentrifuge filters correspond to approximately 1.5 and 12 nm pore sizes respectively (Granath, 1958; Laurent and Granath, 1967; Dreissig *et al.*, 2011). The filtrates were analysed for total Sr and U concentrations using ICP-MS (Agilent 7500cx) and total Si concentration using ICP-AES (Perkin-Elmer Optima 5300 dual view).

Solid XAS samples were separated from solution by centrifugation (for t = -0.25 h and 0.25 h), or collected on a 3 kDa filter (t = 8 d) and diluted in cellulose (Neill, Morris, Pearce, Sherriff, Burke, *et al.*, 2018). Data collection was carried out at Diamond Light Source B18 beamline, at the U L_{III}-edge using a Si (111) monochromator at liquid nitrogen temperature in transmission mode. The data were analysed using Demeter software package Athena and Artemis, FEFF6 (Ravel and Newville, 2005).

6.4. Results and discussion

6.4.1. Characterisation of the starting material

Ultrafiltration showed the U(IV)-silicate particles formed at pH 11.4 were >220 nm in size and there was an absence of any U, Si or Sr-containing colloidal matter (1.5-220 nm) in this starting sample. This is consistent with previous findings which showed that U(IV)-silicates formed at pH 12 were not stable as a colloid (Neill, Morris, Pearce, Sherriff, Burke, *et al.*, 2018). The majority of the Sr (97 %) was sorbed to the solid U(IV)-silicate phase with only a small amount (3 %) remaining in solution. While the starting material was not colloidal, the pH (11.4) was only slightly outside of the known pH range of U(IV)-silicate colloidal stability (pH 6-10.5 (Dreissig *et al.*, 2011; Neill, Morris, Pearce, Sherriff and Shaw, 2018; Neill, Morris, Pearce, Sherriff, Burke, *et al.*, 2018)).

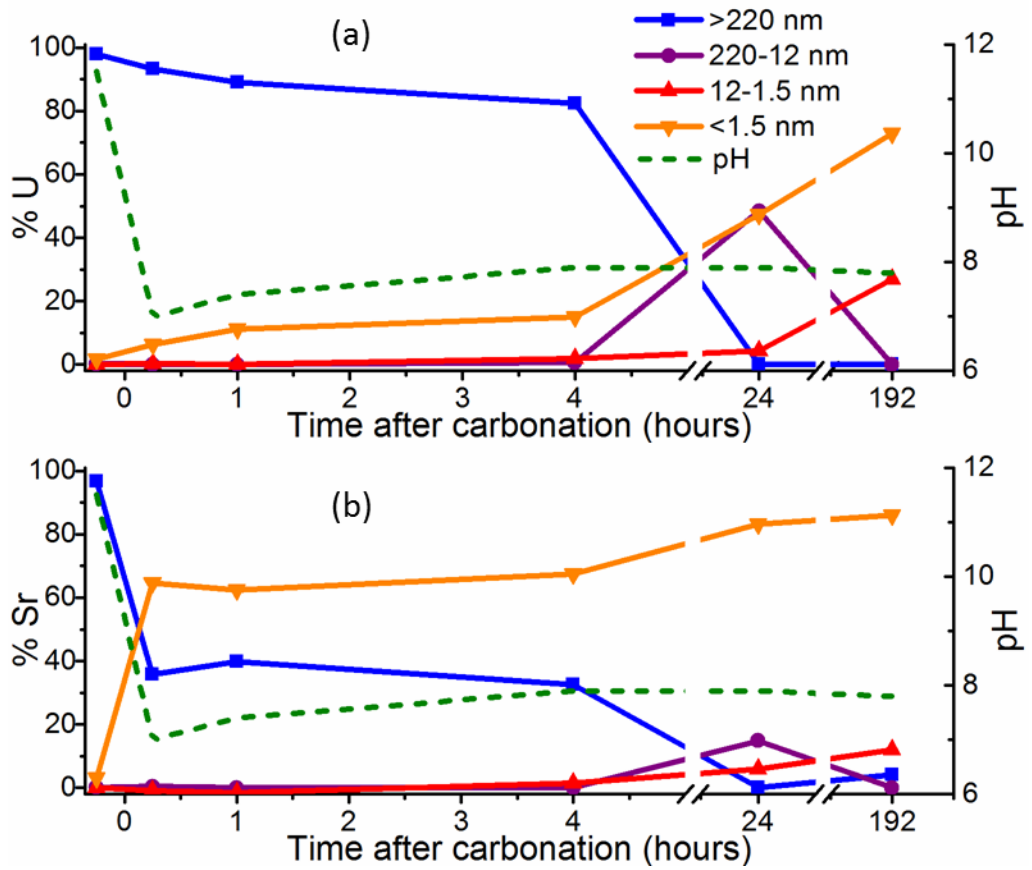

Figure 6.1: U (a) and Sr (b) filtration results from before and up to 192 h (8 d) after carbonation from pH 11.4 to pH 7, showing the percentage of the total U or Sr within each size fraction and pH.

6.4.2. Impact of carbonation on uranium speciation.

Figure 6.1(a) shows the ultrafiltration data for U at time points between -0.25 h before and 8 d (192 h) after carbonation. In the first hour after carbonation, there was a 12 % reduction in U in the >220 nm size fraction and a corresponding increase in the aqueous U (< 1.5 nm) of 12%. In the subsequent 3 hours, an increase in the aqueous U to 16 %, and the presence of 2 % colloidal (1.5-12 nm) U was observed. After 24 h no large particulate U (>220 nm) remained and the U was then distributed between the aqueous (<1.5 nm, 47 %), the large colloid (220-12 nm, 48 %) and the small colloid (1.5 -12 nm, 4 %) fractions. After 8 d, 73 % of the U was aqueous and the remaining 27 % was in the small colloid size fraction (1.5-12 nm).

From the filtration data, it is apparent that the impact of carbonation on the U(IV)-silicate particles is not immediate and this is also seen in the composition of the particles. Figure 6.2 shows the pH and Si:U molar ratios in the solids (>1.5 nm fractions),

at a range of time points after carbonation. Prior to carbonation and in the subsequent 4 hours, the Si:U ratio in the particles was ≤2, with a slight increase from 1.7 to 2.0 between -0.25 and 4 h. At 24 h, the Si:U ratio was 2.6 and after 8 d this ratio increased to 4.0. This increase in the Si:U ratio in later time points coincided with an increase in colloidal U and the formation of colloids at t ≥24 h is likely caused by the increase in Si:U ratio in the particle composition. This is consistent with past work which shows that U(IV)-silicate particles with a higher silicate content display an elevated colloidal stability (Dreissig *et al.*, 2011; Neill, Morris, Pearce, Sherriff, Burke, *et al.*, 2018). Previous work has also shown that U(IV)-silicate colloids are approximately 5 nm in size and with larger aggregates of these smaller particles also present. This suggests that the colloid formation observed during carbonation is likely due to disaggregation of larger, aggregated U(IV)-silicate particles (Neill, Morris, Pearce, Sherriff, Burke, *et al.*, 2018).

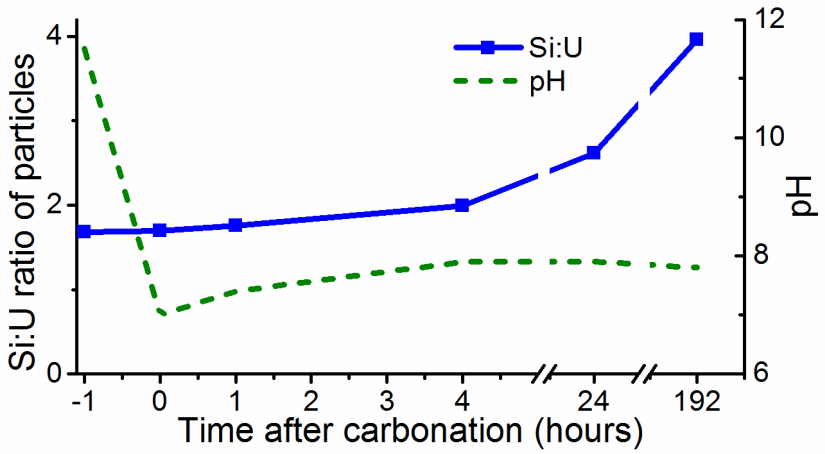

Figure 6.2: Changes in pH and Si:U ratio of particulates before and up to 192 h (8 d) after carbonation from pH 11.4 to 7.

As well as forming a colloid, a large fraction of the U was associated with the aqueous phase after carbonation. At 24 h 47% of U was aqueous (<1.5 nm), and 73 % U was in the aqueous fraction at 8 d. This dissolution of U is presumably due to the formation of U(IV)-carbonate complexes which can significantly increase the solubility of U(IV) (Ciavatta *et al.*, 1983; Rai *et al.*, 1998; Hennig, Emmerling, *et al.*, 2010). Previous studies have shown that up to 50 mM dissolved U(IV) was achievable in 1 M NaHCO3 solutions. Interestingly, in the current experiment, the dissolution of U occurred over several days despite the poorly-ordered, nanoparticulate nature of the U(IV)-silicate phase, which might be expected to lead to rapid dissolution.

6.4.3. Impact of carbonation on strontium speciation

Prior to carbonation, the majority of the Sr was sorbed to the U(IV)-silicate solid phase at pH 11.4 , consistent with past work at pH 12 which suggested Sr would be sorbed to U(IV)-silicate or present as a Sr-silicate precipitate at this pH (Neill, Morris, Pearce, Sherriff and Shaw, 2018). The majority of the Sr associated with the U(IV)-silicate appeared labile; immediately after carbonation, 74% of Sr was present in the aqueous (<1.5 nm) fraction with the remaining 26 % in the >220 nm fraction (Figure 6.1(b)). Additional strontium release was observed alongside U dissolution with increasing aging of the experiment to 8 d, with 85 % Sr dissolved and 11 % colloidal at this time point. At this stage there was also a small amount of Sr observed in the >220 nm size fraction (4 %). No U was present in this size fraction at 8 d, however 2 % of total Si was, suggesting Sr could be associated with this Si. Alternatively, a strontianite ($SrCO_3$) precipitate was formed given the elevated carbonate concentrations in solution post carbonation.

The initial desorption is in accordance with previous investigations into Sr on U(IV) phases (Neill, Morris, Pearce, Sherriff and Shaw, 2018) and other phases (Sureda *et al.*, 2010; Wallace *et al.*, 2012; Fuller *et al.*, 2016) which showed that, at lower pH, Sr sorption is reduced. However, at 0.25 h at pH 7, there was a higher amount of Sr sorbed to U(IV)-silicate (26 %) than at pH 6 (6±5 %), and equivalent sorption at pH 8 (22±5 %) in previous work (Neill, Morris, Pearce, Sherriff and Shaw, 2018). This is likely due to disequilibrium in the experiment after carbonation; the U(IV)-silicate phase composition does not change immediately (Figure 2) and it is possible Sr desorption is also not in equilibrium after 0.25 h. As SIXEP is a rapid process (~10 minutes in total), an increase in Sr retention on U(IV) phases 0.25 h after the carbonation may increase their capacity for ^{90}Sr transport in SIXEP.

6.4.4. U(IV)-silicate particle structure

U L_{III}-edge EXAFS spectra were recorded for samples before (-0.25h), immediately after (0.25 h) and 8 d after carbonation (Figure 6.3, Table 6.1). Fits were informed by previous work on U(IV)-silicates (Neill, Morris, Pearce, Sherriff, Burke, *et al.*, 2018) which showed U(IV)-silicates were generally poorly ordered and had Si enrichment relative to coffinite ($USiO_4$) (Fuchs and Gebert, 1958). The EXAFS fitting for the -0.25 h and 0.25 h samples

showed clear similarities with these previous EXAFS recorded for U(IV) silicates. A split O shell consisting of 4.5 O atoms at 2.28 Å and 3.5 O atoms at 2.46 Å was consistent across both fits. For the -0.25 h data, 1.6 bidentate Si backscatterers at 3.17 Å were fit along with 2 Si monodentate backscatterers at 3.72 Å and 2 U backscatterers at 3.80 Å. The fit for the 0.25 h data was very similar; 1.6 monodentate Si backscatterers at 3.17 Å, 1.7 bidentate Si backscatterers at 3.70 Å and 1.5 U backscatterers at 3.80 Å. This indicated that the U(IV)-silicate phase was unaltered during the early post-carbonation phase. While the 8 d post carbonation EXAFS data were also fitted to a U(IV)-silicate structure, there were modest differences in the fit compared to the other two data sets. Here, the best fit showed the U-O distances increasing to 2.30 and 2.54 Å, and also an increase in the U-Si distance (3.85 Å for monodentate Si) and lower coordination numbers for U-Si backscatterers (1 for monodentate Si), suggesting that the U phase is altering over time after carbonation. Compared to previous EXAFS of U(IV)-silicate prepared at pH 12, there was slightly higher U-Si coordination and reduced U-U coordination in all samples, consistent with these samples being prepared at a slightly lower pH and therefore being more silicate enriched. As with previous investigations into U(IV)-silicates, the EXAFS showed reduced coordination numbers for U-Si and U-U backscatterers relative to crystalline coffinite, confirming that these particles are poorly ordered and/or nanocrystalline.

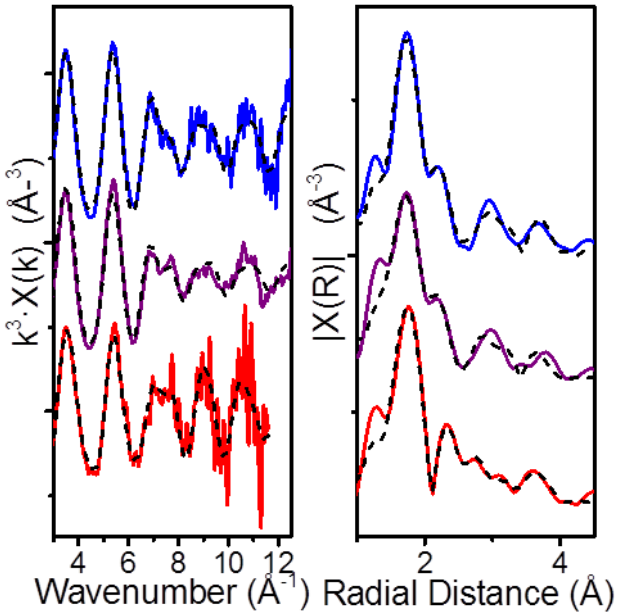

Figure 6.3: EXAFS (left) and Fourier transform EXAFS (right) from 3 U(IV) silicates. Blue (top) -0.25 h sample prior to carbonation, purple (middle) 0.25 h sample immediately after carbonation, and red (bottom) 8 d after carbonation sample. Dashed lines indicate EXAFS fits.

Table 6.1: EXAFS fitting data for U L3-edge EXAFS of U(IV)-silicates before, 0.25 h and 8 d after carbonation

Sample	Path	N	R (Å)	σ^2	$S0^2$	ΔE_0	R
t = -0.25 h	U-O.1	4.5	2.28(1)	0.006(1)[a]	0.86(6)	5.8(7)	0.0073
	U-O.2	3.5	2.46(1)	0.006(1)[a]			
	U-Si.1	1.6	3.17(2)	0.013(3)			
	U-Si.2	2	3.72(3)	0.013(5)			
	U-U	2	3.80(3)	0.014(4)			
t = 0.25 h	U-O.1	4.5	2.28(1)	0.009(1)[a]	1.00(7)	5.0(7)	0.0086
	U-O.2	3.5	2.46(1)	0.009(1)[a]			
	U-Si.1	1.5	3.17(2)	0.012(2)			
	U-Si.2	1.7	3.70(3)	0.013(4)			
	U-U	1.5	3.80(3)	0.015(4)			
t = 8d	U-O.1	4.8	2.30(1)	0.008(1)[a]	1.00(8)	8.8(5)	0.0047
	U-O.2	3.2	2.54(1)	0.008(1)[a]			
	U-Si.1	1.5	3.19(3)	0.009(2)			
	U-Si.2	1	3.85(5)	0.015(7)			
	U-U	1.5	3.82(2)	0.013(3)			
$USiO_4$	U-O.1	4	2.32				
	U-O.2	4	2.51				
	U-Si.1	2	3.13				
	U-Si.2	4	3.83				
	U-U	4	3.83				

Coordination numbers (N), U bond distances (R (Å)), Debye-Waller factors (σ^2), amplitude factor, which was constrained between 0.8 and 1 ($S0^2$), shift in energy from calculated Fermi level (ΔE_0) and 'goodness of fit' factor (R). Coordination numbers were fixed, amplitude factors were fixed as 1, [a] denotes tied σ^2 values. Numbers in parentheses are the standard deviation on the last decimal place. $USiO_4$ coordination numbers and interatomic distances taken from Fuchs and Gerbert (1958).

Overall, EXAFS fitting suggested that the U was present as a U(IV)-silicate phase after carbonation. These results support the ultrafiltration results (Figures 6.1 and 6.2), which indicated that U(IV)-silicate particles persist, and changes to the composition of the particles is a gradual process. -0.25 h and 0.25 h EXAFS fits show that the exposure to CO_2 and the pH reduction does not have an instantaneous effect on the structure of the particles. After 8 d, there are modest changes in the structure and composition of the U(IV) silicate phase. Interestingly, there was not an observable increase in the Si coordination in the 8 d sample in the EXAFS data, despite a significantly higher Si:U ratio in the particles as evidenced by ultrafiltration. Instead, EXAFS fitting indicated shifts in the bond distances towards those which are more characteristic of coffinite ($USiO_4$) (Table 6.1). This is unexpected given that ultrafiltration data showed the silicate content of the particles was increasing and was moving away from the 1:1 Si:U ratio of coffinite. This could be explained by surface precipitation of silica on the U(IV)-silicate, which would only lead to enrichment on silicate on the particle surface. The average U-Si coordination observed in the EXAFS would not be expected to increase significantly in this scenario as only surface U atoms would have increased silicate coordination. This would suggest the particles present after 8 d have highly silicate enriched surface, likely leading to very high colloidal stability, as previous studies have showed high silicate content in U(IV)-silicates is the major factor in colloidal stability (Dreissig *et al.*, 2011; Neill, Morris, Pearce, Sherriff, Burke, *et al.*, 2018).

6.5. Conclusion

This study expands on previous knowledge of the stability of U(IV)-silicate colloids and applies this understanding to a scenario with high relevance to nuclear decommissioning. The U(IV) particles formed in this study were mobilised by the carbonation process over a period of 24 h by both dissolution and disaggregation. EXAFS analyses complemented ultrafiltration by confirming that the particle structure remained U(IV)-silicate after carbonation, with minor changes to the structure and an

increased Si content of particles occurring after 8 d. As the dwell time for effluents during carbonation in SIXEP is short (~10 minutes), this study suggests that U(IV)-silicate particles would not be significantly altered over these timescales. Although the U(IV)-silicate was not colloidal under the experimental conditions at pH 11.4, pH variations and much higher shear during waste retrieval and effluent processing may stabilise U colloids. If this occurs, this study has shown that these colloids are unlikely to be immobilised during carbonation and may act as vectors for other radionuclides.

While carbonation resulted in the removal of the majority of Sr from the U(IV) phase, a small amount of Sr remained sorbed to the U(IV)-silicate. This Sr may be removed from the U(IV)-silicate in the presence of an ion exchanger such as clinoptilolite, as previous work has indicated that Sr is likely to be labile under these condition when sorbed to U(IV) phases (Neill, Morris, Pearce, Sherriff and Shaw, 2018); a favourable scenario for effluent treatment processes. More research is required to fully understand the stability of colloidal phases that could be of concern for effluent treatment. Investigations into different colloidal phases, containing different radionuclides, and also the interactions of these particles with the other steps of SIXEP, the sand bed filters and the clinoptilolite, are all pertinent.

Chapter 7: Conclusions and future work

7.1. Project summary and conclusions

The key aim of this project was to characterise colloidal species that could potentially mobilise U and ^{90}Sr in conditions relevant to SNF storage ponds and effluents. Previously, there was a lack of comprehensive characterisation of intrinsic, radionuclide bearing colloids that could form in alkaline SNF storage and their interactions with other radionuclides. Despite U(IV), Th(IV) and Np(IV)-silicate colloids all previously being identified, their structures were not fully understood and their behaviour at high pH was unknown. Additionally, the interaction of ^{90}Sr with U(IV) phases in SNF is of high importance and had not been systematically investigated. Therefore the investigations into the formation process and particle structure of U(IV)-silicate colloids, and interactions of U(IV)-silicates and UO_2 with Sr were carried out. This knowledge was then utilised for an applied investigation into the effects of carbonation (as part of effluent treatment) on both the U(IV)-silicates and their ability to sorb Sr.

In this project it has been possible to characterise the stability and core-shell nanoparticle structure of U(IV)-silicate colloids using a multi-technique approach (Chapter 4). These colloidal particles, along with UO_2, were shown to interact strongly with Sr and colloid-bond Sr was present in U(IV)-silicate systems (Chapter 5). UO_2, a known SNF corrosion product, showed especially strong Sr sorption and evidence suggested surface incorporation of Sr on UO_2 occurred at pH ≥10. Finally, the impact of effluent treatment processes were investigated, with the carbonation step of SIXEP shown to cause desorption of Sr but have little immediate effect on U(IV)-silicate colloidal stability and particle structure. A gradual mobilisation of U(IV) as both a colloid and solution species observed over several days (Chapter 6).

Chapter 4 focused on U(IV)-silicate colloids and their potential to form under alkaline conditions. It was found that these colloids could form in the presence of silicate at pH 9 and 10.5 but not at pH 12, and that the stability of the particles was highly dependent on their silicate content. In all cases, U(IV)-silicate nanoparticles between 4 and 7 nm formed, and particle aggregation was shown to be the route to colloid destabilisation. Higher silicate concentration, lower pH systems yielded the most stable colloidal

dispersions with the highest Si/U ratio in the particles. Using a combination of EXAFS and X-ray PDF, it was possible to analyse the structure of the particles and results suggested a core-shell structure to the particles. The previously unknown core-shell structure, with a silicate rich particle surface, explains the high colloidal stability of these U(IV)-silicates and their silica-like colloidal behaviour. Additionally, the particle formation mechanism, proposed to be the rapid hydrolysis of U(IV)-hydroxide complexes followed by formation and polymerisation of U(IV)-silicate solution complexes, highlighted several potentially important factors for coffinite formation which warrant further investigation. The novel core-shell particle structure identified in this study is of relevance to other intrinsic An(IV) colloids, explains the high colloidal stability observed in these systems and also highlights the importance of An(IV)-silicate solution complexes. The colloid stability range found in this study also increases the known stability range of these particles to pH 7-10.5 and showed that these particles are not stable at pH 12. Colloidal stability at high pH is highly relevant to both decommissioning and disposal conditions for SNF and the stability of these colloidal particles at alkaline pH means they may be key vectors for radionuclides. Given the wide ranging stability of these particles they are also relevant to U(IV) mobility in a range of environmental scenarios. Finally, the existence of ~5 nm primary particles and particle aggregation as the cause for larger particulates was confirmed using SAXS and TEM to analyse these systems for the first time. This increased understanding of colloid destabilisation in these systems and confirmed the role of surface silicate in preventing aggregation and precipitation as the mechanism for colloid stabilisation.

While the hazard posed by intrinsic U colloids, such as U(IV)-silicates, is not insignificant, the potential for sorption and mobilisation of other radionuclides could increase the risk they pose. Therefore, in Chapter 5, Sr was sorbed to two U(IV) phases, U(IV)-silicate and UO_2. Sorption capacities were measured using ultrafiltration and it was found that Sr sorbed to both U(IV)-silicate and UO_2 and sorption occurred to a greater extent, at lower pH, on UO_2. Although EXAFS analysis showed a highly structured environment for Sr at pH 10 and 12, and TEM showed Sr was co-located with UO_2 particles, acid desorption studies found that this Sr was labile. This was attributed to the incorporation of Sr into the near-surface of UO_2 at pH ≥10. This incorporation occurred at a much lower pH than inner sphere sorption observed in previous Sr sorption studies, suggesting that UO_2 may

be a crucial factor in controlling Sr mobility in alkaline environments such as SNF storage ponds which are maintained at pH 11-11.5 (Maher *et al.*, 2016). Sr also showed an affinity for U(IV)-silicates, with over 40 % of a 0.058 mM solution of Sr being bound to colloidal U(IV)-silicates at pH 10. This amount of Sr in a mobile, colloidal phase certainly warrants further work to explore its relevance to effluent treatment systems at sites such as Sellafield. Indeed, this was the focus of the investigations in Chapter 6. At high pH in the U(IV)-silicate systems Sr formed intrinsic Sr-silicate phases which were present in the sedimented, immobile fraction. These results highlight that Sr silicate phases may be important when considering Sr mobility in alkaline, silicate containing solutions. This research highlights the importance of two previously unstudied U(IV) phases when considering Sr mobility in SNF. The strong sorption observed for UO_2, via surface incorporation at alkaline pH, suggests UO_2 may play a key role in ^{90}Sr mobility in SNF storage. U(IV)-silicate colloids also had a high capacity for Sr sorption and, given their mobile nature, should also be considered when assessing Sr mobility in SNF storage.

In Chapter 6, U(IV)-silicate, with Sr sorbed, was exposed to CO_2 gassing to simulate the behaviour of this system in the carbonation tower of SIXEP. This research applied the previous knowledge and understanding of these systems, acquired in Chapter 4 and Chapter 5, to an effluent treatment scenario. The U(IV)-silicate particles were not colloidal at pH 11.4 prior to carbonation. After carbonation, there was a gradual dissolution of the U(IV) and formation of a U(IV)-silicate colloid after 24 hours. In SIXEP, the effluent does not remain in the plant for long durations, so the effect of carbonation on particles passing through SIXEP is likely to be low. However, in experiments after 24 hours all the U(IV) was either colloidal or dissolved, i.e. mobile. Using previously acquired knowledge, it was reasoned that the U(IV)-silicate formed a colloid due to the increased silicate content of the particles which was caused by the drop in pH. Although the impact of carbonation on particle structure and colloid stability was not immediate, if effluents were not immediately processed then this could cause complications due to the suspension and solubilisation of radionuclides within effluents. Furthermore, after carbonation 26 % Sr remained sorbed to the U particles. It is unknown whether this would be the case in the presence of clinoptilolite, which removes Sr from solution and thus may drive further desorption from U(IV)-silicate particles. This study showed that carbonation would be likely to mobilise U(IV) phases, but not on the timescale of SIXEP,

and that a small but significant fraction of Sr remains associated with U(IV) phases after carbonation. This highlights the potential hazard posed by colloidal phases in effluent streams, and the possibility of these colloids acting as vectors for other radionuclides. However, for the investigated system it is also possible that the existing effluent treatment at SIXEP is capable of removing both U(IV)-silicate particles and sorbed ^{90}Sr from effluents. Further investigations with a more complete SIXEP rig, including all the treatment stages, are required to assess whether U(IV)-silicate particles with Sr sorbed are mobile within the plant.

7.2. Future work

i) Interactions of U(IV)-silicates and UO_2 with additional radionuclides

One of the major hazards posed by mobile U phases, which in themselves have a low radiotoxicity, is the incorporation of other radionuclides. Although ^{90}Sr is of interest in nuclear decommissioning, a range of other radionuclides are of interest in both nuclear decommissioning and long-term geological disposal of nuclear waste. Investigations into the fate of these radionuclides during the formation of colloidal U(IV) phases would help inform safety cases for both nuclear sites and GDFs. Experiments investigating the interactions of radionuclides with U(IV) phases, specifically using ultrafiltration and EXAFS analysis applied in this thesis, would show whether these species could be mobilised, or immobilised, in U(IV) colloid containing systems.

ii) U(IV) particles in tertiary systems

Although U is the dominant radionuclide by mass in SNF, fuel cladding is also abundant and will therefore impact on the physical behaviour of the waste. In legacy storage facilities, a significant amount of corroded Magnox sludge (CMS) is Mg corrosion products such as brucite ($Mg(OH)_2$), Mg-carbonates and Mg-Al-hydroxides (Gregson, Goddard, *et al.*, 2011). Some of these phases are colloidal in SNF storage ponds, and have been shown to contain radionuclides (Pitois *et al.*, 2008; Maher *et al.*, 2016). Investigations into tertiary systems, involving U(IV) particles, Magnox corrosion products and other radionuclides would increase understanding of these systems and the key risk drivers for mobilisation of radionuclides in the complex pond environment. Additionally, through an increased understanding of the underlying scientific drivers for

these interactions, these investigations could underpin the future development of the effluent treatment systems.

iii) Characterisation of corroded metallic U

Comparisons between samples prepared in this project and samples formed in a SNF storage pond-like environment would indicate which particle characteristics of laboratory synthesised U(IV) phases are transferrable to real environmental scenarios. Characterisation of U particles formed from the corrosion of metallic U, at high pH, is one way of making this assessment. Using a similar range of analytical techniques to those used in Chapter 4 would make comparisons between the different phases, and different formation pathways, possible. Interestingly, colloids have been shown to form from the corrosion of metallic U (Kaminski *et al.*, 2005). While these particles were characterised as UO_2 by SAED, it is possible these particles had a silicate like coating, as their colloidal stability, zeta potentials and the presence of silicate (1.5 mM) in the experimental solutions suggests this is true. Additionally, due to the difficulties in extensive characterisation of highly radioactive CMS found in legacy ponds, corroded metallic U is a good simulant for real samples which can be analysed using a wider range of techniques. Combining the findings of these studies with those of this project would give a more holistic view of U behaviour in SNF storage ponds and geodisposal environments.

iv) U(IV)-silicate solution complexes and U(IV)-silicate particle formation

One of the most intriguing aspects of Chapter 4 was the formation pathway of U(IV)-silicate particles and their core-shell structure. Further investigations could yield important details on U(IV)-silicate solution complexes, which appear to be crucial intermediates for U(IV)-silicate solid formation and may also significantly impact on the solubility of U(IV) in engineered environments. Furthering the understanding of U(IV)-silicate solution complexes and their polymerisation would lead to more accurate thermodynamic modelling of U(IV) speciation in silicate containing systems.

List of References

Ahtee, A. *et al.* (1976) 'The structure of orthorhombic SrZrO 3 by neutron powder diffraction', *Acta Crystallographica Section B Structural Crystallography and Crystal Chemistry*, 32(12), pp. 3243–3246. doi: 10.1107/S0567740876010029.

Albarran, N. *et al.* (2011) 'Strontium migration in a crystalline medium: Effects of the presence of bentonite colloids', *Journal of Contaminant Hydrology*. Elsevier B.V., 122(1–4), pp. 76–85. doi: 10.1016/j.jconhyd.2010.11.005.

Albrecht-Schmitt, T. E., Almond, P. M. and Sykora, R. E. (2003) 'Cation−Cation Interactions in Neptunyl(V) Compounds: Hydrothermal Preparation and Structural Characterization of NpO 2 (IO 3) and α- and β-AgNpO 2 (SeO 3)', *Inorganic Chemistry*, 42(12), pp. 3788–3795. doi: 10.1021/ic034124z.

Alessi, D. S. *et al.* (2014) 'The product of microbial uranium reduction includes multiple species with U(IV)-phosphate coordination', *Geochimica et Cosmochimica Acta*. Elsevier Ltd, 131, pp. 115–127. doi: 10.1016/j.gca.2014.01.005.

Alexandre, P. *et al.* (2015) 'Chemical Compositions of Natural Uraninite', *The Canadian Mineralogist*, 53(4), pp. 595–622. doi: 10.3749/canmin.1500017.

Allen, L. H. and Matijević, E. (1969) 'Stability of colloidal silica', *Journal of Colloid and Interface Science*, 31(3), pp. 287–296. doi: 10.1016/0021-9797(69)90172-6.

Amme, M. *et al.* (2005) 'Uranium secondary phase formation during anoxic hydrothermal leaching processes of UO2 nuclear fuel', *Journal of Nuclear Materials*, 341(2–3), pp. 209–223. doi: 10.1016/j.jnucmat.2005.02.004.

Arafat, H. A. *et al.* (2010) 'The application of in situ formed mixed iron oxides in the removal of strontium and actinides from nuclear tank waste', *AIChE Journal*, 56(11), pp. 3012–3020. doi: 10.1002/aic.12197.

Artinger, R. *et al.* (2002) 'A Kinetic Study of Am(III)/Humic Colloid Interactions', *Environmental Science & Technology*, 36(20), pp. 4358–4363. doi: 10.1021/es025594f.

Bailey, J. K. and Mecartney, M. L. (1992) 'Formation of colloidal silica particles from alkoxides', *Colloids and Surfaces*, 63(1–2), pp. 151–161. doi: 10.1016/0166-

6622(92)80081-C.

Ball, R. G. J. (1992) 'Computer simulation studies of ternary uranate phases with alkali and alkaline-earth metals. Part 1.-MUO3', *J. Mater. Chem.*, 2(6), pp. 641–652. doi: 10.1039/jm9920200641.

Barrett, S. A. *et al.* (1982) 'The preparation and structure of barium uranium oxide BaUO 3+ x', *Acta Crystallographica Section B Structural Crystallography and Crystal Chemistry*, 38(11), pp. 2775–2781. doi: 10.1107/S0567740882009935.

Beattie, T. M. and Williams, S. J. (2012) 'An overview of near-field evolution research in support of the UK geological disposal programme', *Mineralogical Magazine*, 76(8), pp. 2995–3001. doi: 10.1180/minmag.2012.076.8.15.

Bekhit, H. M. *et al.* (2006) 'Experimental and numerical investigations of effects of silica colloids on transport of strontium in saturated sand columns', *Environmental Science and Technology*, 40(17), pp. 5402–5408. doi: 10.1021/es060333h.

Bernier-Latmani, R. *et al.* (2010) 'Non-uraninite Products of Microbial U(VI) Reduction', *Environmental Science & Technology*, 44(24), pp. 9456–9462. doi: 10.1021/es101675a.

Bès, R. *et al.* (2016) 'Use of HERFD–XANES at the U L 3 - and M 4 -Edges To Determine the Uranium Valence State on [Ni(H 2 O) 4] 3 [U(OH,H 2 O)(UO 2) 8 O 12 (OH) 3]', *Inorganic Chemistry*, 55(9), pp. 4260–4270. doi: 10.1021/acs.inorgchem.6b00014.

Borai, E. H. *et al.* (2009) 'Efficient removal of cesium from low-level radioactive liquid waste using natural and impregnated zeolite minerals', *Journal of Hazardous Materials*, 172(1), pp. 416–422. doi: 10.1016/j.jhazmat.2009.07.033.

Bots, P. *et al.* (2014) 'Formation of Stable Uranium(VI) Colloidal Nanoparticles in Conditions Relevant to Radioactive Waste Disposal', *Langmuir*, 30(48), pp. 14396–14405. doi: 10.1021/la502832j.

Bower, W. R. *et al.* (2016) 'Characterising legacy spent nuclear fuel pond materials using microfocus X-ray absorption spectroscopy', *Journal of Hazardous Materials*, 317, pp. 97–107. doi: 10.1016/j.jhazmat.2016.05.037.

Bressler, I., Pauw, B. R. and Thünemann, A. F. (2015) 'McSAS: Software for the retrieval

of model parameter distributions from scattering patterns', *Journal of Applied Crystallography*, 48, pp. 962–969. doi: 10.1107/S1600576715007347.

Bruce, D. W., O'Hare, D. and Walton, R. I. (eds) (2014) *Structure from Diffraction Methods*. Chichester, UK: John Wiley & Sons, Ltd. doi: 10.1002/9781118695708.

Bruno, J. and Ewing, R. C. (2006) 'Spent Nuclear Fuel', *Elements*, 2(6), pp. 343–349. doi: 10.2113/gselements.2.6.343.

Burns, P. C. and Finch, R. (1999) *Uranium: Mineralogy, Geochemistry and the Environment*. Edited by P. H. Ribbe. Mineralogical Society of Americe, Washington, DC.

Buscall, R. and Ottewil, R. H. (1985) *Polymer colloids*. Elsevier, New York.

Busenberg, E., Plummer, L. N. and Parker, V. B. (1984) 'The solubility of strontianite (SrCO3) in CO2-H2O solutions between 2 and 91°C, the association constants of SrHCO+3(aq) and SrCO03(aq) between 5 and 80°C, and an evaluation of the thermodynamic properties of Sr2+(aq) and SrCO3(cr) at 25°C and 1 atm total', *Geochimica et Cosmochimica Acta*, 48(10), pp. 2021–2035. doi: 10.1016/0016-7037(84)90383-1.

Calderazzo, F. *et al.* (1978) 'Dialkylcarbamato complexes of transition elements. 1. A new method for the synthesis of N,N-dialkylcarbamato and N,N-dialkyldithiocarbamato complexes of uranium(IV)', *Inorganic Chemistry*, 17(2), pp. 471–473. doi: 10.1021/ic50180a052.

Carroll, S. A. *et al.* (2008) 'Surface complexation model for strontium sorption to amorphous silica and goethite', *Geochemical Transactions*, 9(1), p. 2. doi: 10.1186/1467-4866-9-2.

Chang, H. *et al.* (2011) 'Strontium and Cesium Release Mechanisms during Unsaturated Flow through Waste-Weathered Hanford Sediments', *Environmental Science & Technology*, 45(19), pp. 8313–8320. doi: 10.1021/es2010368.

Chapel, J. P. (1994) 'Electrolyte Species Dependent Hydration Forces between Silica Surfaces', *Langmuir*, 10(11), pp. 4237–4243. doi: 10.1021/la00023a053.

Chawla, F. *et al.* (2010) 'Binding of 239 Pu and 90 Sr to Organic Colloids in Soil Solutions:

Evidence from a Field Experiment', *Environmental Science & Technology*, 44(22), pp. 8509–8514. doi: 10.1021/es101766g.

Choi, S. *et al.* (2006) 'Strontium speciation during reaction of kaolinite with simulated tank-waste leachate: Bulk and microfocused EXAFS analysis', *Environmental Science and Technology*, 40(8), pp. 2608–2614. doi: 10.1021/es051869q.

Chorover, J. *et al.* (2003) 'Linking cesium and strontium uptake to kaolinite weathering in simulated tank waste leachate', *Environmental Science and Technology*, 37(10), pp. 2200–2208. doi: 10.1021/es025980x.

Chorover, J. *et al.* (2008) 'Silicon control of strontium and cesium partitioning in hydroxide-weathered sediments', *Geochimica et Cosmochimica Acta*, 72(8), pp. 2024–2047. doi: 10.1016/j.gca.2008.01.026.

Ciavatta, L. *et al.* (1983) 'Studies on metal carbonate equilibriums. 4. Reduction of the tris(carbonato)dioxouranate(VI) ion, UO2(CO3)34-, in hydrogen carbonate solutions', *Inorganic Chemistry*, 22(14), pp. 2088–2092. doi: 10.1021/ic00156a030.

Clark, D. L., Hobart, D. E. and Neu, M. P. (1995) 'Actinide Carbonte Complexes and Their Importance in Actinide Environmental Chemistry', *Chemical Reviews*, 95(1), pp. 25–48. doi: 10.1021/cr00033a002.

Collins, R. N. and Rosso, K. M. (2017) 'Mechanisms and Rates of U(VI) Reduction by Fe(II) in Homogeneous Aqueous Solution and the Role of U(V) Disproportionation', *The Journal of Physical Chemistry A*, 121(35), pp. 6603–6613. doi: 10.1021/acs.jpca.7b05965.

Cordfunke, E. H. P. *et al.* (1997) 'Structural and Thermodynamic Characterization of the Perovskite-Related Ba1+yUO3+xand (Ba, Sr)1+yUO3+xPhases', *Journal of Solid State Chemistry*, 131(2), pp. 341–349. doi: 10.1006/jssc.1997.7392.

Cordfunke, E. H. P. and Ijdo, D. J. W. (1994) 'Sr2UO4.5: A New Perovskite-Type Strontium Uranate', *Journal of Solid State Chemistry*, 109(2), pp. 272–276. doi: 10.1006/jssc.1994.1103.

Crossland, I. (2012) *Nuclear fuel cycle science and engineering*. Woodhead Publishing.

Deditius, A. P. *et al.* (2010) 'Precipitation and alteration of coffinite (USiO4·nH2O) in the presence of apatite', *European Journal of Mineralogy*, 22(1), pp. 75–88. doi: 10.1127/0935-1221/2010/0022-1990.

Deditius, A. P., Utsunomiya, S. and Ewing, R. C. (2008) 'The chemical stability of coffinite, USiO4·nH2O; 0<n<2, associated with organic matter: A case study from Grants uranium region, New Mexico, USA', *Chemical Geology*, 251(1–4), pp. 33–49. doi: 10.1016/j.chemgeo.2008.02.009.

Defra (2007) *Policy for the Long Term Management of Solid Low Level Radioactive Waste in the United Kingdom*.

Degueldre, C. and Wernli, B. (1993) 'Association Behaviour of 241Am on SiO2 (amorphous) and SiO2(quartz) Colloids', *Journal of environmental radioactivity*, 20, pp. 151–167.

Delegard, C. and Schmidt, A. (2008) 'Uranium Metal Reaction Behaviour in Water, Sludge and Grout Matrices- Technical Report, PNNL-17815', (September), pp. 1–20, 44–48.

Department of Energy & Climate change (2014) *Implementing Geological Disposal*.

Derjaguin, B. and Landau, L. (1993) 'Theory of the stability of strongly charged lyophobic sols and of the adhesion of strongly charged particles in solutions of electrolytes', *Progress in Surface Science*, 43(1–4), pp. 30–59. doi: 10.1016/0079-6816(93)90013-L.

Diamond, J. J. (1955) 'Flame Photometric Determination of Strontium in Portland Cement', *Analytical Chemistry*, 27(6), pp. 913–915. doi: 10.1021/ac60102a013.

Doelsch, E. *et al.* (2003) 'Chemistry and structure of colloids obtained by hydrolysis of Fe(III) in the presence of SiO4 ligands', *Colloids and Surfaces A: Physicochemical and Engineering Aspects*, 217(1–3), pp. 121–128. doi: 10.1016/S0927-7757(02)00566-6.

Downward, L. *et al.* (2007) 'A variation of the F-test for determining statistical relevance of particular parameters in EXAFS fits', *AIP Conference Proceedings*, 882(2), pp. 129–131. doi: 10.1063/1.2644450.

Dreissig, I. *et al.* (2011) 'Formation of uranium(IV)-silica colloids at near-neutral pH', *Geochimica et Cosmochimica Acta*, 75(2), pp. 352–367. doi: 10.1016/j.gca.2010.10.011.

Duan, H. M. and Liu, S. Q. (2014) 'Functions of SiO2-Shells in Core-Shell Structured Particles', *Applied Mechanics and Materials*, 670–671, pp. 279–282. doi: 10.4028/www.scientific.net/AMM.670-671.279.

Ehrl, L. *et al.* (2009) 'Role of counterion association in colloidal stability', *Langmuir*, 25(5), pp. 2696–2702. doi: 10.1021/la803445y.

Elizondo-Villarreal, N. *et al.* (2016) 'Nanomodification of a natural clinoptilolite zeolite', *Reviews on Advanced Materials Science*, 47(1–2), pp. 74–78.

Elless, M. P. and Lee, S. Y. (1998) 'Uranium Solubility of Carbonate-Rich Uranium-Contaminated Soils', *Water, Air, and Soil Pollution*, 107(1/4), pp. 147–162. doi: 10.1023/A:1004982515941.

Espriu-Gascon, A. *et al.* (2018) 'Retention of cesium and strontium by uranophane, Ca(UO2)2(SiO3OH)2·5H2O', *Journal of Hazardous Materials*, 353, pp. 431–435. doi: 10.1016/j.jhazmat.2018.04.051.

Evans, H. T. (1963) 'Uranyl Ion Coordination', *Science*, 141(3576), pp. 154–158. doi: 10.1126/science.141.3576.154.

Fanghänel, T. and Neck, V. (2002) 'Aquatic chemistry and solubility phenomena of actinide oxides/hydroxides', *Pure and Applied Chemistry*, 74(10). doi: 10.1351/pac200274101895.

Farr, J. D., Schulze, R. K. and Honeyman, B. D. (2000) 'Aqueous Pu (IV) sorption on brucite', *Radiochimica Acta*, 88(9–11/2000), p. 675.

Farrow, C. L. *et al.* (2007) 'PDFfit2 and PDFgui: computer programs for studying nanostructure in crystals', *Journal of Physics: Condensed Matter*, 19(33), p. 335219. doi: 10.1088/0953-8984/19/33/335219.

Felmy, A. R. *et al.* (2003) 'The formation of Sr silicates at low temperature and the solubility product of tobermoritelike Sr5Si6O16(OH)25H2O', *American Mineralogist*, 88(1), pp. 73–79. doi: 10.2138/am-2003-0109.

Fischer, K. and Schmidt, M. (2016) 'Pitfalls and novel applications of particle sizing by dynamic light scattering', *Biomaterials*, 98, pp. 79–91. doi:

10.1016/j.biomaterials.2016.05.003.

Fleischer, M. (1995) *Glossary of mineral species*. 7th edn. Mineralogical Record, Tucson, AZ.

Fletcher, K. E. *et al.* (2010) 'U(VI) Reduction to Mononuclear U(IV) by Desulfitobacterium Species', *Environmental Science & Technology*, 44(12), pp. 4705–4709. doi: 10.1021/es903636c.

Flury, M., Mathison, J. O. N. B. and Harsh, J. B. (2002) 'In Situ Mobilization of Colloids and Transport of Cesium in Hanford Sediments', (509), pp. 5335–5341. doi: 10.1021/es025638k.

Fuchs, L. H. and Gebert, E. (1958) 'X-ray studies of synthetic coffinite, thorite and uranothorites', *The American Mineralogist*, 43, pp. 243–248.

Fuger, J., Haire, R. G. and Peterson, J. R. (1993) 'Molar enthalpies of formation of BaCmO3 and BaCfO3', *Journal of Alloys and Compounds*, 200(1–2), pp. 181–185. doi: 10.1016/0925-8388(93)90491-5.

Fujino, T., Yamashita, T. and Tagawa, H. (1988) 'Phase Relations and Crystal Chemistry of Solid Solution, SryU1-yO2+x', *Journal of Solid State Chemistry*, 73, pp. 544–555.

Fujita, Y. *et al.* (2004) 'Strontium incorporation into calcite generated by bacterial ureolysis', *Geochimica et Cosmochimica Acta*, 68(15), pp. 3261–3270. doi: 10.1016/j.gca.2003.12.018.

Fuller, A. J. *et al.* (2016) 'EXAFS Study of Sr sorption to Illite, Goethite, Chlorite, and Mixed Sediment under Hyperalkaline Conditions', *Langmuir*, 32(12), pp. 2937–2946. doi: 10.1021/acs.langmuir.5b04633.

Gebauer, D. *et al.* (2014) 'Pre-nucleation clusters as solute precursors in crystallisation', *Chem. Soc. Rev.*, 43(7), pp. 2348–2371. doi: 10.1039/C3CS60451A.

Glatter, O. and Kratky, O. (1982) *Small Angle X-ray Scattering*. London: Academic Press.

Gorman-Lewis, D. *et al.* (2008) 'Solubility measurements of the uranyl oxide hydrate phases metaschoepite, compreignacite, Na-compreignacite, becquerelite, and clarkeite', *Journal of Chemical Thermodynamics*, 40(6), pp. 980–990. doi:

10.1016/j.jct.2008.02.006.

Granath, K. A. (1958) ‘Solution properties of branched dextrans’, *Journal of Colloid Science*, 13(4), pp. 308–328. doi: 10.1016/0095-8522(58)90041-2.

Grasso, D. *et al.* (2002) ‘A review of non-DLVO interactions in environmental colloidal systems’, *Reviews in Environmental Science and Biotechnology*, 1(1), pp. 17–38. doi: 10.1023/A:1015146710500.

Gray, J., Jones, S. R. and Smith, A. D. (1995) ‘Related content Discharges to the environment from the Sellafield site , 1951-1992 Discharges to the environment from the Sellafield Site’, *Journal of Radiological Protection*, 15(2), pp. 99–131.

Greaux, S. *et al.* (2008) ‘Structural characterization of natural UO2 at pressures up to 82 GPa and temperatures up to 2200 K’, 93(October), pp. 1090–1098. doi: 10.2138/am.2008.2735.

Gregson, C. R., Hastings, J. J., *et al.* (2011) ‘Characterisation of plutonium species in alkaline liquors sampled from a UK legacy nuclear fuel storage pond’, *Analytical Methods*, 3(9), p. 1957. doi: 10.1039/c1ay05313b.

Gregson, C. R., Goddard, D. T., *et al.* (2011) ‘Combined electron microscopy and vibrational spectroscopy study of corroded Magnox sludge from a legacy spent nuclear fuel storage pond’, *Journal of Nuclear Materials*. Elsevier B.V., 412(1), pp. 145–156. doi: 10.1016/j.jnucmat.2011.02.046.

Grenthe, I. *et al.* (1984) ‘Studies on metal carbonate equilibria. Part 10. A solubility study of the complex formation in the uranium(<scp>VI</scp>)–water–carbon dioxide (g) system at 25 °C’, *J. Chem. Soc., Dalton Trans.*, (11), pp. 2439–2443. doi: 10.1039/DT9840002439.

Grenthe, I. *et al.* (1992) *Chemical Thermodynamics of Uranium*. 1st edn. Elsevier, New York.

Gubel, N. R. *et al.* (2013) *Introduction to Uranium. In: Morrell J., Jackson M. (eds) Uranium Processing and Properties.* New York, NY: Springer.

Guillaumont, R. *et al.* (2003) ‘Update on the chemical thermodynamics of uranium,

neptunium, plutonium, americium and technetium', *Chemical Thermodynamics*, 5, p. 919.

Guinier, A. and Fourner, G. (1955) *Small-Angle Scattering of X-rays*, *Wiley*. New York, NY.

Guo, X. *et al.* (2015) 'Thermodynamics of formation of coffinite, $USiO_4$', *Proceedings of the National Academy of Sciences*, 112(21), pp. 6551–6555. doi: 10.1073/pnas.1507441112.

He, B. B. (2009) 'Introduction', in *Two-Dimensional X-Ray Diffraction*. Hoboken, NJ, USA: John Wiley & Sons, Inc., pp. 1–27. doi: 10.1002/9780470502648.ch1.

Hennig, C., Emmerling, F., *et al.* (2010) 'Comparative investigation of the solution species [U (CO 3) 5] 6 −', pp. 1–4.

Hennig, C., Ikeda-Ohno, A., *et al.* (2010) 'Comparative investigation of the solution species [U(CO3)5]6- and the crystal structure of Na6[U(CO3)5].12H2O.', *Dalton transactions*, 39(15), pp. 3744–50. doi: 10.1039/b922624a.

Hennig, C. *et al.* (2013) 'Solid-state properties and colloidal stability of thorium(IV)–silica nanoparticles', *Geochimica et Cosmochimica Acta*, 103, pp. 197–212. doi: 10.1016/j.gca.2012.10.051.

Hicks, T. W., White, M. J. and Hooker, P. J. (2009) *Role of Bentonite in Determination of Thermal Limits on Geological Disposal Facility Design*.

Hiemenz, P. C. and Rajagopalan, R. (1997) *Principles of Colloid and Surface Chemistry, Third Edition*. 3rd edn. Marcel Dekker, Inc. New York.

Hilton, B. A. (2000) *Review of oxidation rates of DOE spent nuclear fuel : Part 1 : nuclear fuel.* Argonne, IL. doi: 10.2172/775264.

Honetschlägerová, L. *et al.* (2015) 'Enhanced colloidal stability of nanoscale zero valent iron particles in the presence of sodium silicate water glass', *Environmental Technology*, 36(3), pp. 358–365. doi: 10.1080/09593330.2014.977825.

Huang, J. *et al.* (1997) 'Investigation of vaporization thermodynamics of SrUO3 by means of mass spectrometry', *Journal of Nuclear Materials*, 247, pp. 17–20. doi: 10.1016/S0022-3115(97)00060-3.

Huber, F. *et al.* (2011) 'Sorption reversibility kinetics in the ternary system radionuclide–bentonite colloids/nanoparticles–granite fracture filling material', *Applied Geochemistry*, 26(12), pp. 2226–2237. doi: 10.1016/j.apgeochem.2011.08.005.

Hunt, R. D. *et al.* (2005) 'Monosodium Titanate in Hydrous Titanium Oxide Spheres for the Removal of Strontium and Key Actinides from Salt Solutions at the Savannah River Site', *Separation Science and Technology*, 40(14), pp. 2933–2946. doi: 10.1080/01496390500333210.

Husain, A. (1984) 'Charge development at the uranium oxide-solution interface', *Journal of Colloid and Interface Science*, 102(2), pp. 389–399. doi: 10.1016/0021-9797(84)90241-8.

Husar, R. *et al.* (2015) 'Formation of Neptunium(IV)–Silica Colloids at Near-Neutral and Slightly Alkaline pH', *Environmental Science & Technology*, 49(1), pp. 665–671. doi: 10.1021/es503877b.

Iler, R. K. (1979) *The chemistry of silica*.

Janeczek, J. and Ewing, R. C. (1992a) 'Dissolution and alteration of uraninite under reducing conditions', *Journal of Nuclear Materials*, 190(C), pp. 157–173. doi: 10.1016/0022-3115(92)90084-X.

Janeczek, J. and Ewing, R. C. (1992b) 'Structural formula of uraninite', *Journal of Nuclear Materials*, 190(C), pp. 128–132. doi: 10.1016/0022-3115(92)90082-V.

Johnson, A.-C. J. H. *et al.* (2008) 'Aggregation of Nanosized Colloidal Silica in the Presence of Various Alkali Cations Investigated by the Electrospray Technique', *Langmuir*, 24(22), pp. 12798–12806. doi: 10.1021/la8026122.

Kadish, K. M. *et al.* (1988) 'First example of a trimeric metalloporphyrin. Synthesis, electrochemical, and spectroelectrochemical studies of [(P)Th(OH)2]3 where P is the dianion of octaethyl- or tetraphenylporphyrin. Crystal structure of a dihydrated trinuclear complex of dihydroxy(5', *Journal of the American Chemical Society*, 110(19), pp. 6455–6462. doi: 10.1021/ja00227a027.

Kaminski, M. . and Goldberg, M. . (2002) 'Aqueous corrosion of aluminum-based nuclear fuel', *Journal of Nuclear Materials*, 304(2–3), pp. 182–188. doi: 10.1016/S0022-

3115(02)00881-4.

Kaminski, M. D. *et al.* (2005) 'Colloids from the aqueous corrosion of uranium nuclear fuel', *Journal of Nuclear Materials*, 347(1–2), pp. 77–87. doi: 10.1016/j.jnucmat.2005.07.009.

Kaplun, E. V *et al.* (1992) 'Kinetics of metal ion sorption on clinoptilolite', *Russian Chemical Bulletin*, 1(2), pp. 201–204.

Kellermeier, M. *et al.* (2012) 'Colloidal stabilization of calcium carbonate prenucleation clusters with silica', *Advanced Functional Materials*, 22(20), pp. 4301–4311. doi: 10.1002/adfm.201200953.

Kersting, A. B. *et al.* (1999) 'Migration of plutonium in ground water at the Nevada Test Site', *Nature*, 397(6714), pp. 56–59. doi: 10.1038/16231.

Kersting, A. B. (2013) 'Plutonium Transport in the Environment', *Inorganic Chemistry*, 52(7), pp. 3533–3546. doi: 10.1021/ic3018908.

Kirillov, S. A., Lisnycha, T. V. and Pendelyuk, O. I. (2006) 'Appraisal of Mixed Amorphous Manganese Oxide/Titanium Oxide Sorbents for the Removal of Strontium-90 from Solutions, with Special Reference to Savannah River Site and Chernobyl Radioactive Waste Simulants', *Adsorption Science & Technology*, 24(10), pp. 895–906. doi: 10.1260/026361707781421979.

Knope, K. E. *et al.* (2011) 'Synthesis and Characterization of Thorium(IV) Sulfates', *Inorganic Chemistry*, 50(17), pp. 8621–8629. doi: 10.1021/ic201175u.

Knope, K. E. *et al.* (2012) 'Thorium(IV)-selenate clusters containing an octanuclear Th(IV) hydroxide/oxide core', *Inorganic Chemistry*, 51(7), pp. 4239–4249. doi: 10.1021/ic202706s.

Knope, K. E. and Soderholm, L. (2013) 'Solution and solid-state structural chemistry of actinide hydrates and their hydrolysis and condensation products', *Chemical Reviews*, 113(2), pp. 944–994. doi: 10.1021/cr300212f.

Kobayashi, Y. *et al.* (2016) 'Stabilization of silica-coated silver iodide nanoparticles by ethanol-washing', *Pigment & Resin Technology*, 45(2), pp. 99–105. doi: 10.1108/PRT-10-

2014-0083.

Koopal, L. K. (1996) 'Mineral hydroxides: From homogeneous to heterogeneous modelling', *Electrochimica Acta*, 41(14 SPEC. ISS.), pp. 2293–2306. doi: 10.1016/0013-4686(96)00059-X.

Kozai, N., Ohnuki, T. and Iwatsuki, T. (2013) 'Characterization of saline groundwater at Horonobe, Hokkaido, Japan by SEC-UV-ICP-MS: Speciation of uranium and iodine', *Water Research*. Elsevier Ltd, 47(4), pp. 1570–1584. doi: 10.1016/j.watres.2012.12.017.

Labs, S. *et al.* (2013) 'Synthesis of Co ffi nite, USiO 4 , and Structural Investigations of U'.

Laurent, T. C. and Granath, K. a (1967) 'Fractionation of dextran and Ficoll by chromatography on Sephadex G-200.', *Biochimica et biophysica acta*, 136(2), pp. 191–8. doi: 10.1016/0304-4165(67)90063-3.

Livens, F. R. and Baxter, M. S. (1988) 'Chemical associations of artificial radionuclides in Cumbrian soils', *Journal of Environmental Radioactivity*, 7(1), pp. 75–86. doi: 10.1016/0265-931X(88)90043-4.

Lumetta, G. J., Wagner, M. J. and Carlson, C. D. (1996) 'ACTINIDE, STRONTIUM, AND CESIUM REMOVAL FROM HANFORD RADIOACTIVE TANK SLUDGE', *Solvent Extraction and Ion Exchange*, 14(1), pp. 35–60. doi: 10.1080/07366299608918325.

Maher, Z. *et al.* (2016) 'Americium and plutonium association with magnesium hydroxide colloids in alkaline nuclear industry process environments', *Journal of Nuclear Materials*. Elsevier B.V, 468, pp. 84–96. doi: 10.1016/j.jnucmat.2015.11.010.

Marshall, T. A. *et al.* (2015) 'Uranium fate during crystallization of magnetite from ferrihydrite in conditions relevant to the disposal of radioactive waste', *Mineralogical Magazine*, 79(6), pp. 1265–1274. doi: 10.1180/minmag.2015.079.6.02.

Maruyama, T. *et al.* (2001) 'Mechanism of bovine serum albumin aggregation during ultrafiltration', *Biotechnology and Bioengineering*, 75(2), pp. 233–238. doi: 10.1002/bit.10001.

Mayer, T. D. and Jarrell, W. M. (1996) 'Formation and stability of iron(II) oxidation products under natural concentrations of dissolved silica', *Water Research*, 30(5), pp.

1208–1214. doi: 10.1016/0043-1354(95)00265-0.

Mesbah, A. *et al.* (2015) 'Coffinite, USiO 4 , Is Abundant in Nature: So Why Is It So Difficult To Synthesize?', *Inorganic Chemistry*, 54(14), pp. 6687–6696. doi: 10.1021/ic502808n.

Michen, B. *et al.* (2015) 'Avoiding drying-artifacts in transmission electron microscopy: Characterizing the size and colloidal state of nanoparticles', *Scientific Reports*, 5(1), p. 9793. doi: 10.1038/srep09793.

Minglu, Y., Shijun, L. and Chunkou, Q. (1994) 'Investigation of Sorption and Migration of 90Sr on Clinoptilolite and Mordenite', *Journal of Nuclear and Radiochemistry*, 26(14), pp. 199–204. Available at: inis.iaea.org/search/search.aspx?orig_q=RN:26049864.

Missana, T. and Adell, A. (2000) 'On the Applicability of DLVO Theory to the Prediction of Clay Colloids Stability', *Journal of Colloid and Interface Science*, 230(1), pp. 150–156. doi: 10.1006/jcis.2000.7003.

Moench, R. H. (1962) 'Properties and paragenesis of coffinite from the Woodrow mine, New Mexico', *American Mineralogist*, 47, pp. 26–33.

Möri, A. *et al.* (2003) 'The colloid and radionuclide retardation experiment at the Grimsel Test Site: influence of bentonite colloids on radionuclide migration in a fractured rock', *Colloids and Surfaces A: Physicochemical and Engineering Aspects*, 217(1–3), pp. 33–47. doi: 10.1016/S0927-7757(02)00556-3.

Morin, G. *et al.* (2016) 'Mononuclear U(IV) complexes and ningyoite as major uranium species in lake sediments', *Letter Geochemical Perspectives Letters Geochem. Persp. Let. Persp. Let*, 2(2), pp. 78–86. doi: 10.7185/geochemlet.1608.

Moriyama, H. *et al.* (1999) 'Analysis of Mononuclear Hydrolysis Constants of Actinide Ions by Hard Sphere Model', *Radiochimica Acta*, 87(3–4). doi: 10.1524/ract.1999.87.34.97.

Mougel, V., Pécaut, J. and Mazzanti, M. (2012) 'New polynuclear U(<scp>iv</scp>)–U(<scp>v</scp>) complexes from U(<scp>iv</scp>) mediated uranyl(<scp>v</scp>) disproportionation', *Chem. Commun.*, 48(6), pp. 868–870. doi: 10.1039/C1CC16646H.

Narayanan, T. (2014) 'Small-Angle Scattering', in *Structure from Diffraction Methods*.

Chichester, UK: John Wiley & Sons, Ltd, pp. 259–324. doi: 10.1002/9781118695708.ch5.

Natrajan, L. *et al.* (2005) 'Practical Synthetic Routes to Solvates of U(OTf) 3 : X-ray Crystal Structure of [U(OTf) 3 (MeCN) 3] n , a Unique U(III) Coordination Polymer', *Inorganic Chemistry*, 44(17), pp. 6115–6121. doi: 10.1021/ic0505652.

NDA (2016) *Strategy Effective from April 2016*.

NDA (2017a) *Radioactive Wastes in the UK: A Summary of the 2016 Inventory*.

NDA (2017b) *Radioactive Wastes in the UK: UK Radioactive Waste Inventory Report*.

Neck, V. *et al.* (2002) 'Solubility of amorphous Th(IV) hydroxide - Application of LIBD to determine the solubility product and EXAFS for aqueous speciation', *Radiochimica Acta*, 90(9–11), pp. 485–494. doi: 10.1524/ract.2002.90.9-11_2002.485.

Neck, V. *et al.* (2007) 'Solubility and redox reactions of Pu(IV) hydrous oxide: Evidence for the formation of PuO2+x(s, hyd)', *Radiochimica Acta*, 95(4). doi: 10.1524/ract.2007.95.4.193.

Neck, V. and Kim, J. I. (2000) 'An electrostatic approach for the prediction of actinide complexation constants with inorganic ligands-application to carbonate complexes', *Radiochimica Acta*, 88(9–11). doi: 10.1524/ract.2000.88.9-11.815.

Neck, V. and Kim, J. I. (2001) 'Solubility and hydrolysis of tretavalent actinides', *Radiochim. Acta*, 89, pp. 1–16.

Neill, T. S., Morris, K., Pearce, C. I., Sherriff, N. K. and Shaw, S. (2018) 'Interactions of Sr with UO2 and U(IV)-silicate phases', *Journal of Hazardous Materials*, (In draft).

Neill, T. S., Morris, K., Pearce, C. I., Sherriff, N. K., Burke, M. G., *et al.* (2018) 'Stability, composition and core-shell particle structure of uranium(IV)-silicate colloids', *Environmental Science & Technology*. doi: 10.1021/acs.est.8b01756.

Newsome, L., Morris, K. and Lloyd, J. R. (2015) 'Uranium Biominerals Precipitated by an Environmental Isolate of Serratia under Anaerobic Conditions', *PLOS ONE*. Edited by P. J. Janssen, 10(7), p. e0132392. doi: 10.1371/journal.pone.0132392.

Nishi, F. (1997) 'Strontium Metasilicate, SrSiO 3', *Acta Crystallographica Section C Crystal*

Structure Communications, 53(5), pp. 534–536. doi: 10.1107/S0108270196015338.

Nocton, G. *et al.* (2010) 'Ligand assisted cleavage of uranium oxo-clusters.', *Chemical communications (Cambridge, England)*, 46(16), pp. 2757–9. doi: 10.1039/b926580e.

O'Day, P. A. *et al.* (2000) 'X-Ray Absorption Spectroscopy of Strontium(II) Coordination', *Journal of Colloid and Interface Science*, 222(2), pp. 184–197. doi: 10.1006/jcis.1999.6621.

van Oss, C. J. (2008) 'Ch 01 General and Historical Introduction', *The Properties of Water and their Role in Colloidal and Biological Systems*, 16(08), pp. 1–9. doi: 10.1016/S1573-4285(08)00201-9.

Park, S.-J. and Seo, M.-K. (2011) 'Intermolecular Force', in *Interface Science and Technology*. Academic Press, pp. 1–57.

Parkhurst, D. L. and Appelo, C. A. J. (2013) 'Description of Input and Examples for PHREEQC Version 3 — A Computer Program for Speciation , Batch-Reaction , One-Dimensional Transport , and Inverse Geochemical Calculations. U.S. Geological Survey Techniques and Methods, book 6, chapter A43, 497 p.', *U.S. Geological Survey Techniques and Methods, book 6, chapter A43*, p. 6–43A. doi: 10.1016/0029-6554(94)90020-5.

Parkman, R. H. *et al.* (1998) 'A study of the interaction of strontium ions in aqueous solution with the surfaces of calcite and kaolinite', *Geochimica et Cosmochimica Acta*, 62(9), pp. 1481–1492. doi: 10.1016/S0016-7037(98)00072-6.

Parry, S. a. *et al.* (2011) 'Plutonium behaviour in nuclear fuel storage pond effluents', *Energy & Environmental Science*, 4(4), p. 1462. doi: 10.1039/c0ee00390e.

Pauw, B. R. *et al.* (2013) 'Improvements and considerations for size distribution retrieval from small-angle scattering data by Monte Carlo methods', *Journal of Applied Crystallography*. International Union of Crystallography, 46(2), pp. 365–371. doi: 10.1107/S0021889813001295.

Perriot, R. *et al.* (2015) 'Diffusion of Zr, Ru, Ce, Y, La, Sr and Ba fission products in UO 2', *Journal of Nuclear Materials*. Elsevier B.V., 459, pp. 90–96. doi: 10.1016/j.jnucmat.2015.01.001.

Pitois, A. *et al.* (2008) 'Magnesium hydroxide bulk and colloid-associated 152Eu in an alkaline environment: colloid characterisation and sorption properties in the presence and absence of carbonate', *Journal of Environmental Monitoring*, 10(3), p. 315. doi: 10.1039/b714636c.

Pohl, R. W. H. *et al.* (2009) 'A New 5,5'-Bitetrazole Thorium(IV) Compound: Synthesis, Crystal Structure and Quantum Chemical Investigation', *European Journal of Inorganic Chemistry*, 2009(17), pp. 2472–2476. doi: 10.1002/ejic.200900152.

Pointeau, V. *et al.* (2009) 'Synthesis and characterization of coffinite', *Journal of Nuclear Materials*. Elsevier B.V., 393(3), pp. 449–458. doi: 10.1016/j.jnucmat.2009.06.030.

Priyadarshini, N. *et al.* (2013) 'A combined spectroscopic and light scattering study of hydrolysis of uranium(VI) leading to colloid formation in aqueous solutions', *Journal of Radioanalytical and Nuclear Chemistry*, 298(3), pp. 1923–1931. doi: 10.1007/s10967-013-2624-6.

Proffen, T. *et al.* (2003) 'Structural analysis of complex materials using the atomic pair distribution function — a practical guide', *Zeitschrift für Kristallographie - Crystalline Materials*, 218(2). doi: 10.1524/zkri.218.2.132.20664.

Proffen, T. *et al.* (2005) 'Atomic pair distribution function analysis of materials containing crystalline and amorphous phases', *Zeitschrift für Kristallographie - Crystalline Materials*, 220(12). doi: 10.1524/zkri.2005.220.12.1002.

Rai, D. *et al.* (1998) 'A Thermodynamic Model for the Solubility of U02(am) in the Aqueous K+-Na+-HCO-3-CO2-3 -OH--H2O System', *Radiochimica Acta*, 82(s1). doi: 10.1524/ract.1998.82.special-issue.17.

Rai, D. *et al.* (2008) 'Thermodynamic model for ThO2(am) solubility in alkaline silica solutions', *Journal of Solution Chemistry*, 37(12), pp. 1725–1746. doi: 10.1007/s10953-008-9344-5.

Ram, R. *et al.* (2013) 'Chemical and micro-structural characterisation studies on natural uraninite and associated gangue minerals', *Minerals Engineering*, 45, pp. 159–169. doi: 10.1016/j.mineng.2013.02.004.

Ramos, A. P. (2017) 'Dynamic Light Scattering Applied to Nanoparticle Characterization',

in *Nanocharacterization Techniques*. Elsevier, pp. 99–110. doi: 10.1016/B978-0-323-49778-7.00004-7.

Ravel, B. and Newville, M. (2005) 'ATHENA , ARTEMIS , HEPHAESTUS : data analysis for X-ray absorption spectroscopy using IFEFFIT', *Journal of Synchrotron Radiation*. International Union of Crystallography, 12(4), pp. 537–541. doi: 10.1107/S0909049505012719.

Roberts, H. E. *et al.* (2017) 'Uranium(V) Incorporation Mechanisms and Stability in Fe(II)/Fe(III) (oxyhydr)Oxides', *Environmental Science and Technology Letters*, 4(10), pp. 421–426. doi: 10.1021/acs.estlett.7b00348.

Rogers, R. D., Bond, A. H. and Witt, M. M. (1991) 'Macrocycle complexation chemistry 34. Polyethylene glycol and glycolate complexes of Th4+. Preparation and structural characterization of [ThCl3(pentaethylene glycol)]Cl·CH3CN and the (Th4+)4 cluster, [Th4Cl8(O)(tetraethylene glycolate)3]·3CH3CN', *Inorganica Chimica Acta*, 182(1), pp. 9–17. doi: 10.1016/S0020-1693(00)85180-4.

Roy, S. B. and Dzombak, D. A. (1996) 'Na+Ca2+ Exchange effects in the detachment of latex colloids deposited in glass bead porous media', *Colloids and Surfaces A: Physicochemical and Engineering Aspects*, 119(2–3), pp. 133–139. doi: 10.1016/S0927-7757(96)03764-8.

RWM (2008) *Geological Disposal Options for High Level Waste and Spent Fuel*.

RWM (2011) *Bentonite – A Review of key properties, processes and issues for consideration in the UK context*.

Sahai, N. *et al.* (2000) 'X-Ray Absorption Spectroscopy of Strontium(II) Coordination', *Journal of Colloid and Interface Science*, 222(2), pp. 198–212. doi: 10.1006/jcis.1999.6562.

Salbu, B. *et al.* (2003) 'Oxidation states of uranium in DU particles from Kosovo', *Journal of Environmental Radioactivity*, 64(2–3), pp. 167–173. doi: 10.1016/S0265-931X(02)00047-4.

Schindler, M. *et al.* (2017) 'Mobilization and agglomeration of uraninite nanoparticles: A nano-mineralogical study of samples from the Matoush Uranium ore deposit',

American Mineralogist, 102(9), pp. 1776–1787. doi: 10.2138/am-2017-5984.

Sellafield Ltd (2014) *Groundwater Monitoring at Sellafield Annual Data Review 2014*.

Sellafield Ltd (2017) *Context Plan (2017-2026)*.

Shannon, R. D. (1976) 'Revised effective ionic radii and systematic studies of interatomic distances in halides and chalcogenides', *Acta Crystallographica Section A*, 32(5), pp. 751–767. doi: 10.1107/S0567739476001551.

Sinkov, S. I., Delegard, C. H. and Schmidt, A. J. (2008) *Preparation and Characterization of Uranium Oxides in Support of the K Basin Sludge Treatment Project*, *PNNL17678*. Richland, WA. doi: 10.2172/940228.

Small, J. S. and Thompson, O. R. (2009) 'Modelling the spatial and temporal evolution of pH in the cementitious backfill of geological disposal facility', *Materials Research Society Symposium Proceedings*, 1124, pp. 327–332.

Smith, M. C. *et al.* (2017) 'Zeta potential: a case study of cationic, anionic, and neutral liposomes', *Analytical and Bioanalytical Chemistry*, 409(24), pp. 5779–5787. doi: 10.1007/s00216-017-0527-z.

Soltis, J. A. *et al.* (2016) 'Cation-Dependent Hierarchical Assembly of U60 Nanoclusters into Macro-Ion Assemblies Imaged via Cryogenic Transmission Electron Microscopy', *Journal of the American Chemical Society*, 138(1), pp. 191–198. doi: 10.1021/jacs.5b09802.

Soper, A. K. and Barney, E. R. (2011) 'Extracting the pair distribution function from white-beam X-ray total scattering data', *Journal of Applied Crystallography*. International Union of Crystallography, 44(4), pp. 714–726. doi: 10.1107/S0021889811021455.

Stumm, W. and Morgan, J. J. (1995) *Aquatic Chemistry: Chemical Equilibria and Rates in Natural Waters, 3rd Edition*. John Wiley & Sons Inc.

Sureda, R. *et al.* (2010) 'Sorption of strontium on uranyl peroxide: Implications for a high-level nuclear waste repository', *Journal of Hazardous Materials*. Elsevier B.V., 181(1–3), pp. 881–885. doi: 10.1016/j.jhazmat.2010.05.095.

Suzuki, Y. *et al.* (2002) 'Radionuclide contamination: Nanometre-size products of

uranium bioreduction', *Nature*, 419(6903), pp. 134–134. doi: 10.1038/419134a.

Suzuki, Y. *et al.* (2016) 'Formation and Geological Sequestration of Uranium Nanoparticles in Deep Granitic Aquifer', *Scientific Reports*. Nature Publishing Group, 6(1), p. 22701. doi: 10.1038/srep22701.

Swanton, S. W. and Vines, S. (2003) 'Equilibrium leach tests: Colloid generation and the association of radionuclides with colloids under simulated repository conditions', *Colloids and Surfaces A: Physicochemical and Engineering Aspects*, 217(1–3), pp. 71–79. doi: 10.1016/S0927-7757(02)00561-7.

Szenknect, S. *et al.* (2016) 'First experimental determination of the solubility constant of coffinite', *Geochimica et Cosmochimica Acta*, 181, pp. 36–53. doi: 10.1016/j.gca.2016.02.010.

Tadros, T. (2011) 'Colloid Stability Using Polymeric Surfactants', in *Colloid Stability*. Weinheim, Germany: Wiley-VCH Verlag GmbH & Co. KGaA, pp. 235–262. doi: 10.1002/9783527631070.ch10.

Takao, S. *et al.* (2009) 'First Hexanuclear U IV and Th IV Formate Complexes - Structure and Stability Range in Aqueous Solution', *European Journal of Inorganic Chemistry*, 2009(32), pp. 4771–4775. doi: 10.1002/ejic.200900899.

Tang, X. F., Yang, Z. G. and Wang, W. J. (2010) 'A simple way of preparing high-concentration and high-purity nano copper colloid for conductive ink in inkjet printing technology', *Colloids and Surfaces A: Physicochemical and Engineering Aspects*. Elsevier B.V., 360(1–3), pp. 99–104. doi: 10.1016/j.colsurfa.2010.02.011.

Taylor, P. D., Jugdaohsingh, R. and Powell, J. J. (1997) 'Soluble Silica with High Affinity for Aluminum under Physiological and Natural Conditions', *Journal of the American Chemical Society*, 119(38), pp. 8852–8856. doi: 10.1021/ja964476n.

Taylor, S. R. (1964) 'Abundance of elements in the crust: A new table', *Geochimica and Cosmochimica Acta*, 28, pp. 1273–1285.

Thiyagarajan, P. *et al.* (1990) 'Plutonium (IV) polymers in aqueous and organic media', *Inorganic Chemistry*, 29(10), pp. 1902–1907.

Thomas, S. and Farouq Ali, S. M. (1990) 'Micellar and surfactant solution properties in relation to tertiary oil recovery', in *CHEMECA '90, Australasian Chemical Engineering Conference*. Dep of Min-Met-Petroleum Engineering, Edmonton, Canada, pp. 985–992. Available at: http://www.scopus.com/inward/record.url?eid=2-s2.0-0025593245&partnerID=40&md5=71fc8c9fe30272a2cadafb5fc70053de.

Tits, J. *et al.* (2006) 'Strontium binding by calcium silicate hydrates', *Journal of Colloid and Interface Science*, 300(1), pp. 78–87. doi: 10.1016/j.jcis.2006.03.043.

Tobler, D. J., Shaw, S. and Benning, L. G. (2009) 'Quantification of initial steps of nucleation and growth of silica nanoparticles: An in-situ SAXS and DLS study', *Geochimica et Cosmochimica Acta*. Elsevier Ltd, 73(18), pp. 5377–5393. doi: 10.1016/j.gca.2009.06.002.

Tschapek, M. and Sanchez, R. M. T. (1976) 'The stability of silica and quartz suspensions', *Journal of Colloid and Interface Science*, 54(3), pp. 460–461. doi: 10.1016/0021-9797(76)90329-5.

Valle-Delgado, J. J. *et al.* (2005) 'Hydration forces between silica surfaces: Experimental data and predictions from different theories', *The Journal of Chemical Physics*, 123(3), p. 034708. doi: 10.1063/1.1954747.

van Veelen, A. *et al.* (2012) 'Uranium uptake onto Magnox sludge minerals studied using EXAFS', *Mineralogical Magazine*, 76(8), pp. 3095–3104. doi: 10.1180/minmag.2012.076.8.24.

Verwey, E. J. W. (1947) 'Theory of the Stability of Lyophobic Colloids.', *The Journal of Physical and Colloid Chemistry*, 51(3), pp. 631–636. doi: 10.1021/j150453a001.

Vilks, P. and Baik, M. H. (2001) 'Laboratory migration experiments with radionuclides and natural colloids in a granite fracture', *Journal of Contaminant Hydrology*, 47(2–4), pp. 197–210. doi: 10.1016/S0169-7722(00)00149-2.

Vilks, P. and Laboratories, W. (1991) 'Natural colloids and suspended particles in the Whitesheli Research Area, Manitoba, Canada, and their potential effect on radiocolioid formation', *Applied Geochemistry*, 6, pp. 565–574.

Wallace, S. H. *et al.* (2012) 'Effect of groundwater pH and ionic strength on strontium

sorption in aquifer sediments: Implications for 90Sr mobility at contaminated nuclear sites', *Applied Geochemistry*. Elsevier Ltd, 27(8), pp. 1482–1491. doi: 10.1016/j.apgeochem.2012.04.007.

Wallace, S. H. *et al.* (2013) 'Alteration of sediments by hyperalkaline k-rich cement leachate: Implications for strontium adsorption and incorporation', *Environmental Science and Technology*, 47(8), pp. 3694–3700. doi: 10.1021/es3051982.

Walther, C. *et al.* (2009) 'New insights in the formation processes of Pu(IV) colloids', *Radiochimica Acta*, 97(4–5). doi: 10.1524/ract.2009.1595.

Wang, Y. *et al.* (2013) 'Mobile uranium(IV)-bearing colloids in a mining-impacted wetland', *Nature Communications*. Nature Publishing Group, 4(May), pp. 1–9. doi: 10.1038/ncomms3942.

Weatherill, J. S. *et al.* (2016) 'Ferrihydrite Formation: The Role of Fe 13 Keggin Clusters', *Environmental Science & Technology*, p. acs.est.6b02481. doi: 10.1021/acs.est.6b02481.

Wieland, E. *et al.* (2008) 'Strontium Uptake by Cementitious Materials', *Environmental Science & Technology*, 42(2), pp. 403–409. doi: 10.1021/es071227y.

Williams, D. B. and Carter, C. B. (2009) *Transmission Electron Microscopy*. Boston, MA: Springer US. doi: 10.1007/978-0-387-76501-3.

Willmott, P. (2011) 'Scattering Techniques', in *An Introduction to Synchrotron Radiation*. Chichester, UK: John Wiley & Sons, Ltd, pp. 133–221. doi: 10.1002/9781119970958.ch5.

Wilson, P. D. (1996) *The Nuclear Feul Cycle: From Ore to Waste*. Oxford University Press, Oxford.

Wolthoorn, A., Temminghoff, E. J. M. and van Riemsdijk, W. H. (2004) 'Effect of synthetic iron colloids on the microbiological NH4+ removal process during groundwater purification', *Water Research*, 38(7), pp. 1884–1892. doi: 10.1016/j.watres.2003.12.026.

Yamanaka, T., Hirai, N. and Komatsu, Y. (2002) 'Structure change of Ca 1− x Sr x TiO 3 perovskite with composition and pressure', *American Mineralogist*, 87(8–9), pp. 1183–1189. doi: 10.2138/am-2002-8-917.

Yotsumoto, H. and Yoon, R.-H. (1993) 'Application of Extended DLVO Theory: II. Stability

of Silica Suspensions', *Journal of Colloid and Interface Science*, pp. 434–441. doi: 10.1006/jcis.1993.1206.

Zänker, H. *et al.* (2016) 'Oxyhydroxy Silicate Colloids: A New Type of Waterborne Actinide(IV) Colloids', *ChemistryOpen*, 5(3), pp. 174–182. doi: 10.1002/open.201500207.

Zänker, H. and Hennig, C. (2014) 'Colloid-borne forms of tetravalent actinides: A brief review', *Journal of Contaminant Hydrology*. Elsevier B.V., 157, pp. 87–105. doi: 10.1016/j.jconhyd.2013.11.004.

Appendix 1:UV-vis spectra

A1.1. UV-vis spectra of U(IV).HCl and U(IV)-carbonate solutions

UV-vis was used to screen for oxidation in samples due to the formation of a characteristic multiplet at 400-475 nm which is present when dissolved $U(VI)O_2^{2+}$ complexes are present. Due to the high carbonate concentrations in many of the experiments in this project, any oxidation of U(IV) to U(VI) would result in the dissolution of the oxidised U(VI), which would be detectable using UV-vis spectroscopy.

Solutions from U(IV).HCl and U(IV)-carbonate stock solutions were periodically analysed for evidence of oxidation. Figure A1.1 shows UV-vis spectra for these two stock solutions (both 20 mM U). Figure A1.2 shows UV-vis spectra for U(IV)-silicate colloidal dispersion (4 mM Si, pH 9) and an oxidised U(IV)-silicate sample, containing dissolved U(VI)-carbonate (both 1 mM U). The U(VI) sample shows a characteristic multiplet at 400-475 nm which is absent in all of the other samples, as shown in Figure A1.3. This multiplet was absent in all of the other systems, indicating oxidation had not occurred.

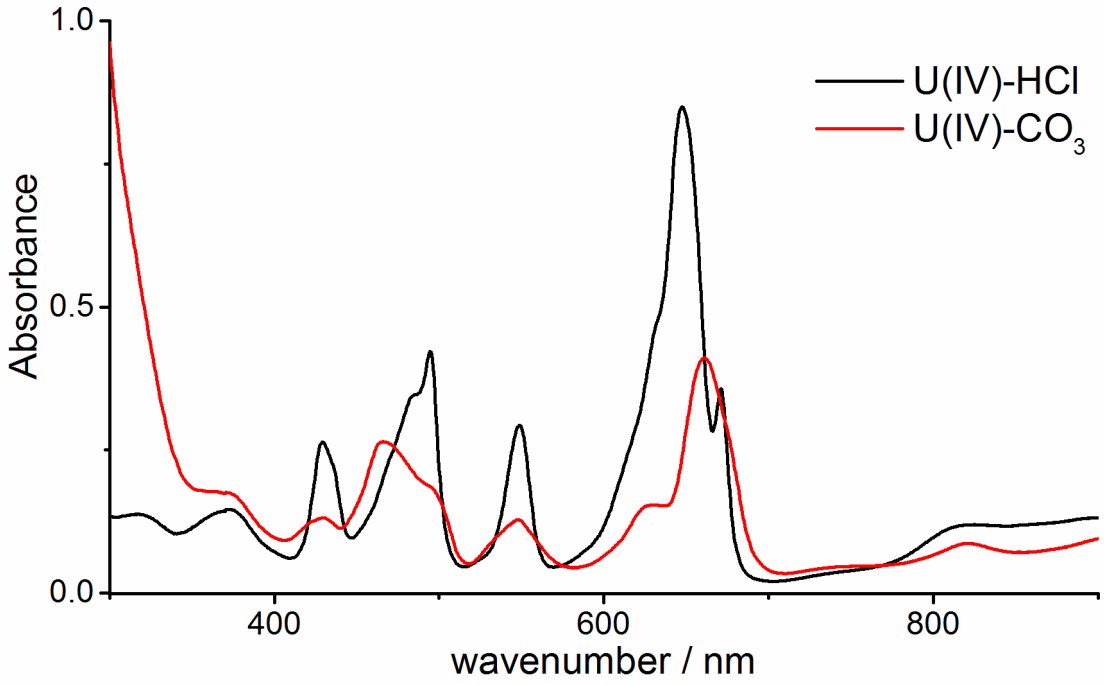

Figure A1.1: UV-vis spectra of U(IV).HCl (20 mM U(IV) in 0.1 M HCl) and U(IV)-carbonate (20 mM U(IV) in 1 M NaHCO3) solutions.

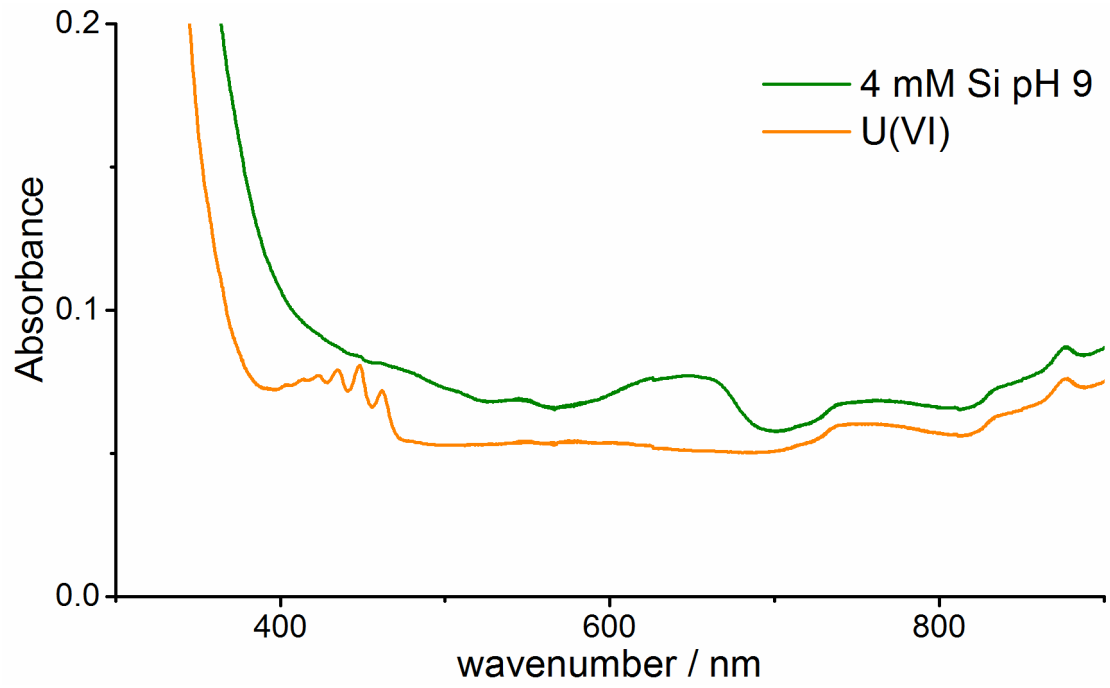

Figure A1.2: UV-vis spectra of U(IV)-silicate colloid (4 mM Si pH 9 system) and U(VI) generated by exposure of U(IV) to air for 1 week. U(VI) showing characteristic multiplet of peaks at 400-475 nm.

Figure A1.1:

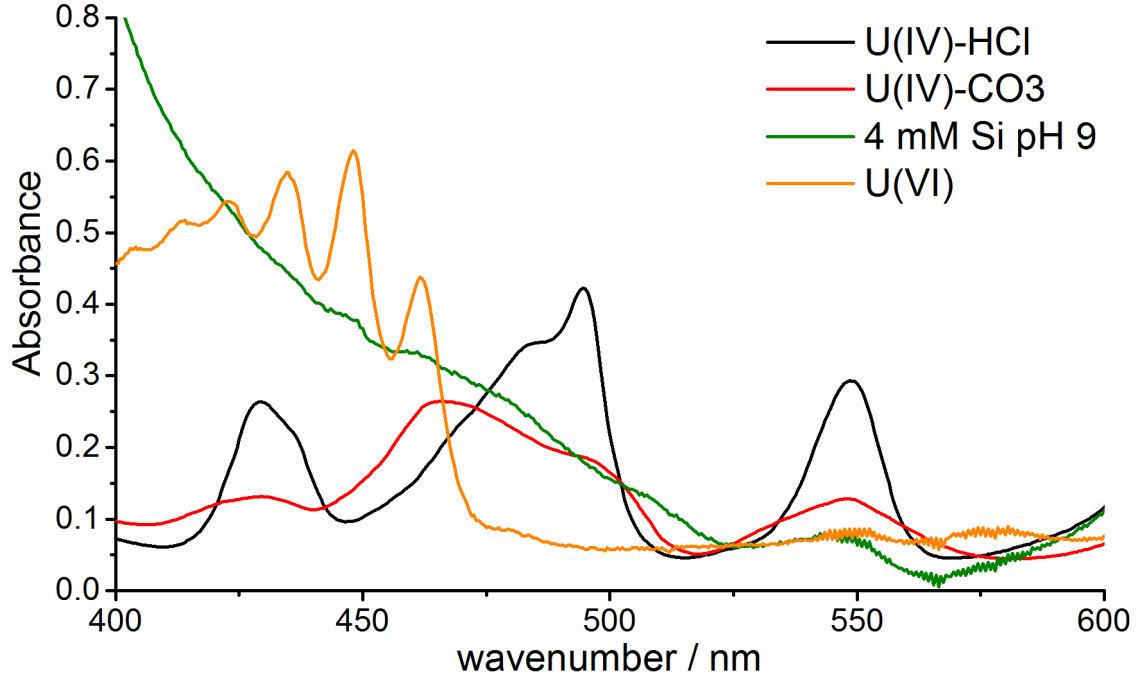

Figure A1. 3: Higher resolution UV-vis spectra of all 4 samples shown in Figure A.1 and A.2, highlighting the absence of a multiplet at 400-475 nm in the U(IV) systems. 4 mM Si pH 9 and U(VI) spectra have been scaled to correct for lower concentrations in samples.

Appendix 2: Conference Presentations

A2.1. Oral presentations:

- **American Chemical Society's Spring Meeting**, New Orleans, USA (March 2018)
- **Sellafield/NNL Learning From Experience (LFE) Meeting**, Workington, UK (September 2017)
- **Joint MinSoc Redox meeting**, Manchester, UK (June 2017)
- **Actinide XAS,** Oxford, UK (April 2017)
- **Effluents Presentation Day,** Dalton Cumbrian Facility, UK (April 2017)
- **Sellafield Research Day,** Manchester, UK (February 2017)
- **Sellafield/NNL Learning From Experience (LFE) Meeting**, Workington, UK (November 2016)
- **3rd Dalton Day Symposium**, Manchester, UK (November 2016)
- **9th International Nuclear and Radiochemistry Conference**, Helsinki, Finland (September 2016)
- **Environmental Mineralogy Group Research in Progress Meeting**, Bristol, UK (June 2016)
- **Sellafield Research Day**, Manchester (January 2016)
- **Sellafield Research Day**, Manchester (January 2015)

A2.2. Poster presentations

- **Frontiers in Environmental Radioactivity**, London, UK (January 2016)